ulm university universität
uulm

**University of Ulm** | 89069 Ulm | Germany

**Institute of Experimental Physics**
Head of department:
Prof. Dr. Othmar Marti

# Integrin and cell type specific traction force generation and the impact of extrinsic and intrinsic factors

## Dissertation

zur Erlangung des Doktorgrades Dr. rer. nat. der Fakultät
für Naturwissenschaften der Universität Ulm

vorgelegt von **Maja Gulic**

aus Ehingen/Donau

2016

Supervised by Prof. Dr. Kay-Eberhard Gottschalk, University of Ulm

Dean in office of the Faculty of Natural Sciences: Prof. Dr. Peter Dürre

First referee: Prof. Dr. Kay-Eberhard Gottschalk, University of Ulm

Second referee: Prof. Dr. Paul Walther, University of Ulm

Day of doctoral completion: 14.10.2016

# Contents

# 1 Introduction

Studying the fundamentals of the functionality of cells helps gaining insight into yet unknown pathways and connections regarding the organisation of cells and reaction to environmental influences. The aim of such studies is to understand the complexity of cells and find possibilities to create markers for diseases or even manipulate cell behaviour in terms of disease prevention, progress inhibition or even cure. Several methods have been developed in the past decades to analyse different components of the cell and their correlation. Genetics and proteomics are fields of study where molecular pathways and signalling cascades are unraveled, to better understand the machinery of the cell system. In recent years, parts of the emerging field of biophysics try to highlight physical aspects of cell behaviour and connect these to molecular pathways. Different methods have been developed to study the elasticity of cells, the unfolding of membrane proteins, or test the physical properties of the cytoskeleton.

One particular field of study is cell traction force microscopy. Cells adhering to and migrating over substrates generate forces on these substrates via a complex machinery. Membrane spanning proteins, so called integrins, attach to extracellular proteins deposited on the substrate. Inside the cell integrins are connected to the cyoskeleton through various proteins forming a complex. How exactly the process of force transduction is working is not yet fully understood due to the complexity of the system. To study the forces that are generated by the cell on the substrate, the displacement of it can be analysed. Starting with the simple observation of substrate wrinkling during cell adhesion and migration, methods got more advanced and precise. Today there are highly developed computational methods to calculate the displacement of fluorescent embedded beads in deformable and biocompatible substrates during cell migration. Another approach is the usage of elastic micropost arrays. Arrays of cylindrical posts in micrometer range are build with a biocompatible elastomer. Cells can be seeded on top of these microposts, that are deflected due to the forces applied on them during cell adhesion and migration. The applied force can be calculated from the deflection of the microposts. The benefit of this method is the cost efficiency in creating the substrate and the easier way of computing the displacement and the decoupling of stiffness and topology.

In the present study we used cell traction force microscopy with micropost arrays as method of choice, to gain insight into the force generation apparatus of different cell types. Therefore we created micropost arrays made of polydimethylsiloxane (PDMS), an elastic biocompatible polymer, and established an own implementation of displacement detection.
The first part of this thesis covers the basic theory to understand how traction forces are generated by cells, what components are involved and what plays a role in influencing them. In the next chapter we explain and discuss how we manufactured PDMS and measured the elasticity, which is necessary for the force calculation during cell traction force microscopy. In the following chapter our method of micropost array fabrication is explained in detail, as well as the procedure of traction force microscopy and micropost displacement detection. We compared two different methods and tested the detection accuracy of the method of choice for the later applications. The results are discussed at the end of that chapter.
We used the established cell traction force microscopy method for three different applications. All methods used for the applications are described in a separate chapter. The application chapters show the obtained results and the discussion. In the first application we analysed the difference in traction force generation for the distinct integrins a5b1 and av-class integrins avb3 and avb5. Therefore we used fibroblasts where only these integrins are expressed, either a5b1 or avb3 and avb5 separately or in combination. As control we used NIH/3T3 fibroblasts. We performed traction force microscopy under different conditions. We changed the substrate stiffness and geometry, we applied external shear stress and manipulated the cytoskeleton by inhibiting non-muscle myosin II or by disrupting actin or vimentin. We also looked at the direction of force generation and cell migration under shear stress, as well as on the difference in focal adhesion formation and the influence on cytoskeletal arrangement by observing the cell height. The goal was to detect differences regarding traction force generation in dependence on different parameters for the two integrins, and to analyse the behaviour when both integrins cooperate.
For the second application we concentrated on the force generation of two distinct cell lines derived from lung tissue. R3/1 and A549 cells. These are two cells lines that are commonly used as model cells for the alveolar type I and type II cells. These cells together build the alveolus and are responsible for gas exchange and surfactant release in lungs. Since shear stress can occur during several lung diseases, we were interested how differently the cells react to applied shear stress in terms of traction force generation and what role non-muscle myosin II plays. In addition we analysed the different role of vimentin in traction force generation for the two cell lines. We also looked at the direction of force generation and cell mi-

gration under shear stress, as well as on focal adhesion formation and cell height. In the third application we focused on the osteocyte-like cell line MLO-Y4. Osteocytes are exposed to shear stress that might occur in the canalicular system in bones. Therefore we were interested in traction forces during applied shear stress. In addition we were interested in the involvement of vimentin and smooth muscle myosin kinase in traction force generation, since lately a large amount of muscle-related proteins were detected in osteocytes. Again, the direction of force generation under shear stress, as well as focal adhesion formation and cell height were analysed to get better insight into the traction force results.
At the end of this thesis there will be a chapter summarising the results and insights we achieved and give an outlook about further possible measurements.

# 2 Theory

## 2.1 The cytoskeleton

Various organelles reside outside the nucleus in the cytosol of an eucaryotic cell. Everything together builds the cell's cytoplasm that is enclosed by the cell membrane, a semipermeable phospholipid bilayer containing embedded proteins like integrins, that are responsible for the connection to the surrounding of the cell (extracellular matrix). In between the organelles the cytoskeleton is located. The cytoskeleton consists of three distinct parts: the microfilaments or actin filaments, the microtubules and the intermediate filaments. They vary in size, protein composition and function.

**Filamentous actin** (F-actin) is composed of actin monomers, the globular or G-actin. Two helical, interlaced strands build the microfilaments. The persistence length of these filaments is $\sim 10\mu$m, the diameter 5-10nm and the Young's modulus around $10^3$MPa[77]. The persistence length quantifies the flexibility of a polymer. The persistence length and the Young's modulus are proportional to each other.
Actin filaments are polarised with a slow-growing pointed (-) end and a fast-growing barbed (+) end. The cytoskeletal protein Filamin A cross-links F-actin following the actin network being anchored to the cell membrane. Spectrin links F-actin to intermediate filaments. Plektin is a linker for all three cytoskeletal components[117]. It also acts as connector of the cytoskeleton to junctions[117]. Actin has a functional role in cell migration by rapidly polymerising at the front and depolymerising at the retracting rear of a moving cell and therefore driving protrusion.
Tension can be generated actively by association with the motor protein non-muscle myosin II to form contractile microfilaments. The cytoskeleton becomes prestressed. Stress fibers are formed by several of these filaments. They contain parallel oriented actomyosin filaments and are linked by actin-binding proteins. These bundles have a diameter of 0.2-1$\mu$m and an elastic modulus of $\sim 10^3$kPa[77] which is much lower than the one from single actin filaments. That means stress fibers are less stiff and more extensible than actin filaments. This is an important feature since stress fibers are therefore able to bear intracellular stresses[31]. These

stress fibers can be subcategorised into transverse arcs, dorsal stress fibers and ventral stress fibers. The transverse arcs run parallel to the cell periphery. They are connected to focal adhesions via dorsal stress fibers. The latter ones are emanating from peripheral focal adhesions running parallel to the dorsal membrane. Ventral stress fibers are oriented parallel to the ventral membrane and are connected to focal adhesions at both ends.

**Intermediate filaments** are built from different monomers like vimentin, keratin, lamin or desmin, depending on the cell type. Epithelial cells express a group of keratins, mesenchymal, endothelial and hematopoietic cells express vimentin and muscle cells express desmin[65]. The subunits of intermediate filaments are built by $\alpha$-helical rods that arrange into ropelike filaments. Their persistence length is $\sim 1\mu$m and the diameter $\sim$10nm[77]. The elastic modulus is in the range of 1-10MPa[77]. They have a high tensile strength and are therefore important to provide mechanical support in the cell. Although they are not known to be actively involved in traction force generation, they might indirectly participate, since they are also connected to the actin cytoskeleton[193].

**Microtubules** consist of $\alpha$- and $\beta$-tubulin dimers that build hollow tubes with an outer diameter of $\sim$25nm and an inner diameter of $\sim$12nm[77]. The elastic modulus is $\sim 10^3$MPa and the persistence length $\sim 10^3\mu$m[77]. They provide a 'road-like' structure for motor proteins like dyneins and kinesins. Microtubule formation begins at the microtubule organising centers. Apart from structural relevance as supporting component and transportation, microtubules are necessary for chromosome division during cell mitosis and meiosis. The assembly and disassembly was shown to generate intracellular forces, necessary to position chromosomes and nuclei[35]. Micotubules are important for the directionality of cell movement[118]. Although micrutubules alone are not known to be actively involved in traction force generation, a recent study found that traction forces increase after microtubule depolymerisation[134]. As for the intermediate filaments, microtubules are connected to other cytoskeletal parts and therefore might have an indirect role in traction force generation[102].

## 2.2 Integrins and the focal adhesion machinery

The actin cytoskeleton is connected to focal adhesion, located at the cell membrane and containing membrane spanning proteins, so called integrins. Integrins are heterodimeric, transmembrane glycoproteins containing an $\alpha$ and a $\beta$ subunit that form receptors for extracellular matrix molecules like fibronectin or collagen. The

subunits are non-covalently linked. In mammals there are 18 $\alpha$ and 8 $\beta$ subunits[8]. Each subunit has a large extracellular domain, a single membrane-spanning domain and a short non-catalytic cytoplasmatic tail. Different combinations of these subunits form twenty-four known types of integrins. Several integrins are usually co-expressed in mammalian cells.
Binding to a ligand outside the cell leads to clustering into focal contacts that contain actin-associated proteins (e.g. talin, paxilin, vinculin, $\alpha$-actinin, and zyxin) which link the integrin to the cytoskeleton (see Fig.1).

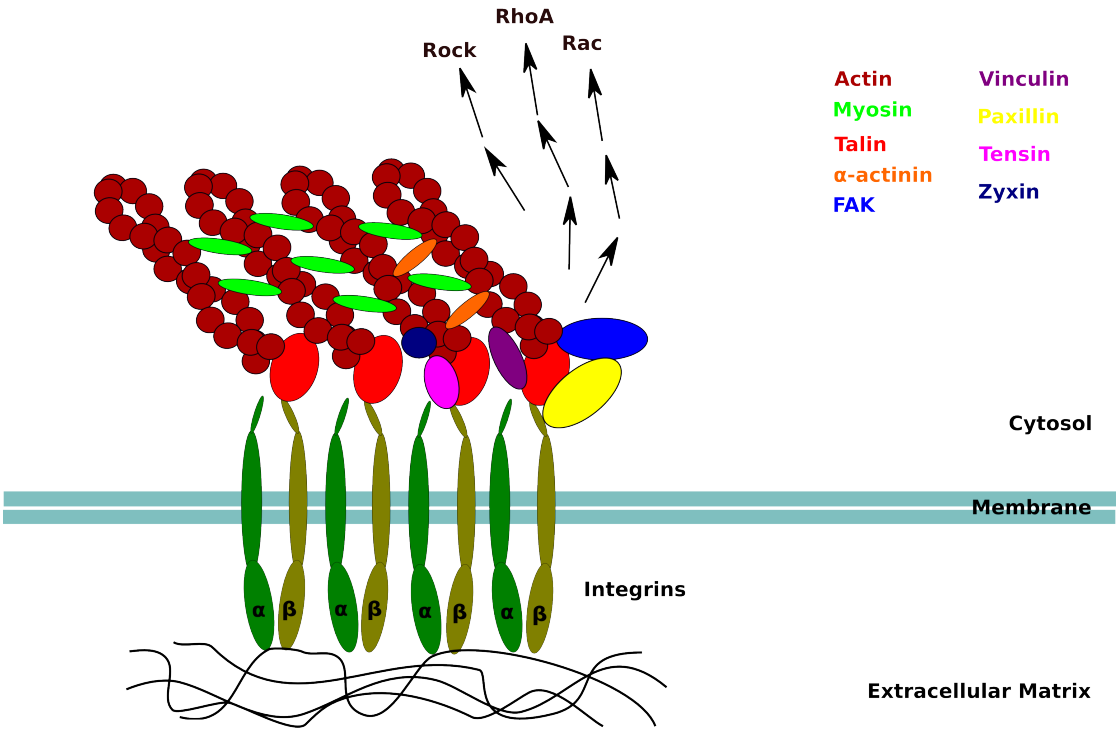


Figure 1: Simplified draft of a focal adhesion complex composed of integrins linked to the extracellular matrix outside the cell and proteins and the actin cytoskeleton inside the cell. The signalling process is indicated with arrows leading to different proteins involved in mechanotransduction.

Integrins are necessary for attachment of the cell to the extracellular matrix, but also for signal transduction inside the cell influencing e.g. cell survival, proliferation, angiogenesis, gene expression, and morphology[8]. Integrins are influencing several diseases like autoimmune diseases, cardiovascular diseases, and cancer in terms of tumour cell migration, invasion, proliferation, and survival[8][33]. a5b1 and avb3 are amongst others correlated with lymph node metastasis in melanoma and the latter one also in pancreatic tumours[33], tumour metastasis and angiogenesis[103][144]. Integrins influence tumour cells both in the ligated and in the

unligated state, meaning that the cells are able to survive anchorage independent. a5b1 is known to act as 'catch-bond', it switches to a high affinity state in response to force, leading to adhesion strength reinforcement [44] [51] [92] [98] [141]. avb3 and a5b1 act as mechanosensors and trigger downstream events inside the cell [12] [55] [179].
After adhesion to the extracellular matrix cells are able to actively migrate. Cell migration plays an important role in tissue formation, tissue repair, immune surveillance and several diseases like vascular disease, cancer or osteoporosis [140]. A migrating cell polarises and attaches at the front to the substrate, at the rear detachment takes place. It extends membrane protrusions like lamellopodia (actin builds branching networks) and filopodia (long parallel actin bundles). The driving force for protrusion is believed to be an elastic Brownian ratchet mechanism, meaning that thermal energy bends nascent short filaments storing elastic energy that is released during unbinding and provide driving force [140].
Lamellopodia are built through actin polymerisation, regulated by Rho GTPases (hydrolase enzymes that can bind and hydrolyse guanosine triphosphate (GTP)) Rac and Cdc42. Integrins are recruited to these protrusions and bind to an extracellular ligand like fibronectin. The cytoplasmic integrin tail binds to actin via talin, which acts as anchoring protein, and the actin stabilising proteins vinculin and paxillin. After binding they expose binding sites to the signalling proteins Focal Adhesion Kinase (FAK), major tension-sensor of the cell, and Src. Following additional integrin recruitment a nascent focal complex has built. Nascent adhesions are less than 0.25$\mu$m in diameter [53] and produced by small forces derived from membrane tension and actin polymerisation. At the lamellipodia-lamellar transition zone nascent adhesions enlarge into focal complexes and further develop into focal adhesions [93] via traction forces applied by the growing end of an actin stress fiber, leading to recruitment of zyxin and other proteins as well as additional integrins.
Focal complexes at the leading edge of migrating cells generate high traction stresses (around $10^3$Pa) before clustering into mature focal adhesions [13]. Clustering of focal adhesions leads to an 'molecular clutch' behaviour, meaning a reinforcement of the bond under tension, reduction of actin retrograde flow rates around adhesion sites and an increase in traction stresses. There seems to be an optimal threshold of integrin-ECM bond strength where cells migrate. Below the threshold they detach and above they cannot move [3]. The lifetime of focal adhesions within the lamella of cells is $\sim$20min. At the rear cell body focal adhesions are disassembled during cell movement [8]. Focal adhesions vary in length from 1-10$\mu$m [9] [14], whereas large adhesion size does not automatically mean larger traction force [122]. Mature focal adhesions are precursors to fibrillar adhesions. They are located towards the cell center. a5b1 integrins link fibrillar adhesions to

fibronectin[125].
An important component of the focal adhesion machinery is non-muscle myosin II. It is a hexamer built from two long heavy chains, two regulatory light chains, and two essential light chains[3]. Nascent adhesions are non-muscle myosin II-independent. Adhesion maturation is driven by non-muscle myosin II activity and additional protein recruitment. Myosin II is necessary for cross-linking F-actin into stress fibers and retrograde flow. It interacts with actin upon myosin light chain (MLC) phosphorylation. When myosin binds to actin, catalytic sites with ATPase activity found in the amino-terminal head region are activated. Energy is provided by hydrolysis of ATP into phosphate and ADP. As a consequence C-terminal domains self associate into filaments, which allows their heads to bind to actin after phosphate release and exert tension via a power stroke after ADP release.[176]. Myosin II contractility recruits focal adhesion related proteins like Focal Adhesion Kinase (FAK), zyxin, vinculin, $\alpha$-actinin and paxillin[147]. Several signalling molecules like vinculin change their conformation depending on tension. The interaction between non-muscle myosin II and F-actin generates mechanical forces that are necessary for cell migration, division and shape modification[115][176].

## 2.3 The extracellular matrix and cell traction forces

The surrounding of cells, composed of different types of molecules is called the extracellular matrix (ECM). It provides structural stability, is important in growth processes, wound healing and influences cell behaviour in a chemical and physical manner. Different molecules are secreted by cells via exocytosis depending on the cell type and function. Important components are fibronectin (FN), collagen, fibrillar proteins that give structural support, elastin for the elasticity and laminin that forms web-like structures and occurs in the basal laminae. Fibronectin is a glycoprotein (around 440kDa) binding to integrins and therefore connecting cells to other ECM components like collagen. It consists of two almost identical monomers linked by disulfide bonds. It is secreted mainly by fibroblasts. The RDG sequence (Arg-Gly-Asp) is the binding site for a5b1 and avb3 integrins. In case of a5b1 integrins random cell migration and thin cell protrusions occur whereas with avb3 a persistent migration and broad lamellopodia are observed[29]. By actomyosin generated force on the fibronectin fibers a cryptic binding site, the synergy site, is exposed to the a5b1 domain and enhances binding[3]. The resistance to force was shown to be higher for FN-a5b1 bonds than for FN-avb3 bonds[141].
Cytoskeletal tension exerted on the ECM through focal adhesions is called traction

force. Single focal adhesions exert forces in the range of 10 nN [9] [20] [161]. These forces are exerted during adhesion and movement of the cell and are involved in several physiological processes like wound healing, inflammation, angiogenesis, or cancer metastasis [8] [73] [140].
Several different pathways correlated with focal adhesions are involved in regulating adhesion and migration and therefore force generation. Cytoskeletal properties as well as environmental cues also influence force exertion in terms of magnitude and direction. Chemotaxis, reacting to chemical stimulus and durotaxis, sensing the stiffness of the extracellular matrix are examples of these external factors. Together with substrate stiffness also the geometrical shape of the surface has an influence on cell traction forces [34] [39] [148] [168]. Cells sense and respond to these external mechanical parameters by tension generation inside the cell and biochemical processing via molecular pathways [111].
The ECM has an influence on the cell in terms of cytoskeletal rearrangement and traction force generation. Increase in fibronectin density promotes integrin activation and enhances traction forces. This requires Rho kinase and myosin activity. The stiffness has an influence on cell adhesion and migration and is, together with the composition, important for the understanding of tumour growth and invasion. ECM stiffness has been shown to affect adhesion, migration, proliferation, differentiation, cell spreading and also tumour growth [56] [94] [101] [127] [129] [195]. Also durotaxis was observed, meaning that cells migrate towards stiffer substrates [3] [34] [68] [90] [178]. Increased substrate stiffness or prestress due to cytoskeletal tension leads to adhesion reinforcement by enlargement to resist the force. The mechanism implies stretching of proteins and therefore switching into a high-affinity binding state or unmasking additional binding sites [111] [145]. Reacting to stiffer substrate, several molecular mechanisms are involved deriving from increased integrin clustering and therefore triggering of upstream events inside the cell [3]. Cancer cells are able to modify the mechanical properties of their environment, e.g. increasing the ECM stiffness to enhance proliferation by extracellular matrix deposition and reorganisation [28].

## 2.4 External shear stress as physiological parameter

One physiological important cue besides the extracellular matrix is shear stress. Laminar shear stress is e.g. observed in the vascular system, in the lung, and as canalicular flow on osteocytes in bones. Shear stress is known to alter cell shape, gene expression, cytoskeletal organisation and it regulates airway epithelial barrier

functions[105][132][150]. In the vascular system fibroblasts are exposed to interstitial flow shear stress in vessels and capillaries. Previous studies showed an influence of shear stress on NIH/3T3 fibroblast migration as well as an increase in traction forces after applying stretching forces through flexible substrates[114][155].
During breathing the lung tissue is exposed to mechanical cyclic stretching forces[186] as well as shear stress. During rest breathing a laminar shear stress is exerted on airway epithelial cells in the order of 0.05-0.3 Pa[150]. Since lung epithelial cells act as barrier at the air-liquid interface to the environment, they sense and respond to changes in mechanical load. In pulmonary diseases and clinical therapies like surfactant replacement therapy in premature infants, propagating liquid plugs in the lung might produce high fluid wall shear stress during breathing leading to cell damage and injury[64][75][105][163]. The epithelial cell layer in lungs at the air-liquid interface is build by two distinct cell types. Alveolar type I cells are large flat cells that cover more than 95% of the alveolar wall and therefore build the basic structure and permit gas exchange. Alveolar type II cells cover 2–5% of the surface area, act as progenitor cells for the AT I cells and are able to secrete pulmonary surfactant that lowers surface tension at the alveolar gas-liquid interface and therefore control alveolar fluid levels. Commonly used in vitro models for these cell types are the the alveolar type I like rat epithelial cell line R3/1 and the alveolar type II like adenocarcinomic human alveolar basal epithelial cell line A549.
Fluid shear stress also occurs in the canalicular system in bones. Osteocytes are known to sense and react to this fluid shear stress[76]. These cells are embedded within the mineralised matrix of bones and are thought to translate mechanical loading into biochemical signals[19]. In vitro studies showed upregulation of cell proliferation and release of paracrine factors after inducing fluid shear stress[76]. A common model cell line for osteocytes are MLO-Y4 cells.

## 2.5 Cell traction force microscopy

Studying cell traction forces, depending on influences of the environment as well as on manipulation of the force generation apparatus in the cell, helps gaining insight into yet unknown parts of signalling pathways and understanding their role in force sensing and exerting.
Cell traction force microscopy is a method to study forces exerted by cells on the substrate. Different approaches have been used in previous studies to determine traction forces. One qualitative approach used a soft polymer surface to analyse the wrinkling of the surface during cell migration[69]. A more advanced approach uses fluorescent beads embedded into a planar acrylamide substrate[127]. Forces

were analysed quantitatively by comparing the movement of the beads over time. Several groups used this method with slight changes in the experimental approach and mathematical calculation of bead displacement [22] [32] [194]. Yet another method is to use a micropost array as force-sensing substrate [37] [161]. The advantage here is the decoupling of stiffness and topology. By changing the height and diameter of the microposts one can vary the stiffness of the substrate, but also influence the size and number of focal adhesions on one micropost.

# 3 Polydimethylsiloxane characterisation

This chapter covers the manufacturing of Polydimethylsiloxane as elastic substrate for cell traction force microscopy. The detailed manufacturing process as well as the determination of the Young's modulus are explained. The latter one is crucial for the correct force calculation during cell traction force microscopy.

## 3.1 Method

### 3.1.1 Polydimethylsiloxane fabrication

Polydimethylsiloxane (PDMS)(Dow Corning, SYLGARD® 184 Silicone Elastomer Kit) was used as biocompatible, elastic, inert, and optically clear substrate for the cells. It is a silicon based organic polymer that is, for example, used in contact lenses[175].
It consists of two components, the base and the curing agent. Depending on the desired elasticity the ratio of base to curing agent has to be chosen accordingly. If not stated otherwise the ratio 1:10 (curing agent to base) was used for all measurements. Using a scale the two components were pipetted together. The base is very viscous whereas the curing agent is more fluid. The components were mixed with a spatula and afterwards placed in the exsiccator. Vacuum was applied until all air bubbles were removed from the mixture. The next step includes casting the polymer into the desired mold. Again air bubbles have to be removed with the exsiccator. The cross-linking of base and curing agent takes place at 60°C over night (15h) in a drying oven. Cross-linked PDMS remains optically clear, elastic and hydrophobic. With plasma oxidation the surface can be made hydrophilic by adding SiOH groups.
To peel of PDMS from glass or from photoresist, the surface has to be silanized to ensure separation[164].

### 3.1.2 Young's modulus determination of Polydimethylsiloxane

To determine the Young's modulus of the PDMS, Force-Distance Curves were performed on flat PDMS surfaces in Millipore water with the JPK Nano Wizard 3 Ultra. Three different ratios of curing agent to base were measured: 1:10, 1:20 and 1:30.

Therefore 1mg of the PDMS mixture was prepared as described in the section before and casted on a glass object slide. The thickness of the PDMS layer was >300$\mu$m. This was determined via a Witec Alpha300 microscope with a calibrated z focus. Therefore the height difference was determined between focusing on the top of the PDMS layer, which was marked with a coloured dot and focusing at the glass bottom at a part, where a piece of the PDMS was scratched off. Two samples from two different days were measured for each ratio with thickness values of 427 ± 16$\mu$m for the 1:10 ratio, 360 ± 3$\mu$m for the 1:20 ratio and 439 ± 5$\mu$m for the 1:30 ratio.

For the Young's modulus nine measurements were performed for the 1:10 and 1:20 ratio and seven measurements for the 1:30 ratio from three different samples on different spots on the sample.

Cantilevers with a spherical tip with a diameter of 1.9µm and gold coating were used (CP-PNPS-SiO-A-5 (Colloidal Probe Pyrex-Nitride probes, sQube® colloidal probe; sphere material: silicon dioxide (SiO2) with sphere diameter A=1.9$\mu$m ± 5% on PNP-TR cantilever; length 100$\mu$m, width 13,5$\mu$m, thickness 0,6$\mu$m, Force Const. 2N/m, 65nm chromium/gold backside). The exact spring constant was calibrated for each measurement with the calibration setup of the JPK Nano Wizard 3, using the thermal noise method[104].

Quantitative imaging (QI) was performed, a force curve based imaging method, measuring a square of 128 x 128 Force-distance curves. The exact settings are specified on the following page.

- Feedback Control:
  - I Gain: 50Hz
  - P Gain: 0.001Hz
  - Setpoint: 85nN
- QI Control:
  - Setpoint: 500nN
  - Z length: 1400nm
  - Extend Time: 40ms
  - Retract Time: 40ms
- Grid:
  - Fast: 30$\mu$m
  - Slow: 30$\mu$m
  - X Offset: 0
  - Y Offset: 0
  - Pixel: 128 x 128
  - Grid Angle: 0
- Advanced Settings:
  - Extend Sample Rate: 50kHz
  - Extend Sample Time: 40ms
  - Extend Sample Speed: 35$\mu$m/s
  - Retract Sample Rate: 50kHz
  - Retract Sample Time: 40ms
  - Retract Sample Speed: 35$\mu$m/s
  - Add Retract: 700nm
  - Motion Time: 2ms
  - Acceleration: 1ms
  - Next Line Delay: 10ms
  - Next Line Retract: 100nm

The Young's modulus was calculated with the JPK software using the Hertz fit model. The Poisson's ratio was chosen as 0.5 and the fit was performed from the contact point to infinity. The fit range starting from the contact point was tested using following values: 100nm, 200nm, 300nm and infinite. The infinite range had the smallest standard deviation and was therefore used for all measurements. Since the thickness of the PDMS layer was much larger, we did not run the risk to measure the glass surface.

## 3.2 Results

Table 1 shows the mean Young's modulus and the according standard deviation for the measured PDMS ratios. The Young's modulus decreases with a higher base proportion.

Table 1: Young's modulus of the three measured PDMS ratios, showing the mean and the standard deviation.

| **Ratio curing agent to base** | **Young's modulus** |
|---|---|
| 1:10 | 1201 ± 229kPa |
| 1:20 | 495 ± 72kPa |
| 1:30 | 269 ± 64kPa |

## 3.3 Discussion

Literature values for the Young's modulus of different PDMS mixtures vary largely. Several factors influence the result like accuracy of the mixture ratio, curing time, curing temperature, and measurement tools[80] [130]. Previous studies used different analysis methods, like stretching of the PDMS[83] [127], atomic force microscopy[11], nanoindentation[185] or macroscopic compression[184]. Whereas the accuracy of the mixture is dependent on precise performance, the curing time and temperature can be chosen individually but has to stay the same to avoid large deviations in the Young's modulus. For the curing agent to base ratio 1:10 and a curing time of 15h at 60°C we measured a Young's modulus of 1201 ± 229kPa. Other groups using similar curing temperature and time measured 1500kPa[37](no measurement method stated) and 2100kPa[83](tensile test). It is not useful to compare the measured results with other methods where different curing times and temperatures were chosen, since the variation can be as large as approx. 750kPa to 4000kPa[5] [46] [80] [130]. As expected the Young's modulus decreases using less amount of curing agent. We used the ratio 1:10, that is also the company recommended ratio, in all our experiments, because one has to consider, that with less curing agent the PDMS samples may contain a higher amount of uncrosslinked oligomers, that might have an influence on the cells[137].

# 4 Cell traction force microscopy technique

This chapter explains the detailed process of PDMS micropost array fabrication and the procedure of traction force microscopy and micropost displacement detection. Two different detection methods were compared and for the method of choice, used for the later applications, the detection accuracy was tested.

## 4.1 Method

### 4.1.1 Micropost array fabrication

Arrays of uniformly shaped, hexagonal ordered, and cylindrical microposts were fabricated as substrate for cell traction force microscopy. Briefly, a mould with holes was created via photolithography and PDMS was casted on the mould. After curing, the finished PDMS micropost array is peeled off.
The first step to create a mould for the micopost array is to design an exact two-dimensional sketch of the desired structure. AutoCAD from Autodesk Inc. was used to create the structures (see Figure 2 and 4). This sketch was used to create a photomask from quartz glass with a chromium structure. The chromium was etched until the given structure is formed (Yakiv Men, Institute of Electron Devices and Circuits, University of Ulm). The dimensions of the sketch used for our measurements were:

- 5$\mu$m circle diameter, 10$\mu$m centre-to-centre distance
- 4$\mu$m circle diameter, 8$\mu$m centre-to-centre distance

The exact dimensions of the microposts have to be measured with electron microscopy since they are slightly changed during the manufacturing process. Images were taken with the Hitachi S5200.

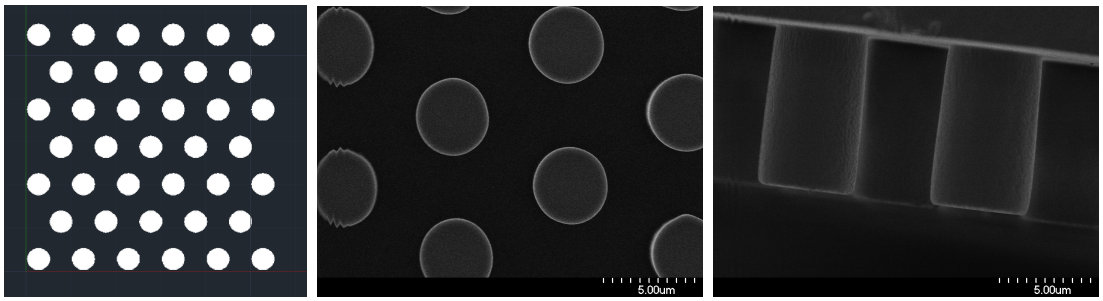


Figure 2: AutoCAD drawing of the structure template for the chromium structure on the quartz glass mask (left). Electron microscope images of PDMS micopost arrays from the top (middle) and from the side (right).

The stiffness of the microposts can be varied by changing the radius and length of the microposts, while the Young's modulus of the PDMS is kept constant. To change the radius of the microposts the chromium structure has to be changed accordingly. To change the length of the microposts, the following photolithography process has to be adapted.
The next step was performed in the clean room using photolithography technique. The used protocol was kindly provided by Claudio Rolli, formerly post-doc at the Max-Planck Institute in Stuttgart. The exact protocol is shown below.
Briefly, a silicon wafer is coated with a thin layer of SU-8-10 (MikroChem Corp.) using a spin coater. A softbake step is necessary to evaporate the solvent and densify the film. In the next step the photomask and the SU-8 coated wafer are placed into a mask aligner and brought into vacuum contact, following an exposure with i-line (365nm). During the exposure process formation of a strong acid takes place (see Figure 3(a)[183]). During the the post exposure bake an acid-initiated, thermally driven epoxy cross-linking takes place (see Figure 3(b)[183]). A developing step removes the not crosslinked parts of the photoresist. The sample is then rinsed with isopropanol and dried with a nitrogen stream. A hard bake step ensures a better stabilisation of the form.

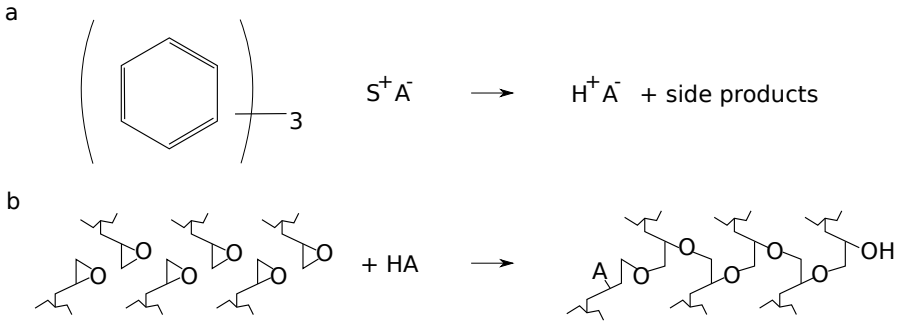


Figure 3: UV-induced reaction of SU-8 during i-line exposure (a) and temperature induced reaction of SU-8 during the post exposure bake (b)[183].

**Photolithography protocol for micropost array moulds:**

- **Cleaning of the silicon wafer:** Rinse the wafer in acetone, then in isopropanol and finally in Millipore water. Dry it with nitrogen and place it on the heating plate at 200°C for 10min. to evaporate remaining water.
- **Spin coating:** Place the cleaned wafer on the chuck of the spin coater with vacuum contact, pour 1.5ml SU-8-10 (MicroChem Corp.) in the middle of the wafer and immediately start the spin coating programme with following parameters:

  **time:** 5sec **speed:** 500rpm **acceleration:** 100rpm/$s^2$
  **time:** 35sec **speed:** 3000rpm **acceleration:** 300rpm/$s^2$

- **Soft bake step**

  **time:** 3min. **temperature:** 65°C
  **time:** 10min. **temperature:** 95°C

- **Exposure:** 5sec with 365nm i-line in vacuum contact with WEC settings (MJB4 SÜSS MicroTec)
- **Post bake step**

  **time:** 2min. **temperature:** 65°C
  **time:** 4min. **temperature:** 95°C

- **Developing:** Immerse the sample in mr-DEV 600 microresist (MicroChem Corp.) for at least 3min.
- **Hard bake step:** Heat up the sample slowly to 200°C for 1h, cool down slowly to room temperature.

**For higher microposts:**

- **Spin coating**

| | | | | | |
|---|---|---|---|---|---|
| **time:** | 5sec | **speed:** | 500rpm | **acceleration:** | 100rpm/$s^2$ |
| **time:** | 35sec | **speed:** | 2000rpm | **acceleration:** | 300rpm/$s^2$ |

- **Soft bake step**

| | | | |
|---|---|---|---|
| **time:** | 2min. | **temperature:** | 65°C |
| **time:** | 5min. | **temperature:** | 95°C |

- **Post bake step**

| | | | |
|---|---|---|---|
| **time:** | 1min. | **temperature:** | 65°C |
| **time:** | 2min. | **temperature:** | 95°C |

In the next step the finished form must be silanized to enable the separation of cured PDMS from the hardened SU-8 features. Therefore 1ml of 1,1,1,3,3,3-Hexamethyldisilazan (Merck) is dropped into a petridish containing the wafer and then sealed with parafilm. The sample is stored overnight under the flow bench. The next step is to prepare the mixture of PDMS curing agent to base in the ratio 1:10. To remove air bubbles from the mixture it has to be vacuumised in the exsiccator until no air bubbles are visible. Then the PDMS is casted on the mould and exsiccated again to remove additional air. The volume should be enough to ensure a resulting sample thickness of around 1mm. In case of too thick samples the working distance of the microscope objective will be too small and for too thin samples wrinkles will appear. The PDMS is cured at 60°C overnight. The hardened sample is peeled off and cut into smaller pieces of around 5x5 mm that are glued into a petri dish with a small drop of PDMS. Figure 4 shows an overview of all steps described.

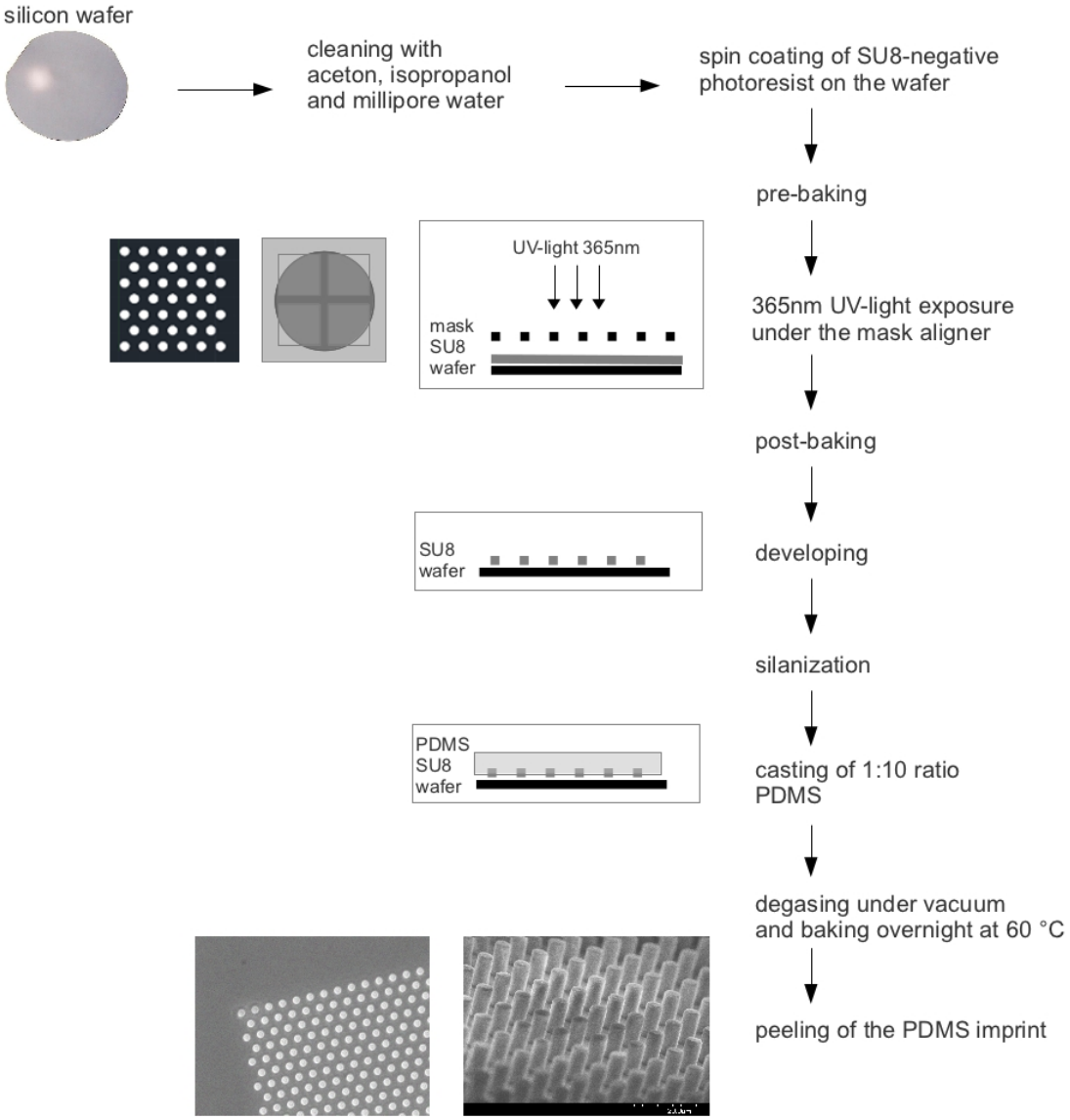


Figure 4: Overview of all steps including photolithography and PDMS micropost array fabrication.

### 4.1.2 Cell culture

Fibroblasts were cultured in Dulbecco's Modified Eagle Medium with 10% fetal calf serum and 5% penicillin/streptomycin (all reagents from gibco® by life technologies™). Cells were splitted three times a week 1:10 with the according medium. Prior to seeding, surfaces were sterilised with ethanol and then coated with $5\mu g/cm^2$ fibronectin. To coat just the top of the PDMS microsposts, a drop of fibronectin was placed on it for 2 hours. Due to the hydrophobicity the solution remained as a droplet. After incubation time the solution was washed off two times with PBS and cells were seeded over night non confluently before measurement.
As a control, scanning electron microscope images were taken of same samples of cells seeded on top of the microposts. For thus, cells were fixed with 4% formaldehyde for 15min. Afterwards the samples were cryo-dried and vapour coated with platinum. Images were taken with the Hitachi S5200.

Figure 5 shows a micropost array with Cy2 labeled fibronectin, covering the top of the microposts and for orientation a three-dimensional scanning electron microscopy image of a microscope array.

Figure 6 shows scanning electron microscope images and phase contrast images of micropost arrays with cells attached to the top of the micoposts.

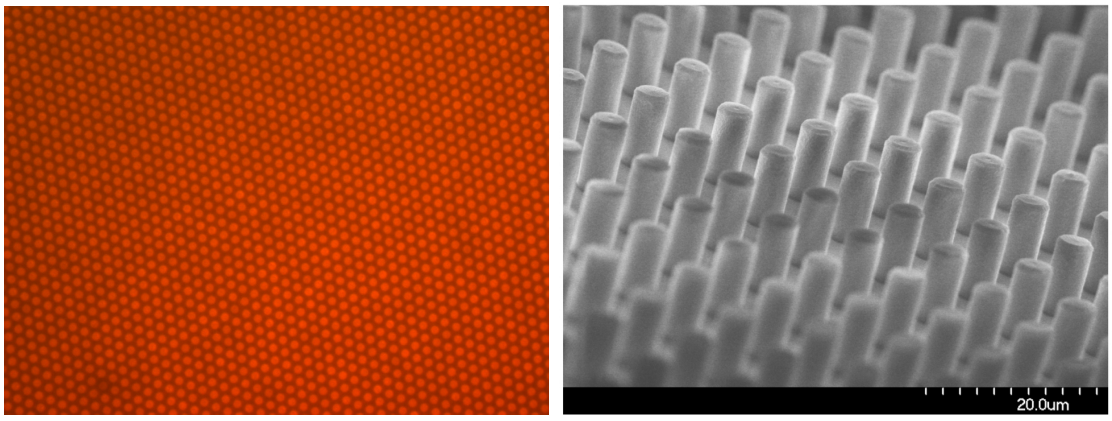


Figure 5: Microscope image of a micropost array coated with fluorescently (Cy2) labeled fibronectin (left) and a scanning electron microscope image of an PDMS micropost array (right).

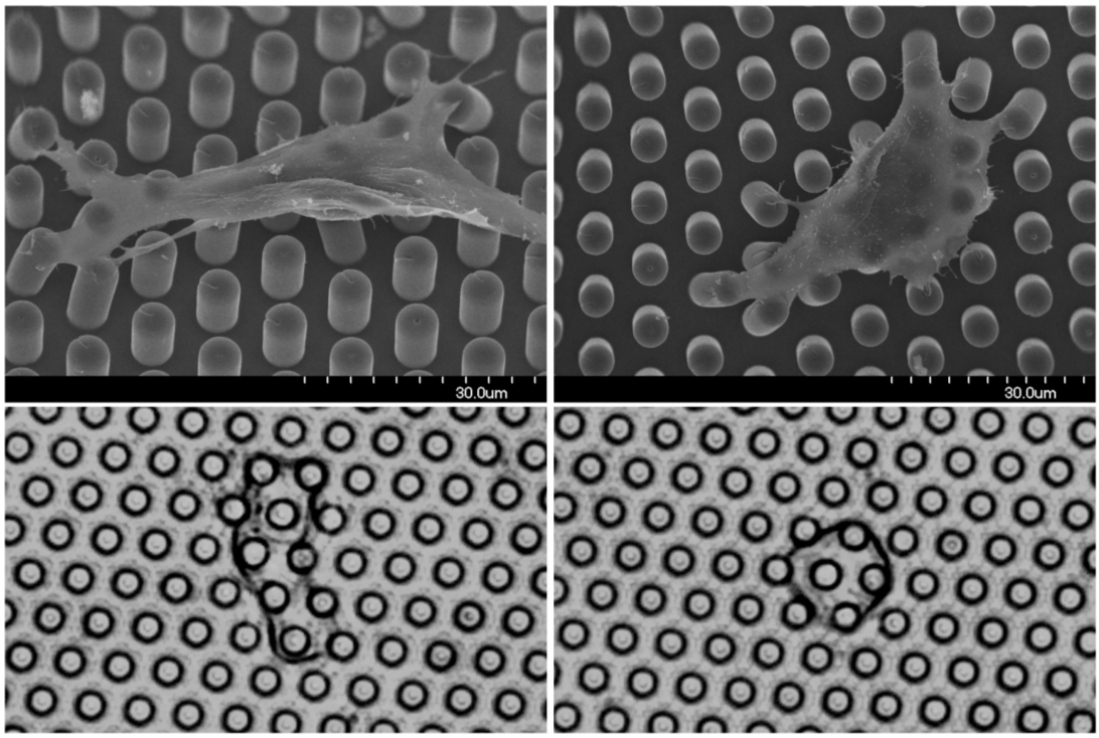


Figure 6: Scanning electron microscope images of fibroblasts attached to the top of the microposts (top). The strong bending of the microposts is an artefact due to the fixation of the cell. Phase contrast images of fibroblasts on PDMS microposts (bottom).

### 4.1.3 Image taking and analysis

For the detection of the micropost displacement under force generation by cells, a method has to be used, that is both time efficient and accurate. In this respect the experiment has to be optimised, whereas the image taking as well as the calculation can be varied.

Two different experimental approaches, described in the following chapter, were tested to detect the micropost deflection: the trypsin and the hexagonal grid method. For the trypsin method two images are taken, one with and one without the cell and directly compared to get the deflection. In contrast only one image with the cell is taken using the second method and the micropost deflection is calculated by alignment of the microposts to a hexagonal grid. For all experiments conducted the hexagonal grid method was used, which is described more detailed in the following. The hexagonal grid method is more time-efficient compared to the trypsin method. One image of an attached cell is taken, focusing on the outline of the micropost tops. During analysis the micropost positions are compared to an ideal hexagonal grid, that is constructed based on the undeflected microposts around the attached cell. Therefore two undeflected microposts have to be selected whereas a grid is generated that aligns to the centres of all undeflected microposts.

The difference for the trypsin method is, that two pictures of the same area are taken, focusing on the outline of the micropost top. The first image with the attached cell and the second image after the cell is removed with trypsin. In this case the image without the cell represents the undeflected state of the microposts[95].
Images were taken with a Zeiss Observer D1 and an Axio Cam Mrc from Zeiss. A 40x objective was used, leading to a total magnification of 400x (1 pixel corresponds to 256nm).
To detect the micropost centres a Hough transformation for circular objects in grey scale images was used. Therefore a script available from the file exchange from the Matlab Central was used (Detect circles with various radii in gray scale image via Hough Transform, Tao Peng, Department of Mechanical Engineering, University of Maryland, Version: Beta, Revision: Mar. 07, 2007). Several parameters can be changed using this circular Hough detection as described. The minimum and maximum radius range for the circles to be detected can be adapted. A smaller range can save computational time and memory. Since the radius for the microposts is known, a close range is chosen accordingly with 9-15 pixel, corresponding to 2.3-3.84$\mu$m. The Hough transformation on one image is performed multiple times and all images are added up to one picture, the accumulation array. For the search of local maxima in the accumulation array the radius of the filter was set to ten, the minimum value is three. A larger radius is useful to detect circles with less perfect shape. Therefore distorted circles that resemble an ellipse are still represented in the accumulation array. A two-dimensional pyramid filter is used to smooth irregular circle edges.
To analyse the images, a custom made Matlab script (written by Thomas Kerst) is used. It first calls for an empty image section, containing only microposts, but no cells. This is used for drift correction. Next, an image section containing a cell is selected. Each detected micropost is marked with a red dot representing the center and a blue circle representing the outline (see Figure 7). The center positions are then subtracted from the calculated center positions of the hexagonal grid points, that represent the undeflected micropost state. The obtained values represent the magnitude of the displacement $\Delta$x and the direction. In case of the trypsin method the center positions were subtracted from the center positions of the same image section after cell removal.
In case of wrongly or not detected microposts it is possible to manually select or deselect them. For the analysis of the quality of the circle center detection it is useful to observe the peaks in the accumulation array (see Figure 7)

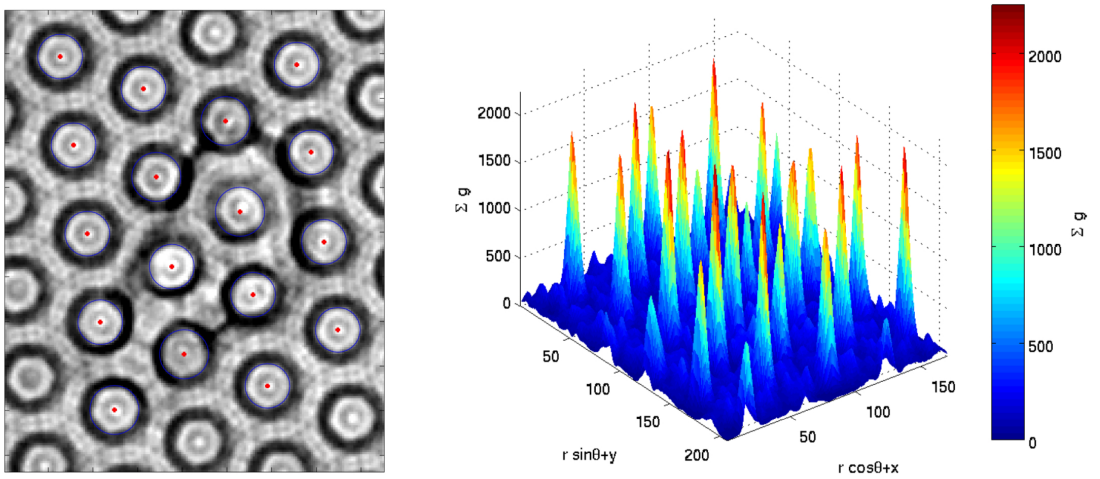


Figure 7: Phase contrast image of a cell attached to microposts. The blue circles mark the outline of each microposts and the red dot represents the circle center (left). The associated accumulation array indicates the circle centres as peaks. (right).

The applied force F can be calculated with known Young's modulus E of the PDMS and radius r and length L of the microposts (equation (4.1) and Figure 8[37]. The stress on each micropost is calculated by dividing the force through the area of the micropost top.

$$F = \frac{3}{4}\pi\frac{r^4}{L^3}E\Delta x \tag{4.1}$$

E: Young's modulus of the PDMS
F: Force
$\Delta x$: Displacement
L: Length of the micropost
r: Radius of the micropost

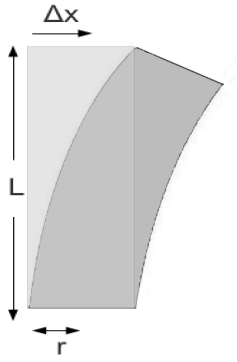


Figure 8: Draft of a bend micropost.

Two compare the hexagonal grid and the trypsin method we analysed eight cells (same cell type, different passages). For this we chose the same parameter values (radius range 9-15 pixel, filter radius 10 pixel) for the Hough transformation and the exact same image section.

### 4.1.4 Testing the detection accuracy of the hexagonal grid method

To analyse the accuracy and therefore the detection limit of micropost displacement magnitude, phase contrast images from microposts were manually changed with a graphics program in a way that one circle was moved by a defined value. By rescaling of the images it was possible to generate displacement values of 256nm, 128nm, 64nm, 32nm and 16nm. This was done for five different microposts. In the next step a Gaussian blur filter with different sigma values was applied to all images after displacement using ImageJ Version 1.46a. Convolution with a normalised Gaussian function is used for smoothing, where sigma is the radius of decay to e-0.5 ˜ 61%, i.e. the standard deviation $\sigma$ of the Gaussian. In figure 9 an example of a micropost with different displacements and Gaussian blur values is shown. For the largest displacement value the accumulation arrays are shown on the right side. For larger sigma values the peaks are getting smaller.
To simulate distorted circle outlines, microposts that are placed underneath a cell edge are cut out from a different part of the image. The same displacement values were used for ten different microposts. In figure 10 all distorted microposts and the displacement of one with the associated accumulation array as top view are shown.
All measurements were analysed with varying radius range for circle detection (9-12 pixel, 9-15 pixel and 1-20 pixel) and radius of the filter for search of local maxima in the accumulation array (filter radius of 4, 10 and 15 pixel). As analysis method the hexagonal grid was used.
The inaccuracy of the grid or the noise level was tested by analysing a random area of five micropost arrays without a cell.

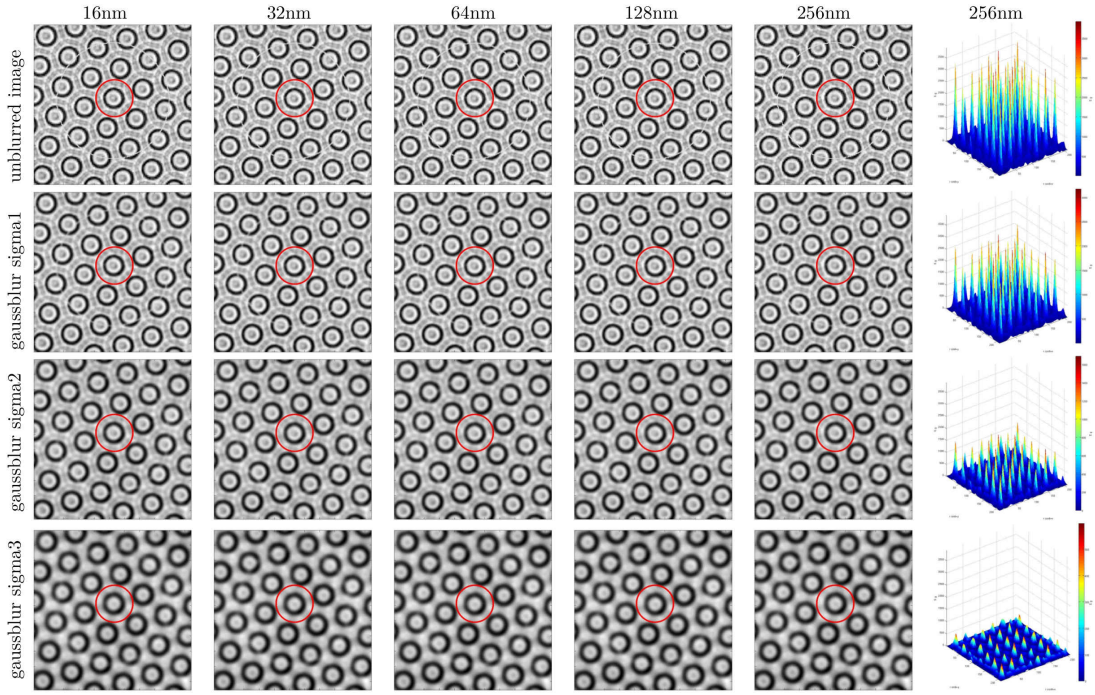


Figure 9: Example of an un-distorted micropost (encircled in red) with 16nm, 32nm, 64nm, 128nm and 256nm displacement, each without and with a Gaussian blur filtering with sigma values 1,2 and 3. The accumulation array is shown for a displacement of 256nm.

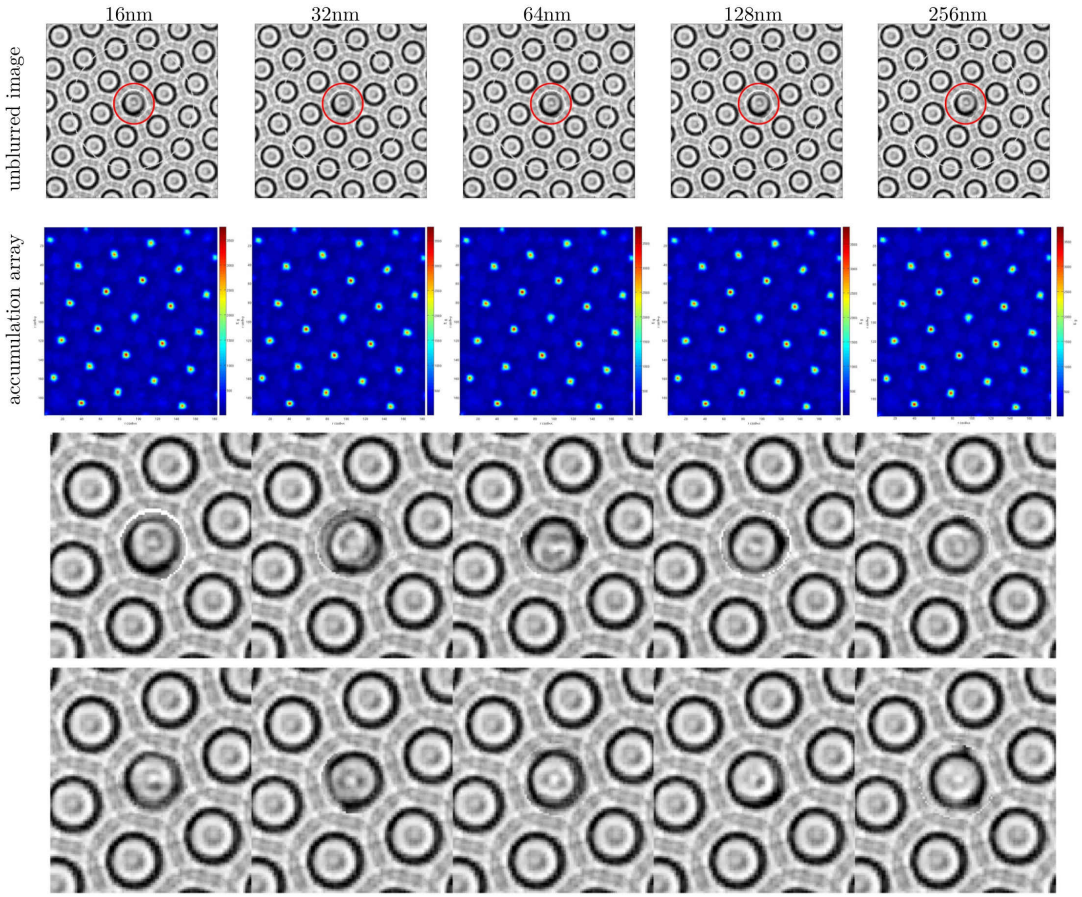


Figure 10: Example of a distorted micropost (encircled in red) with 16nm, 32nm, 64nm, 128nm and 256nm displacement. The according accumulation array as top view is shown below each image. Images of all ten analysed microposts with a distorted outline are shown at the bottom (the distorted micropost is in the center).

## 4.2 Results

### 4.2.1 Comparison of the trypsin and the hexagonal grid method

Figure 11 shows the force vectors for the resulting displacements for the trypsin method and the hexagonal grid method. There is a high agreement between both methods (Wilcoxon-Mann-Whitney p=0.89). The force vectors around the cell show that for the hexagonal grid method the noise is higher. Figure 12 shows the maximum force per area for all measured cells (n=8). There is no significant difference between both methods.

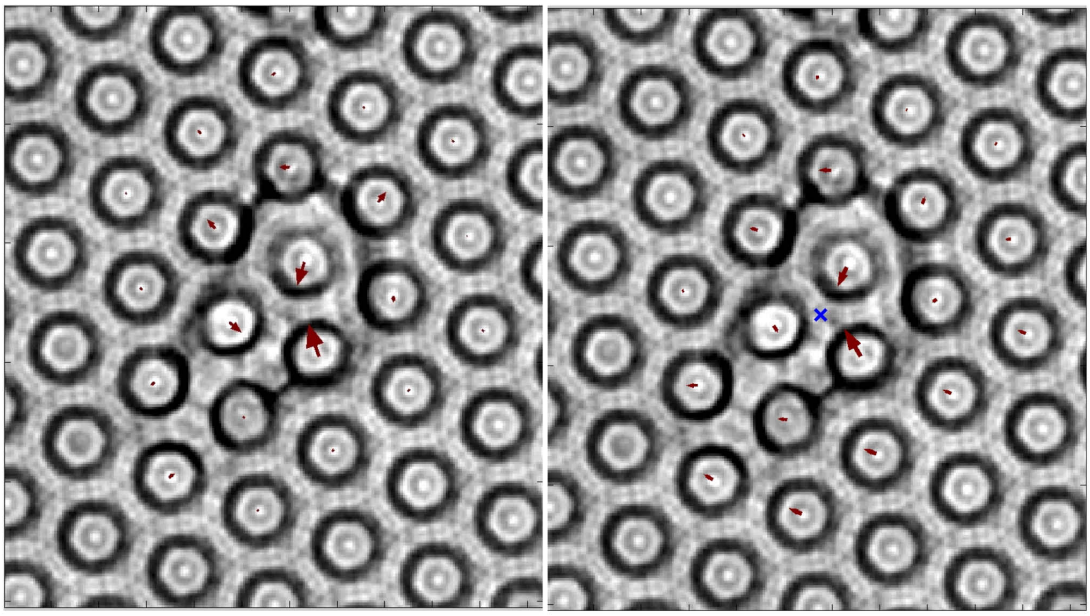

Figure 11: Force vectors for the resulting displacements analysed with the trypsin method (left) and the hexagonal grid method (right). The arrows show the direction of the displacement and the length of the arrow represents the relative magnitude.

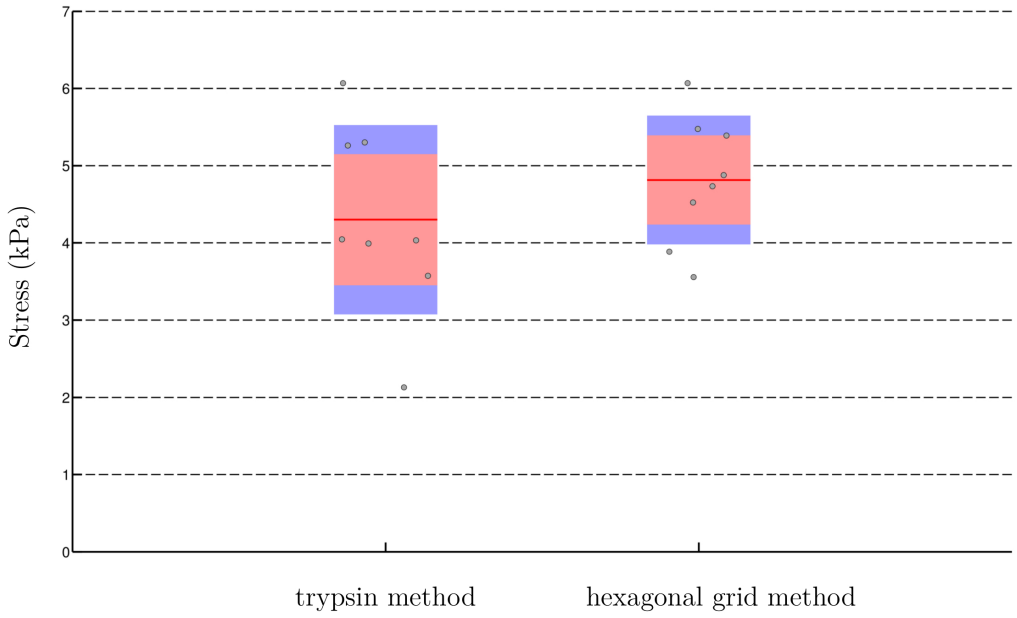


Figure 12: Maximal stress (kPa) for eight cells analysed with the trypsin method and the hexagonal grid method. Grey dots represent single data points. The points are laid over a 1.96 standard error of the mean (95% confidence interval) in red and a 1 standard deviation in blue. The mean is represented as red line. There is no significant difference.

### 4.2.2 Testing the micropost detection accuracy for the hexagonal grid method

Figure 13 shows the results for the mean micropost displacements of distorted (n=5) and un-distorted (n=10) circles, determined with the hexagonal grid method with different parameter settings for the Hough detection. Gaussian blur was tested for all parameter settings, but micropost detection failed for some settings, therefore there is no data shown.

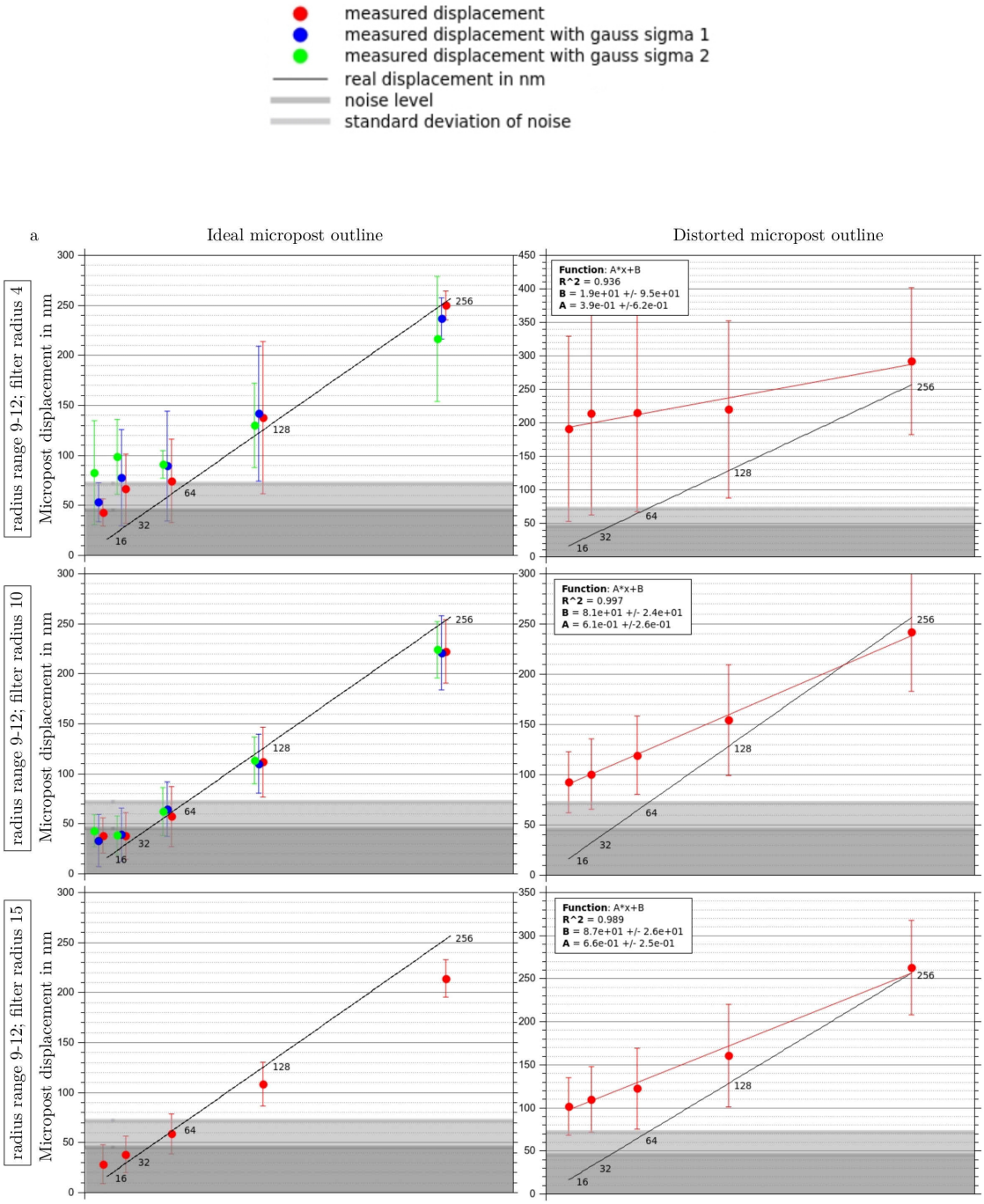
measured displacement
measured displacement with gauss sigma 1
measured displacement with gauss sigma 2
real displacement in nm
noise level
standard deviation of noise
a
Ideal micropost outline
Distorted micropost outline
radius range 9-12; filter radius 4
radius range 9-12; filter radius 10
radius range 9-12; filter radius 15
Micropost displacement in nm
Function: A*x+B
R^2 = 0.936
B = 1.9e+01 +/- 9.5e+01
A = 3.9e-01 +/-6.2e-01
Function: A*x+B
R^2 = 0.997
B = 8.1e+01 +/- 2.4e+01
A = 6.1e-01 +/-2.6e-01
Function: A*x+B
R^2 = 0.989
B = 8.7e+01 +/- 2.6e+01
A = 6.6e-01 +/- 2.5e-01
16
32
64
128
256

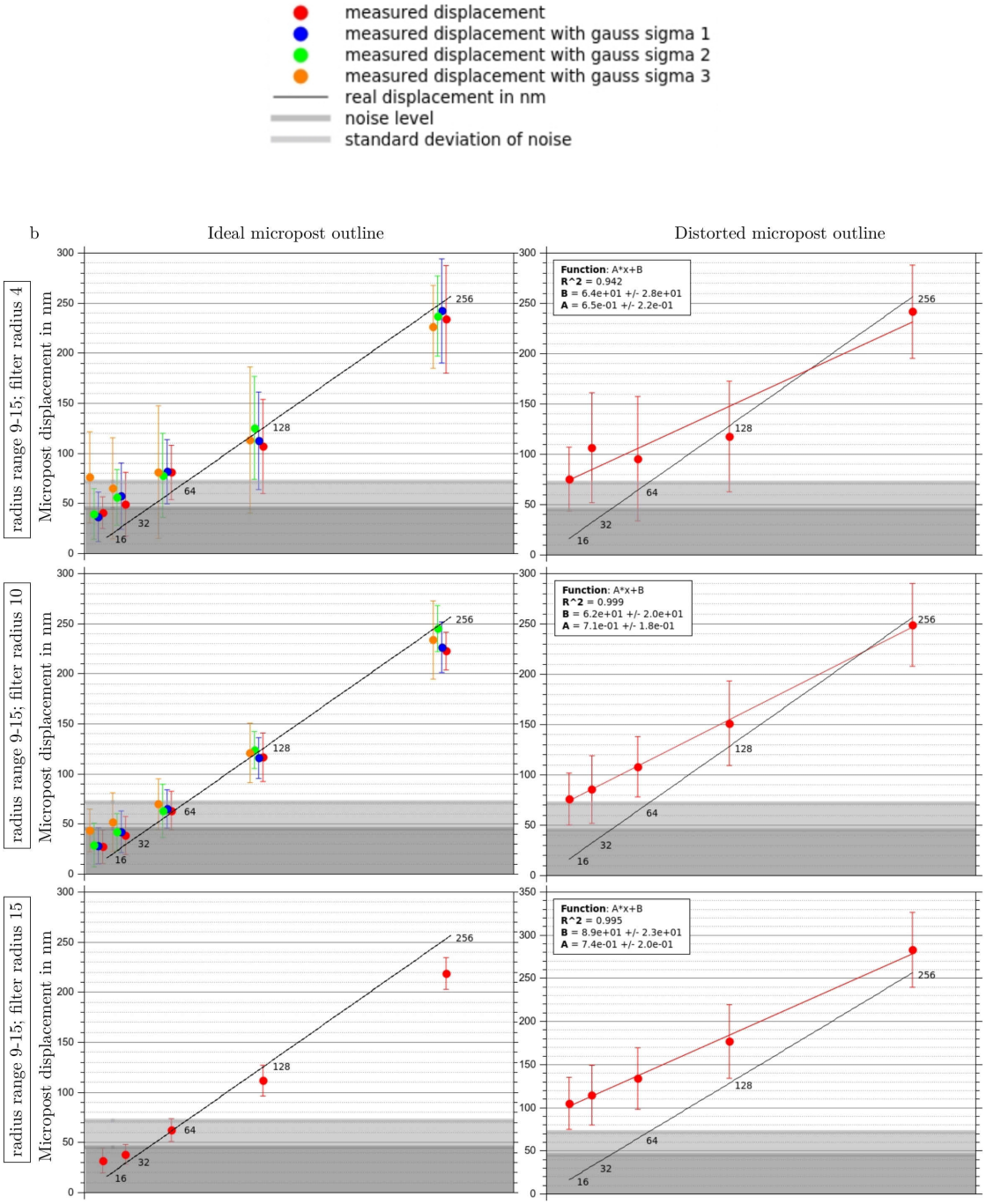
measured displacement
measured displacement with gauss sigma 1
measured displacement with gauss sigma 2
measured displacement with gauss sigma 3
real displacement in nm
noise level
standard deviation of noise
b
Ideal micropost outline
Distorted micropost outline
radius range 9-15; filter radius 4
radius range 9-15; filter radius 10
radius range 9-15; filter radius 15
Micropost displacement in nm
Function: A*x+B
R^2 = 0.942
B = 6.4e+01 +/- 2.8e+01
A = 6.5e-01 +/- 2.2e-01
Function: A*x+B
R^2 = 0.999
B = 6.2e+01 +/- 2.0e+01
A = 7.1e-01 +/- 1.8e-01
Function: A*x+B
R^2 = 0.995
B = 8.9e+01 +/- 2.3e+01
A = 7.4e-01 +/- 2.0e-01
16
32
64
128
256

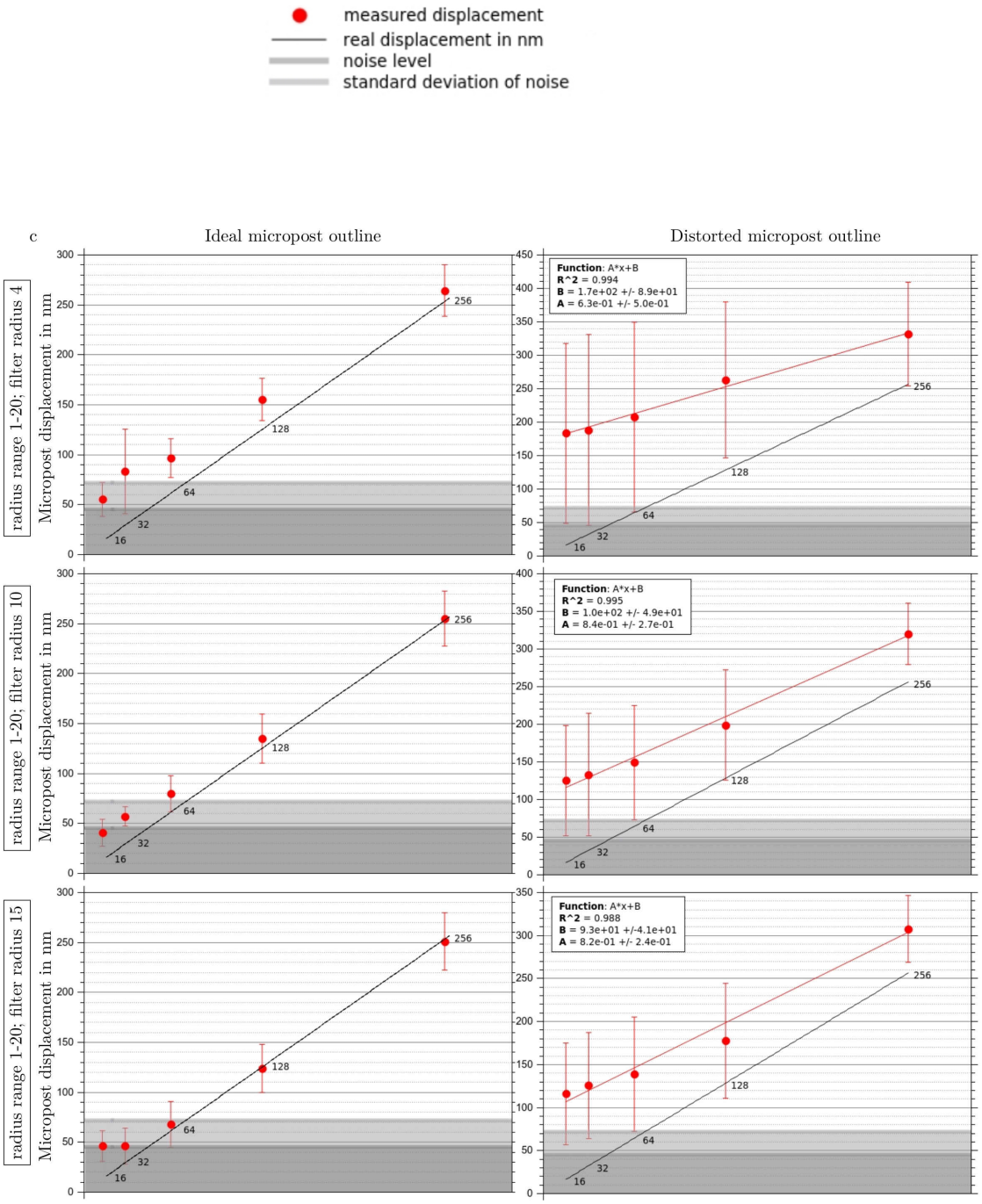


Figure 13: Results for the mean displacement values for five different un-distorted microposts and 10 distorted microposts, error bars show the standard deviation. Red dots represent the unblurred images, blue dots Gaussian blur with sigma 1, green dots sigma 2 and orange dots sigma 3. The black line represents the real displacement values. Each graph shows the results for the parameter values given on the left side.(a) Radius range 9-12 pixels (b) radius range 9-15 pixel and (c) radius range 1-20 pixel. For the distorted micropost outline a linear fit was performed for each parameter range. The fit quality and the linear equation are given in the graphs. The noise level is marked in grey.

For all tested parameter variations the root-mean-square deviation (RMSD) was calculated (Table 2 and Figure 14). The error is smallest for a radius range of 1-20 pixel and filter radius of 15 pixel for the un-distorted micropost outlines and for a radius range of 9-15 pixel and filter radius of 10 pixel for the distorted micropost outlines. For the maximum Gaussian blur applied on the un-distorted micropost outlines the value is slightly higher (18.5nm) than for clear outlines.

Table 2: RMSD values for all tested parameters, calculated from the average displacement from 5 un-distorted and 10 distorted micropost outlines.

| **Radius range for circle detection in pixel** | **Filter radius for local maxima in the accumulation array** | **RMSD values for ideal micropost outline in nm** | **RMSD values for distorted micropost outline in nm** |
|---|---|---|---|
| 9-12 | 4 | 20.6 | 138.1 |
| 9-12 | 10 | 20 | 53.6 |
| 9-12 | 15 | 21.9 | 59.5 |
| 9-15 | 4 | 20.7 | 53.6 |
| 9-15 | 10 | 16.9 | 42.1 |
| 9-15 | 15 | 19.9 | 67.1 |
| 1-20 | 4 | 34.4 | 138.9 |
| 1-20 | 10 | 17.2 | 87.3 |
| 1-20 | 15 | 15.1 | 76.4 |

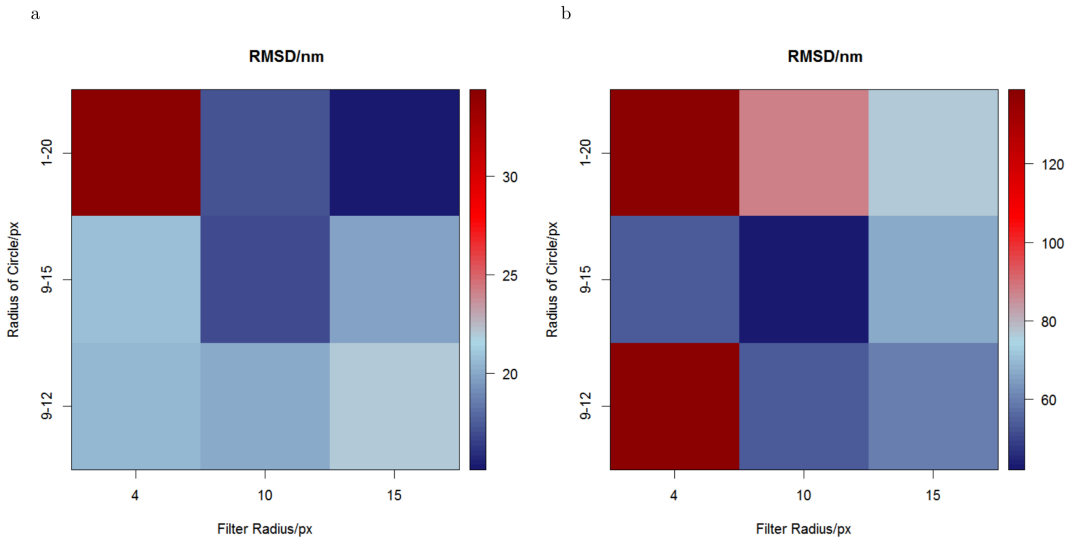


Figure 14: RMSD values for all tested parameters, calculated from the mean displacement of 5 un-distorted (a) and 10 distorted (b) micropost outlines.

The noise level deriving from the inaccuracy of the grid is less than 45nm. Figure 15 shows the noise level and the absolute error for the optimal parameter choice.

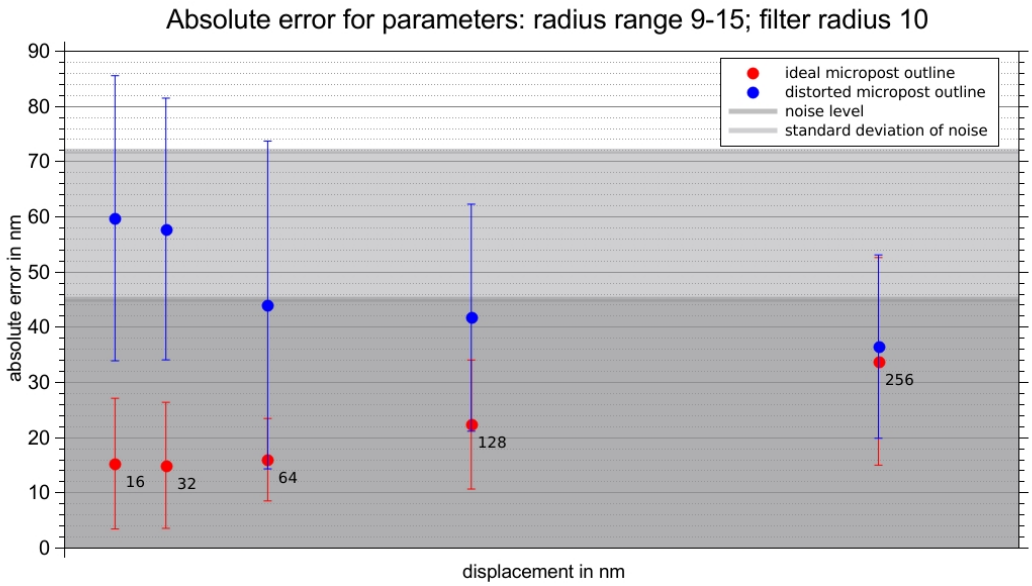


Figure 15: Absolute error in nm for the 5 displacement values (x-axis) for parameter values: radius range 9-15 pixel and filter range 10 pixel, for all 5 evaluated microposts with un-distorted outline (red) and 10 microposts with distorted outline (blue). The noise level is marked in dark grey and the standard deviation of the noise level in light grey. The noise level is calculated by analysing a random area of five micropost arrays without a cell.

## 4.3 Discussion

We used PDMS micropost arrays as measurement tool for cellular traction forces and tested the accuracy and the detection limit. As detection tool for the micropost outlines we used Hough transformation of circular objects. Smolik et al. used an own implementation on transmission images and calculated the displacement with an ideal grid[152]. However the detection limit was not discussed. Heil and Spatz applied the Hough transformation on microposts with a diameter of 5$\mu$m, a length of 11$\mu$m, a spring constant of 0.2N/m and a distance of 50$\mu$m. They used this setup to apply laterally stretch and compression on fibroblasts to analyse focal adhesion assembly under external force. To detect the micropost outlines from phase contrast images they used a combination of the Hough transformation and an own implemented algorithm. The reference to calculate the displacement was an unbend neighbouring micropost[71].
We changed the parameter settings of the Hough detection to find the optimal set for the individual image quality. Therefore we varied the radius range of the detected circles and the filter radius for the detection of maxima in the accumulation array. The detection rate of the micropost outlines in all cases was nearly 100%, meaning only very few false positive or undetected circles.
The best result for un-distorted microposts was achieved with a radius range of 1 to 20 pixel and a filter radius of 15 pixel. The RMSD between detected and real displacement was 15.1nm. To test against errors caused by defocussing, we applied Gaussian blur on the images. The RMSD for the maximum Gaussian blur applied on the un-distorted microposts was 18.6nm, slightly higher then without blur, concluding that the method is robust against defocussing errors.
The most accurate result for the distorted micropost outlines was detected for a radius range of 9 to 14 pixel and a filter range of 10 pixel with an RMSD of 42.1nm. Therefore, depending on the image quality and the distortion of the micropost outlines, the parameters have to be changed to get optimal results. The results show that a distortion of the micropost outline, caused by cells, leads to a decline in detection quality. The errors in force detection, especially for the distorted microposts, follow a linear dependency, whereas small displacements are overestimated and large displacements are underestimated. This error might result from the comparison of the distorted microposts with the ideal grid. The positioning error is larger for small displacements compared with large displacements, therefore the reported detection error is an upper limit, convoluting detection errors and positioning errors.
We detected an average displacement of the microposts from the ideal grid of 45nm in regions containing no cells or distortions. Therefore the inhomogeneities

of the substrate seem to cause the lower limit of the detectable forces rather than detection errors. For distorted microposts the detection limit of the Hough transformation and the accuracy of the setup are in the same order, but for un-distorted microposts the accuracy of the setup is surpassed. Together with previous studies[199] our results show that errors in the setup of the system are the main cause for resolution limitation. An improvement could be achieved using better objectives and most of all more planar substrates. Important is to avoid bending or wrinkling of the micropost array.

Previous studies had comparable resolutions, e.g. du Roure et al. had a resolution of around 50nm using bright-field posts as waveguides and applying Gaussian fit to detect the centres and using an ideal hexagonal grid to calculate the displacement[37]. Ganz et al. used a similar method applying Gaussian fit on bright field images and using an hexagonal grid for displacement calculation. They have an accuracy of about 30nm for un-distorted microposts[49]. Another approach was used by Tan et al. where they stained the microposts with a fluorescent dye and simultaneously used bright field images. They assigned coordinates to posts with and without cells manually. In addition they used an ideal grid to minimise the difference between the coordinates of the undeflected microposts and the ideal grid. They used posts with a diameter of 3$\mu$m and a height of 11$\mu$m, resulting in a spring constant of 32nN/$\mu$m. The force detection limit was around 12nN (1.7kPa) calculated from the standard deviation of the posts of 0.2$\mu$m[161]. Yang et al. used as model two-dimensional Gaussian fits from intensity profiles of fluorescent micropost images and a non linear least-square fit to determine the post positions[192]. Interpolation was performed with posts without cells as reference points to determine the positions of the undeflected state of the posts. For posts with 3$\mu$m diameter and 10$\mu$m height and a PDMS Young's modulus of around 2.5 MPa, according to a spring constant of 32nN/$\mu$m an error of 1-2nN (0.14-0.28 kPa) per post is expected, corresponding to a displacement of 30-60nm[153][161]. Fu et al. applied a localised tresholding algorithm for centroid detection[107] following a two-dimensional Gaussian fit for the grey scale intensity profile modelling and a nonlinear least-squares fit[45]. An image processing algorithm utilising the least-squares circle detection was developed by Ghanbari et al.[57]. They applied it to a study analysing the migration of C. elegans in between microposts. They had a visual resolution of 0.5 pixel for the micropost deflection, according to a force of 2.07$\mu$N for a micropost stiffness of 3.5N/m[57].

Zheng and Zhang used a different approach based on optical moiré fringe technique as an Fourier-based fringe analysis[198]. Therefore a periodic substrate is illuminated with two symmetric light beams to generate a moiré pattern. They have a displacement calculation error of about 40nm for a micropost periodicity of

4$\mu$m, since the algorithm is able to determine the fringe location with an accuracy of 1/100 of a fringe order.

We compared two methods to analyse the micropost displacement. The first using an ideal hexagonal grid to align the detected microposts and then calculate the displacement and the second taking an image with the cell and one exactly at the same position after cell removal with trypsin, therefore getting a before image with the deflected and one after image with the undeflected micropost state[95]. The hexagonal grid method can have errors, deriving from tilting of the sample, bending or slight inaccuracy in the array, therefore the latter method is more accurate since these deviations are included in the after image. A disadvantage of the second method is the throughput since only one cell can be analysed per experiment. An automised x-y stage can compensate for that. There is no significant difference between the two methods, although the trypsin method shows a trend to smaller force values. This shows that the method using an ideal grid is an useful alternative to the slower trypsin method for traction force analysis, but one has to be more accurate in sample preparation and handling.
We are interested in traction forces that are triggered by large substrate stiffness. Previous studies explored that large substrate stiffness might trigger cell events, that cannot be observed on soft substrates, e.g. triggering of cancer progression[34][120][195]. Therefore we used microposts with a high spring constant of 294nN/$\mu$m and tested our resolution limit especially for stiff substrate. Since we are testing small displacements, we can assume, that for softer microposts the resolution would be even better, because larger displacements can be observed. Our displacement detection limit is below 50nm, according to a force resolution of around 14nN. Forces of individual focal adhesions are around 10nN and the approximate area is around 2$\mu$m$^2$[9]. The surface area of the used microposts is 21$\mu$m$^2$, therefore more then one focal adhesion can be formed per post. This is confirmed by the fact that the stress generated per micropost from a cell is in the range of 2-6kPa for our measurements, corresponding to forces over 30nN and therefore multiple focal adhesions. In addition fluorescence imaging of focal adhesions on microposts shows that multiple focal adhesions are built[174] (also see Chapter 6, e.g. Figure 38). Previous studies measured stresses on focal adhesions for fibroblasts of around 3-5.5kPa[9][160]. Therefore the stresses lie 3-9 times over our resolution limit.
The accuracy of the tested approach can be improved by using fluorescence labelling of the micropost tops or fluorescent quantum dots for a better contrast[2]. However, this would be more expensive, time consuming and requires more equipment and a more complicated sample preparation, than just using phase contrast

images. Hence, our approach, using phase contrast images, Hough transformation and the hexagonal grid method, offers a compromise of detection accuracy, with a limit below 50nm and is therefore sufficient to measure cellular forces.

# 5 Cell traction force microscopy: Methods

The described cell traction force microscopy method was used for three different applications with different cell types. This chapter explains the methods used, beginning with the cell types and the cell culture. In the following part the cell manipulation is described, how the cells are influenced in different ways and then tested for their traction forces. In addition methods besides traction force microscopy are explained, where we analysed the cell height, orientation and performed focal adhesion staining.

## 5.1 Cell culture

To analyse integrin specific traction forces, three different mouse fibroblasts cell lines only expressing 5b1 integrins, avb3 and avb5 integrins or a combination of them were used. They were provided by the group of Reinhard Fässler, Department of Molecular Medicine, Max Planck Institute of Biochemistry, 82152 Martinsried[148].
NIH/3T3 mouse embryonic fibroblasts are derived from the Morphology Laboratory, Internal Medicine, University Hospital Ulm.
As model for lung epithelial cells, two lung cell lines were measured: adenocarcinomic human alveolar basal epithelial cell line A549 and rat epithelial cell line R3/1 were provided by the Institute of General Physiology, Ulm University.
As cell line model for osteocytes, murine long bone osteocyte Y4 cell line (MLO-Y4) was used, provided by the Institute of Orthopaedic Research and Biomechanics, Ulm University.

Fibroblasts, R3/1 cells and A549 cells were cultured in Dulbecco's Modified Eagle Medium with 10% fetal calf serum and 5% penicillin/streptomycin (all reagents from gibco® by life technologies™). MLO-Y4 cells were cultured in Minimum Essential Media with 10% fetal calf serum and 5% penicillin/streptomycin (all reagents from gibco® by life technologies™). Cells were splitted three times a week 1:10 with the according medium. Prior to seeding surfaces were sterilised with

ethanol and then coated with $5\mu g/cm^2$ fibronectin (Sigma-Aldrich®) for 2h. In case of MLO-Y4 cells collagen (gibco® by life technologies™) was used as coating agent for 1h (3mg/ml diluted 1:20). To coat just the top of the PDMS microposts, a drop of fibronectin or collagen was placed on it. After incubation time the solution was washed off two times with PBS and cells were seeded over night non confluent before measurement.

## 5.2 Cell manipulation

To test the influence of cell internal and external factors on traction force generation, cells were treated with different drugs to intervene in the internal force generation apparatus. In addition external shear stress was applied and the substrate stiffness and geometry was changed to trigger the cells with environmental factors.

### 5.2.1 Micropost size variation

Three different micropost sizes were used in our experiments to vary the substrate stiffness. Figure 16 shows scanning electron microscope images of the different microposts. For each size the radius and the length of eight different microposts were measured. Table 3 shows the mean values of the results with standard deviation and the calculated spring constant out of the mean values.
Scanning electron microscopy was performed with the Hitachi S5200. Therefore a small strip of the micropost array was cut and glued sideways on a special holder suitable for the sample holder of the microscope and platinum vapour coated. With this it was possible to scan the microposts from the side to take the exact measurements of the length and the diameter. The settings for HV control were 10kV and $10\mu A$.

Micropost A and C have the same radius, but different heights whereas B and C have the same height but different radius.
The microposts are arranged hexagonal with a centre to centre distance of twice the diameter. Therefore the array of microposts B has a higher density then for microposts A and C, but the same total area. If not stated otherwise, for all measurements micropost size C was used.

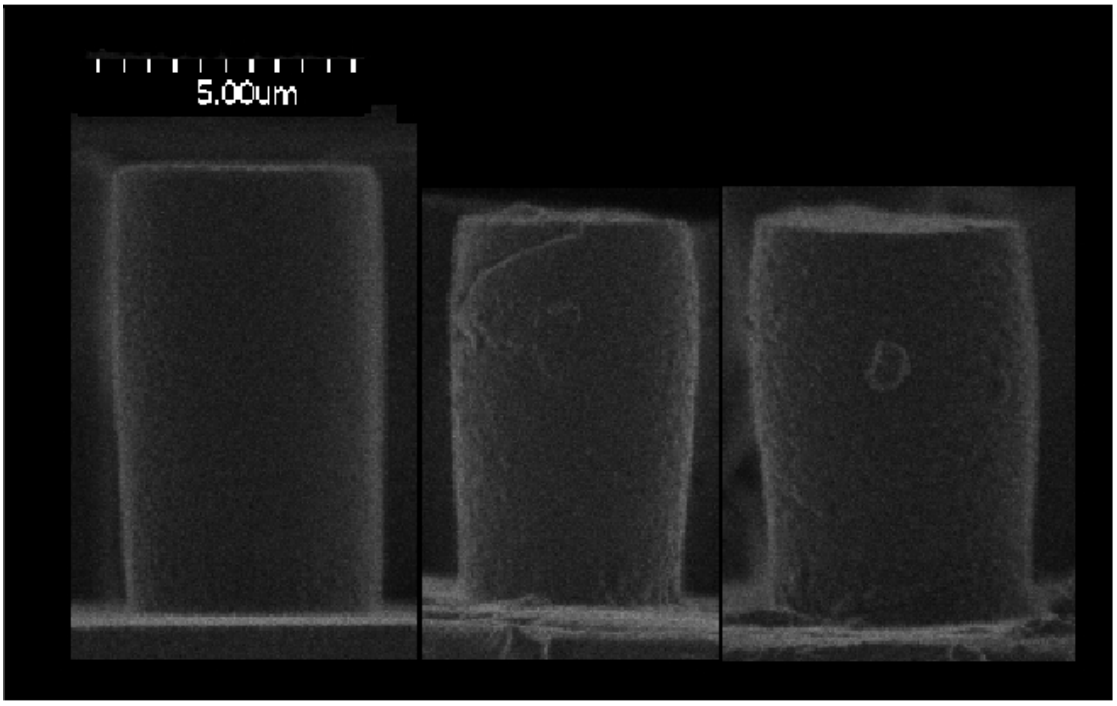


**A** **B** **C**

Figure 16: Scanning electron microscope images of PDMS microposts with different length and radius.

Table 3: Length, radius and calculated spring constant of the different microposts shown in Figure 16

| | A | B | C |
|---|---|---|---|
| Length | 8.721 ± 0.068$\mu$m | 7.459 ± 0.062$\mu$m | 7.691 ± 0.084$\mu$m |
| Radius | 2.624 ± 0.036$\mu$m | 2.184 ± 0.034$\mu$m | 2.623 ± 0.036$\mu$m |
| Spring constant | 202nN/$\mu$m | 155nN/$\mu$m | 294nN/$\mu$m |

### 5.2.2 External shear stress

A fluid shear stress of 2.51dyn/cm2 (0.251Pa) was applied to the cells using the ibidi® Pump System. Home-built flow chambers with integrated micropost arrays were used for cell traction force measurements. The perfusion set yellow/green was used for all experiments, with an inner diameter of 1.6mm and total working volume of 13.6ml. The used $\mu$-Slide I 0.8 Luer has a growth area of 2.5cm$^2$, a channel volume of 200$\mu$l and a channel height of 800µm. The same channel size was used for all experiments, except that for integrated microposts only the upper part was used. Flow was applied over night and measurements were taken after 15h during flow. The detailed operation instructions for the pump system were performed according to the ibidi Pump System Instructions handbook Version 1.5.2.

### 5.2.3 Fabrication of flow chambers with integrated microposts

Figure 17 shows a picture of a home-built flow chamber with integrated microposts. A glass plate was used as stable and flat substrate. PDMS was casted in the ratio 1:5 (curing agent to base) on the glass. The glass surface must be untreated to ensure a strong adhesion of the PDMS.
A small part of the silicon SU-8 mold was cut and placed on the thin PDMS layer. The size was chosen according to the measurements of a self-adhesive slide provided by ibidi$_®$ in order to fit into the channel. A picture of such a sticky-Slide I Luer 0.8 with a channel Volume of 200$\mu$l and a channel height of 800$\mu$m is shown in figure 17.
The sample was degased and then cross-linked over night at 60°C. The resulting mould was then silanized. Silanization was performed as described in the previous section. This step is crucial to enable the release of the PDMS imprint generated in the next step.
To create the imprint with microposts, PDMS in the ratio 1:10 (curing agent to base) was casted on the mold and again degased and cross-linked as described before. To cut out the imprint the sticky slide was placed over the sample to exactly cut the size of the slide and ensure that the microposts are inside the chamber. After gluing the sticky slide to the bottom, the finished slide is fixed with clamps, therefore an object slide is placed underneath the PDMS layer to stabilise the slide. The slide is then sealed additionally with PDMS at the edges to ensure a closed sample.

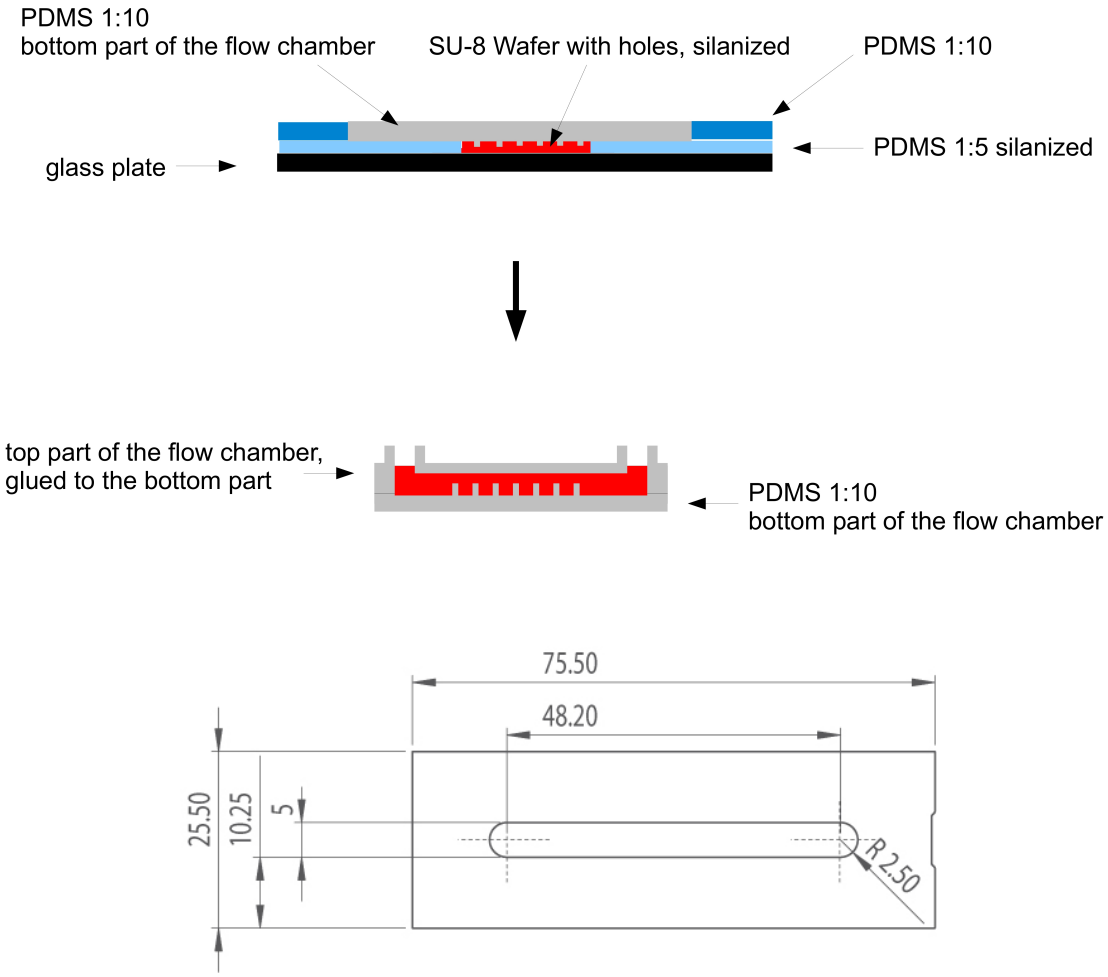


Figure 17: Construction of a flow chamber with sticky slides from ibidi® (top part of the flow chamber). Dimensions of a sticky-Slide I Luer 0.8 from ibidi® [1]. The middle part represents the channel.

### 5.2.4 Myosin inhibition

Blebbistatin is known to block non-muscle myosin II in an actin detached state. It slows down the phosphate release from the active pocket and therefore lowers the affinity for actin[86].
All cells were treated with 10µM blebbistatin (Sigma-Aldrich®) for 1h at 37°C before measurement. In case of no measurable effect the concentration was raised to 20$\mu$M and the incubation time to 3h. Blebbistatin was not washed out during measurement.

### 5.2.5 Actin disruption

Latrunculin A is a cell-permeable marine toxin from sea sponge that disrupts microfilament organisation by binding to monomeric G-actin[27].
Mouse fibroblast were treated with 0.5$\mu$M latrunculin A (Cayman Chemical) for 30min. at 37°C to disrupt actin filaments. Latrunculin a was not washed out during measurement.

### 5.2.6 Vimentin disruption

Acrylamide was shown to disrupt vimentin in intermediate filaments[146].
All cells were treated with 4mM acrylamide (Sigma-Aldrich®) for 1h at 37°C to disrupt vimentin. Acrylamide was not washed out during measurement.

### 5.2.7 Smooth muscle myosin kinase inhibition

Smooth muscle myosin kinase phosphorylates Ser19 in smooth muscle light chains and therefore acts as regulatory enzyme. Myosin light chain kinase (11-19) amide is an effective inhibitor of smooth muscle myosin light chain kinase[126].
MLO-Y4 cells were treated with 20µM myosin light chain kinase (11-19) amide (Enzo Life Sciences,Inc.) for 1h at 37°C. The inhibitor was not washed out during measurement.

### 5.2.8 Integrin blocking

Integrins were blocked separately in avb3/a5b1 with avb3- or a5b1-selective integrin antagonists (integrin-binding peptidomimetics)[136]. The peptides were kindly provided by Dr. Florian Rechenmacher (Institute for Advanced Study at the Department of Chemistry, Technische Universität München (Germany)). As concentration we used 15$\mu$M for the a5b1 antagonist and 3$\mu$M for the avb3 antagonist.

## 5.3 Cell height analysis

To analyse the influence of cell treatment on cell height, cells were seeded non confluent either in ibidi 8-well chambers for static conditions or flow chambers for shear stress conditions. The cell height was measured for all cell types under static conditions, after shear stress application and after vimentin disruption with acrylamide. MLO-Y4 cell height was measured after smooth muscle myosin kinase inhibition and for all other cell types after myosin inhibition with blebbistatin under static conditions and under shear stress.
After treatment cells were stained with CellMask™ Deep Red Plasma membrane stain (Molecular Probes™, Thermo Fisher Scientific ) for 10min. at 37°C then fixed with 4% Formaldehyde (Polysciences, Inc.) for 15min. and stored in PBS at 4°C until measuring.
Images were taken with the iMic digital microscope (Till Photonics, Germany) using structured illumination with a 40x oil objective. Z-stacks are created with an image distance of 200nm and a focus resolution of 0.01$\mu$m. Oligochrom light source with the filter Alexa 641nm wavelength at 75% intensity was used, with an exposure time of 50ms for each image. Images were evaluated with ImageJ Volume Viewer to get the cell height. 20 cells for each condition were measured from one sample.
An alternative method would be measurement of cell height with atomic force microscopy. The disadvantage of this method is the expenditure of time, therefor we decided to use the z-stacks method.

## 5.4 Cell orientation

To analyse the orientation of the cells under shear stress with and without active myosin we analysed the position of the Golgi complex relative to the nucleus. Typically the Golgi complex localises in front of the nucleus towards the leading edge of a cell[118].
The cell orientation was measured for all but the MLO-Y4 cells under static conditions, shear stress and shear stress with simultaneous myosin inhibition. Nucleus staining was performed after treatment with Hoechst 33342 nuclear stain (molecular probes™,invitrogen™) for 10min. at 37°C. All following steps were performed at room temperature. Cells were fixed with 4% formaldehyde for 15min., washed twice with PBS and treated with 0.8% Triton for 10min. After washing three times with PBS, 3% BSA/PBS was added for 30min. For the R3/1 cells as first antibody mouse Golgi 58K (Thermo Fisher Scientific) 1:50 diluted was applied, for all other cells golgin-97 rabbit(Cell Signaling Technology, Inc.) 1:100 diluted in

PBS was applied for 3h. After three times washing with PBS the second antibody Goat Rabbit Cy3 Conjugated (Millipore™) and Cy3-conjugated AffiniPure Goat Anti-Mouse IgG (Jackson ImmunoResearch Laboratories, Inc.) were applied for 3h according to the first antibody. Samples were washed three times with PBS and stored until measurement in PBS at 4°C.
Images were taken with the Zeiss Observer D1 with a 40x objective. At least 10 images were taken from different spots on one sample. For analysis the ImageJ dapi-golgi orientations macro (V.Bindokas, Univ. of Chicago, FEB 2013) was used. It detects the nucleus and the golgi complex in separate images and creates masks from the binary images. Then the angle between the centre of the detected objects was determined to get the orientation of the cell.

## 5.5 Paxillin staining

To characterise the focal adhesion shape and distribution on microposts under different conditions, cells were stained for paxillin after treatment.
All steps were performed at room temperature after treatment. Cells were fixed with 4% formaldehyde for 15min., washed three times with PBS and treated with 0.8% Triton/PBS. After three times washing with PBS cells are blocked for 30min. with 3% BSA/PBS. The first antibody mouse anti paxillin (BD Transduction Laboratories™) is diluted 1:500 in 3% BSA/PBS and incubated for 30min. Washing was performed for 3h every half hour with PBS. Second antibody Cy3 anti mouse (Jackson ImmunoResearch Laboratories, Inc.) was diluted 1:500 in PBS and incubated for 2h. Samples were then washed three times with PBS and stored in Mowiol at 4°C. Images were taken with the Zeiss Observer D1 with a 100x objective. A fluorescent image of the paxillin staining was taken as well as a phase contrast image of the micropost outlines. Focal adhesion area and circularity were analysed using ImageJ.

## 5.6 Statistical test

As statistical test in all cases for the distribution of the data the Wilcoxon rank sum test (Matlab ranksum) was used. It is a nonparametric test for two independent samples. As null hypothesis equal medians for the two samples from continuous distributions are assumed. The default significance level is 5%. Therefore a p-value lower than 0.05 means a rejection of the null hypothesis of equal medians.

# 6 Application I: Integrin specific analysis

To measure integrin specific traction force generation, we analysed the two distinct integrin types a5b1 and avb3, separately and in cooperation, expressed in mouse fibroblasts. As unaltered control cell type we used NIH/3T3 mouse embryonic fibroblasts. We varied external parameters (substrate stiffness and geometry, external applied force with fluid shear stress) and internal parameters (myosin inhibition, actin disruption, vimentin disruption). The goal was to gain better insight into the integrin specific force generation process and the cooperation of the two integrins, by comparing the different responses of the cells.

## 6.1 Results

For each micropost underneath a cell, the traction stress is calculated from the force and of the upper face of the micropost. Further, all traction stresses are summed up for one cell. The data is then plotted as one boxplot per cell type showing the distribution and the median over all measured cells. The central mark is the median, the edges of the box are the 25th and 75th percentiles, the whiskers extend to the most extreme data points, and outliers are plotted as circles. Significant differences are marked with asterisks (* represents p<=0.05, ** represents p<=1E-2 and *** represents p<=1E-3).

### 6.1.1 Integrin a5b1 and avb3 specific cell traction forces

Figure 18 shows the traction forces for avb3 (n=160), a5b1 (n=175) and a5b1/avb3 (n=98) fibroblasts. avb3 cells show significant lower traction forces then a5b1 fibroblasts (p=0.03) and a5b1/avb3 fibroblasts (p=2.92e-04). There is no significant difference between a5b1 and a5b1/avb3 cells.

Figure 19 shows the boxplots for NIH/3T3 cells (n=107) and a5b1/avb3 cells (n=98). There is no significant difference.

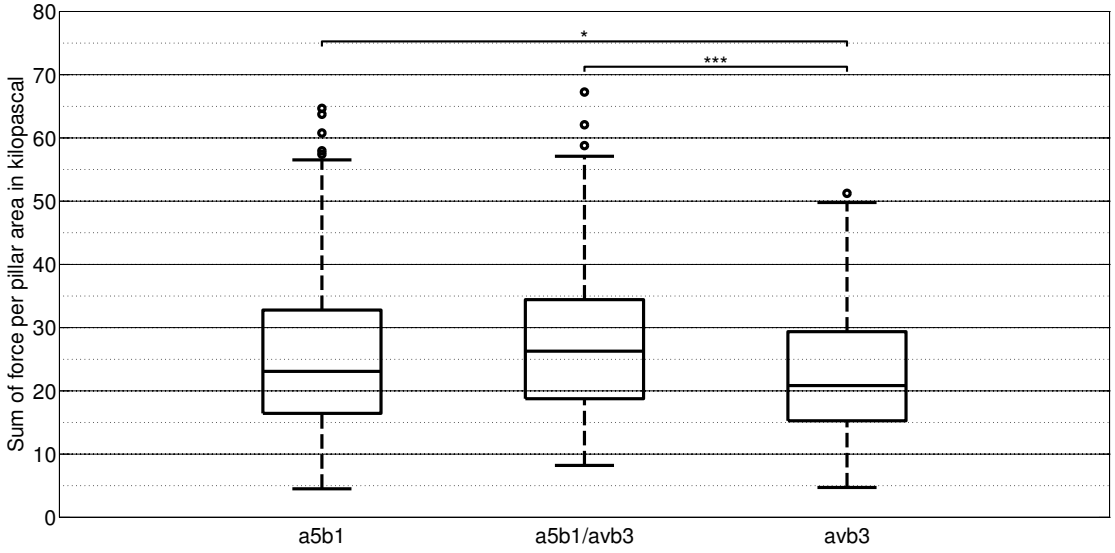


Figure 18: Boxplots of the cell traction forces for a5b1, a5b1/avb3 and avb3 fibroblasts.

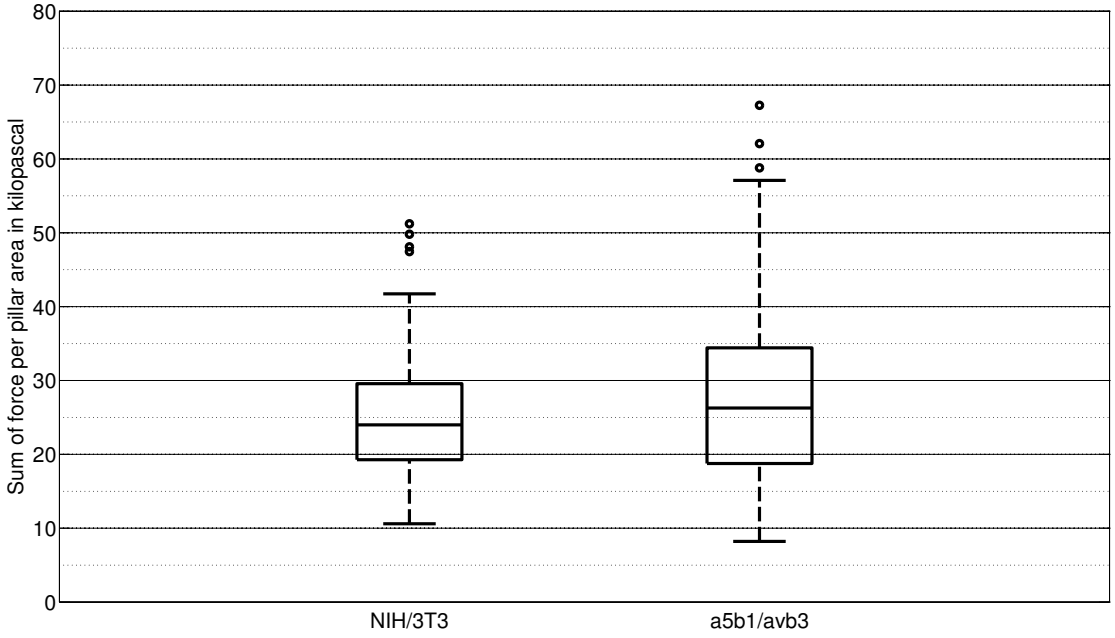


Figure 19: Boxplots of the cell traction forces for NIH/3T3 and a5b1/avb3 fibroblasts.

### 6.1.2 Substrate stiffness and geometry

Figure 20 shows traction forces for a5b1, a5b1/avb3 and avb3 fibroblasts on three different micropost sizes (see Figure 16 and Table 3).
Cell count for micropost A:
a5b1 cells: n=92, a5b1/avb3 cells: n=78, avb3 cells: n=93.
Cell count for micropost B:
a5b1 cells: n=121, a5b1/avb3 cells: n=111, avb3 cells: n=150.
Cell count for micropost C:
a5b1 cells: n=175, a5b1/avb3 cells: n=98, avb3 cells: n=160.

Micropost C (294nN/$\mu$m) is the default size used in all other experiments. For all celltypes there is a significant difference in traction forces between the three micropost sizes. Traction forces are highest on soft microposts (B: 155nN/$\mu$m) with a different density and radius as the other samples, intermediate for the stiffest microposts (C: 294nN/$\mu$m) and lowest for the middle micropost spring constant (A: 202nN/$\mu$m). For the micropost size A there is a significant difference (p=0.01) between a5b1 and a5b1/avb3 cells. The same for the micropost size B (p=0.04).

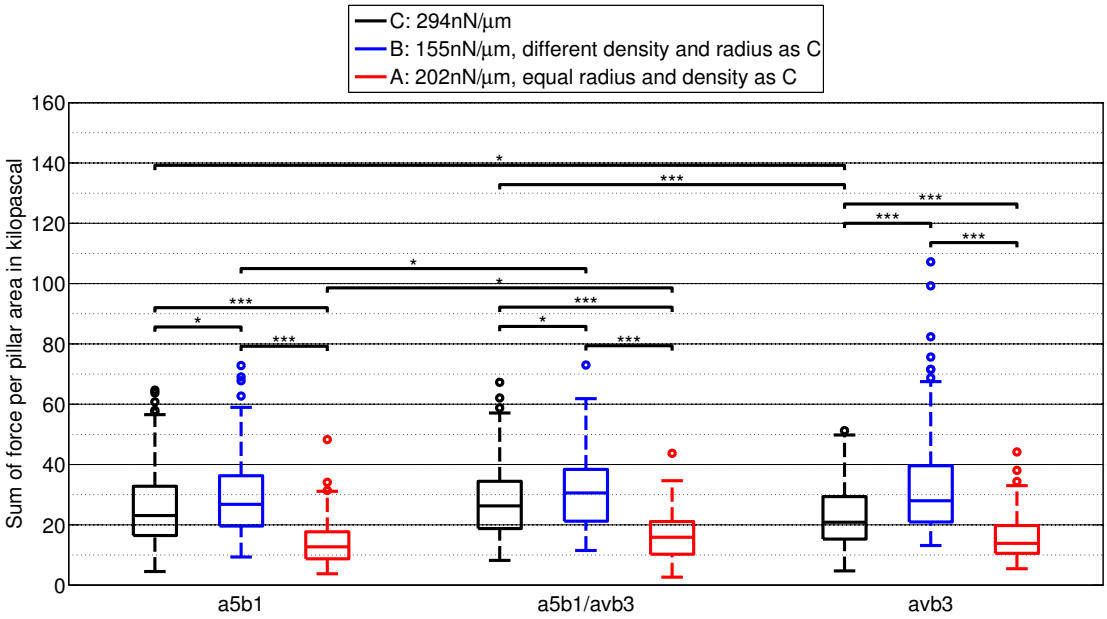


Figure 20: Boxplots of the cell traction forces for a5b1, a5b1/avb3 and avb3 fibroblasts on different micropost sizes.

### 6.1.3 Myosin inhibition, actin disruption and external shear stress

Figure 21 shows traction forces after myosin inhibition for a5b1 (n=80), a5b1/avb3 (n=79) and avb3 (n=92) fibroblasts. Traction forces are significantly lower after myosin inhibition for a5b1/avb3 cells (p=1.64e-07) and a5b1 cells (p=5.9e-07), but not for avb3 cells. Traction forces are significantly different between a5b1 and avb3 cells after myosin inhibition (p=0.01). A higher blebbistatin concentration and longer incubation time (20$\mu$m for 3h) was tested for avb3 cells, but did not yield a different result.

Figure 22 shows traction forces after actin disruption for a5b1 (n=111), a5b1/avb3 (n=109) and avb3 (n=101) fibroblasts. Traction forces are significantly lower after actin disruption for a5b1/avb3 cells (p=1.82e-09) and a5b1 cells (p=9.99e-04), but not for avb3 cells.

Figure 23 shows traction forces after applied fluidic external shear stress for a5b1 (n=126), a5b1/avb3 (n=96) and avb3 (n=99) fibroblasts. Traction forces after shear stress application are significantly higher for all three cell types, with the highest impact on avb3 cells (avb3 cells: p=2.50e-10, a5b1 cells: p=0.03 and a5b1/avb3 cells: p=0.003). Traction forces are significantly different after shear stress application between a5b1 and avb3 cells (p=0.01) and between a5b1 and a5b1/avb3 cells (p=3.60e-04).

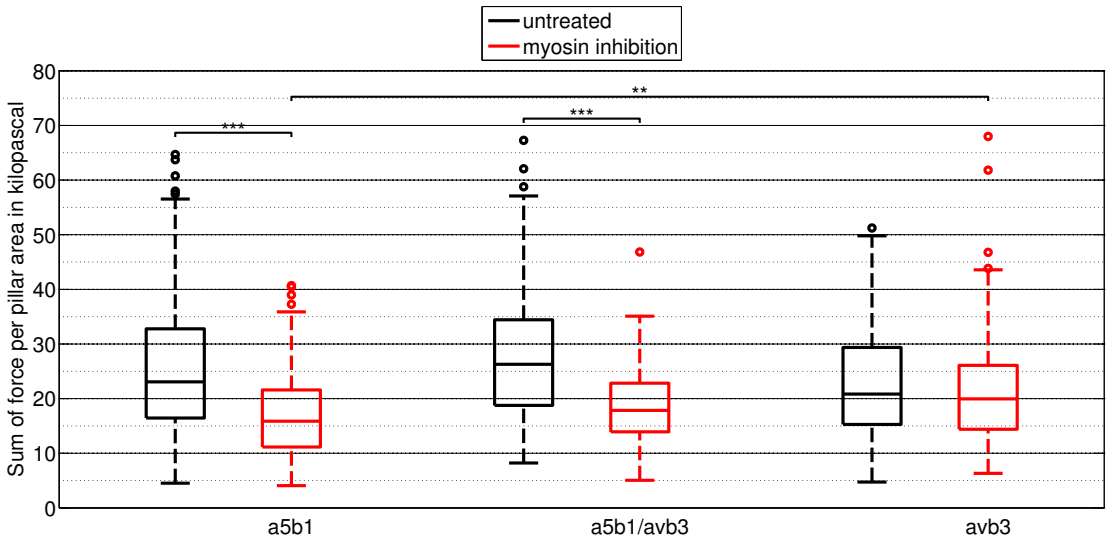


Figure 21: Boxplots of the cell traction forces for a5b1, a5b1/avb3 and avb3 fibroblasts with and without myosin inhibition under static conditions.

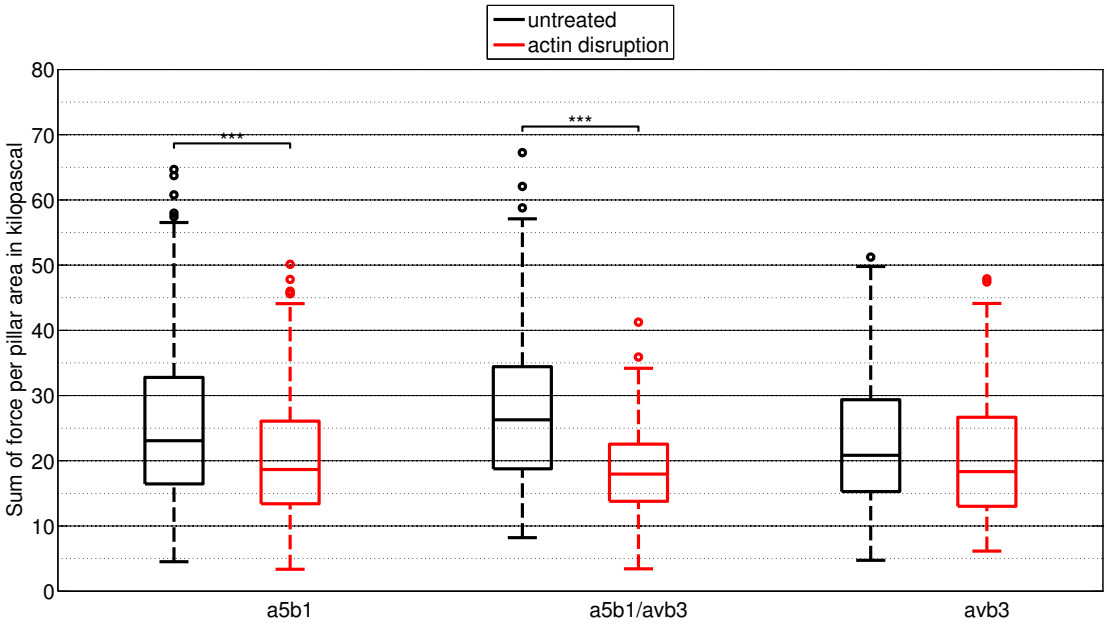


Figure 22: Boxplots of the cell traction forces for a5b1, a5b1/avb3 and avb3 fibroblasts with and without actin disruption under static conditions.

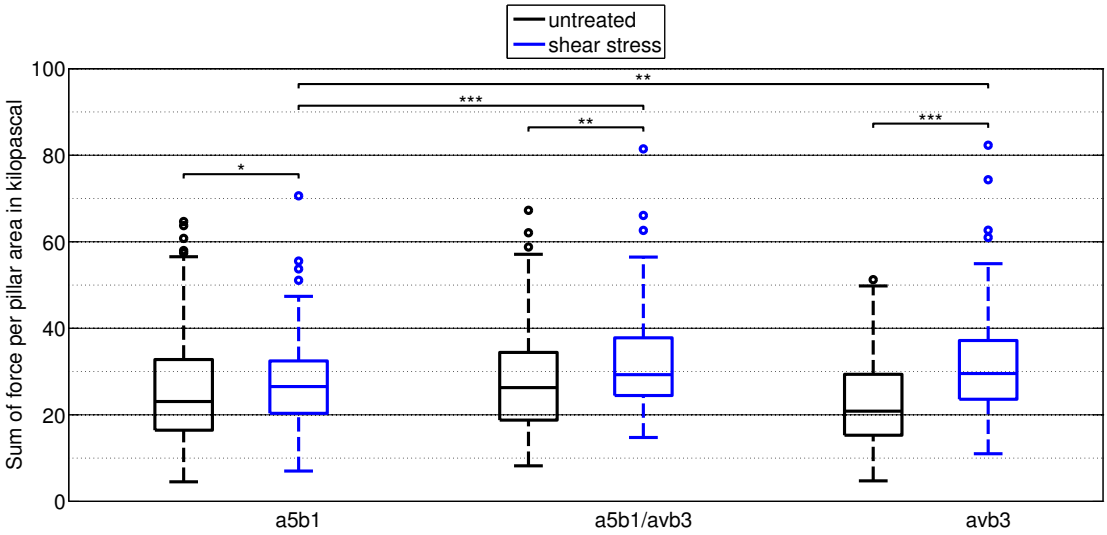


Figure 23: Boxplots of the cell traction forces for a5b1, a5b1/avb3 and avb3 fibroblasts with and without external fluidic shear stress application.

Figure 24 shows traction forces after applied shear stress and concurrent myosin inhibition for a5b1 (n=49), a5b1/avb3 (n=48) and avb3 (n=92) cells. Compared to the untreated state traction forces are not different for all cell types. Looking at the difference between shear stress and concurrent shear stress and myosin inhibition there is a significant reduction for all cell types after myosin inhibition (avb3 cells median difference 6.6±1.9kPa: p=1.35e-06, a5b1 cells median difference 4.6±2kPa: p=0.02 and a5b1/avb3 cells median difference 7±2kPa: p=8.3e-07). Traction forces are significantly higher for all cells when there is a concurrent application of shear stress and myosin inhibition compared with myosin inhibition under static conditions (avb3 cells: p=0.02, a5b1 cells: p=1.36e-05 and a5b1/avb3 cells: p=9.79e-05).

Figure 25 shows traction forces after applied shear stress and concurrent actin disruption for a5b1 (n=48), a5b1/avb3 (n=34) and avb3 (n=68) cells. Compared to the untreated state traction forces are significantly different only for avb3 cells (p=8.67e-04) with a median difference of 5.9±1.8kPa. Looking at the difference between shear stress and concurrent shear stress and actin disruption there is a significant reduction for all cell types after actin disruption (avb3 cells median difference 2.8±2.1kPa: p=0.02, a5b1 cells median difference 6.3±1.9kPa: p=2.91e-04 and a5b1/avb3 cells median difference 3.5±2.3kPa: p=0.02). Traction forces are significantly higher for avb3 and a5b1/avb3 cells when there is a concurrent application of shear stress and actin disruption compared with actin disruption under static conditions (avb3 cells: p=1.24e-05 and a5b1/avb3 cells: p=3.01e-08). Traction forces under shear stress and concurrent actin disruption are significant different between a5b1 and avb3 cells (p=0.003) and between a5b1 and a5b1/avb3 cells (p=0.002).

Figure 26 shows traction forces compared for NIH/3T3 and a5b1/avb3 cells under untreated conditions, with myosin inhibition, with shear stress application and with concurrent shear stress and myosin inhibition. For a clear arrangement the significance for the a5b1/avb3 cells is not shown. A higher blebbistatin concentration and longer incubation time (20$\mu$m for 3h) was used for the NIH/3T3 cells under static and shear stress conditions, because the lower concentration had no significant effect. Traction forces between the two celltypes for all parameters are not significant different. NIH/3T3 cells show the same behaviour as the a5b1/avb3 cells with significant difference between untreated state and myosin inhibition (p=0.01), untreated and shear stress application (p=4.64e-04), myosin inhibition under static and shear stress conditions (p=9.85e-05) and shear stress with and without myosin inhibition (p=0.02). (Cell count for the NIH/3T3 cells:

static untreated condition n=107, myosin inhibition n=66 , shear stress n=67 and shear stress with myosin inhibition n=47.

Figure 27 shows traction forces compared for NIH/3T3 and a5b1/avb3 cells under untreated conditions, with actin disruption, with shear stress application and with concurrent shear stress application and actin disruption. Traction forces between the two celltypes for all parameters are only significant for actin disruption under static conditions (p=6.59e-05). NIH/3T3 cells show the same behaviour as the a5b1/avb3 cells with significant difference between untreated state and actin disruption (p=0.01), untreated and shear stress application (p=4.64e-04), actin disruption under static and shear stress conditions (p=0.04) and shear stress with and without actin disruption (p=5.80e-05). (Cell count for the NIH/3T3 cells: actin disruption n=122 and shear stress with actin disruption n=52.)

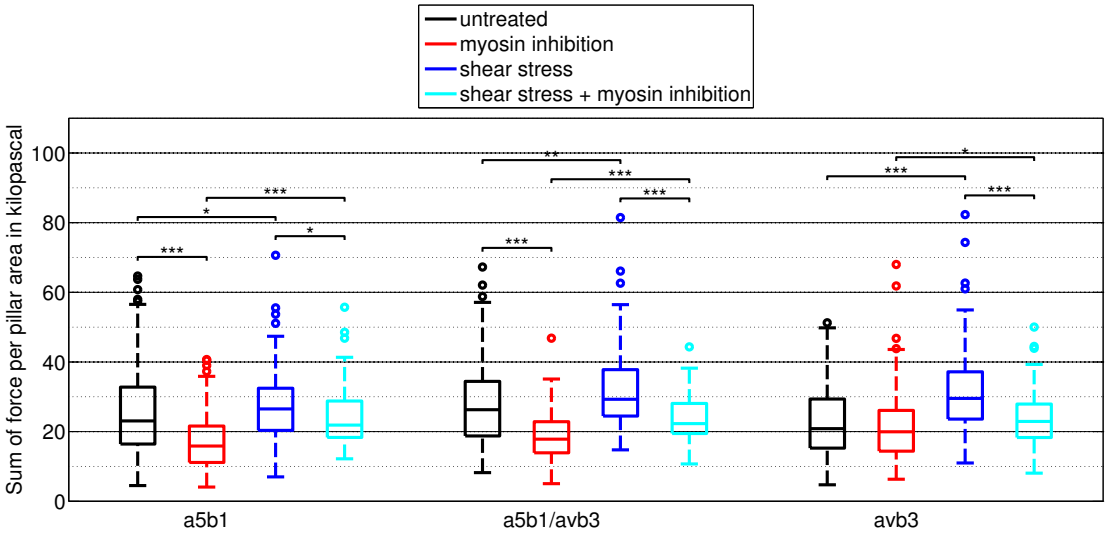


Figure 24: Boxplots of the cell traction forces for a5b1, a5b1/avb3 and avb3 fibroblasts with concurrent shear stress application and myosin inhibition.

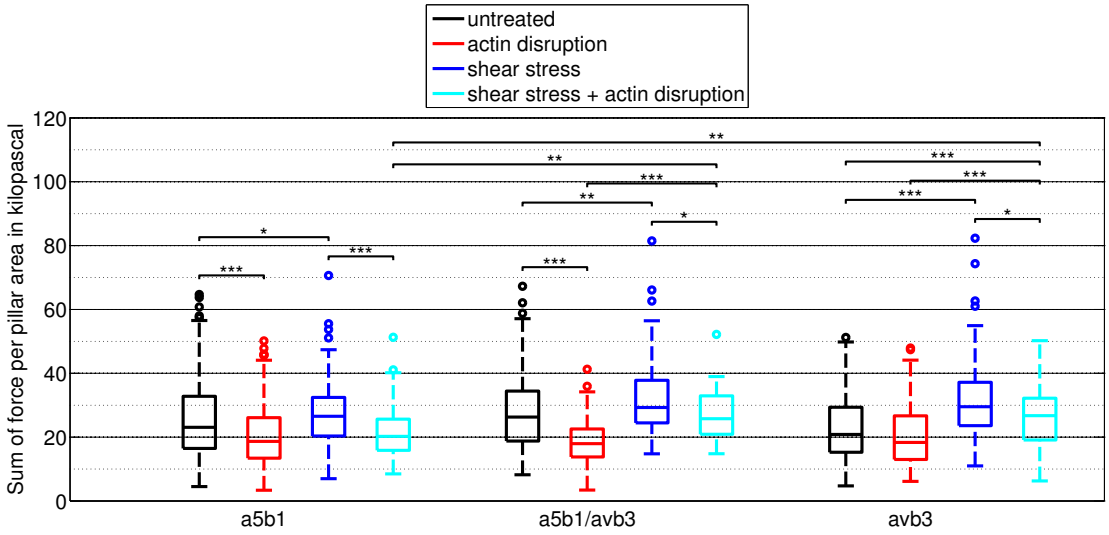


Figure 25: Boxplots of the cell traction forces for a5b1, a5b1/avb3 and avb3 fibroblasts with concurrent shear stress application and actin disruption.

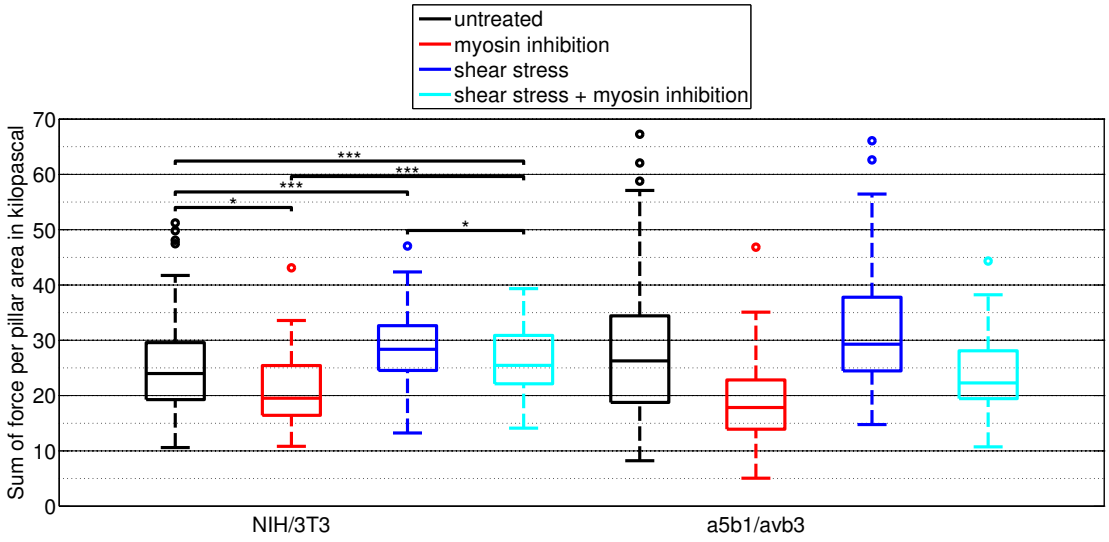


Figure 26: Boxplots of NIH/3T3 fibroblasts and a5b1/avb3 cells under untreated conditions, with myosin inhibition, with shear stress application and with concurrent shear stress application and myosin inhibition.

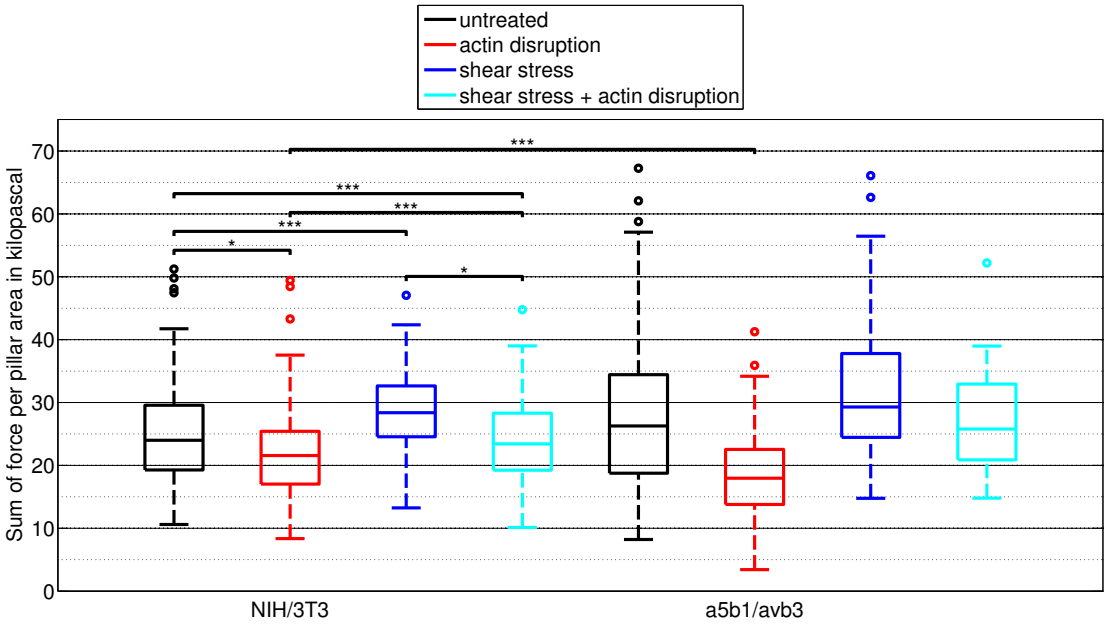


Figure 27: Boxplots of NIH/3T3 fibroblasts and a5b1/avb3 cells under untreated conditions, with actin disruption, with shear stress application and with concurrent shear stress application and actin disruption.

### Absolute difference of the median traction forces

Figure 28 shows the absolute differences of the median values of the cell traction forces for a5b1, a5b1/avb3, avb3 and NIH/3T3 fibroblasts.
The difference for a5b1 cells is higher for myosin inhibition under static compared to shear stress conditions and to actin disruption under static conditions, but similar to actin disruption under shear stress. avb3 cells show a strong difference between traction forces after myosin inhibition under shear stress, but almost no difference under static conditions. The difference for actin disruption is similar under static and shear stress conditions, but smaller than for myosin inhibition under shear stress. a5b1/avb3 cells show a similar difference for myosin inhibition and actin disruption under static conditions and myosin inhibition under shear stress, but a smaller difference for actin disruption under shear stress. NIH/3T3 cells show almost the same differences for all conditions, myosin inhibition under static conditions and actin disruption under shear stress being slightly higher.

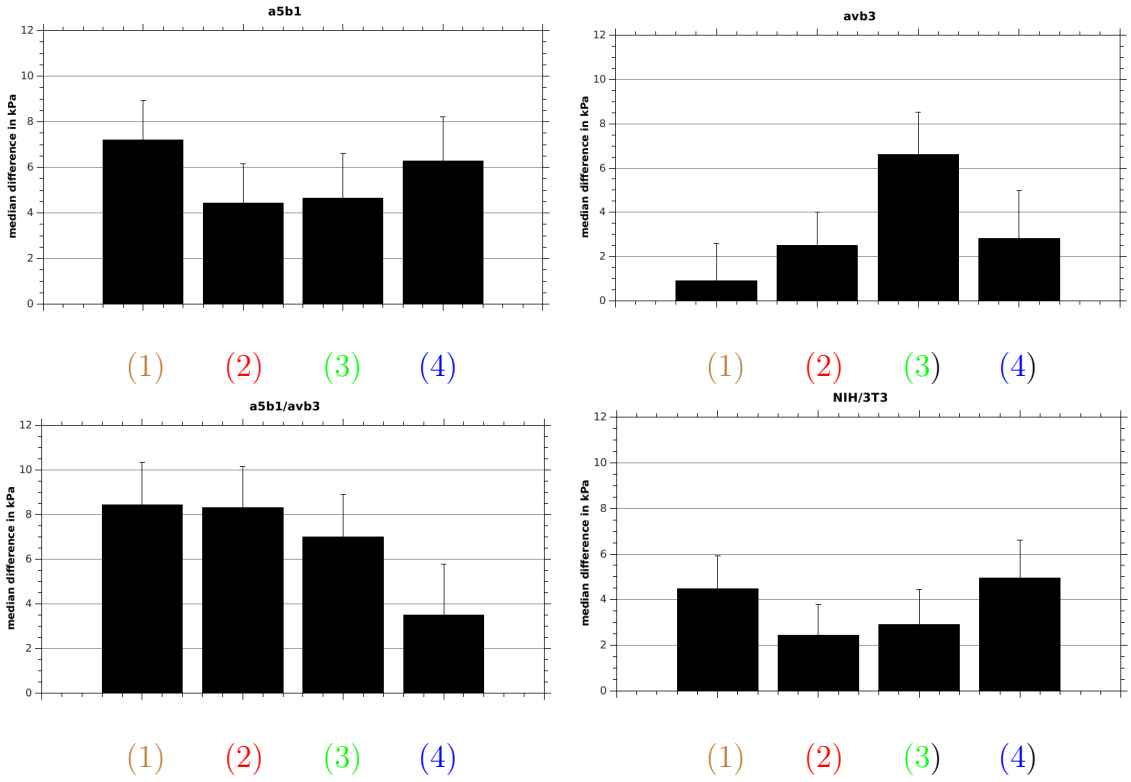


Figure 28: Absolute differences of the median values of cell traction forces showing
(1) the difference static - static and myosin inhibition,
(2) difference static -static and actin disruption,
(3) difference shear stress - shear stress and myosin inhibition,
(4) difference shear stress - shear stress and actin disruption.
Shown are the values for a5b1, a5b1/avb3, avb3 and NIH/3T3 fibroblasts. The error bars represent the standard error of the median.

### Directionality of micropost displacement

The following results have to be interpreted in reference to the direction of the applied shear stress. Therefore the direction of the flow is the same for all measurements and images with an assigned coordinate system. The direction of the flow is always form 0° to 180°. To analyse the direction of generated traction forces in addition to the magnitude, the directional displacement of the microposts underneath a cell was determined in reference to the direction of the shear stress. Therefore the traction forces for one cell were divided into three bins according to the displacement direction: 0-60°, 60-120° and 120-180°. The sum of the traction stress for each bin was calculated for each cell and the mean value over all cells was built.

Figure 29 shows the micropost displacement direction for a5b1 and avb3 cells and figure 30 for a5b1/avb3 and NIH/3T3 cells under static conditions and under shear stress, as well as the absolute difference of traction forces under shear stress minus traction forces under static conditions for the three bins.
Shear stress has only a slight influence on micropost displacement for the a5b1 cells, showing a displacement against the flow (0-60 vs 120-180 p=0.0056, static: 60-120 vs 120-180 p=0.0324). For the avb3 cells there is also a visible displacement against the flow (0-60 vs 120-180 p=0.0071; static 60-120 vs 120-180 p=0.0012), only stronger pronounced than for the a5b1 cells. a5b1/avb3 cells show a slight shift of micropost displacement with the flow (no significance), whereas for the NIH/3T3 cells the displacement direction is evenly distributed.

Figure 31 - 34 show the micropost displacement directions for a5b1, avb3, a5b1/avb3 and NIH/3T3 cells under static conditions, with myosin inhibition under static conditions, with actin disruption under static conditions, under shear stress, with myosin inhibition under shear stress, and with actin disruption under shear stress. Also the absolute difference for the traction stresses with myosin inhibition or actin disruption compared to static or shear stress conditions is shown.
For all four cell types under static conditions the displacement is nearly equally distributed for myosin inhibition, whereas there are differences after actin disruption for a5b1 and avb3 cells (a5b1 with actin disruption: 0-60 vs 120-180 p=0.0136; 60-120 vs 120-180 p=7.43e-004; avb3 with actin disruption: 0-60 vs 60-120 p=0.0087; 60-120 vs 120-180 p=0.0253). For the a5b1 cells the micropost displacement is shifted against the flow under shear stress with myosin inhibition (0-60 vs 120-180 p= 0.05) and with actin disruption, whereas for the latter the difference to the static state is not given (0-60 vs 120-180 p= 0.013 and 60-120 vs 120-180

p=4.03e-004). Therefore for the difference there is no strong shift to one direction detectable. For avb3 cells there is a nearly equal distribution of micropost displacement after myosin inhibition under shear stress, whereas with actin disruption there is a shift with the flow (0-60 vs 120-180 p= 0.0142). The difference shows for myosin inhibition and for actin disruption a shift of displacement against the flow. For a5b1/avb3 cells microposts are displaced more against the flow after myosin inhibition, and show a shift towards perpendicular displacement to the flow after actin disruption (0-60 vs 60-120 p=0.0341). The differences show a shift of displacement with the flow for myosin inhibition and a nearly equal distribution for actin disruption. For NIH/3T3 cells there is as strong perpendicular proportion of displacement with myosin inhibition (0-60 vs 60-120 p=0.0015; 60-120 vs 120-180 p=0.01) and a nearly equal distribution after actin disruption. The difference shows an equal distribution for both cases.

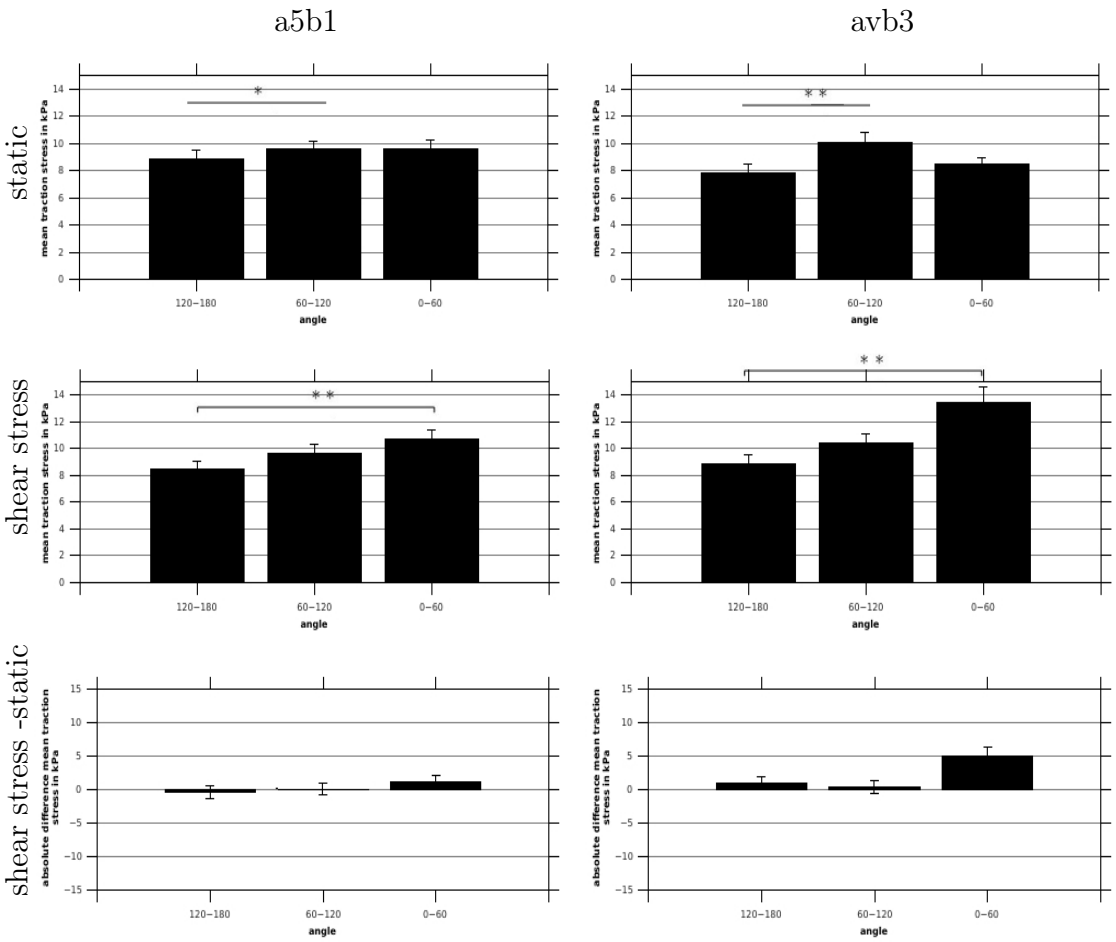


Figure 29: Cell traction forces in reference to the micropost displacement direction for a5b1 and avb3 cells under static conditions and under shear stress. The absolute difference of traction stress under shear stress minus static conditions is shown at the bottom. Error bars represent the standard error of the mean.

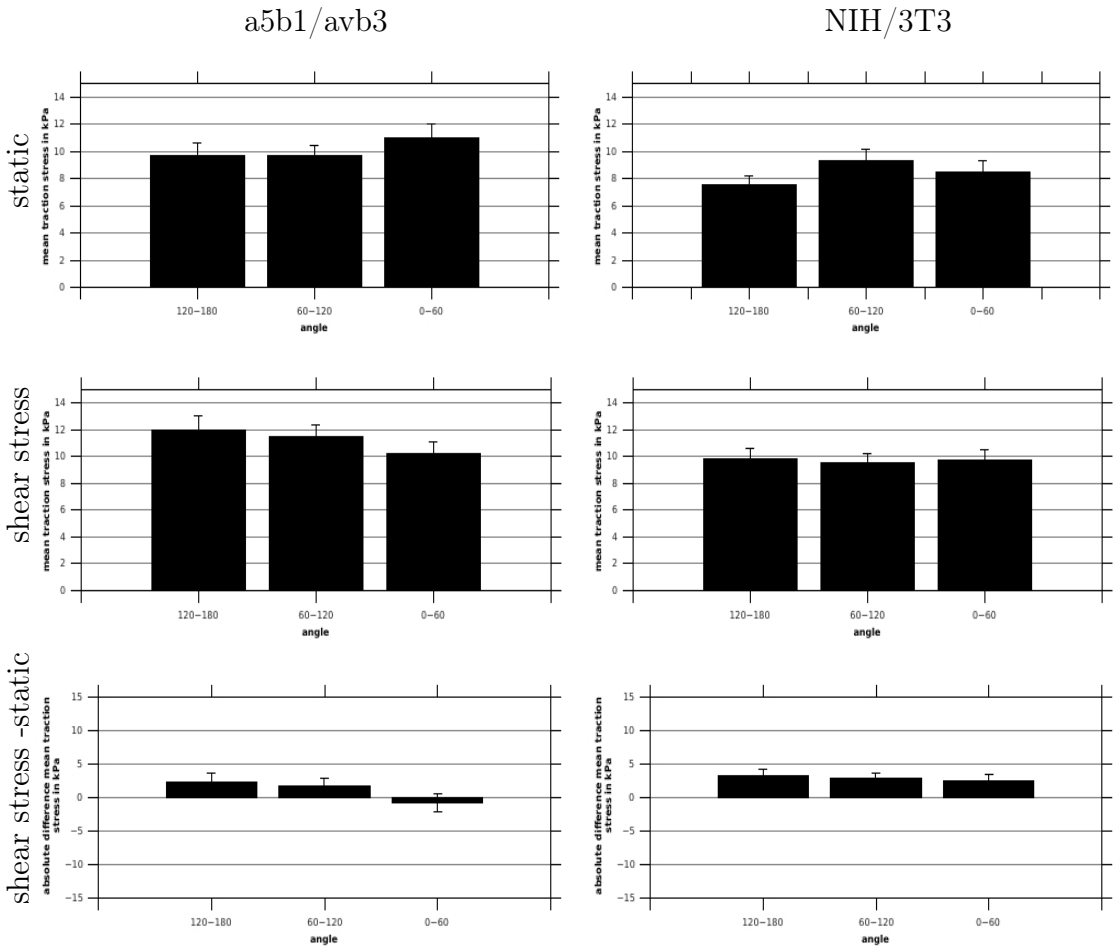


Figure 30: Cell traction forces in reference to the micropost displacement direction for a5b1/avb3 and NIH/3T3 cells under static conditions and under shear stress. The absolute difference of traction stress under shear stress minus static conditions is shown at the bottom. Error bars represent the standard error of the mean.

a5b1

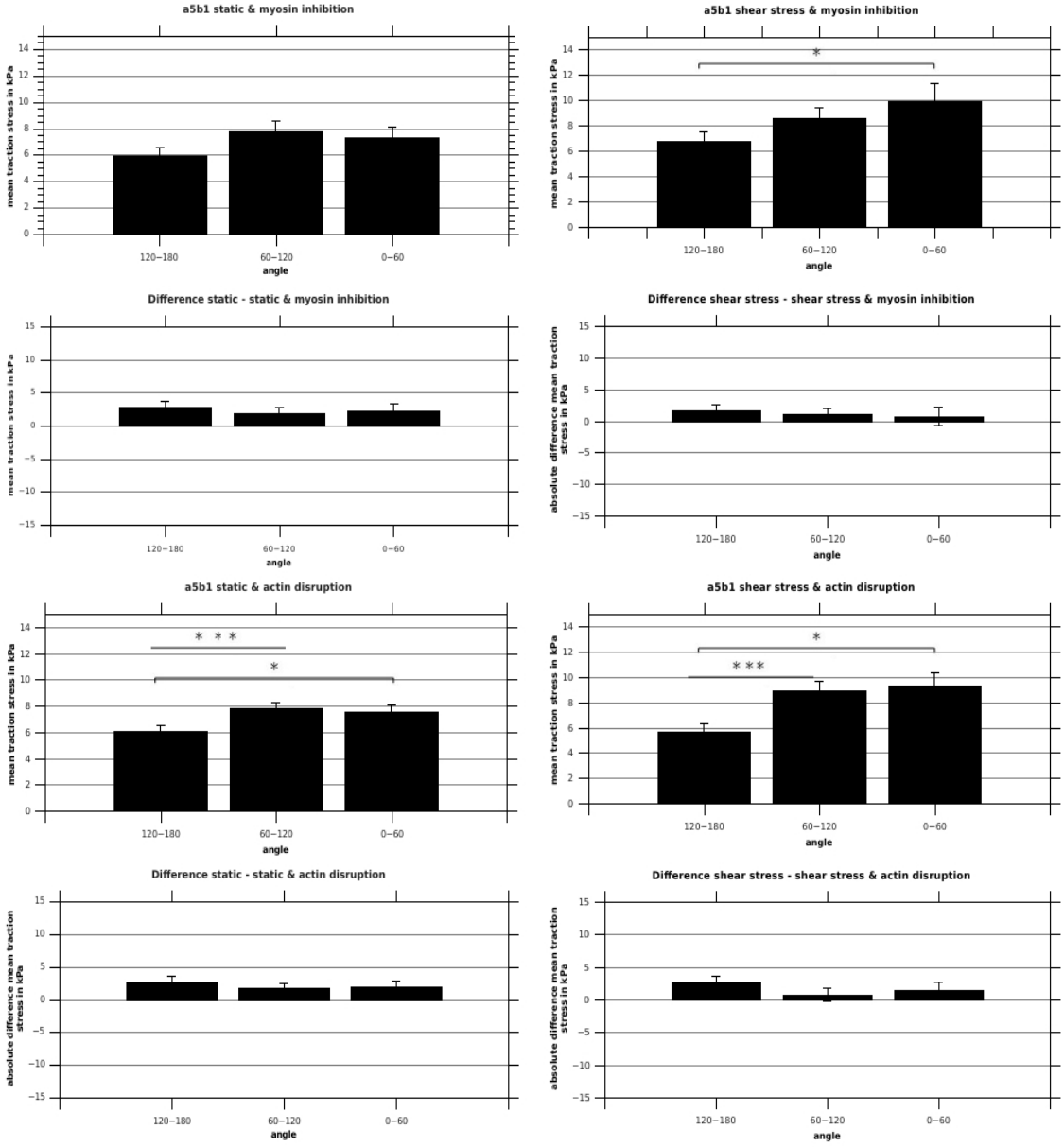


Figure 31: Cell traction forces in reference to the micropost displacement direction for a5b1 cells with myosin inhibition under static conditions and under shear stress and with actin disruption under static conditions and under shear stress. The absolute difference for traction forces with myosin inhibition or actin disruption compared to static conditions or shear stress conditions is shown below. Error bars represent the standard error of the mean.

avb3

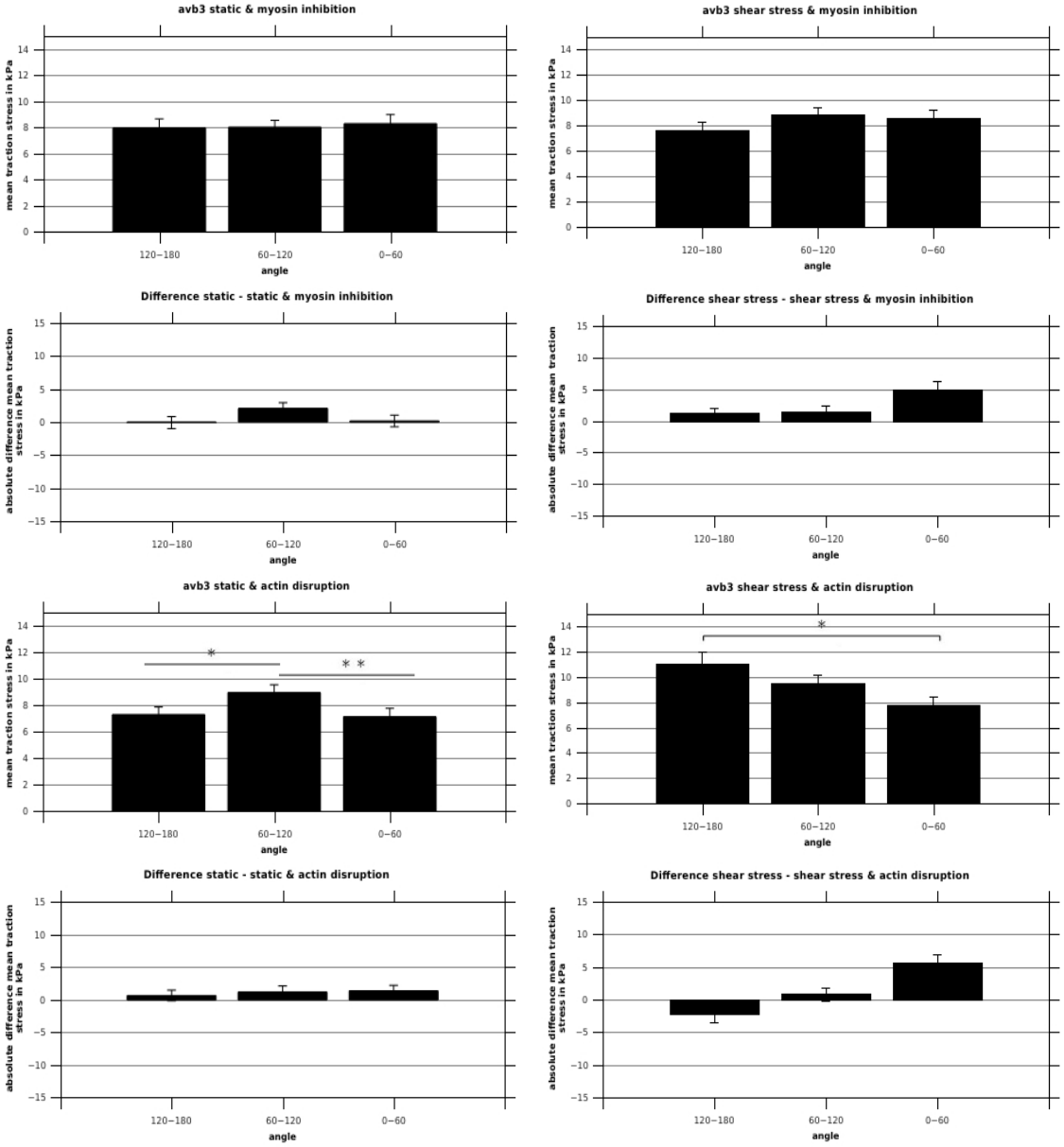


Figure 32: Cell traction forces in reference to the micropost displacement direction for avb3 cells with myosin inhibition under static conditions and under shear stress and with actin disruption under static conditions and under shear stress. The absolute difference for traction forces with myosin inhibition or actin disruption compared to static conditions or shear stress conditions is shown below. Error bars represent the standard error of the mean.

a5b1/avb3

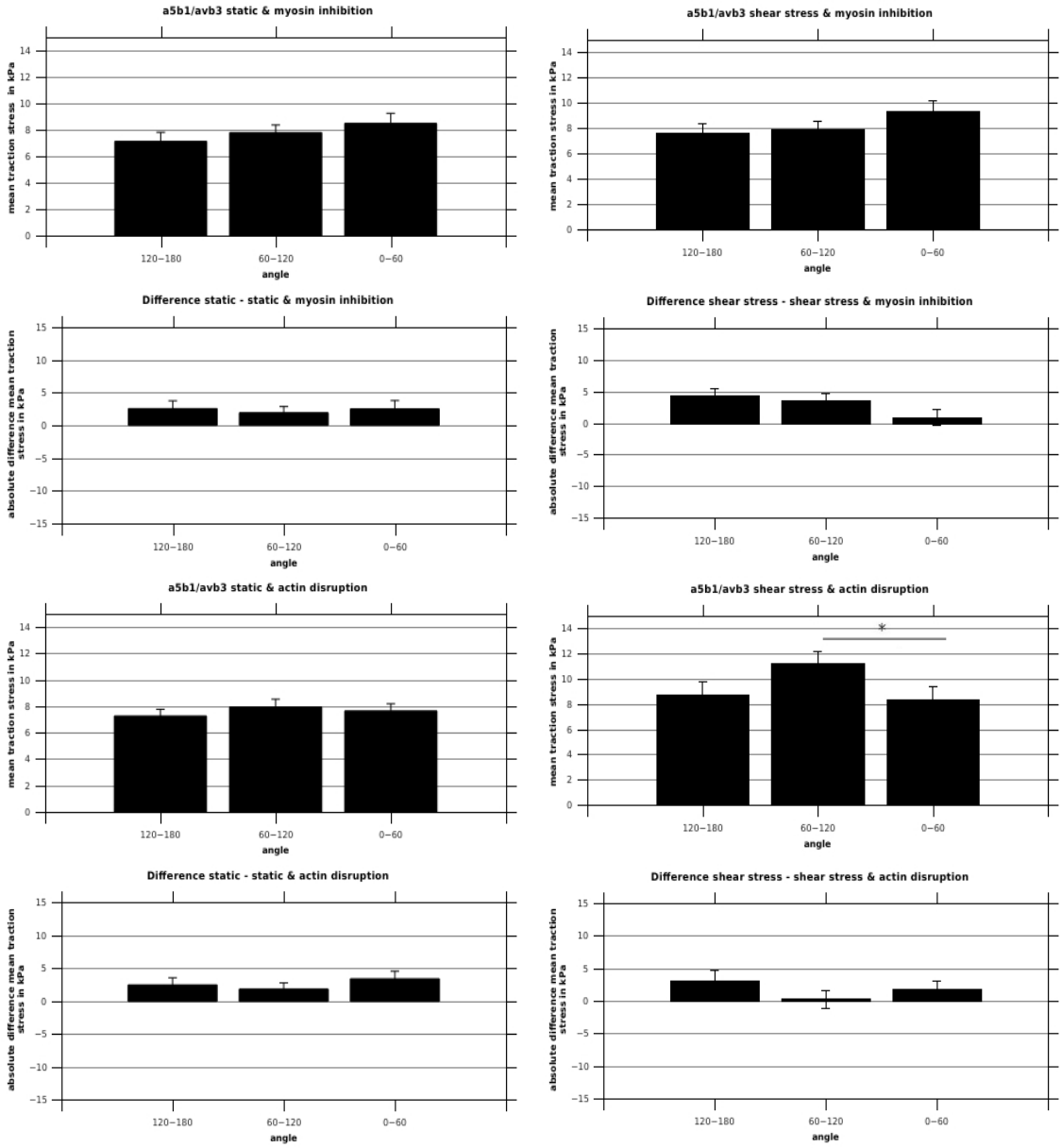


Figure 33: Cell traction forces in reference to the micropost displacement direction for a5b1/avb3 cells with myosin inhibition under static conditions and under shear stress and with actin disruption under static conditions and under shear stress. The absolute difference for traction forces with myosin inhibition or actin disruption compared to static conditions or shear stress conditions is shown below. Error bars represent the standard error of the mean.

NIH/3T3

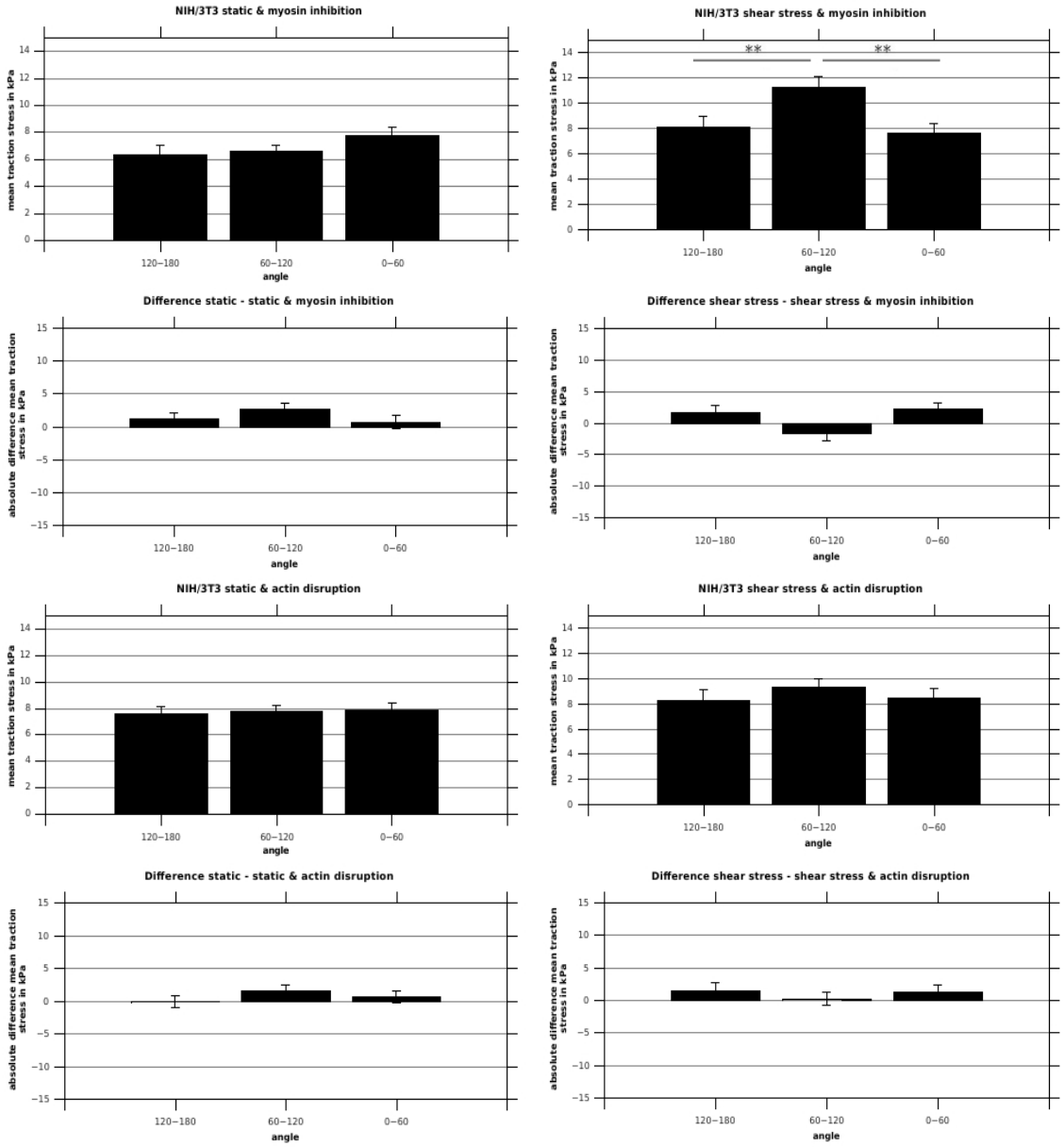


Figure 34: Cell traction forces in reference to the micropost displacement direction for NIH/3T3 cells with myosin inhibition under static conditions and under shear stress and with actin disruption under static conditions and under shear stress. The absolute difference for traction forces with myosin inhibition or actin disruption compared to static conditions or shear stress conditions is shown below. Error bars represent the standard error of the mean.

### Resulting micropost displacement direction

Figure 35 shows the resulting micropost displacement direction for a5b1, a5b1/avb3, avb3 and NIH/3T3 fibroblasts under static conditions, under shear stress and under shear stress with myosin inhibition or actin disruption. The resulting micropost displacement was first calculated for each cell and then the mean value over all cells was built. The results show the same tendency as the micropost displacement directions shown in figures 29 - 34. Table 4 shows the difference of resulting micropost displacements for shear stress - static conditions and under shear stress conditions with and without myosin inhibition and with and without actin disruption.

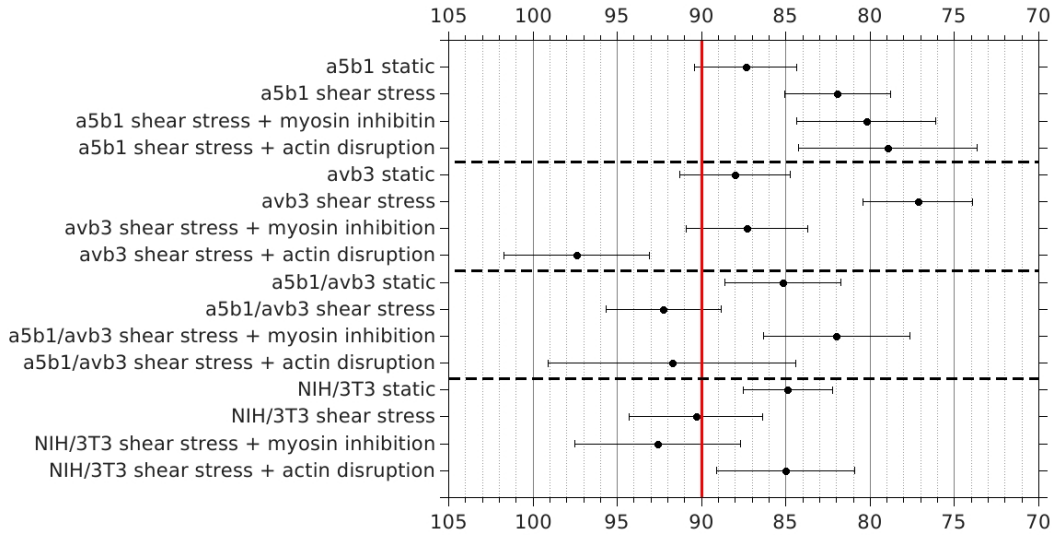


Figure 35: Resulting micropost displacement direction for a5b1, a5b1/avb3, avb3 and NIH/3T3 fibroblasts under static conditions, shear stress and shear stress with myosin inhibition or actin disruption. Shown is the mean value with the standard error of the mean. The x- axis shows the coordinates in degrees.

Table 4: Difference of resulting micropost displacement direction for a5b1, avb3, a5b1/avb3 and NIH/3T3 cells from Figure 35

| **Cell type and conditions** | **Difference in degrees** |
|---|---|
| a5b1 | |
| difference shear stress - static | -5.45 ± 4.34 |
| difference shear stress - (shear stress + myosin inhibition) | 1.70 ± 5.17 |
| difference shear stress - (shear stress + actin inhibition) | 2.97 ± 6.16 |
| avb3 | |
| difference shear stress - static | -10.85 ± 4.62 |
| difference shear stress - (shear stress + myosin inhibition) | -10.14 ± 4.86 |
| difference shear stress - (shear stress + actin inhibition) | -20.23 ± 5.39 |
| a5b1/avb3 | |
| difference shear stress - static | 7.08 ± 4.84 |
| difference shear stress - (shear stress + myosin inhibition) | 10.25 ± 5.52 |
| difference shear stress - (shear stress + actin inhibition) | 0.51 ± 8.09 |
| NIH/3T3 | |
| difference shear stress - static | 5.43 ± 4.76 |
| difference shear stress - (shear stress + myosin inhibition) | -2.26 ± 6.31 |
| difference shear stress - (shear stress + actin inhibition) | 5.32 ± 5.69 |

### Cell orientation

Figure 36 and 37 show the relative histograms of the nucleus to Golgi complex orientation for a5b1, avb3, a5b1/avb3 and NIH/3T3 cells. The leading front of a cell is characterised by the Golgi complex lying in front of the nucleus towards the cell front. The direction is given by the angle were the Golgi complex lies in reference to the nucleus.

Compared to the static orientation there is a shift of cell orientation against the flow direction for all cell types, with the smallest effect for a5b1 cells. After myosin inhibition there is a strong shift against flow direction for a5b1 and avb3 cells, whereas the orientation is nearly random for a5b1/avb3 and NIH/3T3 cells. The difference in oriented cells between shear stress with and without myosin inhibition shows for a5b1 and avb3 cells a shift with the flow. For the a5b1/avb3 and NIH/3T3 cells the difference shows a shift against the flow with a stronger effect for the latter ones.

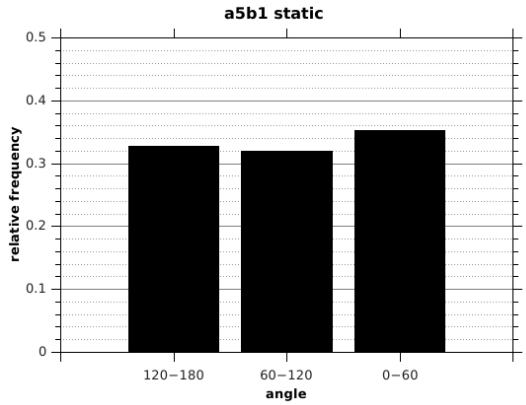
a5b1 static
relative frequency
0.5
0.4
0.3
0.2
0.1
0
120−180
60−120
0−60
angle

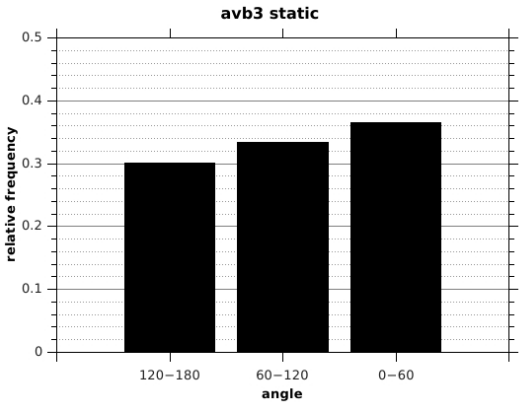
avb3 static
relative frequency
0.5
0.4
0.3
0.2
0.1
0
120−180
60−120
0−60
angle

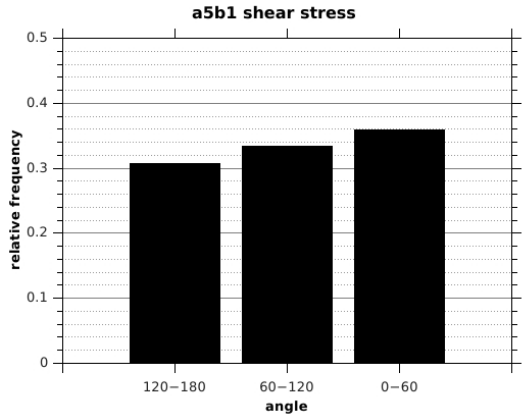
a5b1 shear stress
relative frequency
0.5
0.4
0.3
0.2
0.1
0
120−180
60−120
0−60
angle

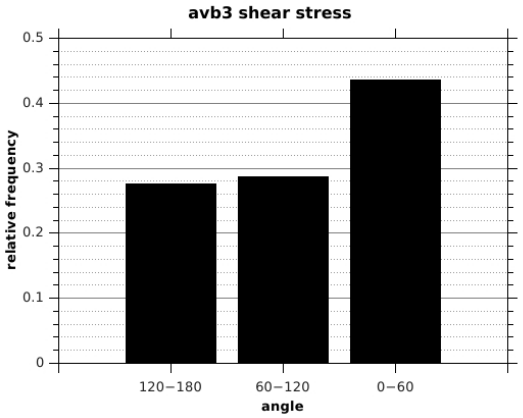
avb3 shear stress
relative frequency
0.5
0.4
0.3
0.2
0.1
0
120−180
60−120
0−60
angle

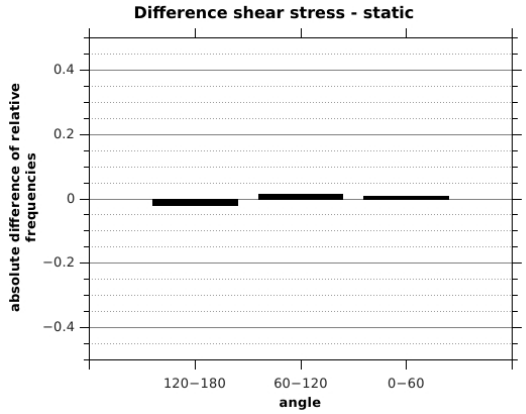
Difference shear stress - static
absolute difference of relative frequencies
0.4
0.2
0
−0.2
−0.4
120−180
60−120
0−60
angle

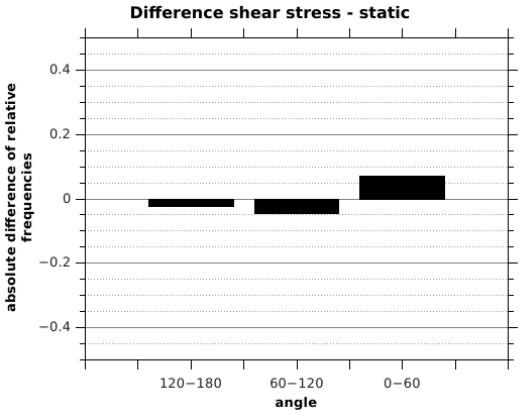
Difference shear stress - static
absolute difference of relative frequencies
0.4
0.2
0
−0.2
−0.4
120−180
60−120
0−60
angle

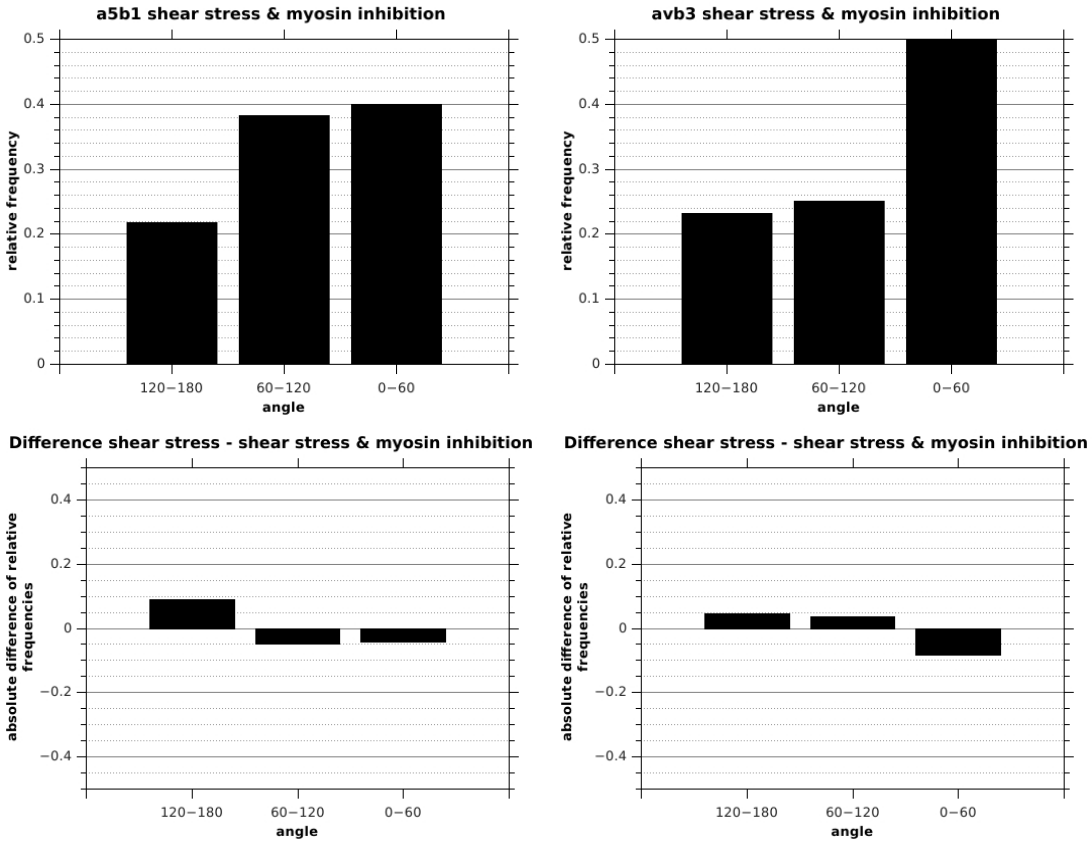


Figure 36: Relative histograms of cell orientation for a5b1 and avb3 cells under static conditions, under shear stress and under shear stress with myosin inhibition. The difference in oriented cells between shear stress and static, as well as shear stress with and without myosin inhibition is shown at the bottom.

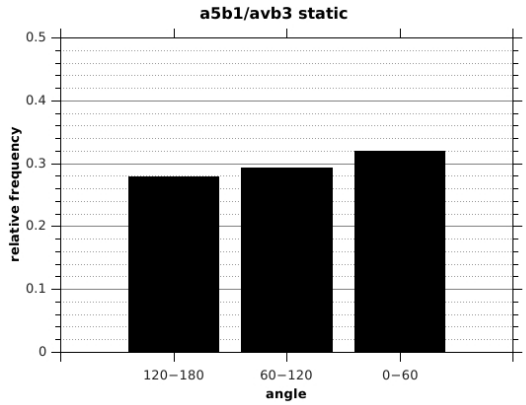
a5b1/avb3 static
relative frequency
0.5
0.4
0.3
0.2
0.1
0
120−180
60−120
0−60
angle

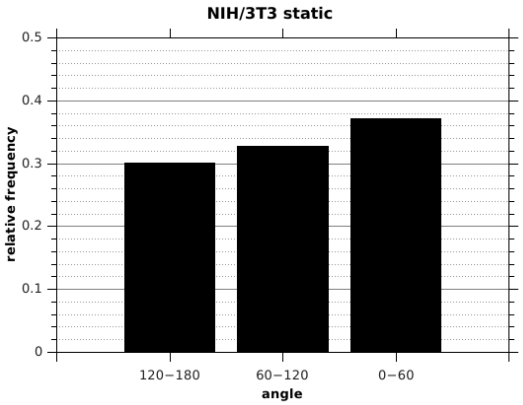
NIH/3T3 static
relative frequency
0.5
0.4
0.3
0.2
0.1
0
120−180
60−120
0−60
angle

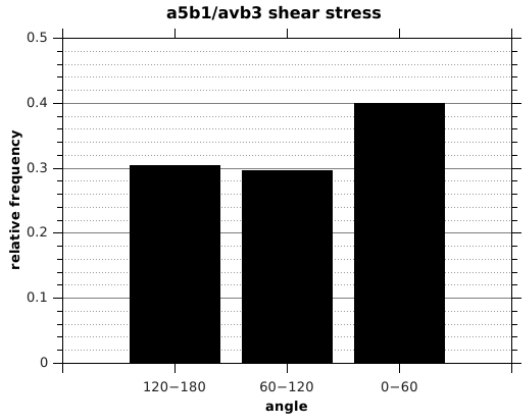
a5b1/avb3 shear stress
relative frequency
0.5
0.4
0.3
0.2
0.1
0
120−180
60−120
0−60
angle

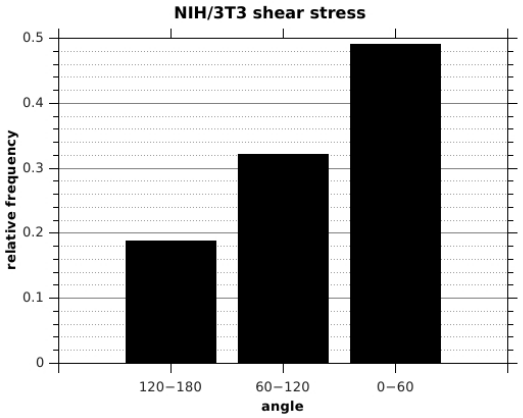
NIH/3T3 shear stress
relative frequency
0.5
0.4
0.3
0.2
0.1
0
120−180
60−120
0−60
angle

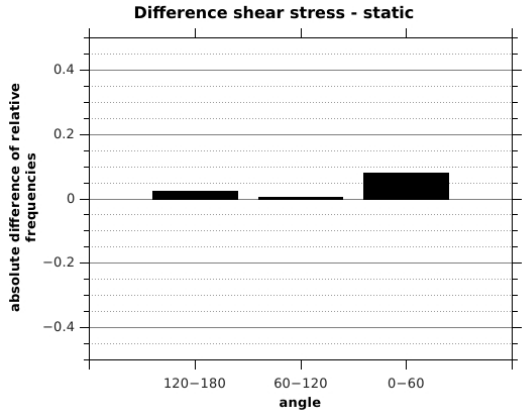
Difference shear stress - static
absolute difference of relative frequencies
0.4
0.2
0
−0.2
−0.4
120−180
60−120
0−60
angle

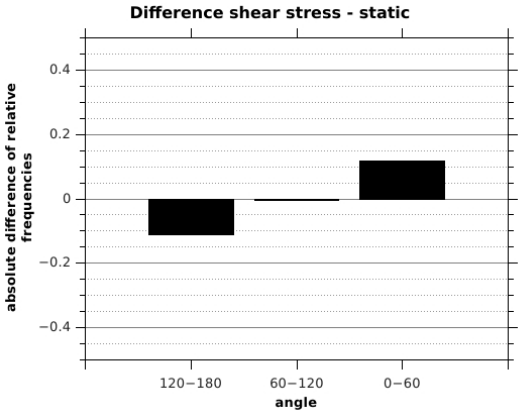
Difference shear stress - static
absolute difference of relative frequencies
0.4
0.2
0
−0.2
−0.4
120−180
60−120
0−60
angle

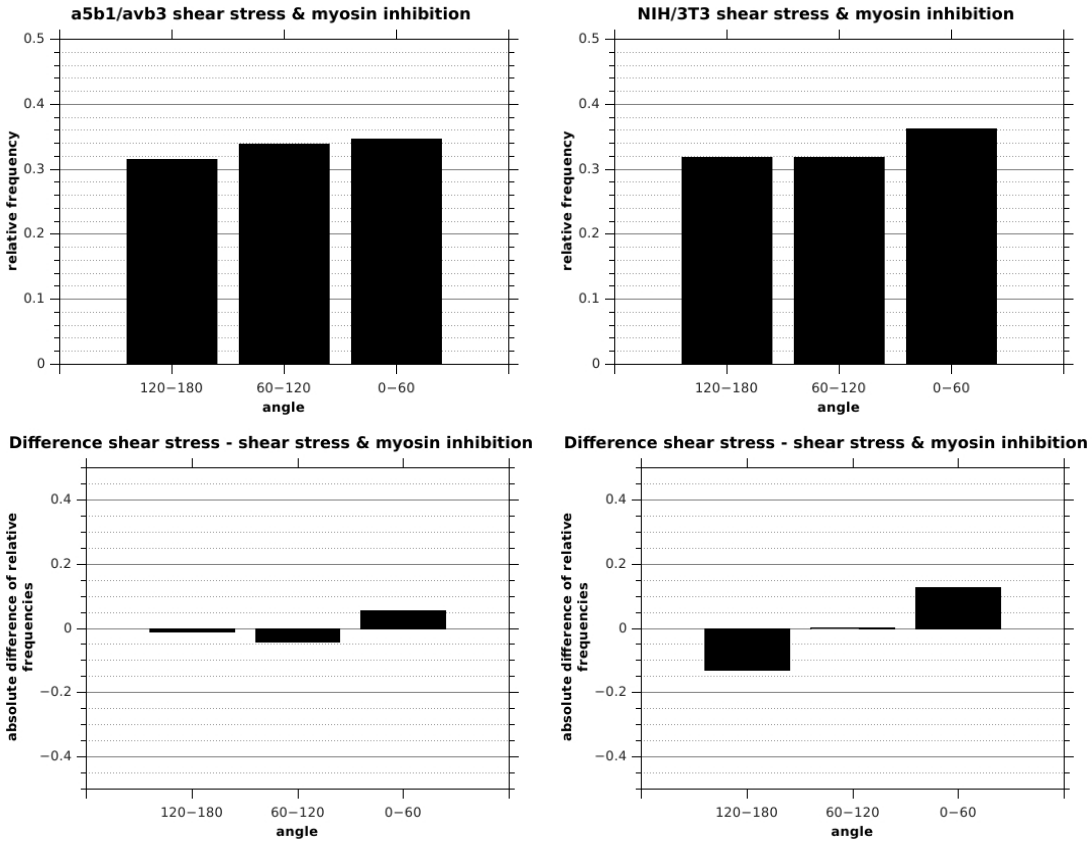


Figure 37: Relative histograms of cell orientation for a5b1/avb3 and NIH/3T3 cells under static conditions, under shear stress and under shear stress with myosin inhibition. The difference in oriented cells between shear stress and static, as well as shear stress with and without myosin inhibition is shown at the bottom.

### Paxillin staining

Figure 38 - 41 show fluorescence images of paxillin stained cells. Shown are a5b1, avb3, a5b1/avb3 and NIH/3T3 cells on microposts under static conditions with and without myosin inhibition and under shear stress with and without myosin inhibition. The micropost outline is shown in grey as well as the cell area, whereas the paxillin staining is shown in orange.
In general two distinct types of focal adhesions are observed. Stripe shaped elongated focal adhesion are placed on top of the microposts that are either short around 0.5$\mu$m or can cover almost the entire diameter of a micropost around 5$\mu$m. Thin circular shaped focal adhesion are observed to be wrapped around the outline of a micropost top. The two types are observed solitary or in combination.
Cytosolic paxillin is detected all over the cell, but focal adhesions exhibit stronger signals on the microposts.

a5b1 cells show stripe like as well as circular shaped focal adhesion wrapped around the microposts. After myosin inhibition the focal adhesions are weaker formed and less elongated. Under shear stress the focal adhesions are strongly build with stripe like and circular shapes as well as under static conditions. After myosin inhibition under shear stress the same effect as under static conditions is observed.
Focal adhesions from avb3 cells seem weaker as for a5b1 cells and with more stripe like shapes than circular. After myosin inhibition under static conditions they seem to be weaker pronounced and tend to build also circular shapes. Under shear stress they are again strongly build and show multiple short stripes on microposts as for static conditions and circular shaped focal adhesions around the microposts in addition. After myosin inhibition under shear stress focal adhesion are weaker and less elongated.
a5b1/avb3 cells build stripe like as well as circular shaped focal adhesion on the microposts, whereas after myosin inhibition they are still observed but less distinct. After shear stress application they are distinct and again stripe like and circular shaped. After myosin inhibition under shear stress the stripe shaped focal adhesions are gone and only small circular ones are left.
NIH/3T3 cells show stripe like focal adhesion on microposts under static conditions, that are weaker and more diffuse after myosin inhibition. After shear stress application they look thicker than under static conditions and again diffuse after myosin inhibition under shear stress.
For actin disruption under static conditions there were no clear focal adhesions visible, but only round cells with cytosolic paxillin stained.

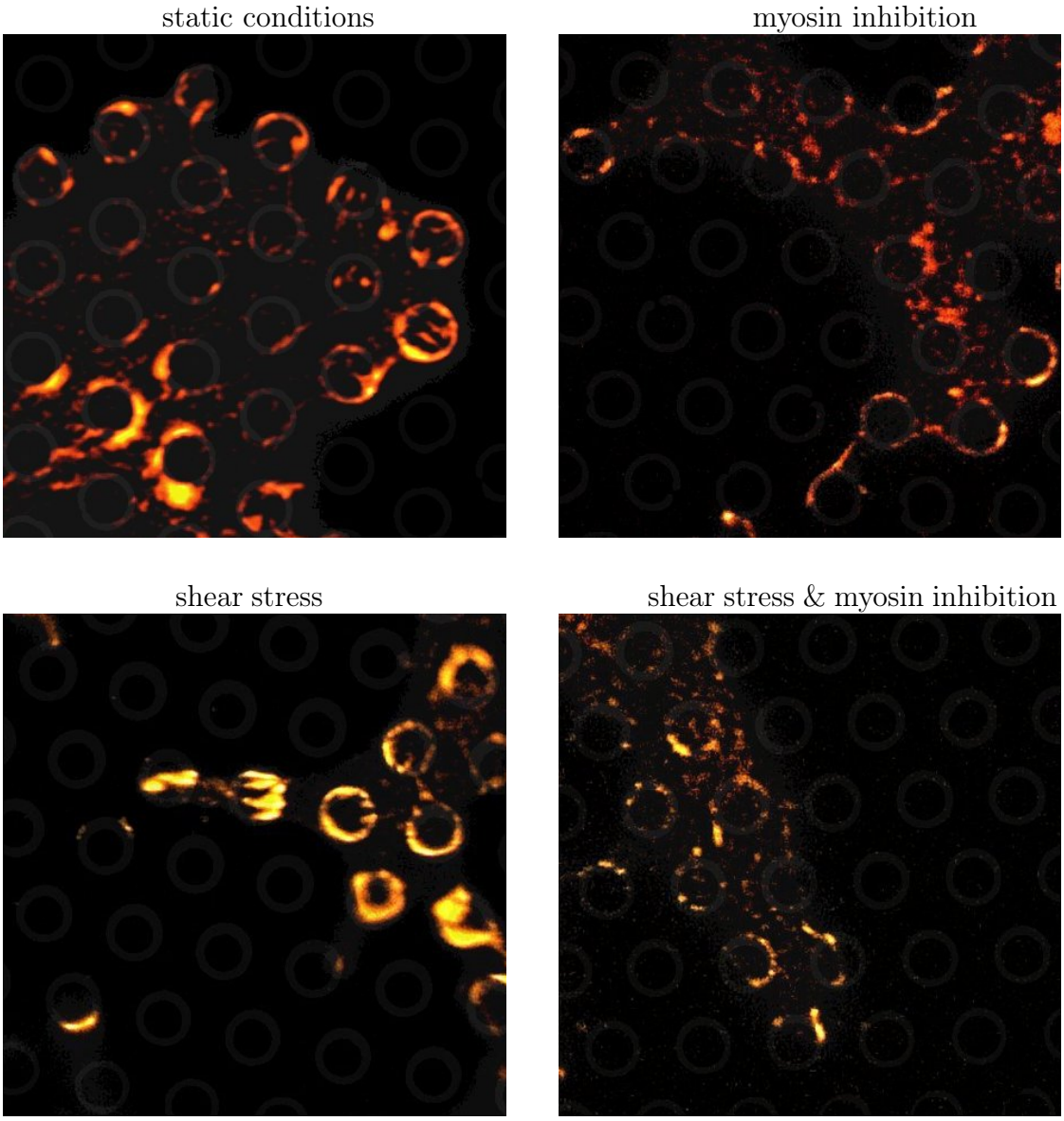


Figure 38: Paxillin staining of a5b1 cells on microposts under static untreated conditions, with myosin inhibition and under shear stress with and without myosin inhibition.

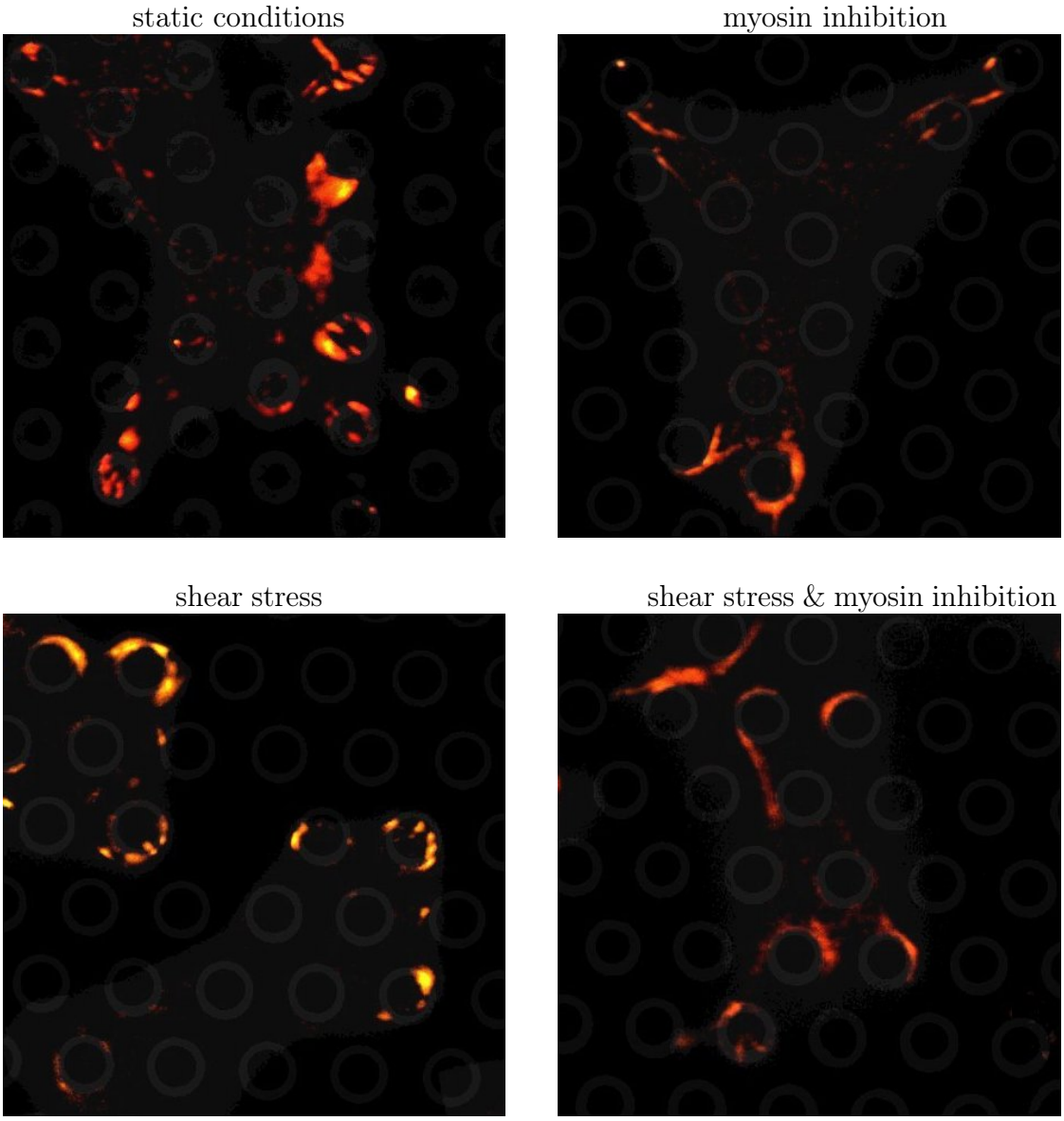


Figure 39: Paxillin staining of avb3 cells on microposts under static untreated conditions, with myosin inhibition and under shear stress with and without myosin inhibition.

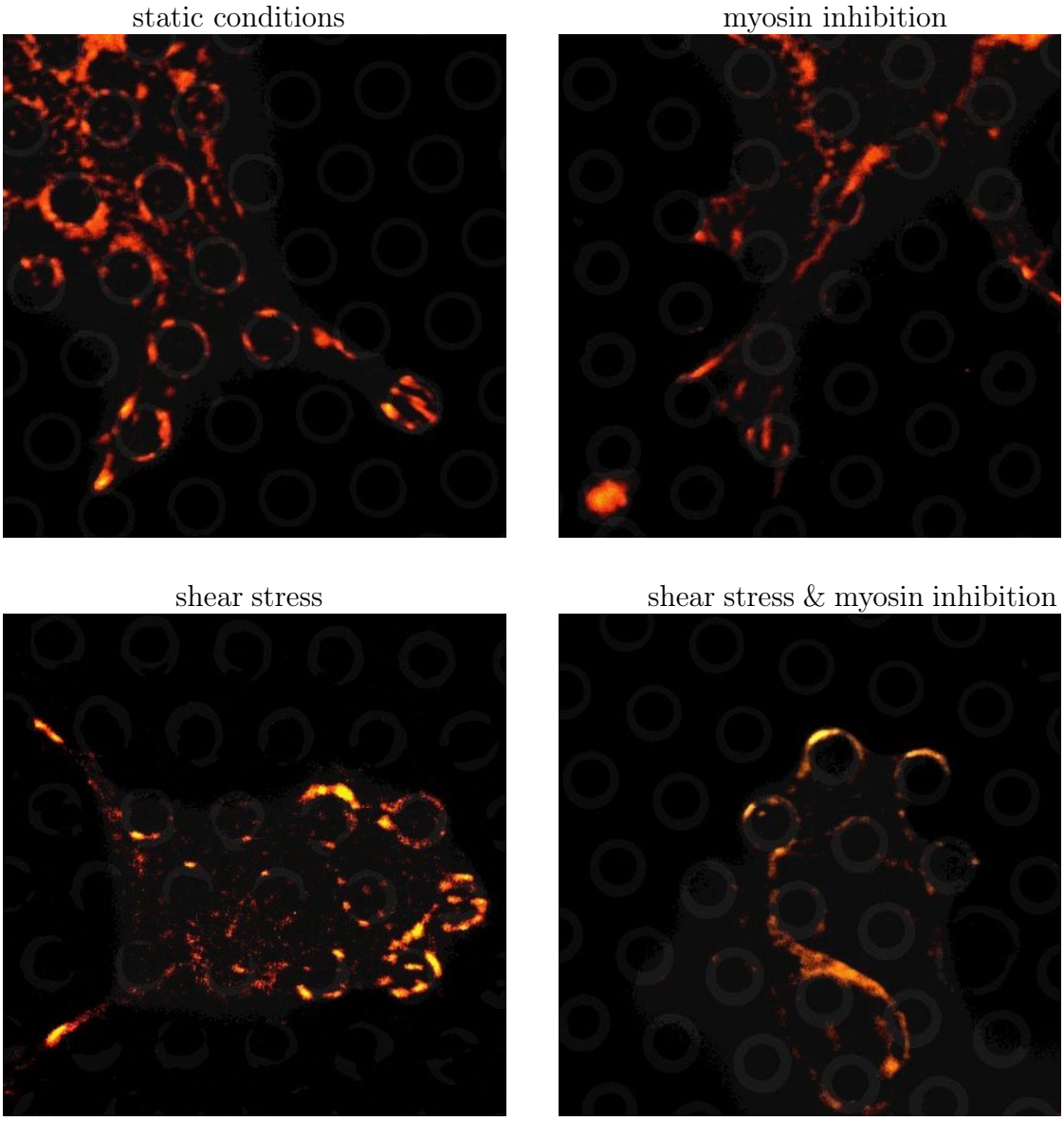


Figure 40: Paxillin staining of a5b1/avb3 cells on microposts under static untreated conditions, with myosin inhibition and under shear stress with and without myosin inhibition.

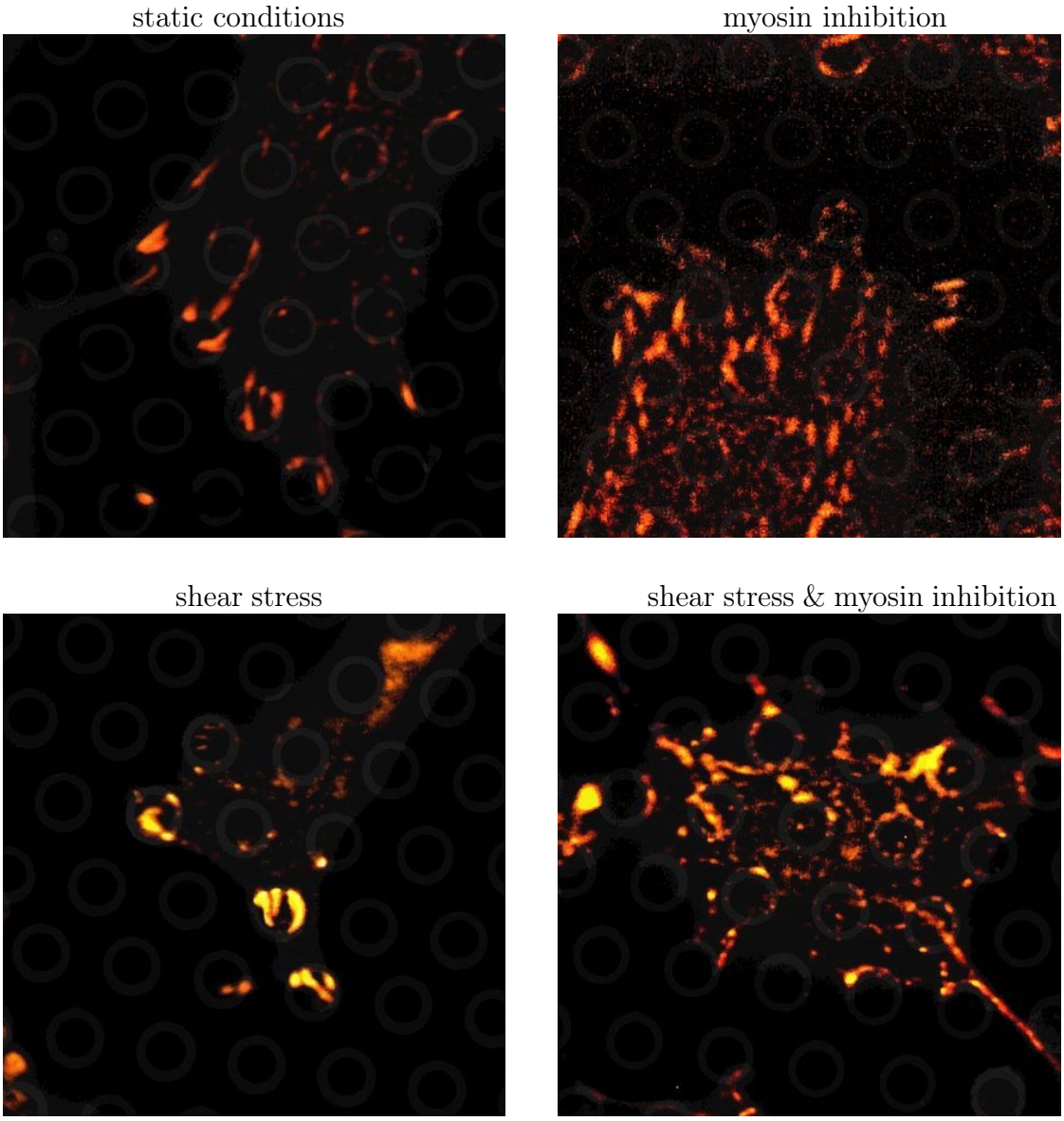


Figure 41: Paxillin staining of NIH/3T3 cells on microposts under static untreated conditions, with myosin inhibition and under shear stress with and without myosin inhibition.

Figure 42, 43 and 44 show the median values of focal adhesion area, circularity and angle for a5b1, avb3, a5b1/avb3 and NIH/3T3 cells. In addition the difference between shear stress - static condition, as well as shear stress - shear stress and myosin inhibition are shown. There is a correlation between area and circularity, smaller focal adhesions showing a more round or dot like shape. a5b1 cells show smaller and less elongated focal adhesions after myosin inhibition under static and shear stress conditions. avb3 cells show a visible difference for myosin inhibition under shear stress, where focal adhesions are much smaller an less elongated. For a5b1/avb3 cells the same effect is observed as for a5b1 cells, also for NIH/3T3 cells. avb3 cells show the largest focal adhesion area.
a5b1 cells show a difference in orientation of the focal adhesions. Under shear stress they are aligned at an approximate right angle to the flow, whereas after myosin inhibition and under both static conditions they are aligned transverse to the flow direction. For a5b1/avb3 cells the orientation is at a right angle to the flow and straight with the flow after myosin inhibition. For avb3 cells the effect is different, showing a more transverse alignment under shear stress with and without myosin inhibition. For NIH/3T3 cells the same effect is observed as for avb3 cells. Since circular focal adhesions cannot show a clear alignment, it is reasonable to discuss the results only regarding elongated focal adhesions.

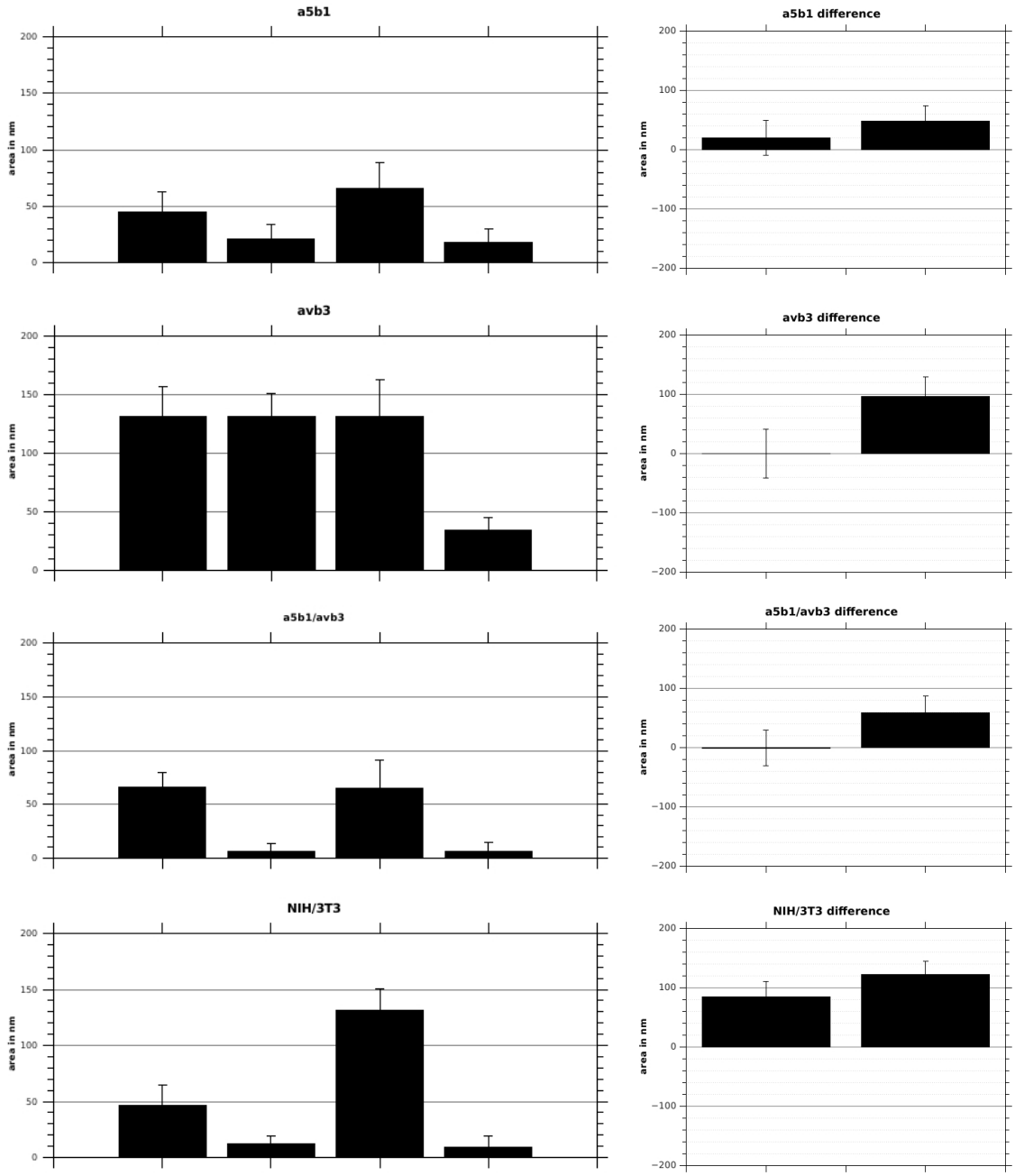


Figure 42: Focal adhesion area for a5b1, avb3, a5b1/avb3 and NIH/3T3 cells for (1) static conditions, (2) static conditions with myosin inhibition, (3) shear stress, (4) shear stress with myosin inhibition and (5) difference of shear stress - static conditions and(6) difference shear stress - shear stress and myosin inhibition. Shown are the median values with the standard error of the median.

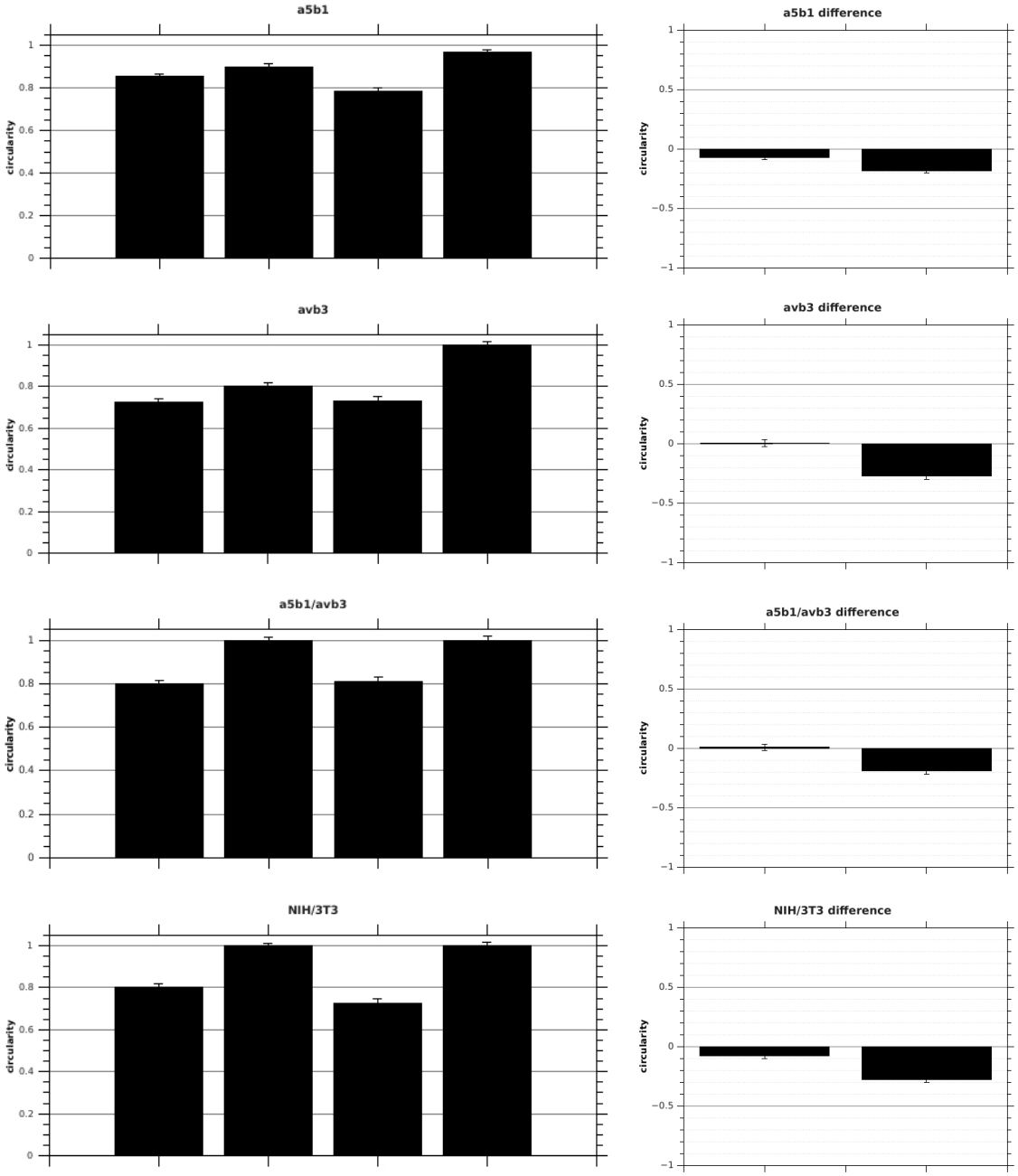


Figure 43: Focal adhesion circularity for a5b1, avb3, a5b1/avb3 and NIH/3T3 cells for (1) static conditions, (2) static conditions with myosin inhibition, (3) shear stress, (4) shear stress with myosin inhibition and (5) difference of shear stress - static conditions and (6) difference shear stress - shear stress and myosin inhibition. Shown are the median values with the standard error of the median.

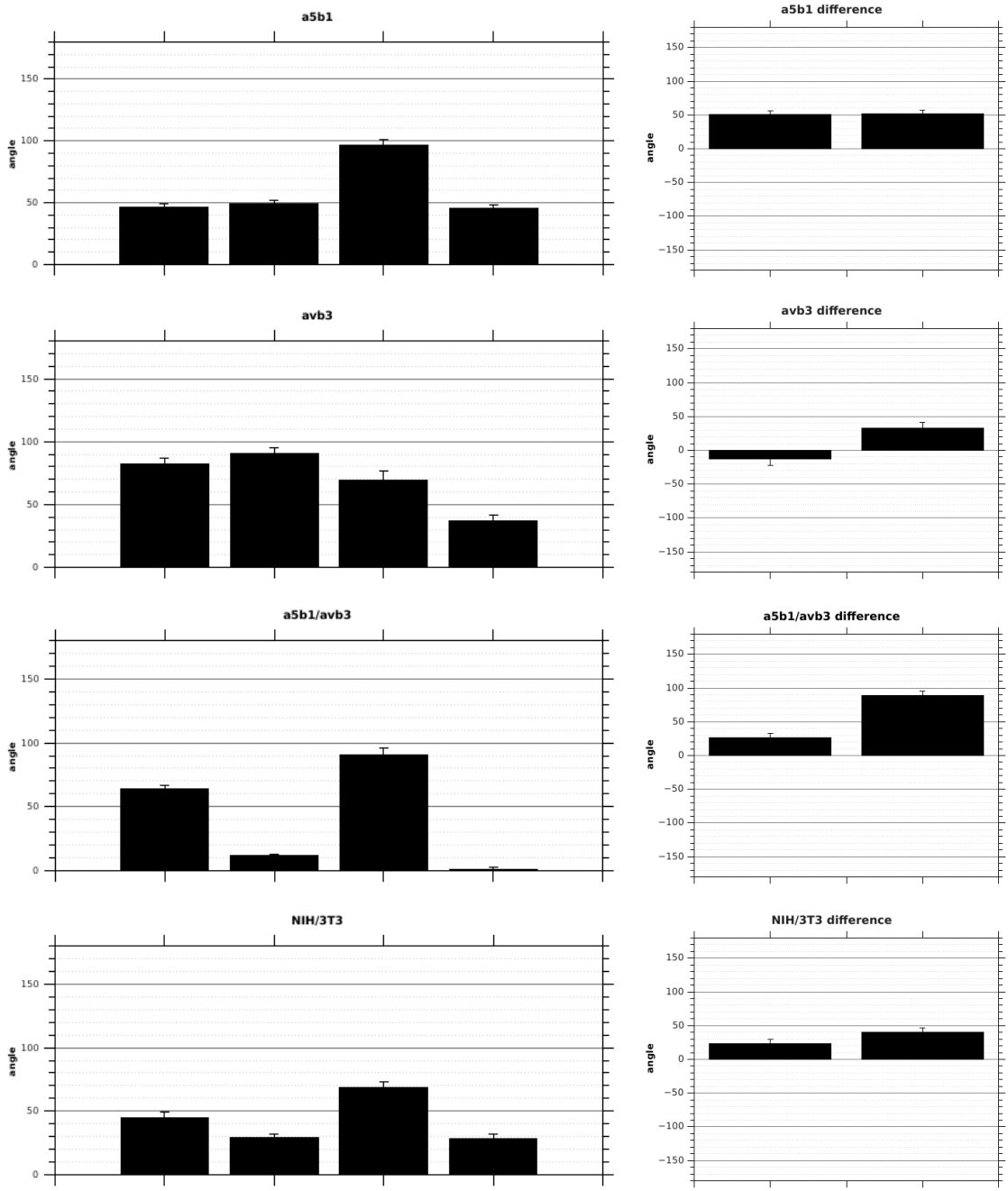


Figure 44: Focal adhesion angle for a5b1, avb3, a5b1/avb3 and NIH/3T3 cells for (1) static conditions, (2) static conditions with myosin inhibition, (3) shear stress, (4) shear stress with myosin inhibition and (5) difference of shear stress - static conditions and(6) difference shear stress - shear stress and myosin inhibition. Shown are the median values with the standard error of the median.

### 6.1.4 Vimentin disruption

Figure 45 shows traction forces for a5b1 (n=96), avb3 (n=125) and a5b1/avb3 (n=90) fibroblasts after vimentin disruption with acrylamide. Traction forces are significantly higher after vimentin disruption for avb3 cells (p=6.66e-07). There is no difference for the other two cell types.

Figure 46 shows traction forces for a5b1/avb3 and NIH/3T3 (n=55) fibroblasts after vimentin disruption with acrylamide. There is no signficant difference for the NIH/3T3 cells and between the two cell types.

Figure 47 shows the relative cell height in µm after vimentin disruption compared to static untreated conditions for a5b1, a5b1/avb3, avb3 and NIH/3T3 fibroblasts. The median value of the cell height of 20 cells for each paramater was used. The cell height is slightly increased after vimentin disruption for a5b1 cells and stronger for NIH/3T3 cells. avb3 and a5b1/avb3 cells show a small decrease in cell height.

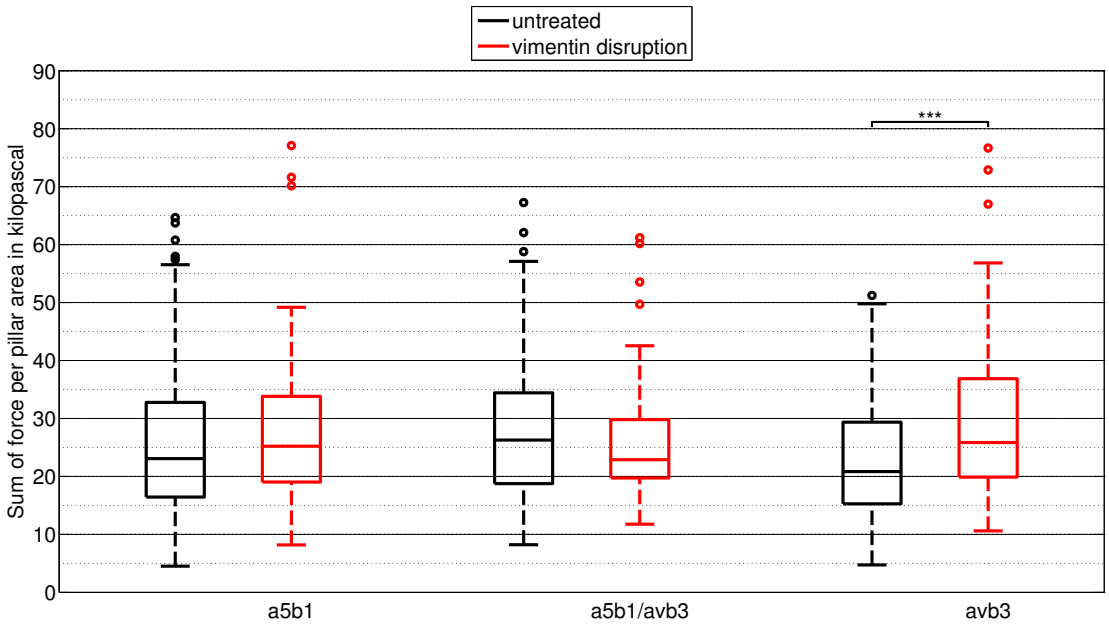


Figure 45: Boxplots of the cell traction forces for a5b1, a5b1/avb3 and avb3 fibroblasts with and without vimentin disruption.

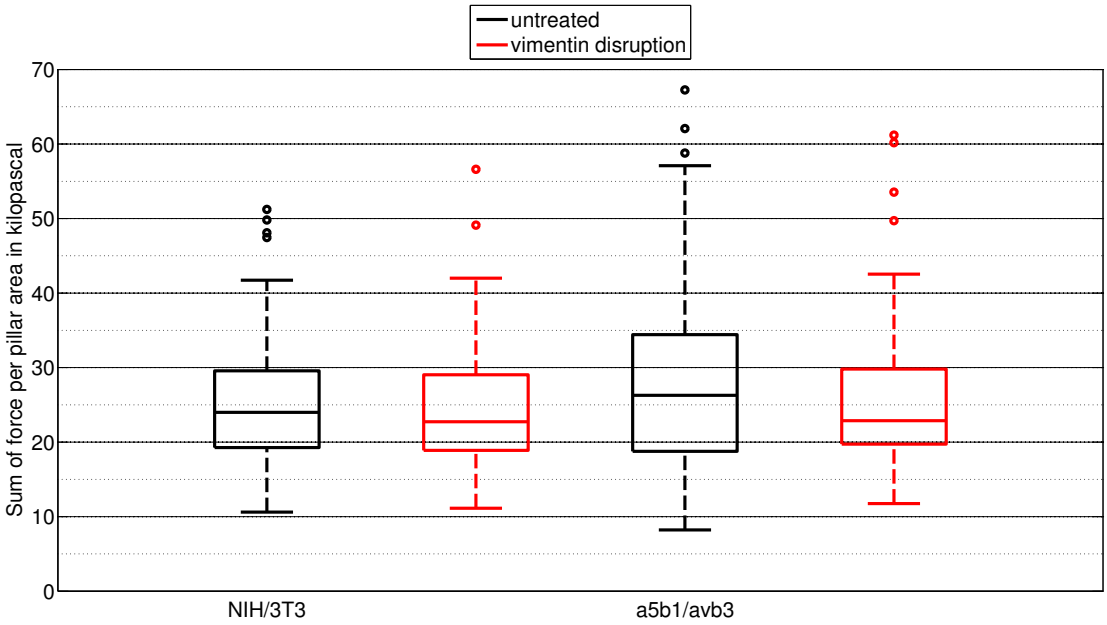


Figure 46: Boxplots of the cell traction forces for a5b1/avb3 and NIH/3T3 fibroblasts with and without vimentin disruption.

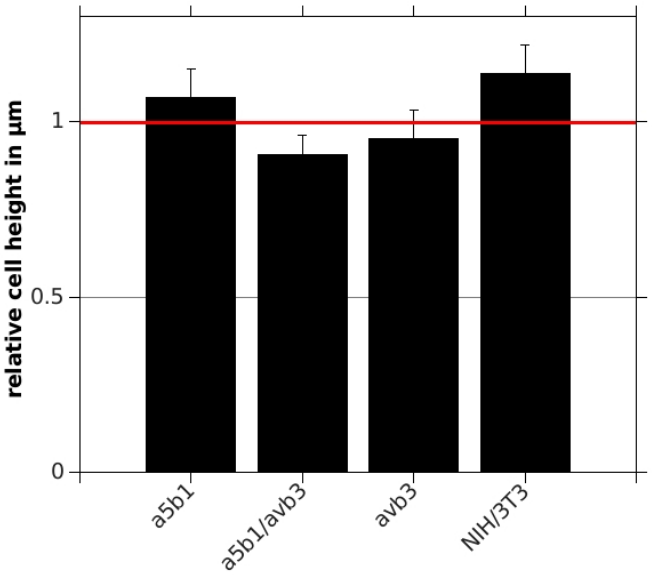


Figure 47: Relative cell height calculated from the median value of 20 measured cell heights. The relative difference in µm compared to static untreated conditions is shown after vimentin disruption. Error bars represent the standard error of the median.

Figure 48 shows traction forces for a5b1 (n=53), a5b1/avb3 (n=60) and avb3 (n=58) fibroblasts after concurrent myosin inhibition and vimentin disruption. Traction forces are significantly higher for avb3 after concurrent myosin inhibition and vimentin disruption compared to the untreated state (p=0.003) and only myosin inhibition (p=0.001). There is no difference to only vimentin disruption. Traction forces are the same after concurrent myosin inhibition and vimentin disruption for a5b1 cells, but significantly higher compared with only myosin inhibition (p=0.001) and lower compared to only vimentin disruption (p=0.003). a5b1/avb3 cells only show a difference in traction forces between concurrent myosin inhibition and vimentin disruption and only myosin inhibition (p=8.58e-06).

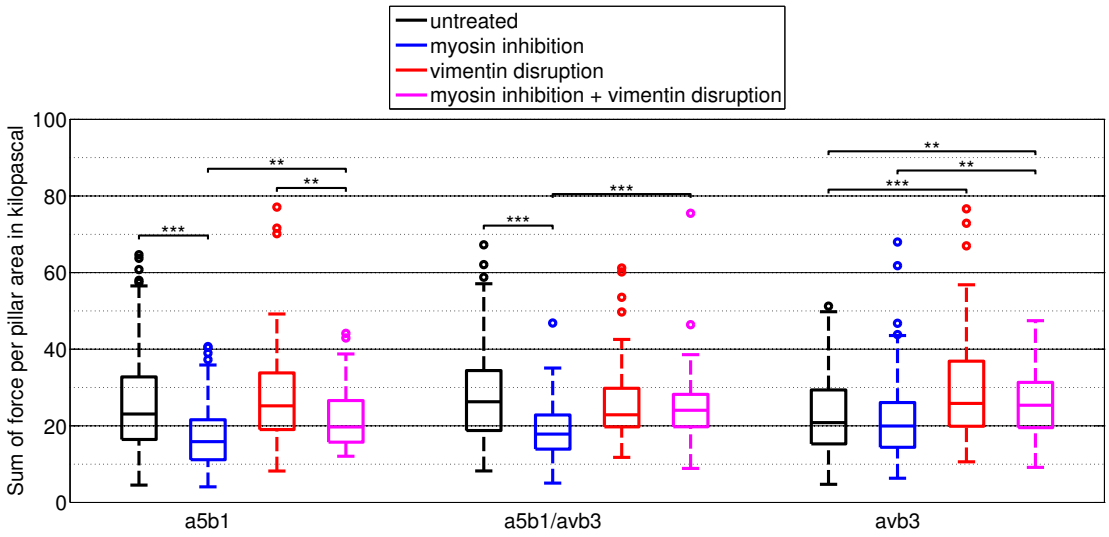


Figure 48: Boxplots of the cell traction forces for avb3, a5b1 and a5b1/avb3 fibroblasts with concurrent myosin inhibition and vimentin disruption.

Figure 49 - 52 show fluorescence images of paxillin stained cells for a5b1, avb3, a5b1/avb3 and NIH/3T3 cells under static conditions with and without vimentin disruption.
Compared to the untreated state there is no observable difference for the focal adhesions for all cell types.

static conditions vimentin disruption

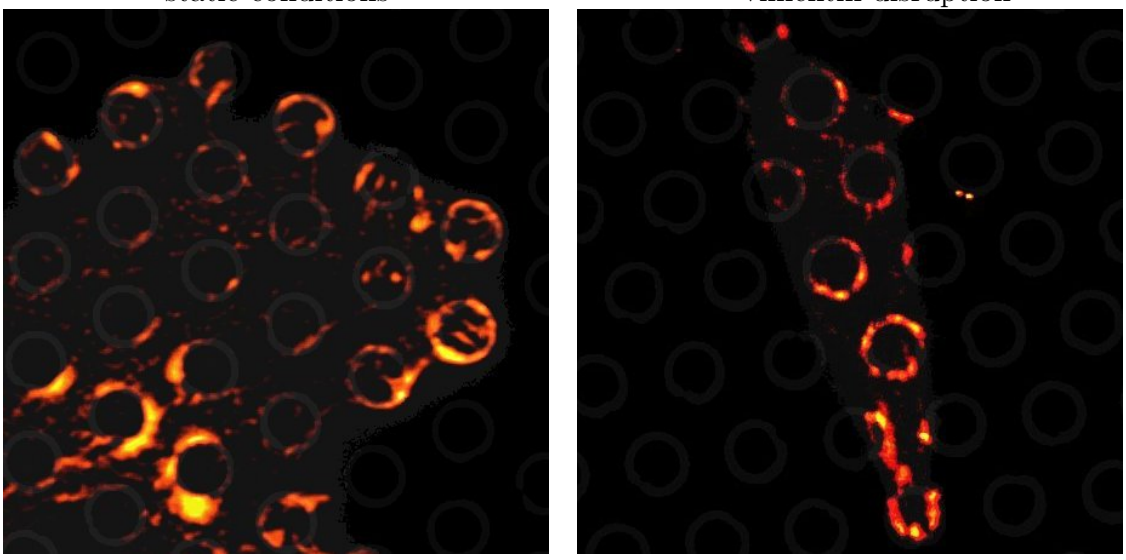

Figure 49: Paxillin staining of a5b1 cells on microposts under static untreated conditions and with vimentin disruption.

static conditions vimentin disruption

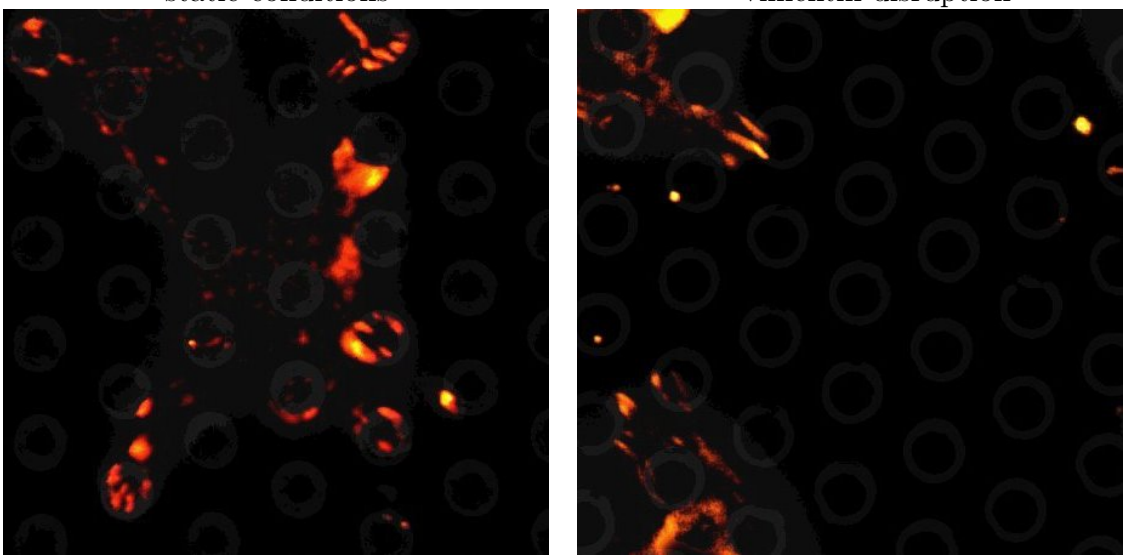

Figure 50: Paxillin staining of avb3 cells on microposts under static untreated conditions and with vimentin disruption.

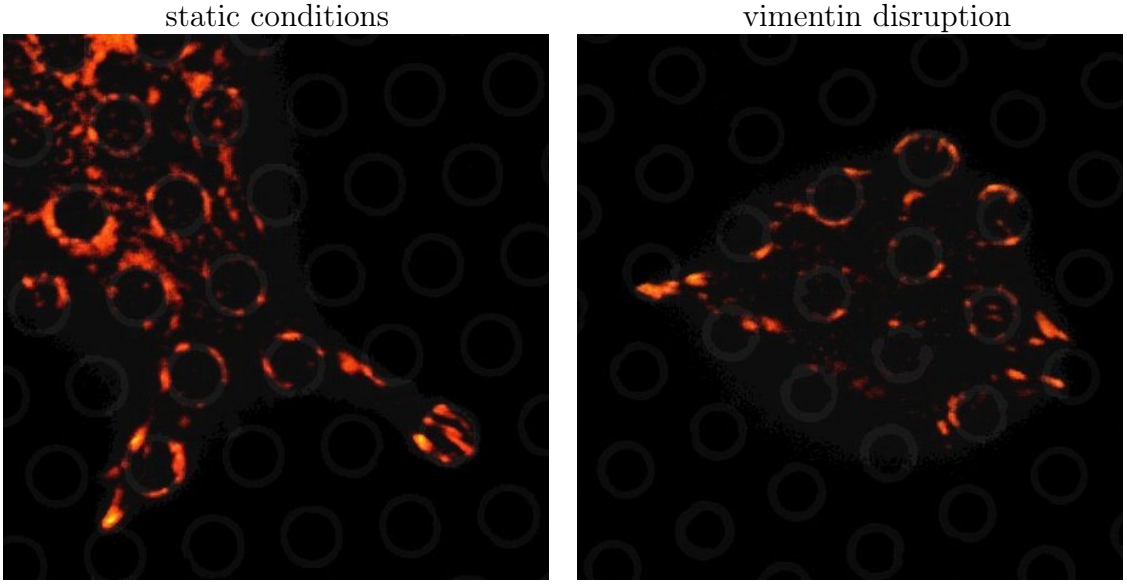


Figure 51: Paxillin staining of a5b1/avb3 cells on microposts under static untreated conditions and with vimentin disruption.

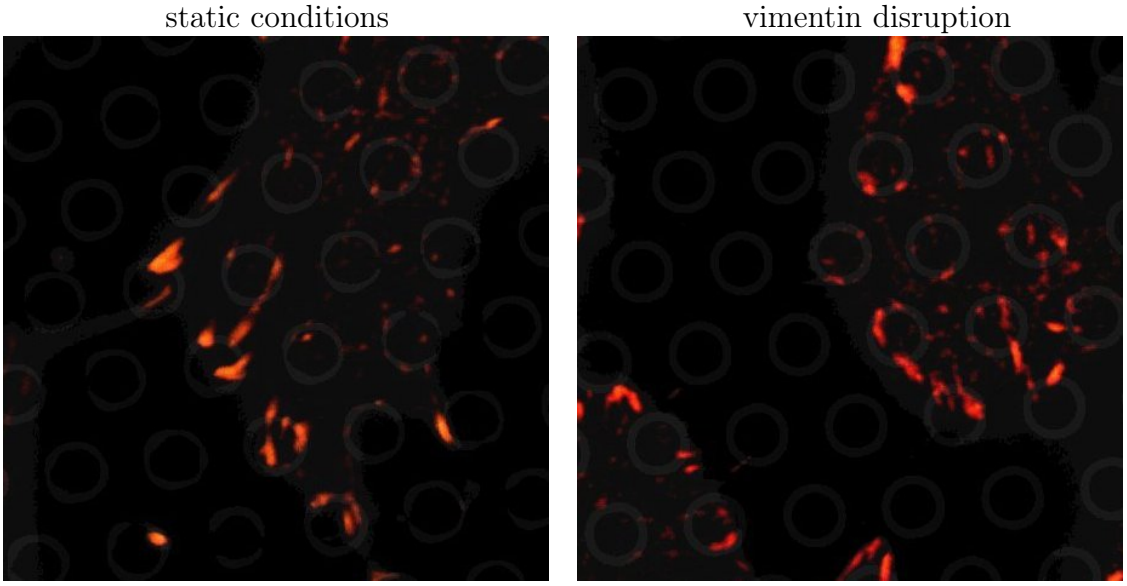


Figure 52: Paxillin staining of NIH/3T3 cells on microposts under static untreated conditions and with vimentin disruption.

Figure 53 shows the median values of focal adhesion area and circularity for a5b1 cells static (1) and with vimentin disruption (2), avb3 static (3) and with vimentin disruption (4), a5b1/avb3 static (5) and with vimentin disruption (6) and NIH/3T3 cells static (7) and with vimentin disruption (8). Figure 54 shows the difference static - vimentin disrutpion in area and circularity for a5b1, avb3, a5b1/avb3 and NIH/3T3 cells

There is no change in focal adhesion area for a5b1 and avb3 cells. For a5b1/avb3 cells focal adhesions become smaller and less elongated after vimentin disruption, whereas for NIH/3T3 cells the area increases and the shape is more elongated.

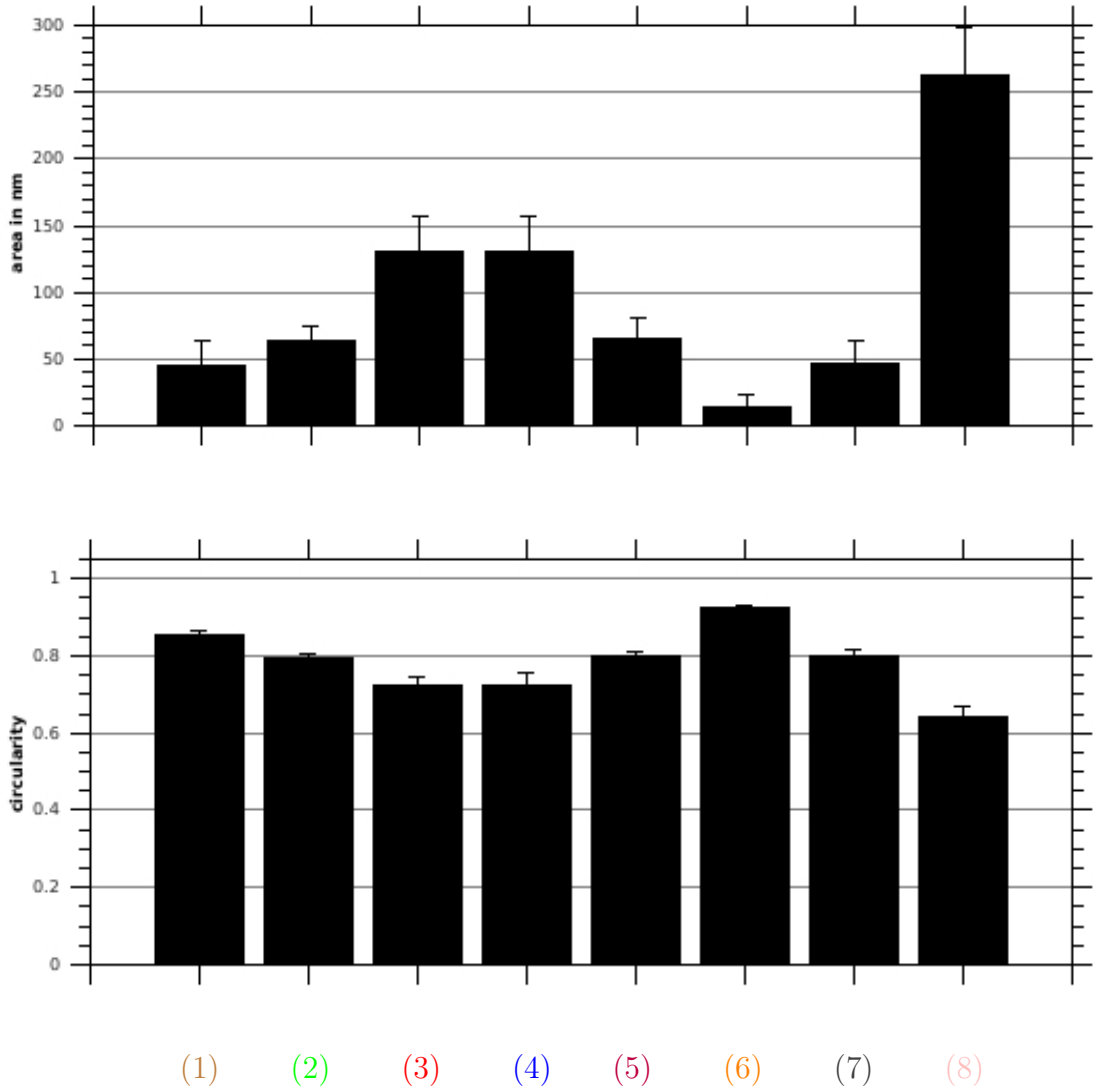


Figure 53: Focal adhesion area (top) and circularity (bottom) for a5b1 cells static (1) and with vimentin disruption (2), avb3 static (3) and with vimentin disruption (4), a5b1/avb3 static (5) and with vimentin disruption (6) and NIH/3T3 cells static (7) and with vimentin disruption (8). Shown are the median values with the standard error of the median.

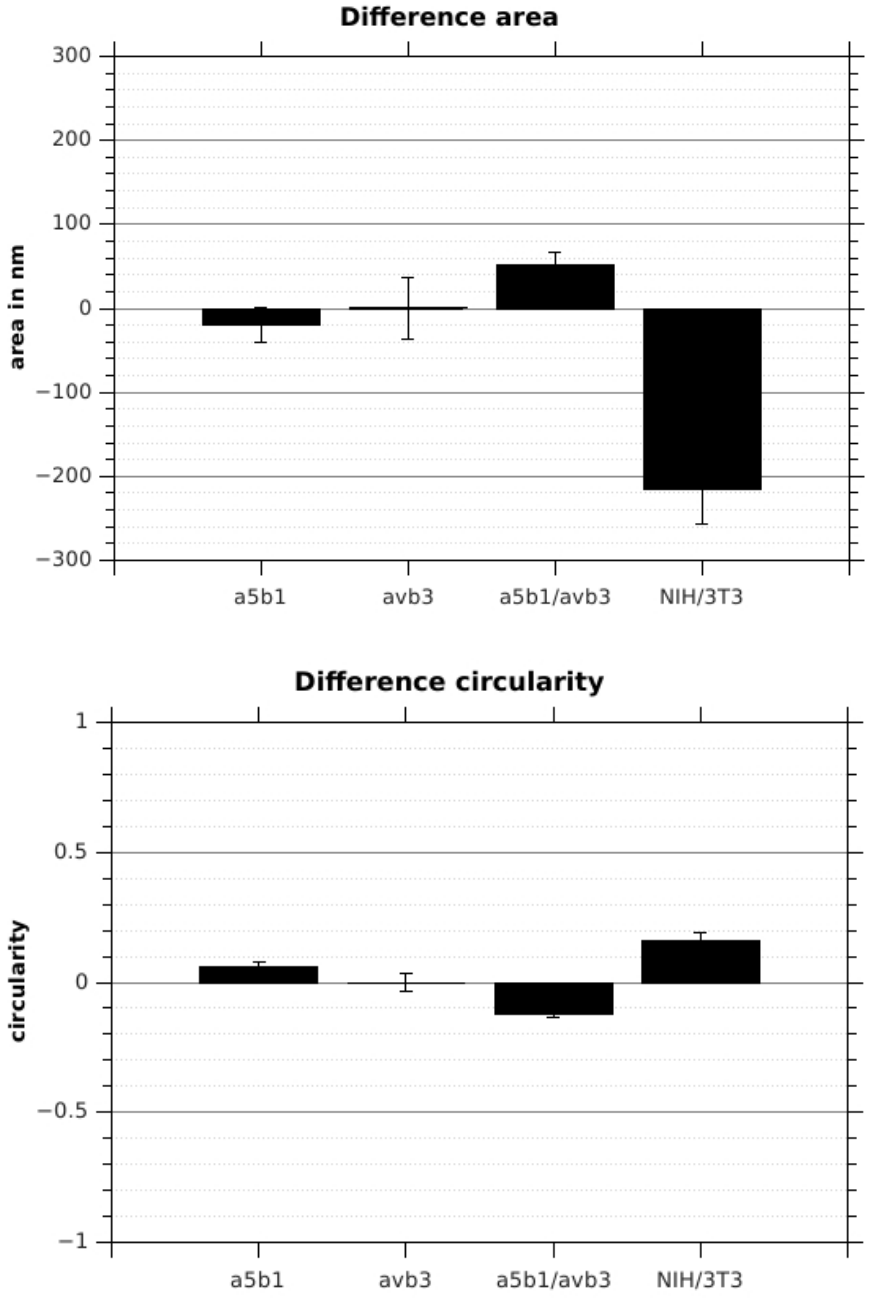


Figure 54: Difference of median values for focal adhesion area (top) and circularity (bottom) for a5b1 cells, avb3 cells, a5b1/avb3 cells and NIH/3T3 cells, static - vimentin disruption.

### 6.1.5 Integrin blocking

We tested the traction force generation of a5b1/avb3 fibroblasts after blocking one of the integrins, but leaving the other one functional.
Figure 55 shows traction forces for a5b1/avb3 fibroblasts after seperate blocking of a5b1 (n=100) or avb3 (n=106) integrins. Traction forces of avb3 and a5b1 cells are shown as comparison. After blocking of avb3 integrins and a5b1 integrins the a5b1/avb3 cells show no difference to the untreated state or between the two blocked states. There is a significant difference between a5b1/avb3 cells with blocked avb3 integrins and a5b1 cells (p=3.19e-04) and a5b1/avb3 cells with blocked a5b1 integrins and avb3 cells (p=2.43e-05).

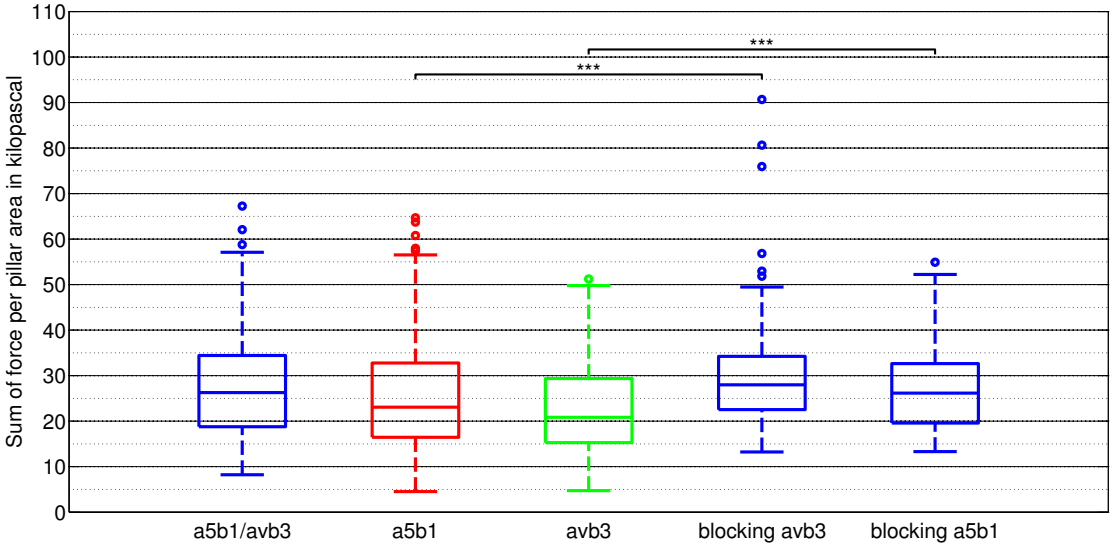


Figure 55: Boxplots of the cell traction forces for avb3, a5b1 and a5b1/avb3 fibroblasts and a5b1/avb3 fibroblasts after blocking of integrin a5b1 and avb3.

## 6.2 Discussion

For the specific analysis of the integrin types a5b1 and avb3, we used cells in which $\beta_1$ and/or $\alpha_v$ class integrins were reconstituted into pan-integrin-deficient fibroblasts[148]. This enabled us to manipulate either environmental cues or cell internal parameters and link the observed effects to the specific integrin type. As main analysis tool traction force microscopy was used. Three cell types were analysed with either $\beta_1$ or $\alpha_v$ class integrins or a combination of both. Schiller et al found that a5b1 integrins were expressed in pKO-$\beta_1$ cells, avb3 and avb5 in pKO-$\alpha_v$ cells, and a5b1, avb3 and avb5 integrins in pKO-$\alpha_v/\beta_1$ cells, whereas FACS analysis revealed an approximate amount of 170 000 a5b1 and 300 000 $\alpha_v$-class integrins on the surface of each cell. Therefore the surface levels for $\beta_1$, $\beta_3$ and $\beta_5$ integrins is equimolar[148]. As control we used unaltered NIH/3T3 mouse embryonic fibroblasts, that express all integrin types.

Our results for traction force microscopy revealed that avb3 cells have the lowest traction forces, whereas a5b1 and a5b1/avb3 cells show no significant difference. a5b1/avb3 cells had the same total traction force as NIH/3T3 cells, therefore we suggest that the interaction of $\beta_1$ and $\alpha_v$ class integrins might be the main contributor for maximum traction force magnitude in fibroblasts.
The median sum of traction stress for the four cell types lies between 20.8-26.3 kPa. Previous studies measured average traction forces around 1-3kPa for migrating NIH/3T3 cells on substrates with Young's moduli between 6.2kPa and 30kPa[32][101][113]. One has to consider, that cell traction forces are depending on the substrate stiffness[34][101][148][195]. Balaban et al. measured constant stress at focal adhesions of 5.5±2kPa on substrates with 10-20kPa Young's modulus[9]. Previous studies found that the forces exerted at single focal adhesions in fibroblasts are around 10nN, with a peak value at 30nN[9][50]. If one focal adhesion would attach to one micropost, this would account to a traction stress of 0.46-1.38kPa in our case. Since there are more then one focal adhesion built out at the top of a micropost, higher traction forces are measured per micropost. Therefore our results are in agreement with reported values.
Schiller et al. measured traction forces for the reconstituted fibroblasts on fibronectin coated crossbow patterns with the same spreading area and shape for all cell types. Experiments on crossbow patterns polarise cells into a low contractile front and a highly contractile rear[170]. They show in agreement with our results, that avb3 cells have the lowest traction forces at the rear and the front. Interestingly, they observed large focal adhesions (6-12$\mu$m$^2$) for avb3 cells[148]. In agreement we see in our measurement on microposts that the focal

adhesion area was larger for avb3 cells than for the other cell types. However, it has to be considered that a positive correlation between focal adhesion size and tension was observed in stationary cells, whereas the opposite was seen using migrating cells[9] [156].

In contrast to our results Schiller et al. found, that the forces for a5b1 cells were intermediate and highest in a5b1/avb3 cells[148]. They show that the difference between the latter ones is high on stiffer substrates (35kPa) but that they were similar on soft substrates (1.4kPa)[148], concluding that adjustment of cell contractility to substrate stiffness is mediated through avb3-fibronectin bonds that are stabilised through actomyosin-mediated tension[148]. Therefore tension-dependent stabilisation of avb3 integrins is necessary for sensing of substrate stiffness. Since the micropost substrate used in our experiments is much stiffer (1200kPa for the PDMS substrate and a spring constant per micropost of 294nN/$\mu$m), we would expect a rather large difference in traction forces between a5b1 and a5b1/avb3 cells. However, the experiments differ in several aspects allowing for various explanations why the cells behave differently. Micropost arrays do not build flat continuous surfaces, they rather have round, flat islands where cells can adhere to and in between the cell sags and has no possibility to build out focal adhesions, and therefore has no direct contact to the substrate. The stiffness can be adjusted like for flat substrates by either varying the elasticity of the PDMS or the micropost dimensions. One has to distinguish here that changing the micropost stiffness has a global influence, whereas changing the PDMS elasticity is working on local scales[79]. What plays an important role is the size of the micropost tops and therefore the adhesion area and the density of the posts.

**The influence of substrate stiffness and geometry on cell traction forces**

We showed that traction forces are higher for all three cell types on stiffer substrates (294nN/$\mu$m) compared to softer substrates (202nN/$\mu$m) with the same geometry. This is in agreement with several previous studies that showed the same effect for different cell types[34] [101] [148] [195].

Cells were observed to spread to a greater extent on stiff substrates[40] [59] and that the spread area has an influence on traction force generation[23] [135] [138] [139] [161] [167]. Correlations between traction forces and changes in cell area and shape, focal adhesions and stress fiber assembly have been observed in previous studies[9] [47] [135]. Oakes et al. found that substrate stiffness, focal adhesion number and cell geometry did not influence the strain energy of the cell and therefore the mechanical work done by the whole cell on the substrate, but cell area alone[121]. Although

stiffer substrates lead to an increase in traction stress magnitude, the strain is decreased and therefore the mechanical output stays constant [121]. For fibroblasts on PAA gels it was shown that on soft gels (Young's modulus <20kPa) the strain is kept constant whereas on stiffer substrates the stress is kept constant [196]. However, Han at al. used micropost arrays to demonstrate that total traction forces increase with increasing substrate stiffness, but that the effect of substrate stiffness on traction forces is independent of cell spreading. They also showed that micropost density rather than cell spreading influences total force generation and that cells on substrates with a higher micropost density produced larger total forces, but lower average forces [67]. We see the same effect, that with softer substrates (155nN/$\mu$m), having a higher micropost density but a smaller micropost radius and therefore the same area as the stiff substrates, the traction forces were higher, concluding that micropost density rather than stiffness and spread area has an influence on traction forces. The different observations seem to depend on the different ways the experiments are conducted and one has to be careful comparing them. We suppose that several factors, like local and global stiffness, micropost density or growth area, have an influence on cell traction forces, but that depending on the conditions one effect might superimpose other effects.

The traction forces for a5b1 cells were significantly lower than for the a5b1/avb3 cells on both softer substrates and the avb3 cells were intermediate, but with no significant difference to both cell types. Somehow the stiffer substrate seems to trigger a stronger traction force generation for a5b1 cells, that can be explained by it's function as 'catch-bond', meaning that the bond strengthens with applied force [142] [119] [154].

**The influence of actomyosin on traction force generation**

To analyse the influence of actin and non-muscle myosin II on traction forces for the two integrin types separately and in cooperation, we disrupted actin with latrunculin A and inhibited non-muscle myosin II with blebbistatin. As a result traction forces were reduced in both cases for a5b1 cells and a5b1/avb3 cells, as well es for NIH/3T3 cells, although a higher blebbistatin concentration over longer incubation time (20$\mu$M, 3h) was necessary to see an effect for the latter one. Traction forces for avb3 cells did not change under both conditions. Also a higher blebbistatin concentration over longer incubation time (20$\mu$M, 3h) had no effect. Focal adhesion area and circularity are unchanged for the avb3 cells in contrast to the other cell types, where the area is decreased and the circularity increased, representing a more dot like shape.

The results for the avb3 cells are in contrast to the findings of Schiller et al.

where they concluded that stabilisation of the avb3-fibronectin bond through actomyosin mediated tension is necessary for the adjustment of cell contractility to a defined substrate stiffness[148]. They also showed that blebbistatin treatment reduced protein recruitment to focal adhesions in avb3 cells and that myosin II and/or stress fibers are required[148]. In areas with high traction forces at the cell rear on crossbow shapes avb3 accumulates and gets lost after myosin inhibition with blebbistatin, whereas a5b1 containing focal adhesions were still forming[148]. On the other hand avb3 cells show large stress fibers together with low pMLC levels, low contractility but high active RhoA. RhoA is not activating Rho kinase and myosin II, but instead it activates DIAP1 (Drosophila melanogaster inhibitor of apoptosis 1) which enables stress fiber formation[148]. Myosin II is known to interact with actin upon myosin light chain phosphorylation. This maybe a hint that another mechanism is generating traction forces in this case than actomyosin. So how can our results be explained in terms of force generation coupled to avb3 integrins alone after non-muscle myosin II inhibition and actin disruption?
a5b1 integrins are coupled to ROCK and myosin II activation and induce Mek1/Erk2 and RhoA/Rock/pMLC pathways[148]. avb3 activates mDia and therefore actin polymerisation, but high RhoA activity in avb3 cells is not coupled to Rock/pMLC[148]. Both integrins are required to activate myosin II, but only a5b1 induces signals to mediate RhoA driven myosin II activity[148]. Focal adhesion growth rate is correlated to retrograde flow rate (rearward movement of actin), but not force, since the rate of lamellar retrograde flow, radial stress fiber assembly and adhesion growth are unaffected by myosin II and therefore intracellular tension inhibition[122]. Several findings led to the idea that stress fibers are driving focal adhesion growth. For example, in the absence of myosin II activity, actin crosslinking was found to be sufficient for adhesion stabilisation[122]. Other groups supposed that actin polymerisation alone and filament bundling at focal complexes might generate contractile forces[52][158]. A previous study showed that myosin inhibition had little effect on dorsal stress fibers and the small nascent focal adhesions that attach them[74]. In contrast to transverse arcs and ventral stress fibers, dorsal stress fibers do not contain myosin II[82]. Beningo et al. demonstrated that myosin independent nascent focal adhesions located at the front of migrating fibroblasts are able to generate strong propulsive forces[10][13]. Tan et al. measured traction forces on flexible microneedles and found small adhesions $<1\ \mu m^2$ with high traction forces, that are equivalent to these nascent adhesions. In general, force transmitted via stress fibers is proportional to the active myosin level within these stress fibers, however regarding dorsal stress fibers the contraction and rearward movement of transverse arcs coupled to the dorsal stress fibers generates contractile forces and adds to the force generation

of the small nascent adhesions at the cell front[13][156][161]. The assembly of dorsal stress fibers is done by formin (mDia1/DRF1)-driven actin polymerisation at focal adhesions. As mentioned above the RhoA effector mDia1 correlates with avb3 integrins[148].
Shutova et al. treated their cells with latrunculin A in the same way we did (0.5$\mu$M for 30min) and observed a disappearance of lamellipodia and most focal complexes, but remaining of mature focal adhesions and large actin bundles. Previous studies showed similar observations for low latrunculin A concentrations with no effect on stress fibers[149]. We did not observe clear focal adhesions after actin disruption, maybe the cytosolic paxillin interfered with the paxillin of the focal adhesion due to the shrunken phenotype of the cells, therefore focal adhesions wrapped around the microposts might be hidden by the background.
Taken together this might explain why we do not see a change in traction forces for the avb3 cells after myosin inhibition and after actin disruption. Forces can still be generated by dorsal stress fibers, that remain intact in both cases. For a5b1 containing cells, however, traction force generation and focal complex forming seem to be dependent on actomyosin since this integrin type is coupled to ROCK and myosin II activation.
However, it also has to be considered that other myosins then non-muscle myosin II may participate in force generation. Blebbistatin is an effective inhibitor of several striated muscle myosins as well as non-muscle myosin IIA and IIB, but not smooth muscle myosin or myosin superfamily members from classes I, V, and X[97]. Some of these molecules were found to be localised at protruding edges of cells[21][180].
Furthermore traction forces are not only depending on living contracting cells but can also be generated by liposomes[116]. Membrane tension during adhesion built up through internal, hydrostatic pressures is balanced by traction stress on the substrate. The measured mean stress is around 70Pa[116].

**The influence of externally applied shear stress and actomyosin on cell traction forces**

Cells are able to sense and also respond to changes in mechanical forces and convert them inside the cell to a biochemical response via tension generation and molecular pathways[111]. We applied fluid shear stress to simulate the influence on cells in physiological terms. Several studies use shear flows in the range of >1Pa, like it occurs for example in arterial flow. We used much weaker pressure like it might occur during venous and interstitial flow[159][189], or during atherosclerosis[106]. Endothelial cells were shown to demonstrate several differences in morphology or orientation for low vs high shear stress[106][128].

After application of external shear stress traction forces are increased for all cell types with the strongest effect on avb3 and a5b1/avb3 cells. Previous studies showed, that shear stress is able to induce integrin activation[78] [172]. The integrin avb3 is known as mechanosensor from previous studies and reinforces under high tension[148]. This was shown for substrate stiffness but can be applied to external generated tension too, e.g. via shear stress. Tzima et al. showed that avb3 is activated by shear stress and that shear stress regulates Rho activity[172]. a5b1 cells have lower traction forces under shear stress than a5b1/avb3 and avb3 cells. Focal adhesion area and circularity is unchanged after shear stress application compared to static conditions for all cells but the NIH/3T3 cells, where a strong increase in focal adhesion area is observed. For a5b1 and a5b1/avb3 cells the focal adhesions seem to be aligned in an approximate right angle to the flow, whereas for avb3 and NIH/3T3 cells they are more transverse aligned to the flow. The results indicate that shear stress triggers an activation of traction force generation for the avb3 cells.

To look at the orientation of the cells we analysed the position of the Golgi complex relative to the nucleus. Typically the Golgi complex localises in front of the nucleus towards the leading edge of a cell[118]. All cells in our experiments show a shift of cell orientation against the flow. A study by Li et al. showed that shear stress induces polarised FAK recruitment and p-FAK(Y397) phosphorylation at focal adhesions in the leading edge[96]. Recent studies demonstrated that FAK is required for mechanosensing and persistent migration of fibroblasts[181]. Polacheck et al. showed that for three dimensional migration of cancer cells a CCR7-dependent pathway, triggering downstream migration and an CCR7-independent, but FAK dependent pathway are involved, the latter one stimulating cells to migrate against the flow. They show that shear stress induces phosphorylation of focal adhesion kinase at Tyr-397 and hypothesise that the upstream migration stimulus is provided by flow-induced tension in integrins[132]. The affinity of avb3 integrins was shown to be increased under shear stress as well as activation of FAK[78] [172]. Previous work already observed a colocalisation of FAK and activated integrins and that FAK activates Src kinase, which is responsible for modulation of traction forces important for cancer cell migration[42] [165]. Lo et al. showed that NIH/3T3 cells migrate towards increased strain, resulting from the tension on integrins[101].

Microposts are displaced more against the flow direction for avb3 cells. A tendency for the same behaviour is observed for a5b1 cells. a5b1/avb3 cells show a slight shift with the flow and NIH/3T3 cells show an almost equal distribution of micropost displacement direction. The direction of micropost displacement is influenced both by actively, e.g. by actomyosin forces or passively, by the shear

stress. Hydrodynamic shear stress generates pushing forces and simultaneous rolling resulting in a torque of the cell. Gallant et al. simulated the cell as spherical object that is under influence of a torque under hydrodynamic shear force. To get a mechanical equilibrium these forces are balanced by a horizontal force, vertical tensile bond forces and compressive forces[48]. Truskey and Proulx approximated the cell shape as a hemispherical cap[169]. The torque dominates when the spread area is smaller then the radius, meaning an increase in cell height. For more spread out cells the pushing component dominates[84]. Hence, the effect of micropost bending against the flow might result from a rotational movement of the cell body due to the shear stress and therefore a shift of micropost bending towards the flow. To distinguish between active forces generated by the cell itself and passive forces acting on the cell due to shear stress, we inhibited myosin or disrupted actin.

Actin disruption and myosin inhibition lower traction forces for all cell types under shear stress, also for the avb3 cells. Focal adhesion area is reduced after myosin inhibition under shear stress for all cell types, the circularity is increased and the angle to the flow is changed. This suggests, that avb3 cells show actomyosin activation during shear stress application compared to static conditions and that traction forces in this case are actively generated by actomyosin.

a5b1 and avb3 cells show an even stronger shift of cell orientation towards the flow direction after myosin inhibition. The difference of oriented cells under shear stress and under shear stress with myosin inhibition supposes an active myosin participation in cell orientation with the flow. We suggest that with active myosin there is more resistance of the nucleus displacement to the flow, therefore the nucleus is not pushed with the flow direction and the cells show an orientation with the flow. a5b1/avb3 and NIH/3T3 cells show nearly random cell orientation after myosin inhibition. Therefore, we suggest in this case an active myosin influence on the orientation against the flow, because of active migration against the flow and not just shear stress resistance, as explained for the a5b1 or avb3 cells.

Actomyosin was shown to be necessary for the relocation of the nucleus during polarisation[43][62][66] and the Microtubule Organisation Center (MTOC)[41][112][173]. Tkachenko et al. found that for endothelial cells the nucleus is pushed downstream by hydrodynamic drag of the blood flow, and therefore serves as sensor for the direction and magnitude of the blood flow[166]. By resistance of the actomyosin cytoskeleton, the sensitivity of polarisation response of endothelial cells to shear flow is controlled[166]. Shear stress and therefore hydrodynamic drag pushing the nucleus downstream is acting on the cells in all cases for our measurements. A dense actin cytoskeleton is able to block polarisation against the flow, as

it was shown in previous studies for non-confluent endothelial cells[166]. Also vimentin contributes to cell stiffening under large strains[109]. Linkage between intermediate filaments and focal adhesions is able to sense differences in force load[63], e.g. in endothelial cells under fluid shear stress vimentin associates with avb3 rich focal contacts[171]. Under flow they grow thick vimentin bundles and large focal contacts, suggesting that vimentin might regulate focal contact size in this case[171]. For 3T3 fibroblasts it was demonstrated that under shear stress, they show a 25-fold increase in cytoplasmic viscosity (meaning a higher resistance to being deformed by shear stress) and a 4-fold increase in elasticity (meaning a decrease in deformability under shear stress)[91]. This shear induced cell stiffening is gone after inhibition of actomyosin interaction or ROCK inhibition[91].
The two isoforms of non-muscle myosin II, A (NMIIA) and B (NMIIB), have distinct functions. NMIIB is involved in directed cell movement, front-back polarity and Golgi and nuclear orientation. Inhibition of NMIIB in fibroblasts lead to more random movement[100]. NMIIA is responsible for retraction and adhesion disassemble at the cell rear[177]. However, Shutova et al. showed that even with inhibited non-muscle myosin II, fibroblasts had directed movement, and long non-contractile cytoplasmic tails, together with microtubule bundling[149]. Regarding traction force generation, central stress fibers are regulated by ROCK and NMIIA, whereas mechanics of peripheral stress fibers are regulated by MLCK and NMIIB. Central stress fiber retraction is controled by the motor and crosslinking functions of NMIIA[24].
Figure 56 shows a draft to better understand the myosin influence on cell behaviour in response to shear stress, as explained in the following. For a5b1 cells, myosin and actin have no effect on the micropost displacement direction, therefore we suggest that bending of the microposts against the flow must be of passive nature, due to rolling of the cell body and therefore bending the microposts against the flow. For avb3 cells myosin and actin have an active effect, triggering micropost bending against the flow. With functional actomyosin the cell is able to withstand the shear forces actively, by a more dense and stiff network. However this might have the indirect effect that cell rolling is enhanced, because of the higher resistance to the shear stress. Therefore myosin and actin would participate in the effect of pillar bending against the flow, which is diminished after myosin inhibition or actin disruption. An explanation why this effect is observed for avb3 but not a5b1 cells might be the stronger effect of actomyosin activation for the avb3 cells after shear stress application compared to the a5b1 cells. The shift of micropost bending with the flow after actin disruption for avb3 cells might be explained by a dominating pushing force over the torque. For a5b1/avb3 cells myosin and actin drive pillar bending with the flow, actin only with a small effect.

This effect could be explained by the active migration that produces pulling forces with the flow, triggered by the cooperation of a5b1 and avb3 integrins. For NIH/3T3 cells myosin and actin trigger even distribution of micropost displacement. After myosin inhibition and actin disruption perpendicular traction forces are enhanced. This suggests an active participation of actomyosin in even distribution of traction forces at the front and the rear to drive a controlled active migration against the flow, as assumed by the cell orientation.

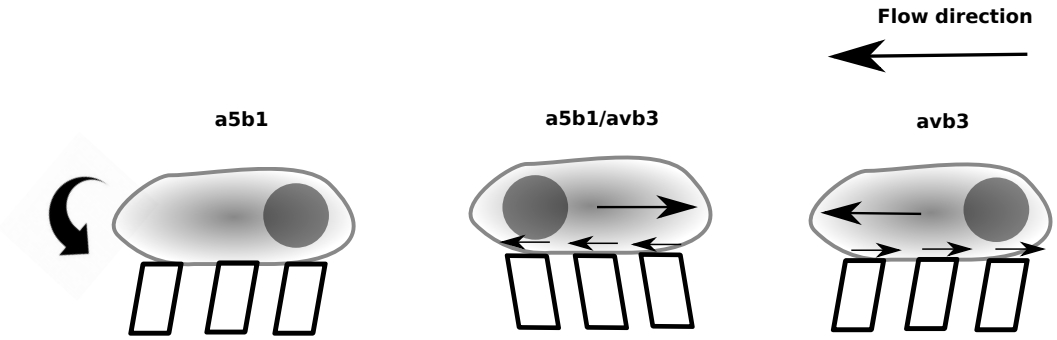


Figure 56: Myosin influence on cell behaviour in response to shear stress.

**Intermediate filaments**

Not just actin plays an important role in focal adhesion formation and therefore cell adhesion and migration, but also intermediate filaments. To study their effect on integrin specific traction force generation we disrupted vimentin with acrylamide.

We observed that traction forces did not change for a5b1, a5b1/av3b and NIH/3T3 cells, but increased for avb3 cells. Focal adhesions where unchanged in our observation for a5b1 and avb3 cells but reduced in area for a5b1/avb3 cells and highly increased in area for NIH/3T3 cells. However, as already mentioned before, focal adhesion size does not necessarily correlate with traction force magnitude.

Vimentin was found to be important for cell motility, invasion and lamellopodia formation[70]. It regulates cell adhesion by entering into focal adhesion sites and binds to $\beta 1$ integrins[88]. Vimentin overexpression enhances focal adhesion turnover[70]. Upregulation of plectin and vimentin was shown in various cell carcinomas, leading to an increase in invasiveness and metastasis potential[63][70]. However, previous studies showed, that missing vimentin leads to more robust focal adhesions and strongly bundled stress fibers[188]. For plectin-deficient fibroblasts similar effects were observed. Plectin is an intermediate filament crosslinking protein and is able to link intermediate filaments to focal adhesions. In both cases cellular stiffness, cytoskeletal tension as well as traction forces and

therefore mechanotransduction were reduced[63] [188]. Also FAK activation was reduced leading to increased RhoA (RhoA is known to increase cell contractility, focal adhesion and actin stress fiber formation) activity and reduced Erk and Src activity, explaining the increase in actin stress fibers and focal adhesion formation but decrease in cell migration. It seems to be a compensatory effect, enhancing actomyosin activity due to the lack of vimentin or plectin[188], but with ineffective outcome.

Since we do not observe a reduction of traction forces in our measurements, we propose that stronger stress fibers might be build (not tested) and then compensate for the vimentin loss and together with intact actomyosin prevent a decrease of traction forces. For avb3 cells even an overcompensation takes place, correlating with the unchanged traction forces after myosin inhibition or actin disruption under static conditions. Indeed, after simultaneous vimentin disruption and myosin inhibition avb3 cells do not show a decrease in traction forces. Also a5b1/avb3 cells do not show decreased traction forces, suggesting a stronger relevance of avb3 integrins in this case. a5b1 cells showed a decrease in traction forces, therefore suggesting that stronger stress fibers might play a minor role for this integrin type compared to myosin.

Compared to untreated conditions the cell height increased for a5b1 cells and NIH/3T3 cells and decreased for avb3 and a5b1/avb3 cells. Epithelial cells were shown to flatten after induced vimentin expression[110] and fibroblasts were shown to be more deformable after vimentin loss[182]. Somehow the effect that avb3 and a5b1/avb3 cells are more flat seems to be triggered by avb3 integrins, showing a stronger effect than a5b1 cells in cooperation. The vimentin loss seems to be compensated with a stronger actin stress fiber network. Cells were shown to be more flat with an intact actin network compared to a depolymerised network[157]. Since NIH/3T3 contain other integrins and are more complex in general, the observed effects might be triggered by other components.

**Integrin blocking**

By blocking either avb3 or a5b1 integrins in a5b1/avb3 cells, we wanted to test, if traction forces would be the same as for the cell types only expressing one of the integrins. As result the traction forces did not significantly differ from the untreated a5ba/avb3 cells, but from the cell types expressing only one integrin type. Although we used a high concentration for both blocking peptides, we only see a trend in traction force change. The concentration for the a5b1 blocking peptide was 15$\mu$M, the tested $IC_{50}$ (half maximal inhibitory concentration) values from Rechenmacher et al. were 2.3±0.02nM for a5b1 blocking and 3001±205nM for avb3 blocking[136]. The concentration for the avb3 blocking peptide was 3$\mu$M in our experiment, the $IC_{50}$ value for avb3 blocking 0.55±0.07nM and for the a5b1 blocking 120±27nM[136]. Since the used concentrations in our experiments are over 5000x higher then the $IC_{50}$ values we would expect a sufficient blocking of the integrins. However the traction force measurement did not yield the expected results. Since both integrins build the cell and it might be that the adhesion of one is enough, it would be useful to test the traction forces after blocking both integrins simultaneously .

# 7 Application II: R3/1 and A549 lung cells

We studied the effect of external shear stress and the contribution of myosin on traction force generation of lung epithelial cells. This was of special interest to us, since fluid wall shear stress is known to play an important role regarding liquid plug formation in lung injury and clinical therapies. Propagation of these plugs generates shear stress on the epithelial cell layer and therefore influences cell response in biochemical and mechanical manner, like changes in traction force generation [64] [75] [105] [163]. Therefore we looked at the difference between the two distinct cell lines representing model systems for primary alveolar type I (R3/1 cell line) and type II (A549 cell line) cells. Alveolar type I cells build the basic structure of the alveolar wall and permit gas exchange, whereas aleveolar type II cells act as progenitor cells for the type I cells and are able to secrete pulmonary surfactant that lowers surface tension at the alveolar gas-liquid interface and therefore control alveolar fluid levels. In addition we analysed the influence of intermediate filaments, respective vimentin, on traction force generation for the two distinct cell types.

## 7.1 Results

For each micropost underneath a cell, the traction stress is calculated from the force and of the upper face of the micropost. Further, all traction stresses are summed up for one cell. The data is then plotted as one boxplot per cell type showing the distribution and the median over all measured cells. The central mark is the median, the edges of the box are the 25th and 75th percentiles, the whiskers extend to the most extreme data points, and outliers are plotted as circles. Significant differences are marked with asterisks (* represents p<=0.05, ** represents p<=1E-2 and *** represents p<=1E-3).

### 7.1.1 External shear stress and myosin inhibition

Figure 57 shows traction forces for R3/1 and A549 lung epithelial cells under static conditions (R3/1: n=98, A549: n=111), with myosin inhibition (R3/1: n=72, A549: n=86), under shear stress (R3/1: n=47, A549: n=49) and under shear stress with myosin inhibition (R3/1: n=53, A549: n=46). A549 cells show significant higher traction forces under static untreated conditions than R3/1 cells (p=0.02). Both cells show reduced traction forces after myosin inhibition for static conditions (R3/1: p=0.003, A549: p=0.02). Cell traction forces are increased significantly for the A549 cells under shear stress (p=1.74e-04), but not for the R3/1 cells. After myosin inhibition under shear stress there is no change of traction forces for the R3/1 cells, but a decrease for the A549 cells (p=8.78e-09). The difference between myosin inhibition under static conditions compared to shear stress conditions is not significant for both cell lines. A549 cells show significant higher traction forces under shear stress conditions than R3/1 cells (p=5.52e-06) and for myosin inhibition under static conditions (p=3.92e-04), but not under shear stress.

Figure 58 shows the absolute difference of the median values for R3/1 and A549 cells under static and shear stress conditions, with and without myosin inhibition. R3/1 cells have a higher difference of traction forces after myosin inhibition under static conditions, whereas A549 cells show a much higher difference of traction forces after myosin inhibition under shear stress.

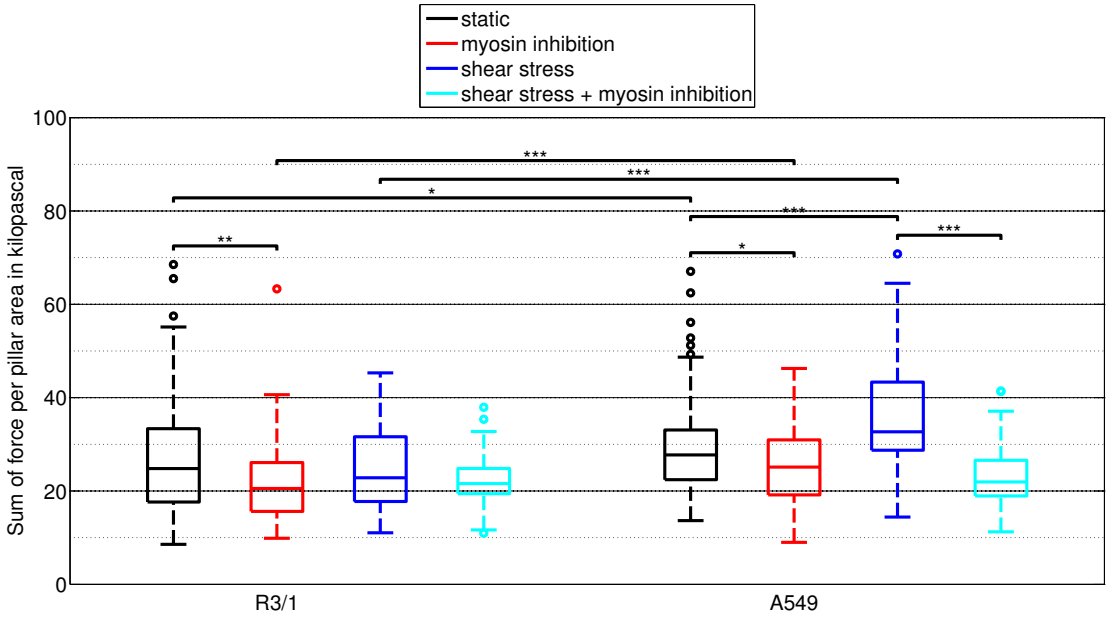


Figure 57: Boxplots of cell traction forces for R3/1 and A549 cells under static conditions and under shear stress, both with and without myosin inhibition.

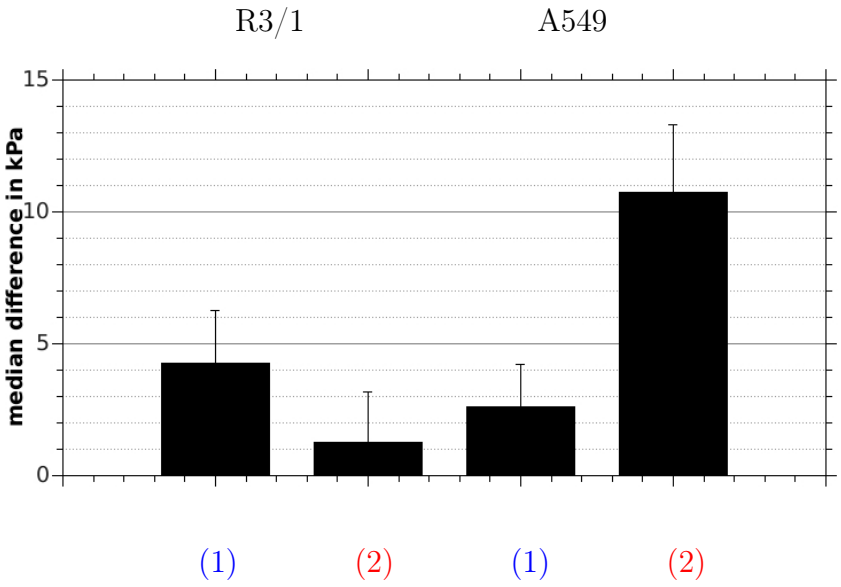


Figure 58: Median difference of cell traction forces for R3/1 and A549 cells under (1) static and (2) shear stress conditions, both with and without myosin inhibition. The error bars represent the standard error of the median.

Figure 59 shows the micropost displacement direction for R3/1 and A549 cells under static conditions and shear stress and the absolute difference between static and shear stress conditions. Both cell types show a shift of micropost displacement direction towards the direction of flow under shear stress, whereas it is only significant for R3/1 cells (R3/1: 60-120 vs 120-180 p=0.01).

Figure 60 shows the micropost displacement direction for R3/1 and A549 cells under static conditions and shear stress, both with and without myosin inhibition and the absolute difference between myosin inhibition and the untreated state for static and shear stress conditions. The difference of shear stress and shear stress with myosin inhibition shows for R3/1 cells a shift against the flow direction and for the A549 cells with the flow direction. The difference shows the trend for A549 cells with the flow direction, but there is a significant difference also under static conditions. (Static and myosin inhibition: R3/1: 60-120 vs 120-180 p=0.04; A549: 0-60 vs 120-180 p=0.03; Shear stress and myosin inhibition: R/1: 0-60 vs 60-120 p= 0.05; A549: 0-60 vs 120-180 p=0.03)

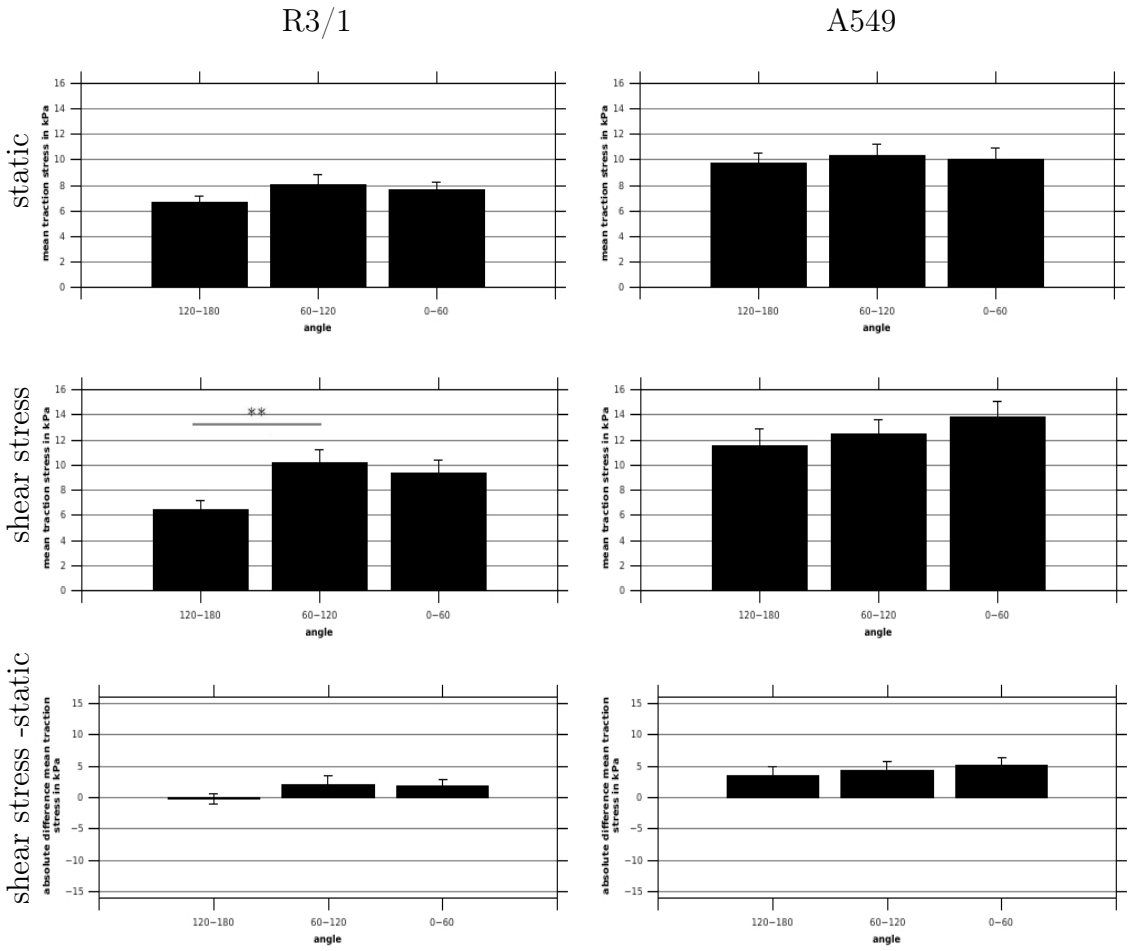


Figure 59: Micropost displacement direction for R3/1 and A549 cells under static conditions and shear stress. The absolute difference of traction forces between static and shear stress conditions is shown at the bottom. Error bars represent the standard error of the mean.

R3/1

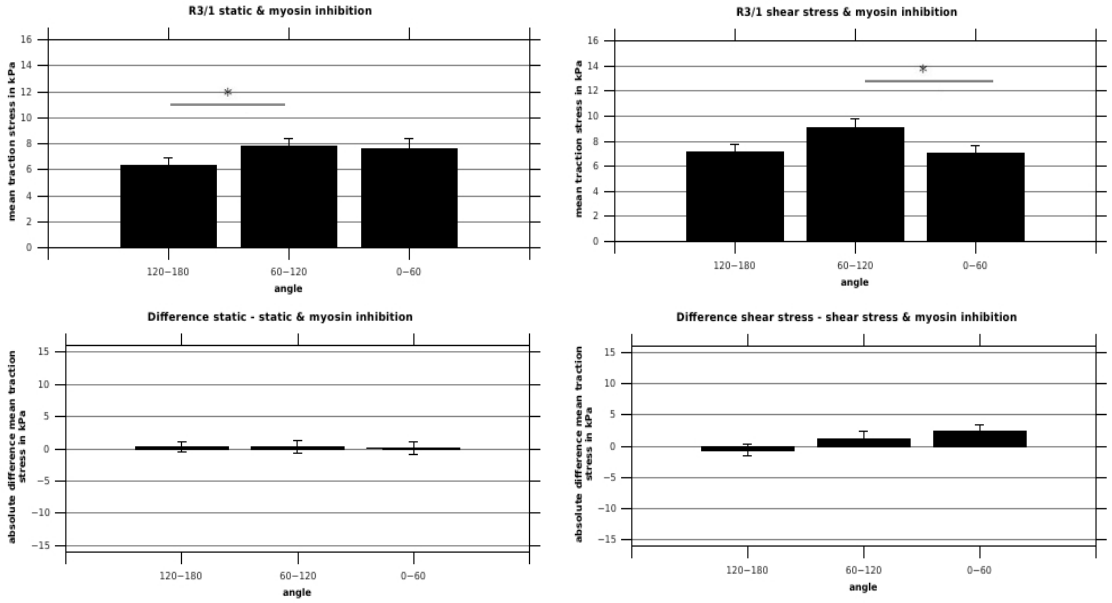


A549

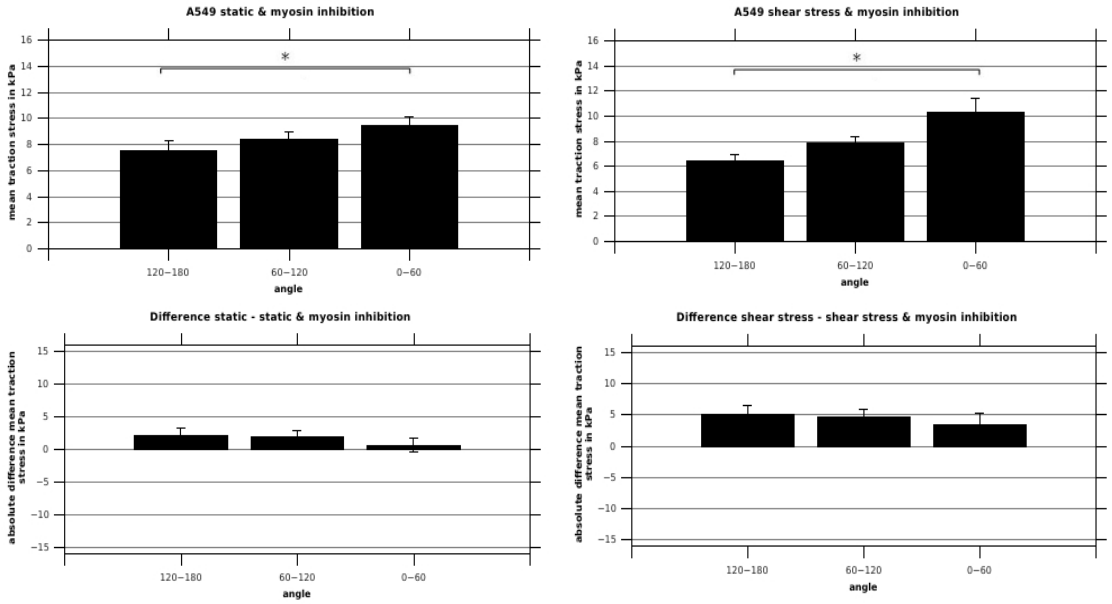


Figure 60: Micropost displacement direction for R3/1 and A549 cells under static and shear stress conditions with myosin inhibition. The difference between untreated state and myosin inhibition for both static und shear stress conditions is shown at the bottom. Error bars represent the standard error of the mean.

Figure 61 shows the resulting micropost displacement direction for R3/1 and A549 cells under static conditions, under shear stress and under shear stress with myosin inhibition. The resulting micropost displacement was first calculated for each cell and then the mean value over all cells was built. The results show the same tendency as the micropost displacement directions shown in figures 59 - 60. Table 5 shows the difference of resulting micropost displacements for shear stress - static conditions and under shear stress conditions with and without myosin inhibition.

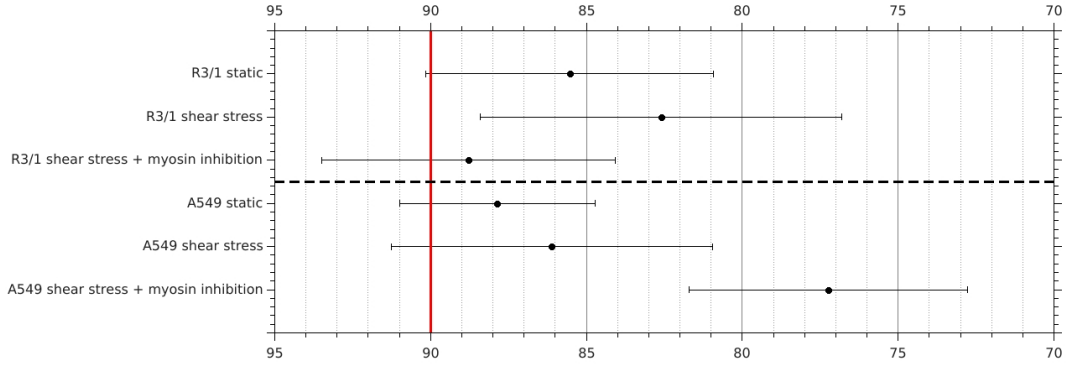


Figure 61: Resulting micropost displacement direction for R3/1 and A549 cells under static conditions, shear stress and shear stress with myosin inhibition. Shown is the mean value with the standard error of the mean. The x- axis shows the coordinates in degrees

Table 5: Difference of resulting micropost displacement direction for R3/1 and A549 cells from Figure 61

| **Cell type and conditions** | **Difference in degrees** |
|---|---|
| R3/1 | |
| difference shear stress - static | -2.93 ± 7.41 |
| difference shear stress - (shear stress + myosin inhibition) | -6.17 ± 7.47 |
| A549 | |
| difference shear stress - static | 1.75 ± 6.02 |
| difference shear stress - (shear stress + myosin inhibition) | 8.87 ± 6.81 |

Figure 62 shows the relative histograms of the nucleus to Golgi complex orientation for R3/1 and A549 cells. The leading front of a cell is characterised by the Golgi complex lying in front of the nucleus towards the cell front. The direction is given by the angle were the Golgi complex lies in reference to the nucleus.
Compared to the cell orientation under static conditions R3/1 cells show a clear

shift of orientation with the flow direction under shear stress, whereas the A549 cells show a shift against the flow direction. The same observation is made under shear stress with myosin inhibition. Looking at the difference for untreated state and with myosin inhibition under shear stress, there is a shift for R3/1 ells with the flow and for the A549 cells against the flow.

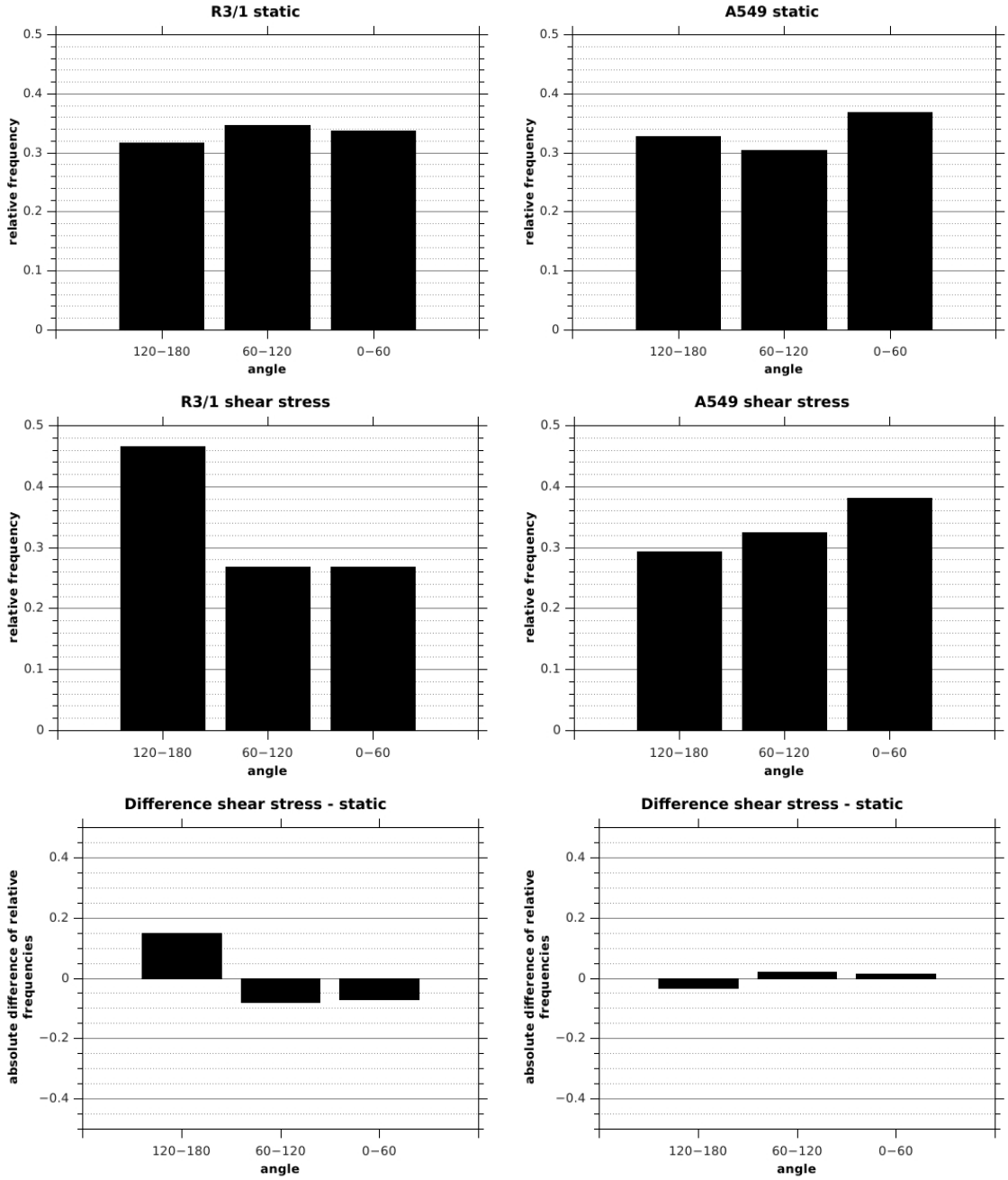

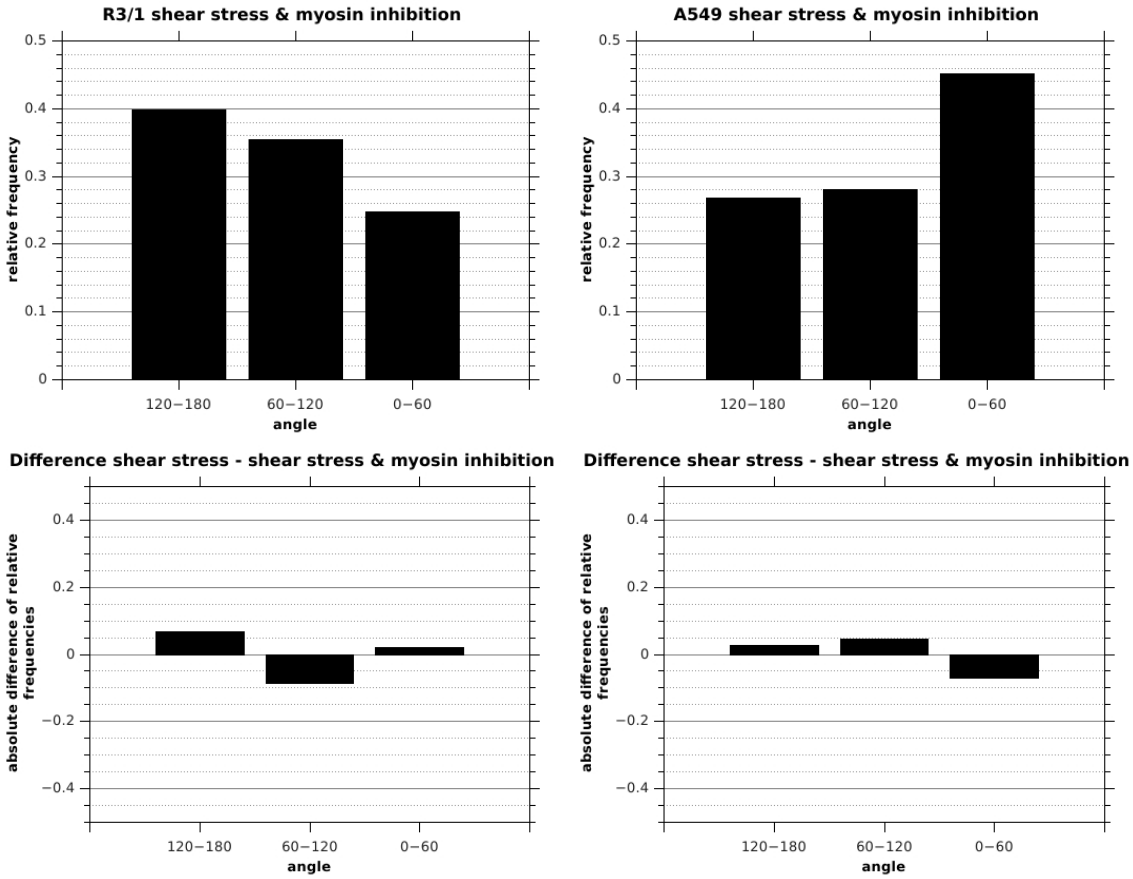


Figure 62: Relative histograms of cell orientation for R3/1 and A549 cells under static conditions, under shear stress and under shear stress with myosin inhibition. The difference in polarised cells between shear stress and static, as well as shear stress with and without myosin inhibition is shown at the bottom.

Figure 63 shows the relative cell height of R3/1 and A549 cells after myosin inhibition under static conditions, after shear stress application and under shear stress and myosin inhibition compared to the static untreated state. After myosin inhibition under static conditions the cell height is increased for R3/1 cells but not for A549 cells. Under shear stress the cell height is unchanged for R3/1 cells but decreased for A549 cells. After myosin inhibition under shear stress the cell height is increased for the R3/1 cells and decreased for the A549 cells compared to the static condition, but the same as under shear stress without myosin inhibition.

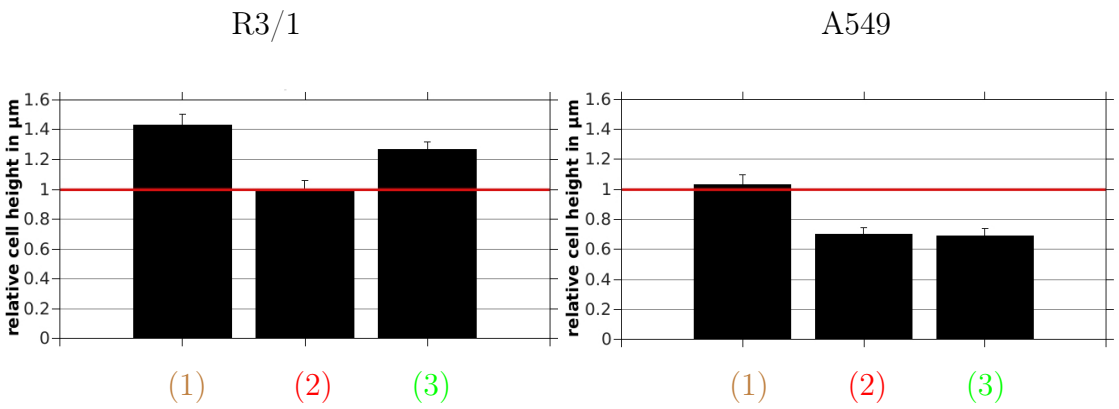


Figure 63: Relative cell height for R3/1 and A549 cells after (1) myosin inhibition, (2) shear stress application and (3) shear stress and myosin inhibition, compared to the static untreated state. Error bas represent the standard error of the median.

Figure 64 and 65 show fluorescence images of paxillin stained cells on microposts. Shown are R3/1 and A549 cells on microposts under static conditions with and without myosin inhibition and under shear stress with and without myosin inhibition. The micropost outline is shown in grey as well as the cell area, whereas the paxillin staining is shown in orange. For R3/1 cells the focal adhesions are built as several stripes on top of the microposts. After myosin inhibition there are less stripes on top of the microposts, but focal adhesions are wrapped around the microposts. Under shear stress there are still clear stripe like focal adhesions visible, whereas after myosin inhibition under shear stress, again focal adhesions tend to build less stripe like forms, but are wrapped around the micropost outlines. For A549 cells, focal adhesions are wrapped around the microposts building arc like structures in all cases, whereas they seem weaker after myosin inhibition under static and shear stress conditions.

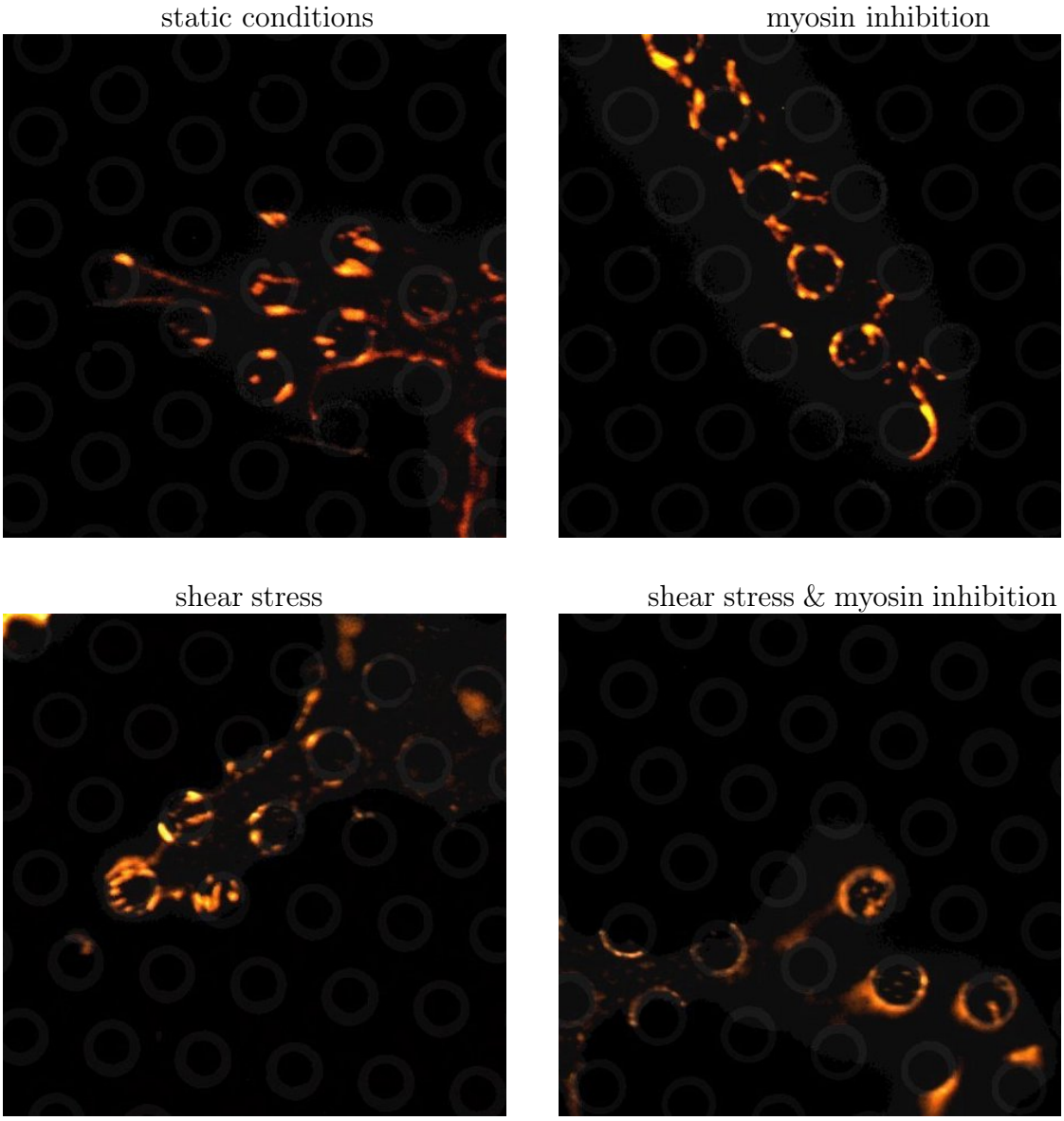


Figure 64: Paxillin staining of R3/1 cells on microposts under static untreated conditions, with myosin inhibition and under shear stress with and without myosin inhibition.

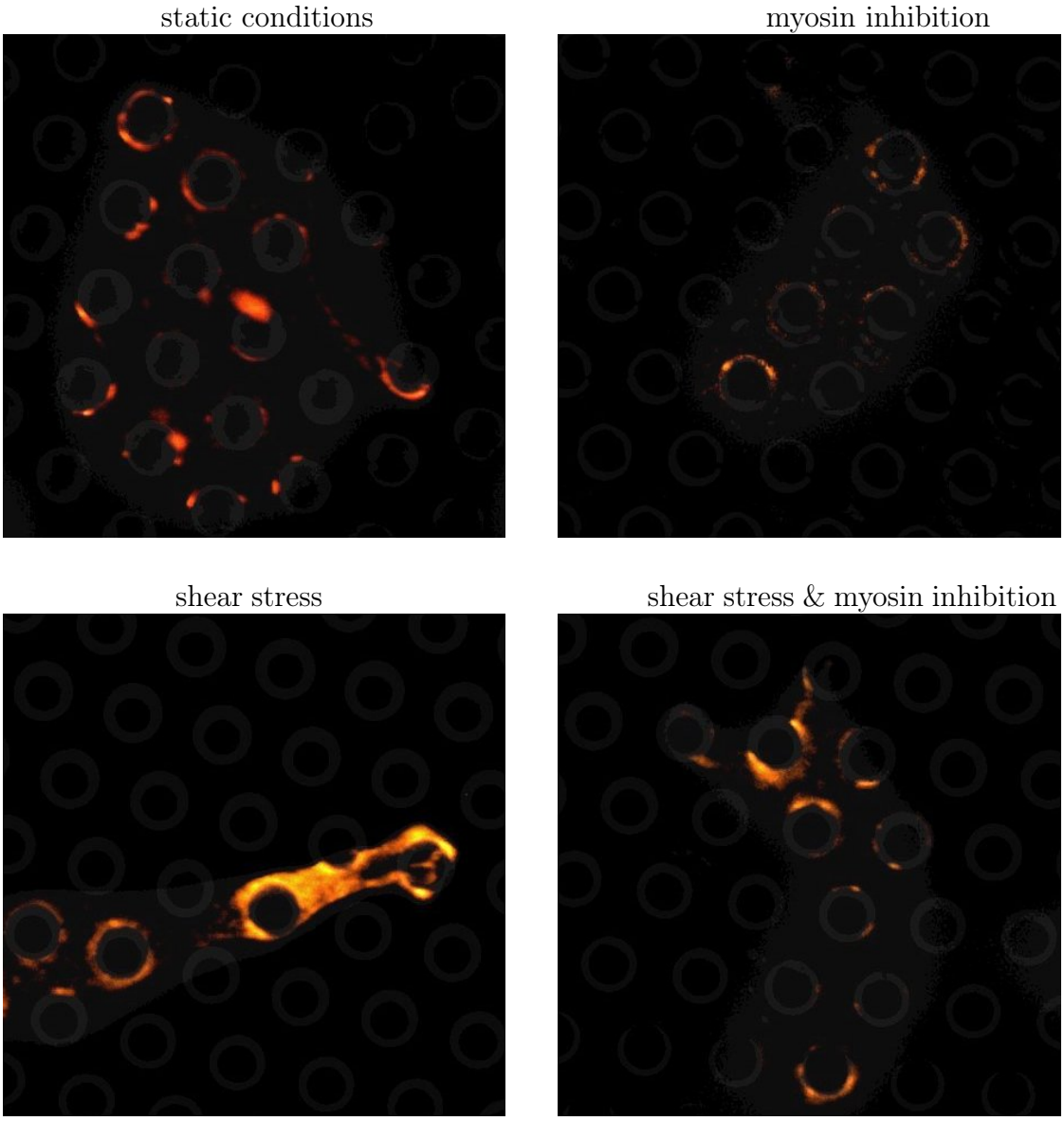


Figure 65: Paxillin staining of A549 cells on microposts under static untreated conditions, with myosin inhibition and under shear stress with and without myosin inhibition.

Figure 66 and 67 show focal adhesion area, circularity and angle for R3/1 and A549 cells under static conditions and under shear stress, both with and without myosin inhibition. R3/1 cells show no change in focal adhesion area or circularity after myosin inhibition and under shear stress compared to the static untreated state. After myosin inhibition under shear stress the focal adhesion area is reduced and the shape is less elongated. The angle is similar for all conditions, showing a transverse orientation to the flow. The A549 cells show a reduction of focal adhesion area for all conditions compared to the static untreated state. The effect is stronger after myosin inhibition than only under shear stress. The

circularity is only changed after myosin inhibition under static conditions with a less elongated shape. The orientation is transverse to the flow.

R3/1

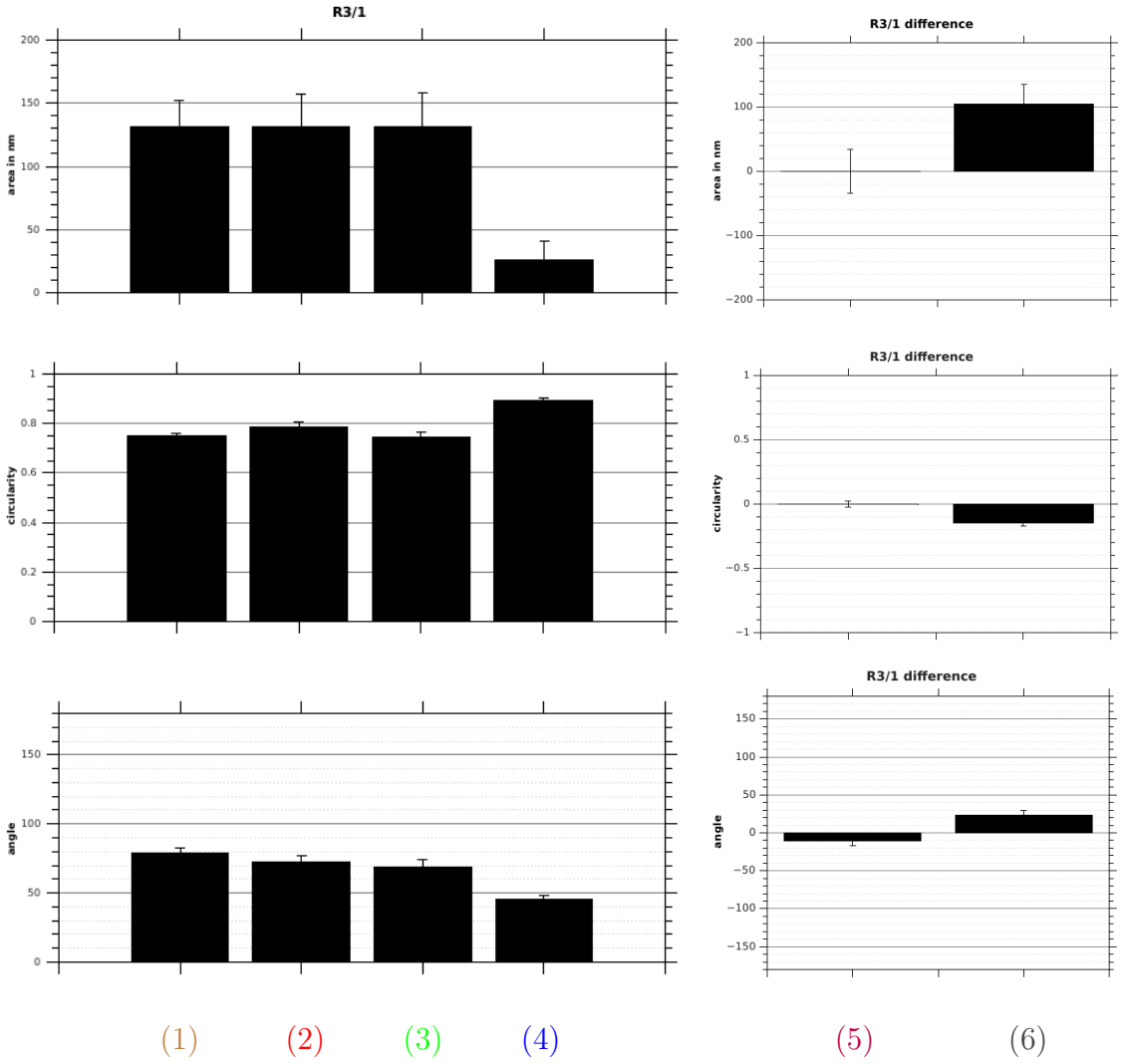


Figure 66: Focal adhesion area (top), circularity (middle) and angle (bottom) for R3/1 cells for (1) static conditions, (2) static conditions with myosin inhibition, (3) shear stress, (4) shear stress with myosin inhibition, (5) difference of shear stress - static conditions and(6) difference shear stress and shear stress and myosin inhibition. Shown are the median values with the standard error of the median.

A549

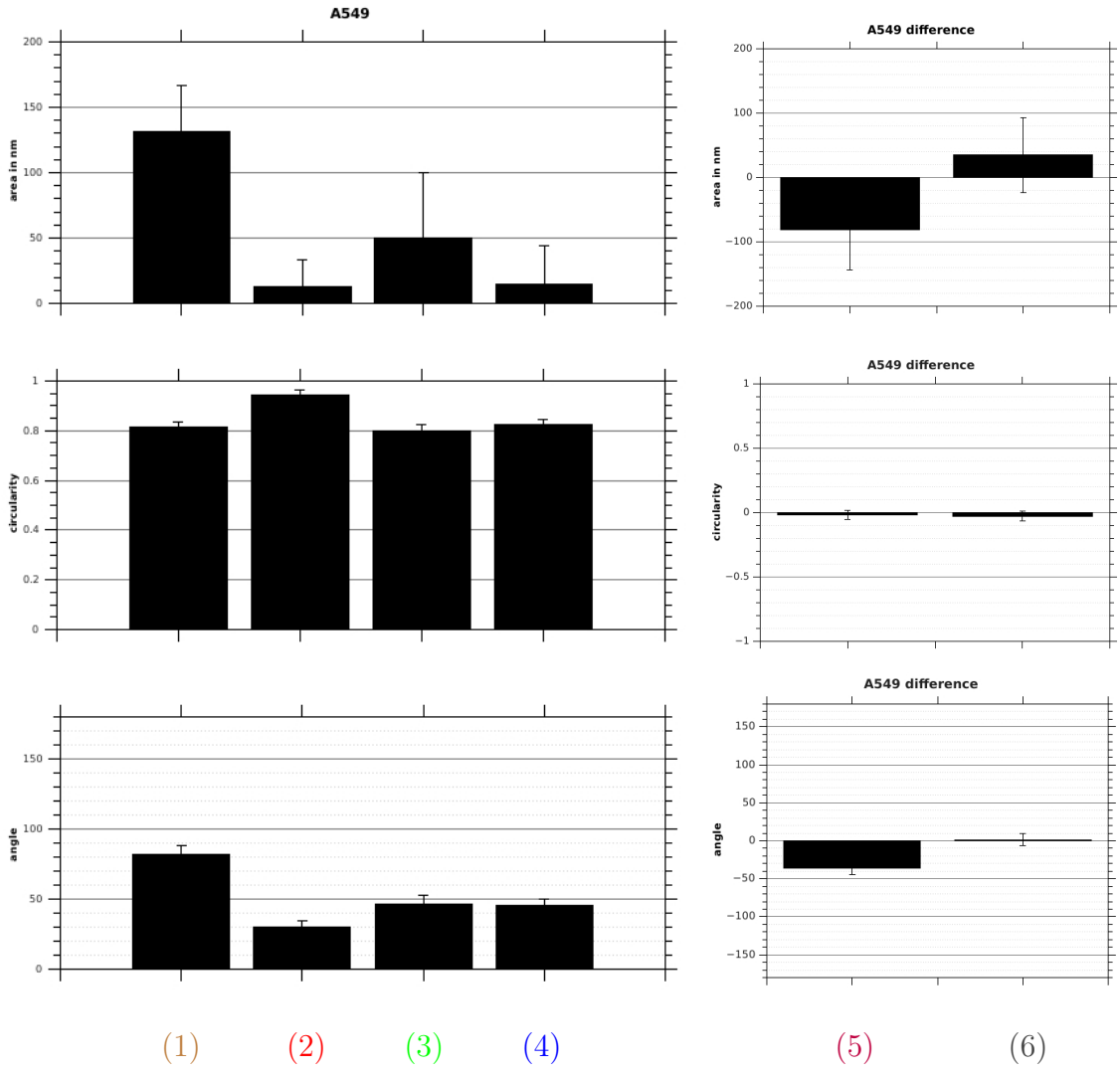


Figure 67: Focal adhesion area (top), circularity (middle) and angle (bottom) for A549 cells for (1) static conditions, (2) static conditions with myosin inhibition, (3) shear stress, (4) shear stress with myosin inhibition, (5) difference of shear stress - static conditions and (6) difference shear stress and shear stress and myosin inhibition. Shown are the median values with the standard error of the median.

### 7.1.2 Vimentin disruption

Figure 68 shows traction forces forces with vimentin disruption for R3/1 (n=57) and A549 (n=59) cells. There is a significant reduction of traction forces after vimentin disruption for R3/1 cells (p=0.002) and for A549 cells (p=8.19e-04). A549 cells show higher traction forces after vimentin disruption than R3/1 cell (p=0.03).

Figure 69 shows the relative cell heights of R3/1 and A549 cells after vimentin disruption compared to the untreated state. The cell height is unchanged for both cell types after vimentin disruption.

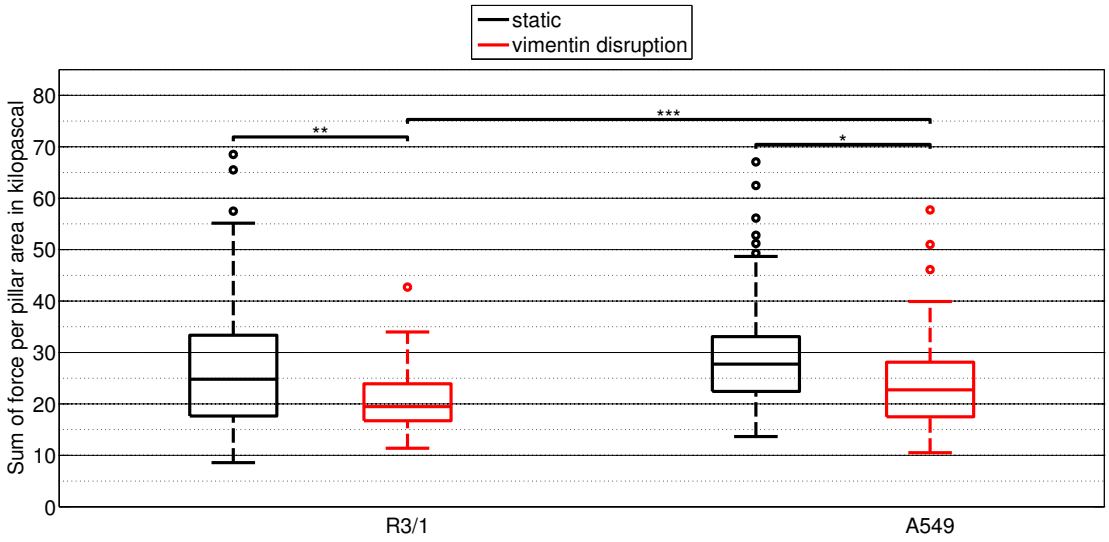


Figure 68: Boxplots of cell traction forces for R3/1 and A549 cells under static conditions and with vimentin disruption.

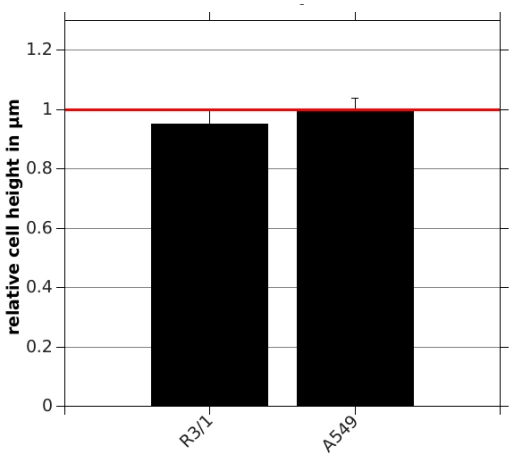


Figure 69: Relative cell height of R3/1 and A549 cells after vimentin disruption compared to static untreated conditions. The error bars represent the standard error of the median.

Figure 70 and 71 show fluorescence images of paxillin stained R3/1 and A549 cells under static untreated conditions and with vimentin disruption. R3/1 cells tend to build more arc like focal adhesions in addition to the stripe formed. For A549 cells there is no markedly change in focal adhesion morphology visible.

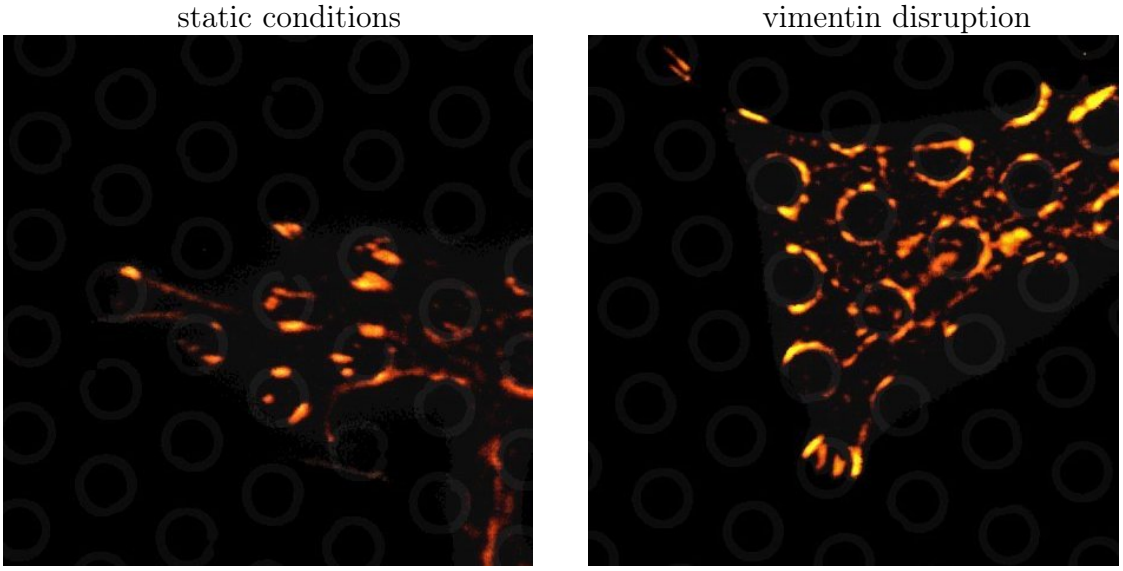


Figure 70: Paxillin staining of R31 cells on microposts under static untreated conditions and with vimentin disruption.

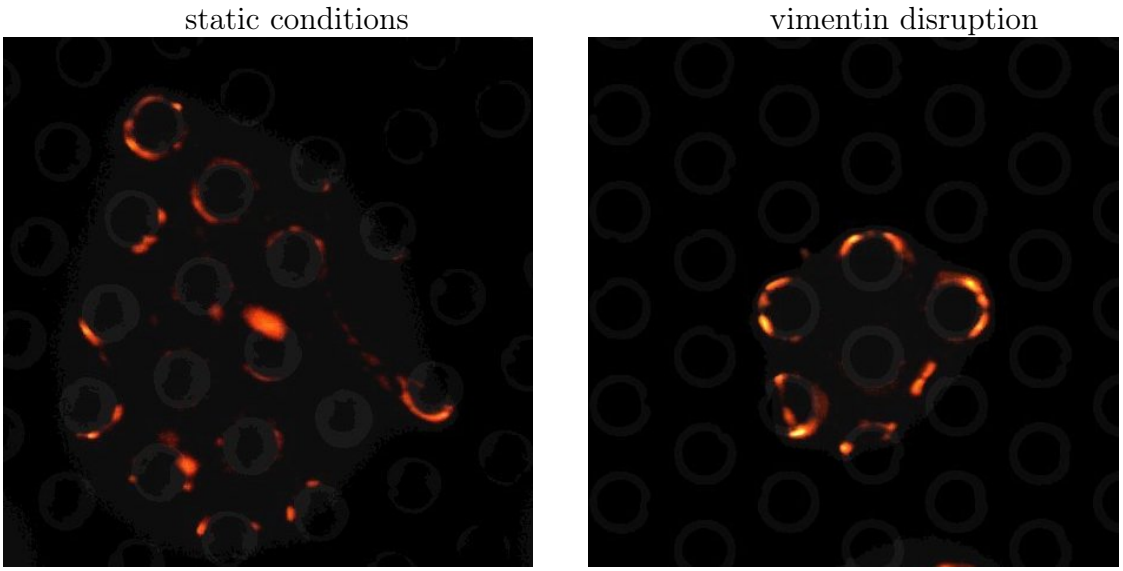


Figure 71: Paxillin staining of A549 cells on microposts under static untreated conditions and with vimentin disruption.

Figure 72 shows focal adhesion area and circularity for R3/1 and A549 cells under static conditions (1) and with vimentin disruption (2). The difference for both cell types static - vimentin disruption is also shown. The focal adhesion area is reduced after vimentin disruption for R3/1 cells and increased for A549 cells. The circularity is unchanged for R3/1 cells and reduced for A549 cells.

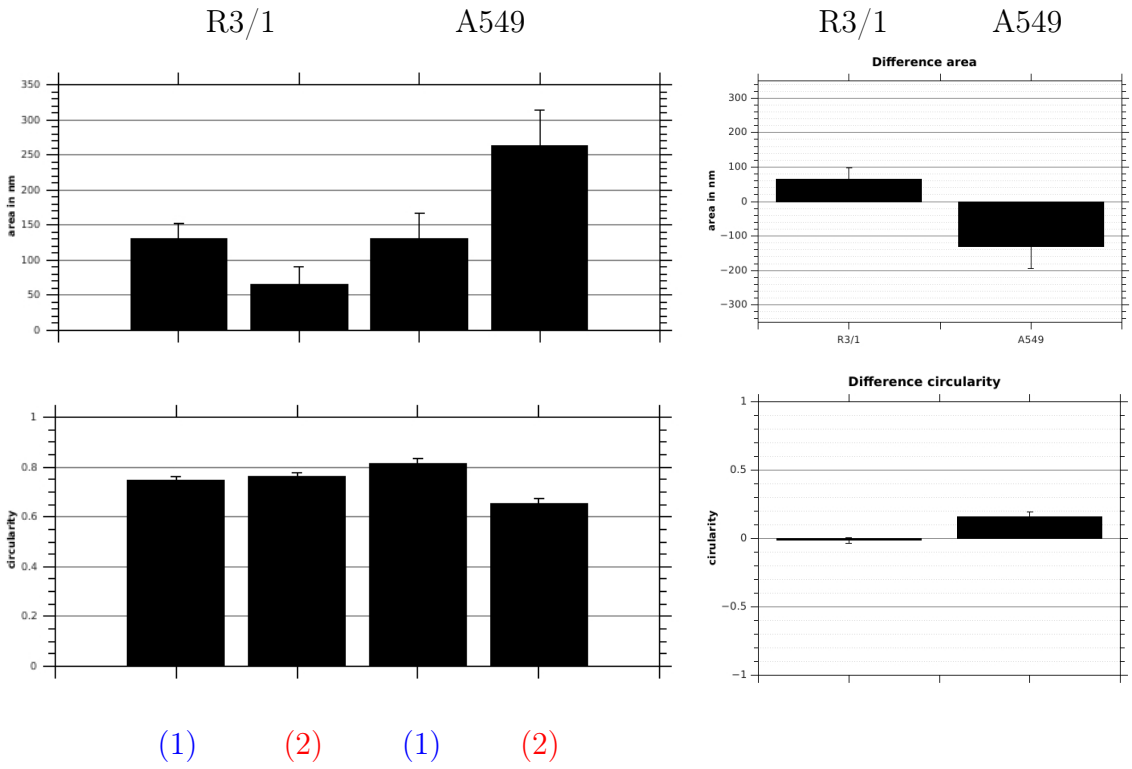


Figure 72: Focal adhesion area (top) and circularity (bottom) for R3/1 and A549 cells under static conditions (1) and with vimentin disruption (2). The difference static - vimentin disruption is shown at the right side for both cell types.
Shown are the median values with the standard error of the median.

## 7.2 Discussion

Fluid wall shear stress plays an important role regarding liquid plug formation in lung injury and clinical therapies. Propagation of these plugs generates shear stress on the epithelial cell layer, influencing cell response in biochemical and mechanical manner[64][75][105][163]. Cells might respond to this stresses amongst others with a change in their force generation apparatus.
We used epithelial lung cell lines R3/1, as analogue for the alveolar type I cells and the A549 cell line, as analogue for alveolar type II cells, to study the effect of fluidic shear stress on traction force generation. In addition we looked at the different influence of myosin and vimentin on traction force generation for both cell types.

**Cell traction forces of R3/1 and A549 cells and the influence of myosin**

Under static untreated conditions, traction forces are higher for A549 cells compared to R3/1 cells. The median sum of traction stress for A549 cells is around 28kPa and for R3/1 cells around 25kPa. Gavara et al. measured a total force magnitude of 55.0±12.0nN for a cell area of 993±57$\mu$m$^2$ (corresponding to 0.06kPa) for non migrating A549 cells, with maximal local tractions of 157.0±17.3Pa and an average traction of 37.0±5.0Pa[54]. Another study measured a net traction force of 200nN on 10kPa polyacrylamide substrate with collagen coating for A549 cells with an area of 600$\mu$m$^2$ (corresponding to 0.3kPa)[87]. These results seem very low compared to our measurements. Also previous studies measured average traction forces around 2-3kPa for migrating 3T3 cells[32][113], which is 50 times higher than the total stress measured by Gavara et al. However, Gavara et al. state that maybe the low traction forces in their measurements derive from the fact that the cells are stationary and not migrating[54]. Compared to previous traction force studies on various cell types our data lies in a resonable range[9][32][50][101][113].
The focal adhesion area is the same for both cell types, whereas the shape seems to be distinct in terms of more elongated focal adhesions for R3/1 cells, forming stripes on the micropost tops, and arc like focal adhesions wrapped around the micropost outlines for A549 cells. Ghibaudo et al. observed the same effect as we did for the A549 cells, that cells on hexagonal micropost arrays build actin arcs around the microposts and corresponding focal adhesions[58]. Although focal adhesion size and shape is not necessarely linked to traction force magnitude, the difference between the two cell types is interesting, pointing to a different organisation of focal adhesion assembly.

However, one has to be careful comparing these two cells types directly, since A549 cells are derived from primary cancer in contrast to the R3/1 cells. Kraning-Rush et al. showed an increase in traction forces for A549 metastatic lung cancer cells compared to non-metastatic cells[87]. Therefore, it is not clear if the higher traction forces for A549 cells might derive from an altered mechanism, due to the cancer genotype.
Traction forces are reduced after myosin inhibition with blebbistatin for both cell types under static conditions, with a larger effect on R3/1 cells, supposing that myosin plays a role in traction force generation for both cell lines. Non-muscle myosin II isoform expression was shown to be prominent in type I cells and it was suggested, that it might play a key role in the regulation of type I cell function and alveolar permeability[131]. Focal adhesion area is not altered for R3/1 cells as well as the circularity, but for A549 cells the area is reduced and focal adhesions are less elongated. Myosin seems to have an effect on focal adhesion formation of A549 cells but not of R3/1 cells. However, it has to be considered that focal adhesion size and traction forces do not necessarily correlate, since for example a positive correlation between focal adhesion size and tension was observed in stationary cells, whereas the opposite was seen using migrating cells[9][156]. The cell height is increased for R3/1 cells, but remains unchanged for A549 cells, assuming a different regulation of cytoskeletal arrangement for the two cell types after myosin loss, for example in terms of actin organisation.

**The influence of external shear stress and myosin on traction forces**

In vitro models of air–liquid interface flow over cells showed that the applied stress can injure epithelial cells[15][75][162][191] and Douville et al. showed that fluid stress transmitted by an air-liquid meniscus has an influence on the increase of the amount of cell detachment[36]. Mahto et al. showed that wall shear stress has an influence on key components of the molecular machinery for the regulation of surfactant secretion of alveolar type II cells in vitro[105]. Our measurements show, that under shear stress R3/1 cells do not react with a change in traction forces, whereas A549 cells show a strong increase. Focal adhesion area is unchanged for R3/1 cells and decreased compared to static conditions for A549 cells. The cell height is the same as under static conditions for R3/1 cells but reduced for A549 cells. Overall R3/1 cell do not show a reaction to shear stress in contrast to A549 cells. Type I cells cover over 95% of the alveolar surface area, therefore it was hypothesized that they are exposed to a greater strain than type II cells, which reside in the relatively protected alveolar corners[99]. It is suggested, that type II cells are more vulnerable to mechanical induced injury than type I cells[99]. Previous studies showed, that A549 cells under static conditions or low shear

stress values (4dyn/cm$^2$) show polymerised and well-organised actin filaments[105]. For higher shear stress values the actin cytoskeleton showed disorganised and fragmented actin filaments, therefore limiting the number of lamellar bodies fusion events, necessary for pulmonary surfactant secretion, as for their primary analogues[105]. The result suggests that R3/1 cells are more robust against shear stress, because the purpose of their primary analogue is to build the main part of the alveolus whereas the type II cells react sensitive, because of their regulatory function. As well as the alveolar type II cells, the A549 cells have been shown to produce and release surfactant proteins[17].
We observed, that the direction of cell polarisation is opposed for both cell lines, whereat R3/1 cells are polarised with the flow and A549 cells against the flow. Micropost displacement direction is shifted against the flow for R3/1 cells and for A549 cells. Since these observations can be influenced passive by the shear stress and active by cell internal parameters, we also analysed the influence of myosin on the observed effects.

Myosin inhibition under shear stress has no effect on traction forces of R3/1 cells, but there is a strong reduction of traction forces for A549 cells. Hence, shear stress seems to trigger a strong myosin upregulation in A549 cells. After myosin inhibition under shear stress R3/1 cells show an increase of cell height, as for myosin inhibition under static conditions. A549 cells have the same height as for untreated conditions under shear stress, and therefore show no change as under static conditions. Therefore the cell height is changed in the same way as after myosin inhibition under static conditions. Focal adhesion area is reduced for both cell types after myosin inhibition under shear stress, also for the R3/1 cells in contrast to the static conditions. The focal adhesion angle is similar after myosin inhibition for both cell types.
The direction of cell polarisation is with the flow direction for R3/1 cells and against the flow for A549 cells, and therefore the same as under untreated shear stress conditions. Looking at the difference for polarisation direction under shear stress with and without myosin inhibition, there seems to be an active myosin contribution to polarisation direction with the flow for R3/1 cells and an active myosin contribution for polarisation against the flow for A549 cells. The drag force of the flow is able to relocate the nucleus downstream. An intact actomyosin network can resist this force and enable an active relocation of the nucleus upstream to change the migration direction with the flow[43] [62] [66] [166]. This effect is reduced after myosin inhibition for R3/1 cells, but not completely disabled, suggesting that another part of the cytoskeleton is still able to resist the drag force and maintain an upstream relocation of the nucleus. For A549 cells there

seems to be less resistance after myosin inhibition to the drag force of the flow, explaining the even stronger occurrence of polarised cells against the flow.
For R3/1 cells myosin triggers a shift of micropost bending against the flow, that correlates with the polarisation direction and therefore could be explained by active pulling of the cell on the substrate in migration direction, bending the microposts against the flow. Myosin seems to be responsible to a larger extent for the orientation of the cell and the migration with the flow, that might be facilitated by the pushing of the flow and therefore needs less traction forces to propel the cell forward. For A549 cells the microposts are displaced with the flow by active myosin participation, correlating with the polarisation direction, therefore the cell actively pulls on the substrate to migrate against the flow. The overall bending against the flow might be explained by cell rolling[48][84][169], that effects both cell types.

In general, shear stress acts in different ways on the two cell types. For the A549 cells by activating myosin, that triggers an active migration against the flow that produces larger traction forces, and in the other case for the R3/1 cells by triggering myosin to migrate with the flow and produce equal traction forces to the static state.

**The influence of vimentin on traction force generation**
Vimentin disruption reduces traction forces for both cell types, assuming a major role of intermediate filaments in traction force generation for both cell types. Rogel et al. showed that vimentin expression in alveolar epithelial cells enhances cell migration and therefore wound closures[143]. Several other studies also demonstrated a functional role of vimentin in migration of epithelial cells[38][60][72][151]. Dauphin et al. showed in a clinical study, that in non small cell lung carcinomas vimentin is expressed and is associated with metastases[30]. The cell height is unchanged compared to untreated conditions for both cell types. Either vimentin is not a contributor of cytoskeletal arrangement in terms of cell morphology in this case, or a compensatory effect sets in, maybe concerning the actin cytoskeleton. Focal adhesion area is reduced for R3/1 cells with unchanged circularity and increased for A549 cells with a more elongated shape. The opposed effect seems to be a hint, that different pathways may play a role in focal adhesion formation in terms of vimentin influence.
The opposite results to the fibroblasts from the previous section are interesting. We suppose a cell type specific difference between fibroblasts and epithelial cells, that seems to influence traction force generation differently during the absence of vimentin, in the special case of our setup.

# 8 Application III: MLO-Y4 osteocyte-like cells

Since osteocytes are known to sense and react to fluid shear stress in the canalicular system of bones[76], we wanted to study the effect of shear stress on the force generation of the model cell line MLO-Y4. In addition we studied the contribution of smooth muscle myosin kinase (SMMK) on traction force generation. SMMK was of special interest, since a study by Baik et al. postulated, that phasic contractility in MLO-Y4 cells might be mediated through smooth muscle myosin[7]. Further we analysed the influence of vimentin on traction force generation.

## 8.1 Results

For each micropost underneath a cell, the traction stress is calculated from the force and of the upper face of the micropost. Further, all traction stresses are summed up for one cell. The data is then plotted as one boxplot per cell type showing the distribution and the median over all measured cells. The central mark is the median, the edges of the box are the 25th and 75th percentiles, the whiskers extend to the most extreme data points, and outliers are plotted as circles. Significant differences are marked with asterisks (* represents p<=0.05, ** represents p<=1E-2 and *** represents p<=1E-3).

### 8.1.1 External shear stress and SMMK inhibition

Figure 73 shows traction forces for MLO-Y4 cells under static conditions (n=78), under static conditions with SMMK inhibition (n=43), under shear stress (n=51) and under shear stress with SMMK inhibition (n=38).
There is a significant reduction of traction forces under SMMK inhibition compared to untreated conditions (p=0.007). Shear stress increases traction forces significantly (p=0.003). There is no difference in traction forces after SMMK inhibition under shear stress compared to only shear stress. Traction forces for SMMK inhibition under shear stress are significant higher than for static conditions (p=2.5e-06) and SMMK inhibition under static conditions (p=0.007).

Figure 74 shows the absolute difference of the median values for SMMK inhibition and untreated state under static and shear stress conditions. The difference is larger under static conditions than under shear stress conditions.

Cells were also treated with blebbistatin to inhibite non-muscle myosin II (Figure 75), but there was no significant difference observable, neither under static conditions, nor under shear stress.

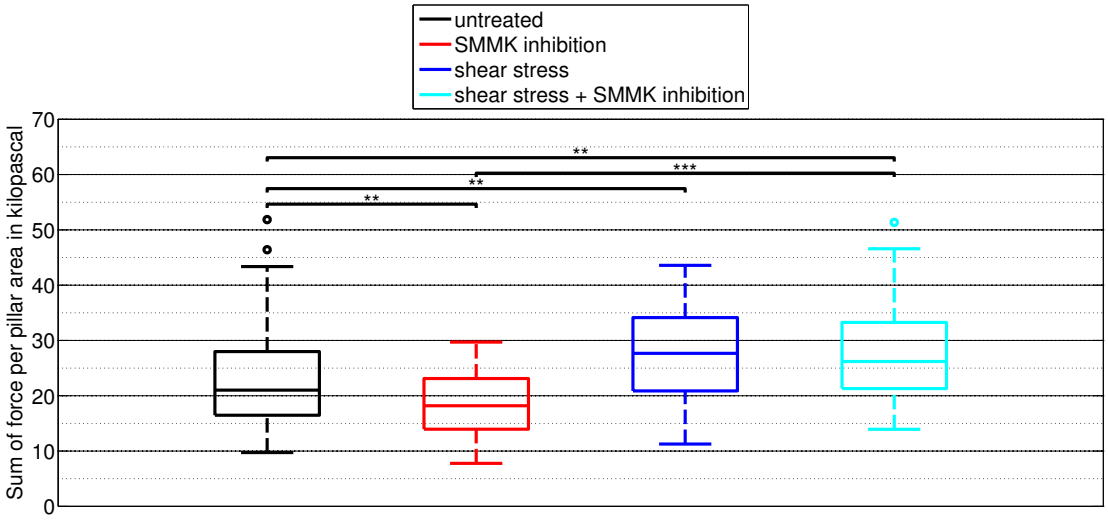


Figure 73: Boxplots of the cell traction forces for MLO-Y4 cells under static conditions, under static conditions with SMMK inhibition, under shear stress and under shear stress with SMMK inhibition.

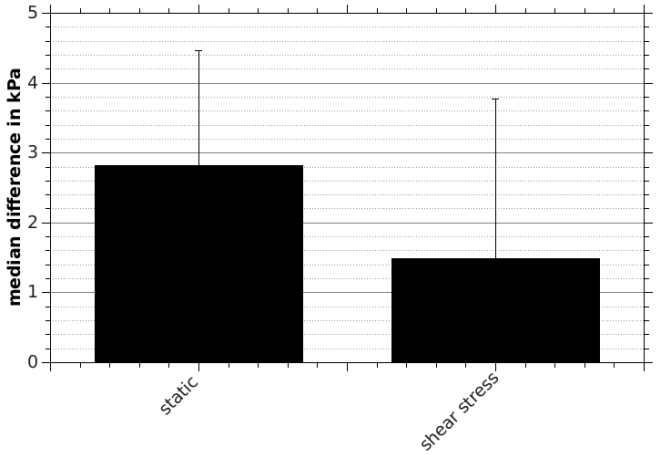


Figure 74: Absolute difference of the median values for MLO-Y4 cells for SMMK inhibition and untreated state under static and shear stress conditions. Error bars represent the standard error of the median.

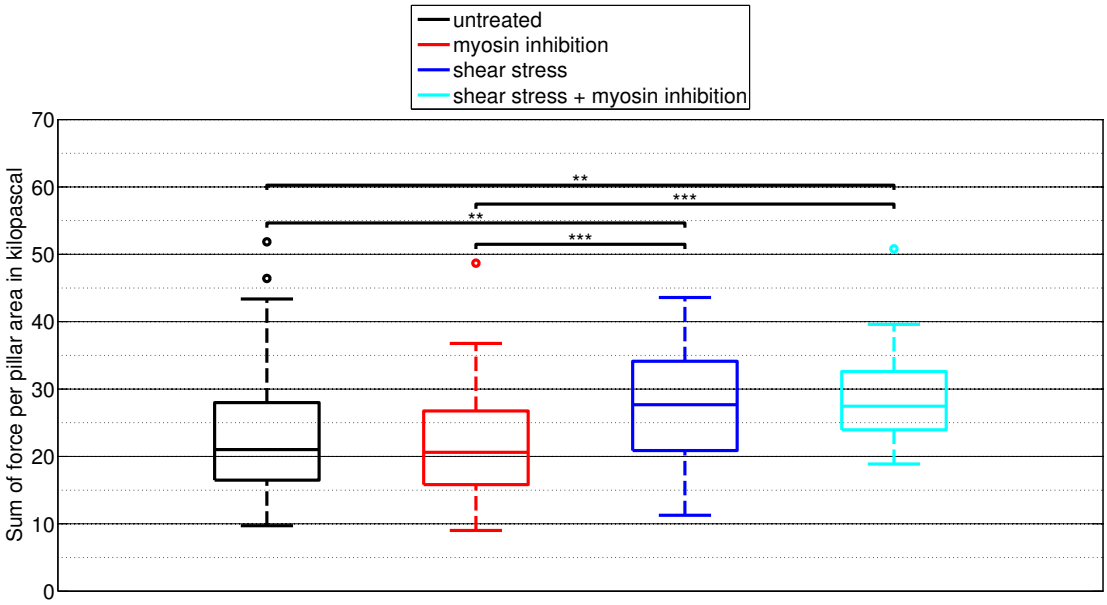


Figure 75: Boxplots of the cell traction forces for MLO-Y4 cells under static conditions, under static conditions with non-muscle myosin II inhibition, under shear stress and under shear stress with non-muscle myosin II inhibition.

Figure 76 shows the micropost displacement direction for MLO-Y4 cells under static conditions and shear stress and the absolute difference. There is a trend for a shift of micropost displacement with the flow direction under shear stress (no significance).

Figure 77 shows the micropost displacement direction for MLO-Y4 cells under static conditions und shear stress, both with and without SMMK inhibition (Static and SMMK inhibition: 0-60 vs 60-120 p=0.03, 60-120 vs 120-180 p=0.03; shear stress and SMMK inhibition: 0-60 vs 60-120 p=0.002, 60-120 vs 120-180 p=0.05). The difference for SMMK inhibition to the untreated state for static and shear stress conditions is shown at the bottom. There is a shift to perpendicular micropost displacement visible after SMMK inhibition and the difference shows a shift with the flow.

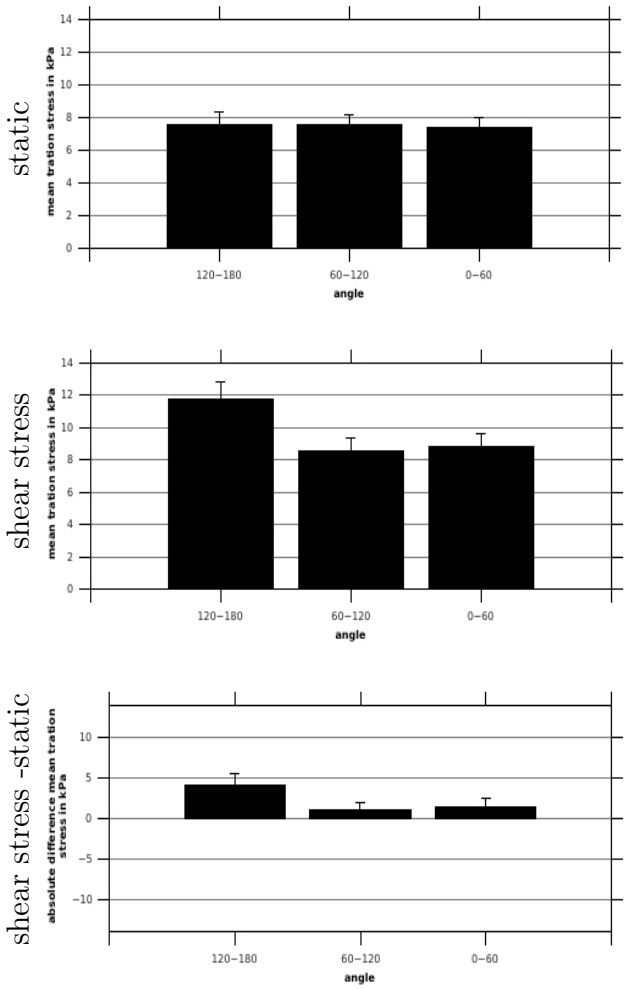


Figure 76: Micropost displacement direction for MLO-Y4 cells under static conditions and with shear stress and the absolute difference. Error bars represent the standard error of the mean.

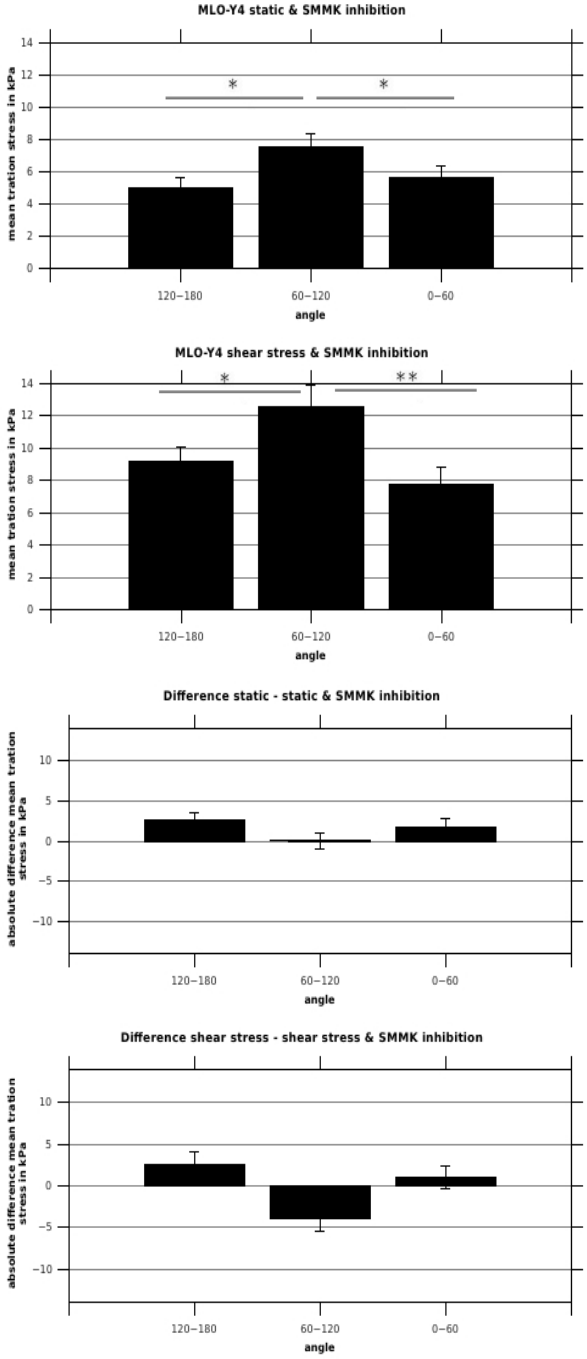


Figure 77: Micropost displacement direction for MLO-Y4 cells under static conditions and with shear stress, both with SMMK inhibition. The absolute differences between SMMK inhibited and untreated state are shown at the bottom. Error bars represent the standard error of the mean.

Figure 78 shows the resulting micropost displacement for MLO-Y4 cells under static and shear stress conditions, both with and without SMMK inhibitition. The resulting micropost displacement was first calculated for each cell and then the mean value over all cells was built. The results show the same trend as for the micropost displacement directions from figure 76 and 77. Table 6 shows the difference between shear stress and static conditions and shear stress conditions with and without SMMK inhibition.

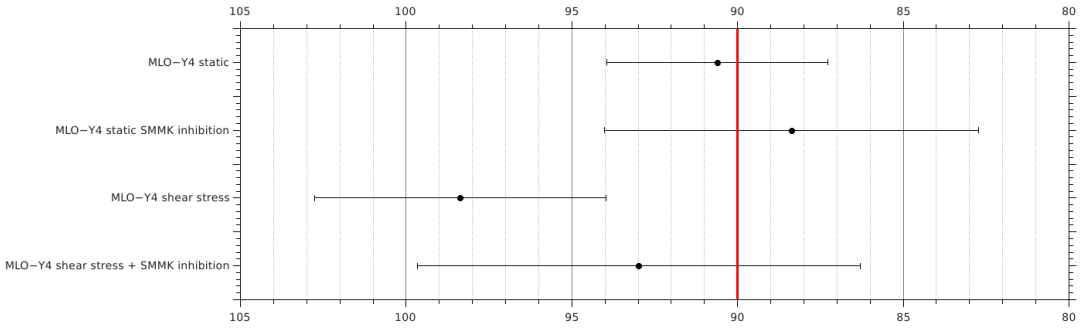


Figure 78: Resulting micropost displacement direction for MLO-Y4 cells under static conditions and shear stress, both with and without SMMK inhibition. Shown is the mean value with the standard error of the mean. The x- axis shows the coordinates in degrees.

Table 6: Difference of resulting micropost displacement direction for MLO-Y4 cells from Figure 78

| **Conditions** | **Difference in degrees** |
|---|---|
| difference shear stress - static | 7.76 ± 5.51 |
| difference shear stress - (shear stress + myosin inhibition) | 5.39 ± 7.99 |

Figure 79 shows fluorescence images of paxillin stained MLO-Y4 cells on microposts. The focal adhesions under static untreated conditions show an arc like shape, wrapped around the micropost outline. After SMMK inhibition the focal adhesions have the same shape. Under shear stress the shape is more stripe like and the focal adhesions lie on top of the microposts, the same after SMMK inhibition under shear stress.

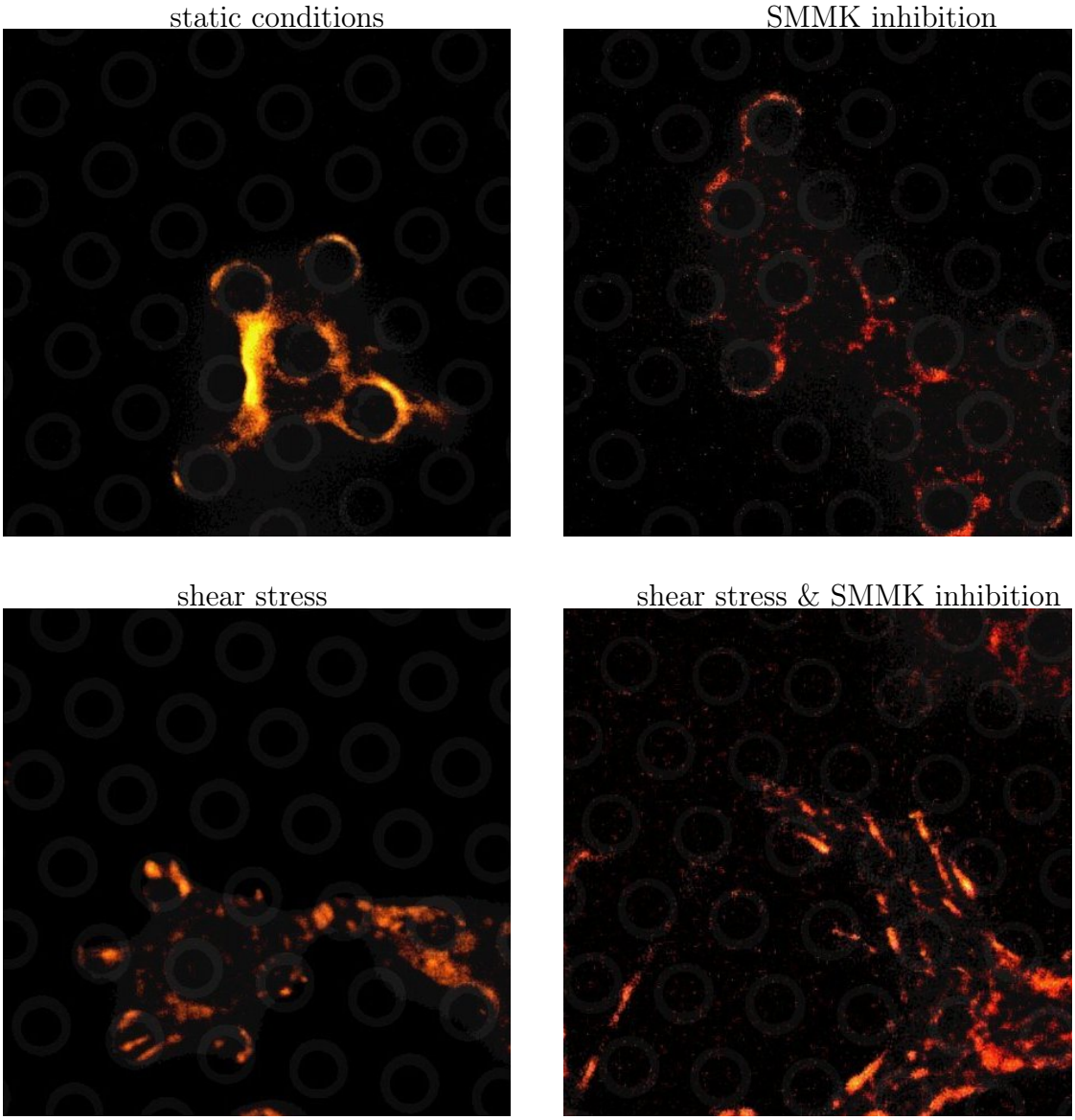


Figure 79: Paxillin staining of MLO-Y4 cells on microposts under static conditions and under shear stress with and without SMMK inhibition.

Figure 80 shows focal adhesion area, circularity and angle for MLO-Y4 cells for (1) static conditions, (2) static conditions with SMMK inhibition, (3) shear stress and (4) shear stress with SMMK inhibition and the difference shear stress - static conditions (5) and shear stress - shear stress and SMMK inhibition. There is a trend that the area is larger after SMMK inhibition under static conditions, and smaller under shear stress. The circularity is slightly larger under shear stress conditions. The angle of the focal adhesions is transverse to the flow. For circular focal adhesions the angle cannot be determined correctly.

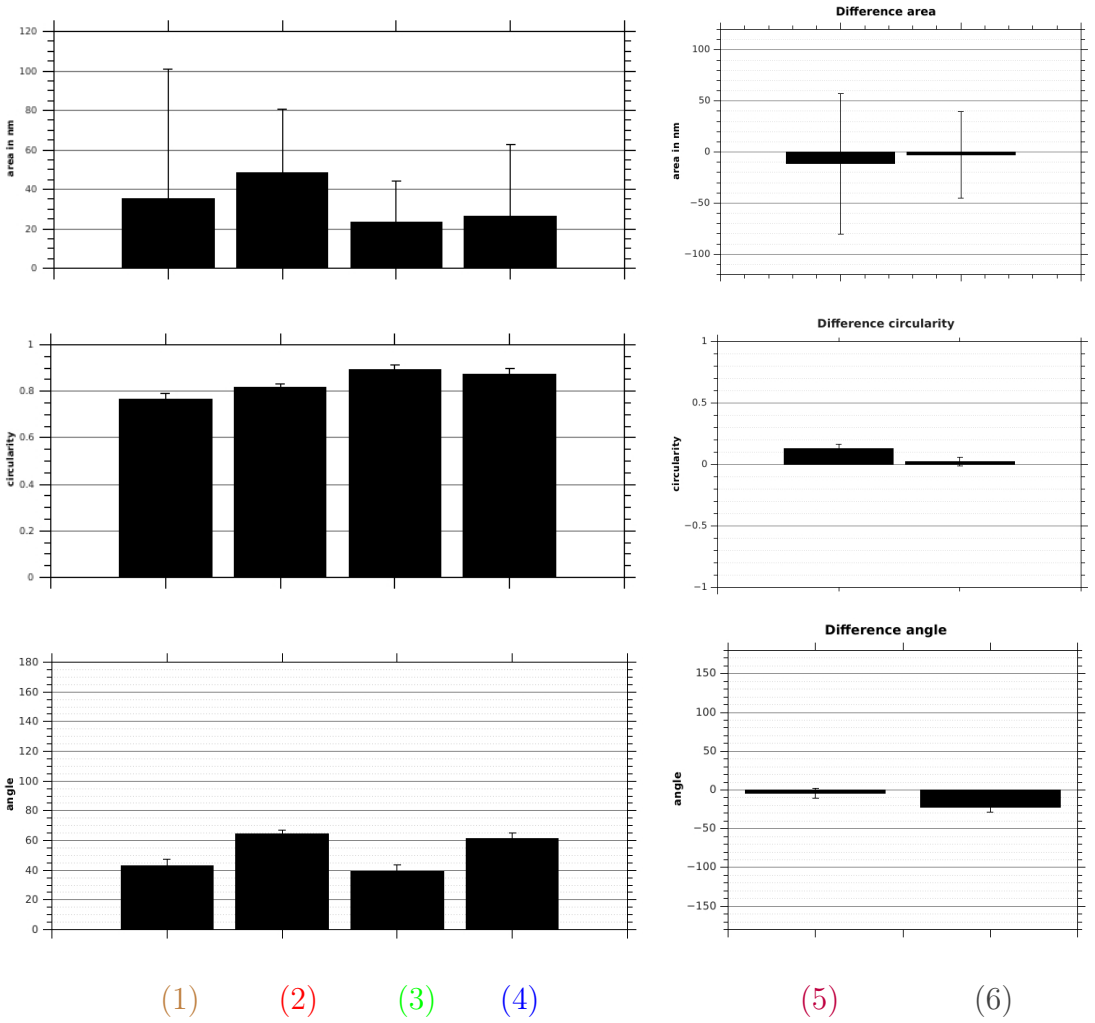


Figure 80: Focal adhesion area (top), circularity (middle) and angle (bottom) for MLO-Y4 cells for (1) static conditions, (2) static conditions with SMMK inhibition, (3) shear stress, (4) shear stress with SMMK inhibition, (5) difference of shear stress - static conditions and (6) difference shear stress and shear stress - SMMK inhibition. Shown are the median values with the standard error of the median.

Figure 81 shows the relative cell height in $\mu$m compared to static conditions for SMMK inhibition, shear stress application and shear stress with SMMK inhibition. The cell height is reduced after SMMK inhibition under static and under shear stress conditions. There is an increase in cell height with shear stress application.

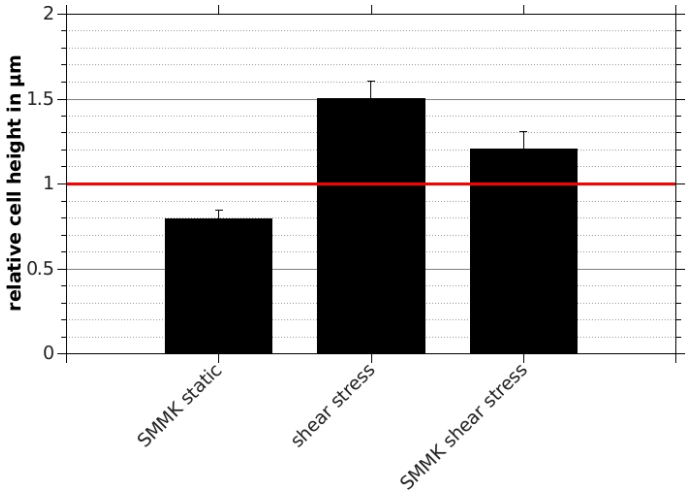


Figure 81: Relative cell height of MLO-Y4 cells for SMMK inhibition, shear stress and shear stress with SMMK inhibition compared to static conditions. The error bars represent the standard error of the median.

### 8.1.2 Vimentin disruption

Figure 82 shows traction forces for MLO-Y4 cells under static conditions compared to cells after vimentin disruption (n=80). There is no significant difference.

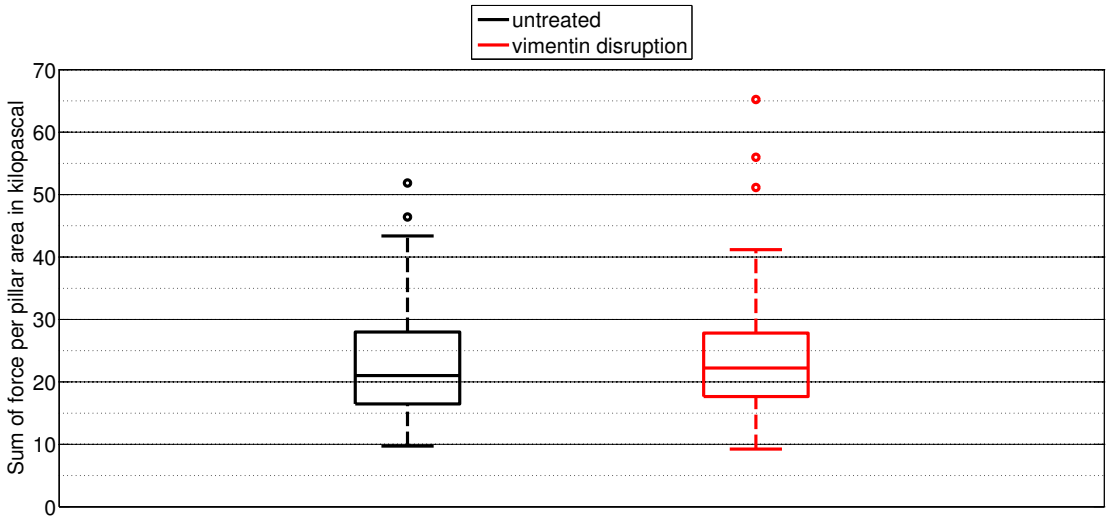


Figure 82: Boxplots of the cell traction forces for MLO-Y4 cells under static conditions and with vimentin disruption.

Figure 83 shows fluorescence images of paxillin stained MLO-Y4 cells under static conditions with and without vimentin disruption. There are still focal adhesions observable after vimentin disruption, although they seem to be more stripe like and not so much wrapped arround the micropost outlines as under untreated conditions.

Figure 84 shows focal adhesion area and circularity for MLO-Y4 cells under static conditions with and without vimentin disruption. The focal adhesion area after vimentin disruption is increased and the shape is more elongated.

Figure 85 shows the relative cell height of MLO-Y4 cells after vimentin disruption compared to the untreated state. There is a reduction in cell height after vimentin disruption visible.

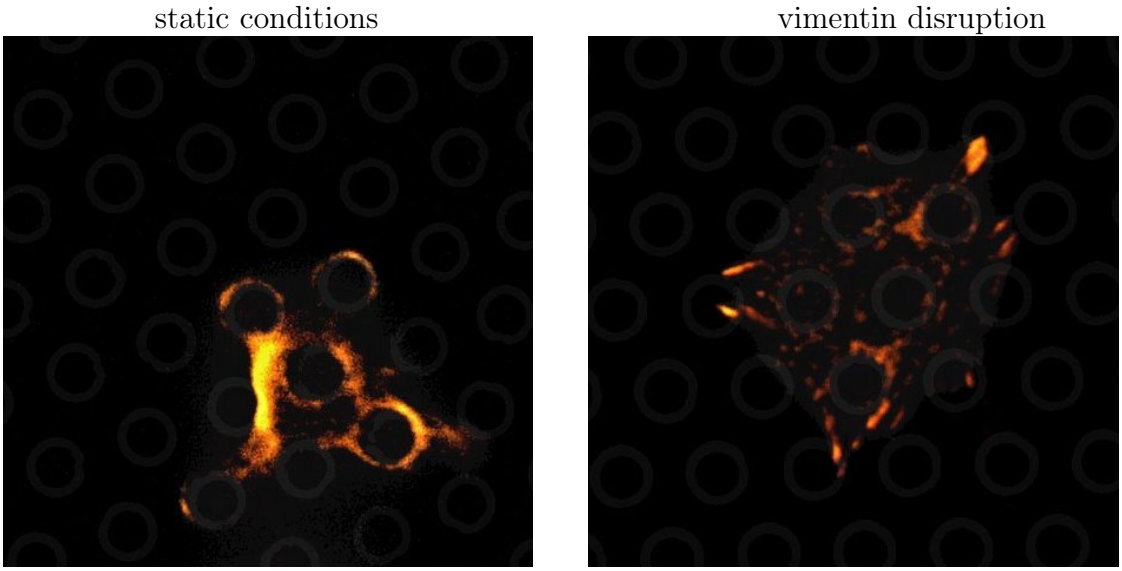


Figure 83: Paxillin staining of MLO-Y4 cells on microposts under static untreated conditions and with vimentin disruption.

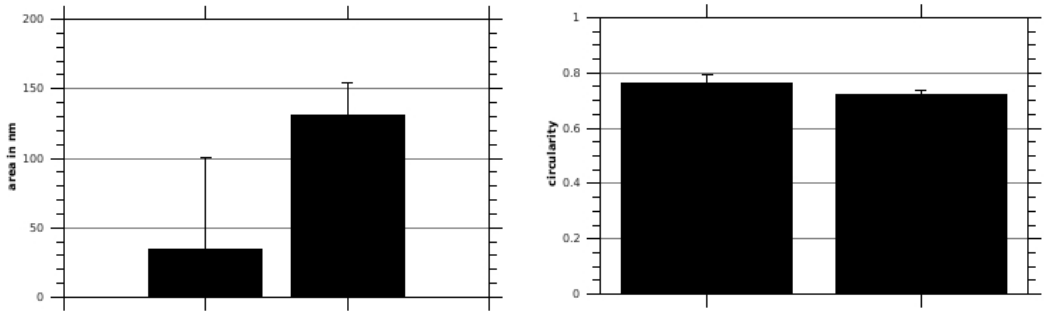


Figure 84: Focal adhesion area (left) and circularity (right) for MLO-Y4 cells static (1) and with vimentin disruption (2). Shown are the median values with the standard error of the median.

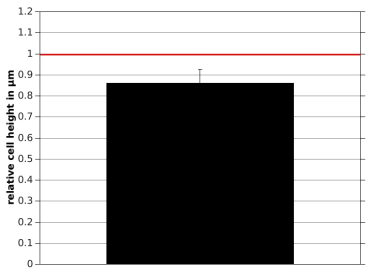


Figure 85: Relative cell height of MLO-Y4 cells after vimentin disruption compared to the untreated state. The error bar represents the standard error of the median.

## 8.2 Discussion

Osteocytes are known to sense and react to fluid shear stress occurring in the canalicular system in bones[85]. To study the traction force generation under the influence of external shear stress, we measured traction forces under static conditions and under the influence of external shear stress, using the osteocyte-like cell line MLO-Y4.
A large amount of muscle-related proteins were detected in osteocytes[124] and a previous study by Baik[7] postulates that phasic contractility in MLO-Y4 cells might be mediated through smooth muscle myosin. To examine that finding, and to test if smooth muscle myosin might have an influence on traction force generation in MLO-Y4 cells, we inhibited smooth muscle myosin kinase (SMMK) under static conditions, as well as under shear stress. In addition, we studied the influence of intermediate filaments, respectively vimentin, on traction force generation.

**The influence of external shear stress and SMMK on traction force generation**
We observed that MLO-Y4 cells react to fluid shear stress with an increase in traction forces. Osteocytes are known to act as mechanosensors and previous studies already demonstrated a sensitivity of MLO-Y4 cells to fluid flow[4][18][26][81][133][190]. In vitro studies showed upregulation of cell proliferation and release of paracrine factors after inducing fluid shear stress[76] as well as an active response by an increase in gene expression and higher expression of the avb3 integrins[25][190]. Also integrin-associated molecules vinculin, OPN and CD44 were found to be upregulated in MLO-4 cells after fluid flow shear stress[190]. Ponik et al. showed that after 24 hours of unidirectional flow robust, organised stress fibers were formed under a shear stress of 0.8Pa[133]. The magnitude of fluidic shear in bone tissues is around 0.8–3Pa[187]. We used unidirectional flow with a low pressure of 0.25Pa, that was still able to induce changes in traction forces after 12 hours of application, concluding that MLO-Y4 cells react with increased traction forces even to small shear stress magnitude.
The cell height is increased after shear stress application. Bacabac et al. demonstrated for MLO-Y4 cells, that a round cell shape was shown on the one hand to support a less stiff cytoskeleton than flat cell shape, and on the other hand to be much more mechanosensitive then a stretched out cell shape[6]. Previous studies found that osteocytes in vivo have a round morphology being placed in ellipsoidal lacunae, that are exposed to fluid flow[108][123]. They seem to respond to rather small strains, therefore implying that cells with a more three-dimensional

morphology have a higher mechanosensivity[6]. That correlates with the fact, that in our study MLO-Y4 cells react to rather small shear stress with an increase in traction forces.
Interestingly the focal adhesions show a different shape after shear stress application, with stripes forming on top of the microposts, in contrast to the arc like elongated structures formed around the micropost outlines under static conditions. The area is slightly reduced with shear stress application, with an increase in circularity, agreeing with the observed shape. There is not necessarily a correlation between the focal adhesion structure or area and force magnitude, since we saw the opposite behaviour for other cell types (see chapter I and II). However, the different structures can point to a different pathway involved in focal adhesion assembly for static and shear stress conditions, leading to different formation of focal adhesions.
Smooth muscle myosin kinase phosphorylates Ser19 in smooth muscle light chains and therefore acts as regulatory enzyme[126]. After inhibition of smooth muscle myosin kinase, traction forces are reduced under static conditions, but not under shear stress in our measurements. This suggests an influence on traction force generation under static conditions, but no involvement under shear stress triggered conditions.
Under static conditions with SMMK inhibition, focal adhesions show a slightly larger area, whereas the circularity is unchanged. The cell height is reduced. After SMMK inhibition under shear stress focal adhesions are unchanged, whereas the cell height is reduced as under SMMK inhibition under static conditions. Therefore SMMK seems to trigger traction forces and focal adhesion assembly under static conditions, but not under shear stress. However, the height is influenced under both conditions, suggesting that the cytoskeleton might be influenced in some way by SMMK, whereas under shear stress another pathway might be involved that is responsible for traction force generation.
There is a shift of micropost displacement direction with the flow direction, that seems to be partly triggered by smooth muscle myosin kinase. After inhibition of SMMK, there is a stronger perpendicular bending of microposts observable. Goldman et al. showed that fluid shear stress regulates migration of smooth muscle cells by mediation of myosin light chain kinase[61]. We suppose, that under shear stress active migration of MLO-Y4 cells against the flow takes place, pulling more microposts with the flow, whereas after SMMK inhibition, migration is reduced, but active contraction still takes place. The visible increase in traction forces thus has to be triggered by another mechanism under shear stress. Since we did not see a reduction of forces after non-muscle myosin II inhibition with blebbistatin as well under static as shear stress conditions, other

motor proteins might be involved. Since blebbistatin does not inhibit myosin superfamily members from classes I, V, and X[97], one has to consider the possibility, that one of these myosin might be involved in force generation in this case. Zhang et al. identified myosin X as integrin binding protein and suggest that the interaction with integrins might serve to recruit integrins to adhesive site formation and therefore could function as stabilisator of filipodia structures[197]. Myosin X was also found to play an important role in the integration of actin and microtubule cytoskeleton to position the centrosomes and mitotic spindles in cells[89]. Billington et al. found that myosin 18$\alpha$ coassembles with non-muscle myosin II into mixed bipolar filaments in vitro[16]. They suggest, that myosin 18$\alpha$ might link together adjacent stress fibers and serve to stabilize stress fibers under low levels of active non-muscle myosin II heads[16]. Findings like these impose, that other molecular motors than non-muscle myosin II or smooth muscle myosin migth play a role in force generation on the substrate.

**The influence of vimentin on traction force generation**

Vimentin disruption has no effect on traction force magnitude in our measurements, suggesting no active involvement in traction force generation. However, also a compensatory effect might be considered, for example through enhanced stress fiber formation. Focal adhesions seem more stripe like and the area is largely increased after vimentin disruption. The cell height is slightly reduced. Previous studies showed, that missing vimentin leads to more robust focal adhesions and strongly bundled stress fibers[188], which might explain our observed results.

# 9 Summary and Outlook

We developed an analysis method for micropost array based cell traction force microscopy and applied it to different cell types under different conditions.
For the detection of microposts in simple phase contrast images, we used the circular Hough transformation. We tested two different methods of image taking and analysis, and concluded, that although the trypsin method is more accurate, the method using a hexagonal grid provides a comparable accuracy and is more time efficient. We used this method for all further measurements and tested the accuracy under different parameter settings used for the Hough detection to determine the optimal parameter setting with the lowest error. Our results yielded comparable detection accuracy as in previous studies by other groups. Regarding the fact that we use rather stiff microposts, the detection limit can be pushed even further using softer microposts that show a larger displacement. Taken together we established a cost and time efficient and easy to use method for cell traction force microscopy, using PDMS micropost arrays and Hough transformation of circular objects together with an ideal hexagonal grid for displacement detection.

With our established method we performed cell traction force measurements on different cell types and changed several parameters to test the influence on traction forces.
In the first application we analysed differences in force generation regarding distinct integrin types. By manipulating either environmental cues or cell internal parameters we could link the observed effects to the specific integrin type. Our results for the traction forces are in agreement with reported values. On stiffer substrates with the same geometry the traction forces were higher for all cell types. On softer substrates with higher micropost density, but a smaller micropost radius and therefore the same area as the stiff substrates, the traction forces were higher, concluding that micropost density rather than stiffness and spread area has an influence on traction forces. By using different micropost density and stiffness, these results can be tested more detailed.
We found that while a5b1 type integrins generate larger forces than av-class integrins, the effect was opposed after external shear stress application. Since we did not observe a major role of actomyosin in force generation for av-class

integrins, but a strong involvement after shear stress application, we conclude a triggering of actomyosin after external force application on the av-class cells. After vimentin disruption traction forces are unchanged for a5b1 and a5b1/avb3 cells, but increase for avb3 cells. We propose that vimentin does not play a major role in traction force generation in this case, or that a compensation takes place, leading to an increase of traction forces.
Future measurements might include inhibition of proteins of the focal adhesion complex to unravel the complex interplay of cell components and their influence on traction forces in terms of the individual integrin.

In the second application we compared the two epithelial lung cell lines R3/1 and A549. We applied external shear stress to simulate mechanical stimulation of the cells, as it might occur for their primary analogues, e.g. during liquid plug formation. We observed that R3/1 cells do not react with an increase in traction forces to external shear stress in contrast to A549 cells. These result suggests that R3/1 cells are more robust against shear stress, because the purpose of their primary analogue is to build the main part of the alveolus whereas the type II cells react sensitive, because of their regulatory function. Myosin inhibition under shear stress has no effect on traction forces of R3/1 cells, but there is a strong reduction of traction forces for A549 cells. Hence, shear stress seems to trigger a strong myosin upregulation in A549 cells. Under static conditions traction forces are reduced for both cell types after myosin inhibition, with a larger effect on R3/1 cells, supposing that myosin plays a role in traction force generation for both cell lines under static conditions. Vimentin disruption reduces traction forces for both cell types. Regarding the opposite effect observed from the fibroblasts in the previous chapter, we suppose a cell type specific difference between fibroblasts and epithelial cells, that seems to influence traction force generation differently during the absence of vimentin, in the special case of our setup.
For further studies, testing the surfactant release and the correlation with traction forces under different conditions might help gaining inside, how the force generating apparatus is involved in the physiological relevant function of alveolar type II cells.

In the third application we analysed the osteocyte-like cell line MLO-Y4. We observed that MLO-Y4 cells react to fluid shear stress with an increase in traction forces. After inhibition of smooth muscle myosin kinase, traction forces are reduced under static conditions, but not under shear stress in our measurements. This suggests an influence on traction force generation under static conditions, but no involvement under shear stress triggered conditions.

Since non-muscle myosin II inhibition showed no reduction of traction fores under static and shear stress conditions, we propose that other myosins may have an influence on traction force generation under shear stress. This has to be tested in further measurements. Vimentin disruption has no effect on traction force magnitude, suggesting no active involvement in force generation or a compensatory effect.

As conclusion we successfully established a traction force microscopy method and applied it to different cell types while changing internal cell parameters and external conditions. This method can be applied to other cell types and adapted to the according hypothesis. There are many parameters that can be varied, from micropost stiffness and density, to protein inhibition and changing external conditions. The broad applicability and usefulness of this method promises plenty of exciting future studies, thus justifying further research and improvements.

# List of Figures

# List of Tables

# Bibliography

[1] *Instructions sticky-Slide I Luer (PDF), Version 2.0 (2016-05-31), ibidi GmbH.*

[2] K. A. Addae-Mensah, N. J. Kassebaum, M. J. Bowers II, R. S. Reiserer, S. J. Rosenthal, P. E. Moore, and J. P. Wikswo. A flexible, quantum dot-labeled cantilever post array for studying cellular microforces. *Sensors and Actuators A: Physical*, 136(1):385–397, 2007.

[3] R. Aguilar-Cuenca, A. Juanes-García, and M. Vicente-Manzanares. Myosin ii in mechanotransduction: master and commander of cell migration, morphogenesis, and cancer. *Cellular and Molecular Life Sciences*, 71(3):479–492, 2014.

[4] A. Alford, C. Jacobs, and H. Donahue. Oscillating fluid flow regulates gap junction communication in osteocytic mlo-y4 cells by an erk1/2 map kinase-dependent mechanism. *Bone*, 33(1):64–70, 2003.

[5] D. Armani, C. Liu, and N. Aluru. Re-configurable fluid circuits by pdms elastomer micromachining. In *Micro Electro Mechanical Systems, 1999. MEMS'99. Twelfth IEEE International Conference on*, pages 222–227. Ieee, 1999.

[6] R. G. Bacabac, D. Mizuno, C. F. Schmidt, F. C. MacKintosh, J. J. Van Loon, J. Klein-Nulend, and T. H. Smit. Round versus flat: bone cell morphology, elasticity, and mechanosensing. *Journal of biomechanics*, 41(7):1590–1598, 2008.

[7] A. D. Baik. *Application of a Novel Quasi-3D Microscopy Technique to Investigate Early Osteocyte Mechanotransduction Events*. PhD thesis, Columbia University Academic Commons, 2013.

[8] E. L. Baker and M. H. Zaman. The biomechanical integrin. *Journal of biomechanics*, 43(1):38–44, 2010.

[9] N. Q. Balaban, U. S. Schwarz, D. Riveline, P. Goichberg, G. Tzur, I. Sabanay, D. Mahalu, S. Safran, A. Bershadsky, L. Addadi, et al. Force and focal adhesion assembly: a close relationship studied using elastic micropatterned substrates. *Nature cell biology*, 3(5):466–472, 2001.

[10] C. Ballestrem, B. Hinz, B. A. Imhof, and B. Wehrle-Haller. Marching at the front and dragging behind differential $\alpha$v$\beta$3-integrin turnover regulates focal adhesion behavior. *The Journal of cell biology*, 155(7):1319–1332, 2001.

[11] G. Bar, L. Delineau, R. Brandsch, M. Bruch, and M.-H. Whangbo. Importance of the indentation depth in tapping-mode atomic force microscopy study of compliant materials. *Applied Physics Letters*, 75(26):4198–4200, 1999.

[12] N. Batra, S. Burra, A. J. Siller-Jackson, S. Gu, X. Xia, G. F. Weber, D. DeSimone, L. F. Bonewald, E. M. Lafer, E. Sprague, et al. Mechanical stress-activated integrin $\alpha5\beta1$ induces opening of connexin 43 hemichannels. *Proceedings of the National Academy of Sciences*, 109(9):3359–3364, 2012.

[13] K. A. Beningo, M. Dembo, I. Kaverina, J. V. Small, and Y.-l. Wang. Nascent focal adhesions are responsible for the generation of strong propulsive forces in migrating fibroblasts. *The Journal of cell biology*, 153(4):881–888, 2001.

[14] K. A. Beningo and Y.-L. Wang. Flexible substrata for the detection of cellular traction forces. *Trends in cell biology*, 12(2):79–84, 2002.

[15] A. M. Bilek, K. C. Dee, and D. P. Gaver. Mechanisms of surface-tension-induced epithelial cell damage in a model of pulmonary airway reopening. *Journal of Applied Physiology*, 94(2):770–783, 2003.

[16] N. Billington, J. R. Beach, S. M. Heissler, K. Remmert, S. Guzik-Lendrum, A. Nagy, Y. Takagi, L. Shao, D. Li, Y. Yang, et al. Myosin 18a coassembles with nonmuscle myosin 2 to form mixed bipolar filaments. *Current Biology*, 25(7):942–948, 2015.

[17] F. Blank, B. M. Rothen-Rutishauser, S. Schurch, and P. Gehr. An optimized in vitro model of the respiratory tract wall to study particle cell interactions. *Journal of aerosol medicine*, 19(3):392–405, 2006.

[18] L. F. Bonewald. Establishment and characterization of an osteocyte-like cell line, mlo-y4. *Journal of bone and mineral metabolism*, 17(1):61–65, 1999.

[19] L. F. Bonewald and M. L. Johnson. Osteocytes, mechanosensing and wnt signaling. *Bone*, 42(4):606–615, 2008.

[20] K. Burton, J. H. Park, and D. L. Taylor. Keratocytes generate traction forces in two phases. *Molecular biology of the cell*, 10(11):3745–3769, 1999.

[21] F. Buss, J. Kendrick-Jones, C. Lionne, A. E. Knight, G. P. Côté, and J. P. Luzio. The localization of myosin vi at the golgi complex and leading edge of fibroblasts and its phosphorylation and recruitment into membrane ruffles of a431 cells after growth factor stimulation. *The Journal of cell biology*, 143(6):1535–1545, 1998.

[22] J. P. Butler, I. M. Tolić-Nørrelykke, B. Fabry, and J. J. Fredberg. Traction fields, moments, and strain energy that cells exert on their surroundings. *American Journal of Physiology-Cell Physiology*, 282(3):C595–C605, 2002.

[23] J. P. Califano and C. A. Reinhart-King. Substrate stiffness and cell area predict cellular traction stresses in single cells and cells in contact. *Cellular and molecular bioengineering*, 3(1):68–75, 2010.

[24] C.-W. Chang and S. Kumar. Differential contributions of nonmuscle myosin ii isoforms and functional domains to stress fiber mechanics. *Scientific reports*, 5, 2015.

[25] Y.-H. Chang, R. Brady, O. Brennan, and F. O'Brien. A 3d environment influences osteocyte function. In *BMC Proceedings*, number Suppl 1, page A7. BioMed Central Ltd, 2015.

[26] B. Cheng, S. Zhao, J. Luo, E. Sprague, L. F. Bonewald, and J. X. Jiang. Expression of functional gap junctions and regulation by fluid flow in osteocyte-like mlo-y4 cells. *Journal of Bone and Mineral Research*, 16(2):249–259, 2001.

[27] M. Coué, S. L. Brenner, I. Spector, and E. D. Korn. Inhibition of actin polymerization by latrunculin a. *FEBS letters*, 213(2):316–318, 1987.

[28] T. R. Cox and J. T. Erler. Remodeling and homeostasis of the extracellular matrix: implications for fibrotic diseases and cancer. *Disease models & mechanisms*, 4(2):165–178, 2011.

[29] E. H. Danen, J. van Rheenen, W. Franken, S. Huveneers, P. Sonneveld, K. Jalink, and A. Sonnenberg. Integrins control motile strategy through a rho–cofilin pathway. *The Journal of cell biology*, 169(3):515–526, 2005.

[30] M. Dauphin, C. Barbe, S. Lemaire, B. Nawrocki-Raby, E. Lagonotte, G. Delepine, P. Birembaut, C. Gilles, and M. Polette. Vimentin expression predicts the occurrence of metastases in non small cell lung carcinomas. *Lung cancer*, 81(1):117–122, 2013.

[31] S. Deguchi, T. Ohashi, and M. Sato. Tensile properties of single stress fibers isolated from cultured vascular smooth muscle cells. *Journal of biomechanics*, 39(14):2603–2610, 2006.

[32] M. Dembo and Y.-L. Wang. Stresses at the cell-to-substrate interface during locomotion of fibroblasts. *Biophysical journal*, 76(4):2307–2316, 1999.

[33] J. S. Desgrosellier and D. A. Cheresh. Integrins in cancer: biological implications and therapeutic opportunities. *Nature Reviews Cancer*, 10(1):9–22, 2010.

[34] D. E. Discher, P. Janmey, and Y.-l. Wang. Tissue cells feel and respond to the stiffness of their substrate. *Science*, 310(5751):1139–1143, 2005.

[35] M. Dogterom, J. W. Kerssemakers, G. Romet-Lemonne, and M. E. Janson. Force generation by dynamic microtubules. *Current opinion in cell biology*, 17(1):67–74, 2005.

[36] N. J. Douville, P. Zamankhan, Y.-C. Tung, R. Li, B. L. Vaughan, C.-F. Tai, J. White, P. J. Christensen, J. B. Grotberg, and S. Takayama. Combination of fluid and solid mechanical stresses contribute to cell death and detachment in a microfluidic alveolar model. *Lab on a chip*, 11(4):609–619, 2011.

[37] O. Du Roure, A. Saez, A. Buguin, R. H. Austin, P. Chavrier, P. Siberzan, and B. Ladoux. Force mapping in epithelial cell migration. *Proceedings of the National Academy of Sciences of the United States of America*, 102(7):2390–2395, 2005.

[38] B. Eckes, D. Dogic, E. Colucci-Guyon, N. Wang, A. Maniotis, D. Ingber, A. Merckling, F. Langa, M. Aumailley, A. Delouvée, et al. Impaired mechanical stability, migration and contractile capacity in vimentin-deficient fibroblasts. *Journal of cell science*, 111(13):1897–1907, 1998.

[39] A. Elosegui-Artola, E. Bazellières, M. D. Allen, I. Andreu, R. Oria, R. Sunyer, J. J. Gomm, J. F. Marshall, J. L. Jones, X. Trepat, et al. Rigidity sensing and adaptation through regulation of integrin types. *Nature materials*, 13(6):631–637, 2014.

[40] A. Engler, L. Bacakova, C. Newman, A. Hategan, M. Griffin, and D. Discher. Substrate compliance versus ligand density in cell on gel responses. *Biophysical journal*, 86(1):617–628, 2004.

[41] S. Etienne-Manneville and A. Hall. Integrin-mediated activation of cdc42 controls cell polarity in migrating astrocytes through pkc$\zeta$. *Cell*, 106(4):489–498, 2001.

[42] V. Fincham and M. Frame. The catalytic activity of src is dispensable for translocation to focal adhesions but controls the turnover of these structures during cell motility. *The EMBO journal*, 17(1):81–92, 1998.

[43] E. S. Folker, C. Östlund, G. G. Luxton, H. J. Worman, and G. G. Gundersen. Lamin a variants that cause striated muscle disease are defective in anchoring transmembrane actin-associated nuclear lines for nuclear movement. *Proceedings of the National Academy of Sciences*, 108(1):131–136, 2011.

[44] J. C. Friedland, M. H. Lee, and D. Boettiger. Mechanically activated integrin switch controls $\alpha 5\beta 1$ function. *Science*, 323(5914):642–644, 2009.

[45] J. Fu, Y.-K. Wang, M. T. Yang, R. A. Desai, X. Yu, Z. Liu, and C. S. Chen. Mechanical regulation of cell function with geometrically modulated elastomeric substrates. *Nature methods*, 7(9):733–736, 2010.

[46] D. Fuard, T. Tzvetkova-Chevolleau, S. Decossas, P. Tracqui, and P. Schiavone. Optimization of poly-di-methyl-siloxane (pdms) substrates for studying cellular adhesion and motility. *Microelectronic Engineering*, 85(5):1289–1293, 2008.

[47] C. G. Galbraith, K. M. Yamada, and M. P. Sheetz. The relationship between force and focal complex development. *The Journal of cell biology*, 159(4):695–705, 2002.

[48] N. D. Gallant and A. J. García. Model of integrin-mediated cell adhesion strengthening. *Journal of biomechanics*, 40(6):1301–1309, 2007.

[49] A. Ganz, M. Lambert, A. Saez, P. Silberzan, A. Buguin, R. M. Mège, and B. Ladoux. Traction forces exerted through n-cadherin contacts. *Biology of the Cell*, 98(12):721–730, 2006.

[50] A. J. Garcia and N. D. Gallant. Stick and grip. *Cell biochemistry and biophysics*, 39(1):61–73, 2003.

[51] A. J. Garcia, F. Huber, and D. Boettiger. Force required to break $\alpha 5\beta 1$integrin-fibronectin bonds in intact adherent cells is sensitive to integrin activation state. *Journal of Biological Chemistry*, 273(18):10988–10993, 1998.

[52] M. L. Gardel, B. Sabass, L. Ji, G. Danuser, U. S. Schwarz, and C. M. Waterman. Traction stress in focal adhesions correlates biphasically with actin retrograde flow speed. *The Journal of cell biology*, 183(6):999–1005, 2008.

[53] M. L. Gardel, I. C. Schneider, Y. Aratyn-Schaus, and C. M. Waterman. Mechanical integration of actin and adhesion dynamics in cell migration. *Annual review of cell and developmental biology*, 26:315, 2010.

[54] N. Gavara, R. Sunyer, P. Roca-Cusachs, R. Farre, M. Rotger, and D. Navajas. Thrombin-induced contraction in alveolar epithelial cells probed by traction microscopy. *Journal of Applied Physiology*, 101(2):512–520, 2006.

[55] B. Geiger and A. Bershadsky. Exploring the neighborhood: adhesion-coupled cell mechanosensors. *Cell*, 110(2):139–142, 2002.

[56] P. C. Georges and P. A. Janmey. Cell type-specific response to growth on soft materials. *Journal of Applied Physiology*, 98(4):1547–1553, 2005.

[57] A. Ghanbari, V. Nock, S. Johari, R. Blaikie, X. Chen, and W. Wang. A micropillar-based on-chip system for continuous force measurement of c. elegans. *Journal of Micromechanics and Microengineering*, 22(9):095009, 2012.

[58] M. Ghibaudo, J.-M. Di Meglio, P. Hersen, and B. Ladoux. Mechanics of cell spreading within 3d-micropatterned environments. *Lab on a Chip*, 11(5):805–812, 2011.

[59] M. Ghibaudo, A. Saez, L. Trichet, A. Xayaphoummine, J. Browaeys, P. Silberzan, A. Buguin, and B. Ladoux. Traction forces and rigidity sensing regulate cell functions. *Soft Matter*, 4(9):1836–1843, 2008.

[60] C. Gilles, M. Polette, J.-M. Zahm, J.-M. Tournier, L. Volders, J.-M. Foidart, and P. Birembaut. Vimentin contributes to human mammary epithelial cell migration. *Journal of cell science*, 112(24):4615–4625, 1999.

[61] J. Goldman, L. Zhong, and S. Q. Liu. Negative regulation of vascular smooth muscle cell migration by blood shear stress. *American Journal of Physiology-Heart and Circulatory Physiology*, 292(2):H928–H938, 2007.

[62] E. R. Gomes, S. Jani, and G. G. Gundersen. Nuclear movement regulated by cdc42, mrck, myosin, and actin flow establishes mtoc polarization in migrating cells. *Cell*, 121(3):451–463, 2005.

[63] M. Gregor, S. Osmanagic-Myers, G. Burgstaller, M. Wolfram, I. Fischer, G. Walko, G. P. Resch, A. Jörgl, H. Herrmann, and G. Wiche. Mechanosensing through focal adhesion-anchored intermediate filaments. *The FASEB Journal*, 28(2):715–729, 2014.

[64] J. B. Grotberg. Respiratory fluid mechanics. *Physics of Fluids (1994-present)*, 23(2):021301, 2011.

[65] Y. Gruenbaum and U. Aebi. Intermediate filaments: a dynamic network that controls cell mechanics. *F1000prime reports*, 6, 2014.

[66] G. G. Gundersen and H. J. Worman. Nuclear positioning. *Cell*, 152(6):1376–1389, 2013.

[67] S. J. Han, K. S. Bielawski, L. H. Ting, M. L. Rodriguez, and N. J. Sniadecki. Decoupling substrate stiffness, spread area, and micropost density: a close spatial relationship between traction forces and focal adhesions. *Biophysical journal*, 103(4):640–648, 2012.

[68] B. Harland, S. Walcott, and S. X. Sun. Adhesion dynamics and durotaxis in migrating cells. *Physical biology*, 8(1):015011, 2011.

[69] A. K. Harris, P. Wild, and D. Stopak. Silicone rubber substrata: a new wrinkle in the study of cell locomotion. *Science*, 208(4440):177–179, 1980.

[70] L. Havel, E. Kline, A. Salgueiro, and A. Marcus. Vimentin regulates lung cancer cell adhesion through a vav2–rac1 pathway to control focal adhesion kinase activity. *Oncogene*, 2014.

[71] P. Heil and J. P. Spatz. Lateral shear forces applied to cells with single elastic micropillars to influence focal adhesion dynamics. *Journal of Physics: Condensed Matter*, 22(19):194108, 2010.

[72] M. Hendrix, E. A. Seftor, R. Seftor, and K. T. Trevor. Experimental coexpression of vimentin and keratin intermediate filaments in human breast cancer cells results in phenotypic interconversion and increased invasive behavior. *The American journal of pathology*, 150(2):483, 1997.

[73] J. D. Hood and D. A. Cheresh. Role of integrins in cell invasion and migration. *Nature Reviews Cancer*, 2(2):91–100, 2002.

[74] P. Hotulainen and P. Lappalainen. Stress fibers are generated by two distinct actin assembly mechanisms in motile cells. *The Journal of cell biology*, 173(3):383–394, 2006.

[75] D. Huh, H. Fujioka, Y.-C. Tung, N. Futai, R. Paine, J. B. Grotberg, and S. Takayama. Acoustically detectable cellular-level lung injury induced by fluid mechanical stresses in microfluidic airway systems. *Proceedings of the National Academy of Sciences*, 104(48):18886–18891, 2007.

[76] J. M. Hum, R. N. Day, J. P. Bidwell, Y. Wang, and F. M. Pavalko. Mechanical loading in osteocytes induces formation of a src/pyk2/mbd2 complex that suppresses anabolic gene expression. 2014.

[77] D. E. Ingber, N. Wang, and D. Stamenović. Tensegrity, cellular biophysics, and the mechanics of living systems. *Reports on Progress in Physics*, 77(4):046603, 2014.

[78] S. Jalali, M. A. del Pozo, K.-D. Chen, H. Miao, Y.-S. Li, M. A. Schwartz, J. Y.-J. Shyy, and S. Chien. Integrin-mediated mechanotransduction requires its dynamic interaction with specific extracellular matrix (ecm) ligands. *Proceedings of the National Academy of Sciences*, 98(3):1042–1046, 2001.

[79] K. A. Jansen, D. M. Donato, H. E. Balcioglu, T. Schmidt, E. H. Danen, and G. H. Koenderink. A guide to mechanobiology: Where biology and physics meet. *Biochimica et Biophysica Acta (BBA)-Molecular Cell Research*, 2015.

[80] I. Johnston, D. McCluskey, C. Tan, and M. Tracey. Mechanical characterization of bulk sylgard 184 for microfluidics and microengineering. *Journal of Micromechanics and Microengineering*, 24(3):035017, 2014.

[81] M. A. Kamel, J. L. Picconi, N. Lara-Castillo, and M. L. Johnson. Activation of $\beta$-catenin signaling in mlo-y4 osteocytic cells versus 2t3 osteoblastic cells by fluid flow shear stress and pge 2: Implications for the study of mechanosensation in bone. *Bone*, 47(5):872–881, 2010.

[82] E. Kassianidou and S. Kumar. A biomechanical perspective on stress fiber structure and function. *Biochimica et Biophysica Acta (BBA)-Molecular Cell Research*, 2015.

[83] K. Khanafer, A. Duprey, M. Schlicht, and R. Berguer. Effects of strain rate, mixing ratio, and stress–strain definition on the mechanical behavior of the polydimethylsiloxane (pdms) material as related to its biological applications. *Biomedical microdevices*, 11(2):503–508, 2009.

[84] M. R. King. *Principles of cellular engineering: understanding the biomolecular interface*. Academic Press, 2011.

[85] J. Klein-Nulend, R. Bacabac, and A. Bakker. Mechanical loading and how it affects bone cells: the role of the osteocyte cytoskeleton in maintaining our skeleton. *Eur Cell Mater*, 24:278–91, 2012.

[86] M. Kovács, J. Tóth, C. Hetényi, A. Málnási-Csizmadia, and J. R. Sellers. Mechanism of blebbistatin inhibition of myosin ii. *Journal of Biological Chemistry*, 279(34):35557–35563, 2004.

[87] C. M. Kraning-Rush, J. P. Califano, and C. A. Reinhart-King. Cellular traction stresses increase with increasing metastatic potential. *PloS one*, 7(2):e32572, 2012.

[88] S. Kreis, H.-J. Schönfeld, C. Melchior, B. Steiner, and N. Kieffer. The intermediate filament protein vimentin binds specifically to a recombinant integrin $\alpha 2/\beta 1$ cytoplasmic tail complex and co-localizes with native $\alpha 2/\beta 1$ in endothelial cell focal adhesions. *Experimental cell research*, 305(1):110–121, 2005.

[89] M. Kwon, M. Bagonis, G. Danuser, and D. Pellman. Direct microtubule-binding by myosin-10 orients centrosomes toward retraction fibers and subcortical actin clouds. *Developmental cell*, 34(3):323–337, 2015.

[90] K. A. Lazopoulos and D. Stamenović. Durotaxis as an elastic stability phenomenon. *Journal of biomechanics*, 41(6):1289–1294, 2008.

[91] J. S. Lee, P. Panorchan, C. M. Hale, S. B. Khatau, T. P. Kole, Y. Tseng, and D. Wirtz. Ballistic intracellular nanorheology reveals rock-hard cytoplasmic stiffening response to fluid flow. *Journal of cell science*, 119(9):1760–1768, 2006.

[92] K. R. Legate, S. Takahashi, N. Bonakdar, B. Fabry, D. Boettiger, R. Zent, and R. Fässler. Integrin adhesion and force coupling are independently regulated by localized ptdins (4, 5) 2 synthesis. *The EMBO journal*, 30(22):4539–4553, 2011.

[93] R. E. Leube, M. Moch, and R. Windoffer. Intermediate filaments and the regulation of focal adhesion. *Current opinion in cell biology*, 32:13–20, 2015.

[94] I. Levental, P. C. Georges, and P. A. Janmey. Soft biological materials and their impact on cell function. *Soft Matter*, 3(3):299–306, 2007.

[95] B. Li, L. Xie, Z. C. Starr, Z. Yang, J.-S. Lin, and J. H.-C. Wang. Development of micropost force sensor array with culture experiments for determination of cell traction forces. *Cell motility and the cytoskeleton*, 64(7):509–518, 2007.

[96] S. Li, P. Butler, Y. Wang, Y. Hu, D. C. Han, S. Usami, J.-L. Guan, and S. Chien. The role of the dynamics of focal adhesion kinase in the mechanotaxis of endothelial cells. *Proceedings of the National Academy of Sciences*, 99(6):3546–3551, 2002.

[97] J. Limouze, A. F. Straight, T. Mitchison, and J. R. Sellers. Specificity of blebbistatin, an inhibitor of myosin ii. *Journal of Muscle Research & Cell Motility*, 25(4-5):337–341, 2004.

[98] G. L. Lin, D. M. Cohen, R. A. Desai, M. T. Breckenridge, L. Gao, M. J. Humphries, and C. S. Chen. Activation of beta 1 but not beta 3 integrin increases cell traction forces. *FEBS letters*, 587(6):763–769, 2013.

[99] M. Liu, A. K. Tanswell, and M. Post. Mechanical force-induced signal transduction in lung cells. *American Journal of Physiology-Lung Cellular and Molecular Physiology*, 277(4):L667–L683, 1999.

[100] C.-M. Lo, D. B. Buxton, G. C. Chua, M. Dembo, R. S. Adelstein, and Y.-L. Wang. Nonmuscle myosin iib is involved in the guidance of fibroblast migration. *Molecular biology of the cell*, 15(3):982–989, 2004.

[101] C.-M. Lo, H.-B. Wang, M. Dembo, and Y.-l. Wang. Cell movement is guided by the rigidity of the substrate. *Biophysical journal*, 79(1):144–152, 2000.

[102] M. P. López, F. Huber, I. Grigoriev, M. O. Steinmetz, A. Akhmanova, G. H. Koenderink, and M. Dogterom. Actin–microtubule coordination at growing microtubule ends. *Nature communications*, 5, 2014.

[103] M. Lorger, J. S. Krueger, M. O'Neal, K. Staflin, and B. Felding-Habermann. Activation of tumor cell integrin $\alpha v\beta 3$ controls angiogenesis and metastatic growth in the brain. *Proceedings of the National Academy of Sciences*, 106(26):10666–10671, 2009.

[104] J. Lübbe, M. Temmen, P. Rahe, A. Kühnle, and M. Reichling. Determining cantilever stiffness from thermal noise. *Beilstein journal of nanotechnology*, 4(1):227–233, 2013.

[105] S. K. Mahto, J. Tenenbaum-Katan, A. Greenblum, B. Rothen-Rutishauser, and J. Sznitman. Microfluidic shear stress-regulated surfactant secretion in alveolar epithelial type ii cells in vitro. *American Journal of Physiology-Lung Cellular and Molecular Physiology*, 306(7):L672–L683, 2014.

[106] A. M. Malek, S. L. Alper, and S. Izumo. Hemodynamic shear stress and its role in atherosclerosis. *Jama*, 282(21):2035–2042, 1999.

[107] R. McBeath, D. M. Pirone, C. M. Nelson, K. Bhadriraju, and C. S. Chen. Cell shape, cytoskeletal tension, and rhoa regulate stem cell lineage commitment. *Developmental cell*, 6(4):483–495, 2004.

[108] B. R. McCreadie and S. J. Hollister. Strain concentrations surrounding an ellipsoid model of lacunae and osteocytes. *Computer Methods in Biomechanics and Biomedical Engineering*, 1(1):61–68, 1997.

[109] M. Mendez, D. Restle, and P. Janmey. Vimentin enhances cell elastic behavior and protects against compressive stress. *Biophysical journal*, 107(2):314–323, 2014.

[110] M. G. Mendez, S.-I. Kojima, and R. D. Goldman. Vimentin induces changes in cell shape, motility, and adhesion during the epithelial to mesenchymal transition. *The FASEB Journal*, 24(6):1838–1851, 2010.

[111] S. W. Moore, P. Roca-Cusachs, and M. P. Sheetz. Stretchy proteins on stretchy substrates: the important elements of integrin-mediated rigidity sensing. *Developmental cell*, 19(2):194–206, 2010.

[112] J. T. Morgan, E. R. Pfeiffer, T. L. Thirkill, P. Kumar, G. Peng, H. N. Fridolfsson, G. C. Douglas, D. A. Starr, and A. I. Barakat. Nesprin-3 regulates endothelial cell morphology, perinuclear cytoskeletal architecture, and flow-induced polarization. *Molecular biology of the cell*, 22(22):4324–4334, 2011.

[113] S. Munevar, Y.-l. Wang, and M. Dembo. Traction force microscopy of migrating normal and h-ras transformed 3t3 fibroblasts. *Biophysical journal*, 80(4):1744–1757, 2001.

[114] S. Munevar, Y.-l. Wang, and M. Dembo. Regulation of mechanical interactions between fibroblasts and the substratum by stretch-activated ca2+ entry. *Journal of cell science*, 117(1):85–92, 2004.

[115] M. Murrell, P. W. Oakes, M. Lenz, and M. L. Gardel. Forcing cells into shape: the mechanics of actomyosin contractility. *Nature Reviews Molecular Cell Biology*, 16(8):486–498, 2015.

[116] M. P. Murrell, R. Voituriez, J.-F. Joanny, P. Nassoy, C. Sykes, and M. L. Gardel. Liposome adhesion generates traction stress. *Nature Physics*, 10(2):163–169, 2014.

[117] S. Na, F. Chowdhury, B. Tay, M. Ouyang, M. Gregor, Y. Wang, G. Wiche, and N. Wang. Plectin contributes to mechanical properties of living cells. *American Journal of Physiology-Cell Physiology*, 296(4):C868–C877, 2009.

[118] I. R. Nabi. The polarization of the motile cell. *Journal of Cell Science*, 112(12):1803–1811, 1999.

[119] E. A. Novikova and C. Storm. Contractile fibers and catch-bond clusters: a biological force sensor? *Biophysical journal*, 105(6):1336–1345, 2013.

[120] A. Nukuda, C. Sasaki, S. Ishihara, T. Mizutani, K. Nakamura, T. Ayabe, K. Kawabata, and H. Haga. Stiff substrates increase yap-signaling-mediated matrix metalloproteinase-7 expression. *Oncogenesis*, 4(9):e165, 2015.

[121] P. W. Oakes, S. Banerjee, M. C. Marchetti, and M. L. Gardel. Geometry regulates traction stresses in adherent cells. *Biophysical journal*, 107(4):825–833, 2014.

[122] P. W. Oakes and M. L. Gardel. Stressing the limits of focal adhesion mechanosensitivity. *Current opinion in cell biology*, 30:68–73, 2014.

[123] S. Okada, S. Yoshida, S. H. Ashrafi, and D. E. Schraufnagel. The canalicular structure of compact bone in the rat at different ages. *Microscopy and Microanalysis*, 8(2):104, 2002.

[124] F. Paic, J. C. Igwe, R. Nori, M. S. Kronenberg, T. Franceschetti, P. Harrington, L. Kuo, D.-G. Shin, D. W. Rowe, S. E. Harris, et al. Identification of differentially expressed genes between osteoblasts and osteocytes. *Bone*, 45(4):682–692, 2009.

[125] R. Pankov, E. Cukierman, B.-Z. Katz, K. Matsumoto, D. C. Lin, S. Lin, C. Hahn, and K. M. Yamada. Integrin dynamics and matrix assembly tensin-dependent translocation of $\alpha 5\beta 1$ integrins promotes early fibronectin fibrillogenesis. *The Journal of cell biology*, 148(5):1075–1090, 2000.

[126] R. Pearson, L. Misconi, and B. Kemp. Smooth muscle myosin kinase requires residues on the cooh-terminal side of the phosphorylation site. peptide inhibitors. *Journal of Biological Chemistry*, 261(1):25–27, 1986.

[127] R. J. Pelham and Y.-l. Wang. Cell locomotion and focal adhesions are regulated by substrate flexibility. *Proceedings of the National Academy of Sciences*, 94(25):13661–13665, 1997.

[128] C. M. Perrault, A. Brugues, E. Bazellieres, P. Ricco, D. Lacroix, and X. Trepat. Traction forces of endothelial cells under slow shear flow. *Biophysical journal*, 109(8):1533–1536, 2015.

[129] S. R. Peyton and A. J. Putnam. Extracellular matrix rigidity governs smooth muscle cell motility in a biphasic fashion. *Journal of cellular physiology*, 204(1):198–209, 2005.

[130] V. Placet and P. Delobelle. Mechanical properties of bulk polydimethylsiloxane for microfluidics over a large range of frequencies and aging times. *Journal of Micromechanics and Microengineering*, 25(3):035009, 2015.

[131] E. J. Plosa, K. A. Gooding, R. Zent, and L. S. Prince. Nonmuscle myosin ii regulation of lung epithelial morphology. *Developmental Dynamics*, 241(11):1770–1781, 2012.

[132] W. J. Polacheck, J. L. Charest, and R. D. Kamm. Interstitial flow influences direction of tumor cell migration through competing mechanisms. *Proceedings of the National Academy of Sciences*, 108(27):11115–11120, 2011.

[133] S. M. Ponik, J. W. Triplett, and F. M. Pavalko. Osteoblasts and osteocytes respond differently to oscillatory and unidirectional fluid flow profiles. *Journal of cellular biochemistry*, 100(3):794–807, 2007.

[134] A. Rape, W.-h. Guo, and Y.-l. Wang. Microtubule depolymerization induces traction force increase through two distinct pathways. *Journal of cell science*, 124(24):4233–4240, 2011.

[135] A. D. Rape, W.-h. Guo, and Y.-l. Wang. The regulation of traction force in relation to cell shape and focal adhesions. *Biomaterials*, 32(8):2043–2051, 2011.

[136] F. Rechenmacher, S. Neubauer, J. Polleux, C. Mas-Moruno, M. De Simone, E. A. Cavalcanti-Adam, J. P. Spatz, R. Fässler, and H. Kessler. Functionalizing $\alpha$v$\beta$3-or $\alpha$5$\beta$1-selective integrin antagonists for surface coating: A method to discriminate integrin subtypes in vitro. *Angewandte Chemie International Edition*, 52(5):1572–1575, 2013.

[137] K. J. Regehr, M. Domenech, J. T. Koepsel, K. C. Carver, S. J. Ellison-Zelski, W. L. Murphy, L. A. Schuler, E. T. Alarid, and D. J. Beebe. Biological implications of polydimethylsiloxane-based microfluidic cell culture. *Lab on a Chip*, 9(15):2132–2139, 2009.

[138] C. A. Reinhart-King, M. Dembo, and D. A. Hammer. Endothelial cell traction forces on rgd-derivatized polyacrylamide substrata. *Langmuir*, 19(5):1573–1579, 2003.

[139] C. A. Reinhart-King, M. Dembo, and D. A. Hammer. The dynamics and mechanics of endothelial cell spreading. *Biophysical journal*, 89(1):676–689, 2005.

[140] A. J. Ridley, M. A. Schwartz, K. Burridge, R. A. Firtel, M. H. Ginsberg, G. Borisy, J. T. Parsons, and A. R. Horwitz. Cell migration: integrating signals from front to back. *Science*, 302(5651):1704–1709, 2003.

[141] P. Roca-Cusachs, N. C. Gauthier, A. del Rio, and M. P. Sheetz. Clustering of $\alpha 5\beta 1$ integrins determines adhesion strength whereas $\alpha v\beta 3$ and talin enable mechanotransduction. *Proceedings of the National Academy of Sciences*, 106(38):16245–16250, 2009.

[142] P. Roca-Cusachs, T. Iskratsch, and M. P. Sheetz. Finding the weakest link–exploring integrin-mediated mechanical molecular pathways. *Journal of cell science*, 125(13):3025–3038, 2012.

[143] M. R. Rogel, P. N. Soni, J. R. Troken, A. Sitikov, H. E. Trejo, and K. M. Ridge. Vimentin is sufficient and required for wound repair and remodeling in alveolar epithelial cells. *The FASEB Journal*, 25(11):3873–3883, 2011.

[144] M. Rolli, E. Fransvea, J. Pilch, A. Saven, and B. Felding-Habermann. Activated integrin $\alpha v\beta 3$ cooperates with metalloproteinase mmp-9 in regulating migration of metastatic breast cancer cells. *Proceedings of the National Academy of Sciences*, 100(16):9482–9487, 2003.

[145] T. D. Ross, B. G. Coon, S. Yun, N. Baeyens, K. Tanaka, M. Ouyang, and M. A. Schwartz. Integrins in mechanotransduction. *Current opinion in cell biology*, 25(5):613–618, 2013.

[146] P. R. Sager. Cytoskeletal effects of acrylamide and 2, 5-hexanedione: selective aggregation of vimentin filaments. *Toxicology and applied pharmacology*, 97(1):141–155, 1989.

[147] H. B. Schiller, C. C. Friedel, C. Boulegue, and R. Fässler. Quantitative proteomics of the integrin adhesome show a myosin ii-dependent recruitment of lim domain proteins. *EMBO reports*, 12(3):259–266, 2011.

[148] H. B. Schiller, M.-R. Hermann, J. Polleux, T. Vignaud, S. Zanivan, C. C. Friedel, Z. Sun, A. Raducanu, K.-E. Gottschalk, M. Théry, et al. $\beta 1$-and $\alpha v$-class integrins cooperate to regulate myosin ii during rigidity sensing of fibronectin-based microenvironments. *Nature cell biology*, 15(6):625–636, 2013.

[149] M. S. Shutova, A. Y. Alexandrova, and J. M. Vasiliev. Regulation of polarity in cells devoid of actin bundle system after treatment with inhibitors of myosin ii activity. *Cell motility and the cytoskeleton*, 65(9):734–746, 2008.

[150] V. K. Sidhaye, K. S. Schweitzer, M. J. Caterina, L. Shimoda, and L. S. King. Shear stress regulates aquaporin-5 and airway epithelial barrier function. *Proceedings of the National Academy of Sciences*, 105(9):3345–3350, 2008.

[151] S. Singh, S. Sadacharan, S. Su, A. Belldegrun, S. Persad, and G. Singh. Overexpression of vimentin role in the invasive phenotype in an androgen-independent model of prostate cancer. *Cancer research*, 63(9):2306–2311, 2003.

[152] W. T. Smolik, W. Święszkowski, K. J. Kurzydłowski, A. Bruinink, and N. Danz. Image processing algorithm for cell force sensor with a micropillar patterned substrate. *Biocybernetics and Biomedical Engineering*, 30:49–64, 2010.

[153] N. J. Sniadecki, A. Anguelouch, M. T. Yang, C. M. Lamb, Z. Liu, S. B. Kirschner, Y. Liu, D. H. Reich, and C. S. Chen. Magnetic microposts as an approach to apply forces to living cells. *Proceedings of the National Academy of Sciences*, 104(37):14553–14558, 2007.

[154] E. V. Sokurenko, V. Vogel, and W. E. Thomas. Catch-bond mechanism of force-enhanced adhesion: counterintuitive, elusive, but... widespread? *Cell host & microbe*, 4(4):314–323, 2008.

[155] R. L. Steward, C.-M. Cheng, D. Y. Jonathan, R. M. Bellin, and P. R. LeDuc. Mechanical stretch and shear flow induced reorganization and recruitment of fibronectin in fibroblasts. *Scientific reports*, 1, 2011.

[156] J. Stricker, Y. Aratyn-Schaus, P. W. Oakes, and M. L. Gardel. Spatiotemporal constraints on the force-dependent growth of focal adhesions. *Biophysical journal*, 100(12):2883–2893, 2011.

[157] T. Sugitate, T. Kihara, X.-Y. Liu, and J. Miyake. Mechanical role of the nucleus in a cell in terms of elastic modulus. *Current Applied Physics*, 9(4):e291–e293, 2009.

[158] S. X. Sun, S. Walcott, and C. W. Wolgemuth. Cytoskeletal cross-linking and bundling in motor-independent contraction. *Current Biology*, 20(15):R649–R654, 2010.

[159] M. A. Swartz and M. E. Fleury. Interstitial flow and its effects in soft tissues. *Annu. Rev. Biomed. Eng.*, 9:229–256, 2007.

[160] J. L. Tan, J. Tien, and C. S. Chen. Microcontact printing of proteins on mixed self-assembled monolayers. *Langmuir*, 18(2):519–523, 2002.

[161] J. L. Tan, J. Tien, D. M. Pirone, D. S. Gray, K. Bhadriraju, and C. S. Chen. Cells lying on a bed of microneedles: an approach to isolate mechanical force. *Proceedings of the National Academy of Sciences*, 100(4):1484–1489, 2003.

[162] H. Tavana, C.-H. Kuo, Q. Y. Lee, B. Mosadegh, D. Huh, P. J. Christensen, J. B. Grotberg, and S. Takayama. Dynamics of liquid plugs of buffer and surfactant solutions in a micro-engineered pulmonary airway model. *Langmuir*, 26(5):3744–3752, 2009.

[163] H. Tavana, P. Zamankhan, P. J. Christensen, J. B. Grotberg, and S. Takayama. Epithelium damage and protection during reopening of

occluded airways in a physiologic microfluidic pulmonary airway model. *Biomedical microdevices*, 13(4):731–742, 2011.

[164] M. Théry and M. Piel. Adhesive micropatterns for cells: a microcontact printing protocol. *Cold Spring Harbor Protocols*, 2009(7):pdb–prot5255, 2009.

[165] J. W. Thomas, B. Ellis, R. J. Boerner, W. B. Knight, G. C. White, and M. D. Schaller. Sh2-and sh3-mediated interactions between focal adhesion kinase and src. *Journal of Biological Chemistry*, 273(1):577–583, 1998.

[166] E. Tkachenko, E. Gutierrez, S. K. Saikin, P. Fogelstrand, C. Kim, A. Groisman, and M. H. Ginsberg. The nucleus of endothelial cell as a sensor of blood flow direction. *Biology open*, page BIO20134622, 2013.

[167] I. M. Tolić-Nørrelykke and N. Wang. Traction in smooth muscle cells varies with cell spreading. *Journal of biomechanics*, 38(7):1405–1412, 2005.

[168] L. Trichet, J. Le Digabel, R. J. Hawkins, S. R. K. Vedula, M. Gupta, C. Ribrault, P. Hersen, R. Voituriez, and B. Ladoux. Evidence of a large-scale mechanosensing mechanism for cellular adaptation to substrate stiffness. *Proceedings of the National Academy of Sciences*, 109(18):6933–6938, 2012.

[169] G. A. Truskey and T. L. Proulx. Relationship between 3t3 cell spreading and the strength of adhesion on glass and silane surfaces. *Biomaterials*, 14(4):243–254, 1993.

[170] Q. Tseng, I. Wang, E. Duchemin-Pelletier, A. Azioune, N. Carpi, J. Gao, O. Filhol, M. Piel, M. Théry, and M. Balland. A new micropatterning method of soft substrates reveals that different tumorigenic signals can promote or reduce cell contraction levels. *Lab on a chip*, 11(13):2231–2240, 2011.

[171] D. Tsuruta and J. C. Jones. The vimentin cytoskeleton regulates focal contact size and adhesion of endothelial cells subjected to shear stress. *Journal of Cell Science*, 116(24):4977–4984, 2003.

[172] E. Tzima, M. A. del Pozo, S. J. Shattil, S. Chien, and M. A. Schwartz. Activation of integrins in endothelial cells by fluid shear stress mediates rho-dependent cytoskeletal alignment. *The EMBO journal*, 20(17):4639–4647, 2001.

[173] E. Tzima, M. Irani-Tehrani, W. B. Kiosses, E. Dejana, D. A. Schultz, B. Engelhardt, G. Cao, H. DeLisser, and M. A. Schwartz. A mechanosensory complex that mediates the endothelial cell response to fluid shear stress. *Nature*, 437(7057):426–431, 2005.

[174] H. van Hoorn, R. Harkes, E. M. Spiesz, C. Storm, D. van Noort, B. Ladoux, and T. Schmidt. The nanoscale architecture of force-bearing focal adhesions. *Nano letters*, 14(8):4257–4262, 2014.

[175] D. G. Vanderlaan, I. M. Nunez, M. Hargiss, M. L. Alton, and S. Williams. Soft contact lenses, Dec. 7 1999. US Patent 5,998,498.

[176] M. Vicente-Manzanares, X. Ma, R. S. Adelstein, and A. R. Horwitz. Non-muscle myosin ii takes centre stage in cell adhesion and migration. *Nature reviews Molecular cell biology*, 10(11):778–790, 2009.

[177] M. Vicente-Manzanares, J. Zareno, L. Whitmore, C. K. Choi, and A. F. Horwitz. Regulation of protrusion, adhesion dynamics, and polarity by myosins iia and iib in migrating cells. *The Journal of cell biology*, 176(5):573–580, 2007.

[178] L. G. Vincent, Y. S. Choi, B. Alonso-Latorre, J. C. del Álamo, and A. J. Engler. Mesenchymal stem cell durotaxis depends on substrate stiffness gradient strength. *Biotechnology journal*, 8(4):472–484, 2013.

[179] G. von Wichert, G. Jiang, A. Kostic, K. De Vos, J. Sap, and M. P. Sheetz. Rptp-$\alpha$ acts as a transducer of mechanical force on $\alpha$v/$\beta$3-integrin–cytoskeleton linkages. *The Journal of cell biology*, 161(1):143–153, 2003.

[180] F.-S. Wang, J. S. Wolenski, R. E. Cheney, M. S. Mooseker, and D. G. Jay. Function of myosin-v in filopodial extension of neuronal growth cones. *Science*, 273(5275):660–663, 1996.

[181] H.-B. Wang, M. Dembo, S. K. Hanks, and Y.-l. Wang. Focal adhesion kinase is involved in mechanosensing during fibroblast migration. *Proceedings of the National Academy of Sciences*, 98(20):11295–11300, 2001.

[182] N. Wang and D. Stamenović. Contribution of intermediate filaments to cell stiffness, stiffening, and growth. *American Journal of Physiology-Cell Physiology*, 279(1):C188–C194, 2000.

[183] X.-B. Wang, J. Sun, C.-M. Chen, X.-Q. Sun, F. Wang, and D.-M. Zhang. Thermal uv treatment on su-8 polymer for integrated optics. *Optical Materials Express*, 4(3):509–517, 2014.

[184] Z. Wang, A. A. Volinsky, and N. D. Gallant. Crosslinking effect on polydimethylsiloxane elastic modulus measured by custom-built compression instrument. *Journal of Applied Polymer Science*, 131(22), 2014.

[185] Z. Wang, A. A. Volinsky, and N. D. Gallant. Nanoindentation study of polydimethylsiloxane elastic modulus using berkovich and flat punch tips. *Journal of Applied Polymer Science*, 132(5), 2015.

[186] C. M. Waters, E. Roan, and D. Navajas. Mechanobiology in lung epithelial cells: measurements, perturbations, and responses. *Comprehensive Physiology*, 2011.

[187] S. Weinbaum, S. Cowin, and Y. Zeng. A model for the excitation of osteocytes by mechanical loading-induced bone fluid shear stresses. *Journal of biomechanics*, 27(3):339–360, 1994.

[188] G. Wiche, S. Osmanagic-Myers, and M. J. Castañón. Networking and anchoring through plectin: a key to if functionality and mechanotransduction. *Current opinion in cell biology*, 32:21–29, 2015.

[189] J. W. Wragg, S. Durant, H. M. McGettrick, K. M. Sample, S. Egginton, and R. Bicknell. Shear stress regulated gene expression and angiogenesis in vascular endothelium. *Microcirculation*, 21(4):290–300, 2014.

[190] H. Xu, J. Zhang, J. Wu, Y. Guan, Y. Weng, and P. Shang. Oscillatory fluid flow elicits changes in morphology, cytoskeleton and integrin-associated molecules in mlo-y4 cells, but not in mc3t3-e1 cells. *Biological research*, 45(2):163–169, 2012.

[191] H. C. Yalcin, S. F. Perry, and S. N. Ghadiali. Influence of airway diameter and cell confluence on epithelial cell injury in an in vitro model of airway reopening. *Journal of Applied Physiology*, 103(5):1796–1807, 2007.

[192] M. T. Yang, J. Fu, Y.-K. Wang, R. A. Desai, and C. S. Chen. Assaying stem cell mechanobiology on microfabricated elastomeric substrates with geometrically modulated rigidity. *nature protocols*, 6(2):187–213, 2011.

[193] Y. Yang, J. Dowling, Q.-C. Yu, P. Kouklis, D. W. Cleveland, and E. Fuchs. An essential cytoskeletal linker protein connecting actin microfilaments to intermediate filaments. *Cell*, 86(4):655–665, 1996.

[194] Z. Yang, J.-S. Lin, J. Chen, and J. H. Wang. Determining substrate displacement and cell traction fields?a new approach. *Journal of theoretical biology*, 242(3):607–616, 2006.

[195] T. Yeung, P. C. Georges, L. A. Flanagan, B. Marg, M. Ortiz, M. Funaki, N. Zahir, W. Ming, V. Weaver, and P. A. Janmey. Effects of substrate stiffness on cell morphology, cytoskeletal structure, and adhesion. *Cell motility and the cytoskeleton*, 60(1):24–34, 2005.

[196] A. K. Yip, K. Iwasaki, C. Ursekar, H. Machiyama, M. Saxena, H. Chen, I. Harada, K.-H. Chiam, and Y. Sawada. Cellular response to substrate rigidity is governed by either stress or strain. *Biophysical journal*, 104(1):19–29, 2013.

[197] H. Zhang, J. S. Berg, Z. Li, Y. Wang, P. Lång, A. D. Sousa, A. Bhaskar, R. E. Cheney, and S. Strömblad. Myosin-x provides a motor-based link between integrins and the cytoskeleton. *Nature cell biology*, 6(6):523–531, 2004.

[198] X. Zheng and X. Zhang. An optical moire technique for cell traction force mapping. *Journal of Micromechanics and Microengineering*, 18(12):125006, 2008.

[199] X. R. Zheng and X. Zhang. Microsystems for cellular force measurement: a review. *Journal of Micromechanics and Microengineering*, 21(5):054003, 2011.

# Publications

### Publications

- M. Gulic, T. Kerst, K.-E. Gottschalk, Automated analysis of cellular traction forces measured with microposts, submitted

### Presentations

- Poster presentation at the spring meeting of the 'Deutsche Physikalische Gesellschaft' in Berlin, 2015. M. Gulic, R. Fässler, T. Kerst, K.-E. Gottschalk, Analysing the influence of external shear stress on cellular force generation.
- Poster presentation at the spring meeting of the 'Deutsche Physikalische Gesellschaft' in Dresden, 2014. M. Gulic, R. Fässler, T. Kerst, K.-E. Gottschalk, The Influence of substrate characteristics on integrin mediated cell properties.
- Poster presentation at the conference of the '28th European Cytoskeleton Forum' in Fribourg, Switzerland, 2013. M. Gulic, R. Fässler, T. Kerst, K.-E. Gottschalk, The influence of substrate stiffness on integrin mediated cell properties.
- Oral presentation at the spring meeting of the 'Deutsche Physikalische Gesellschaft' in Regensburg, 2013. M. Gulic, R. Fässler, T. Kerst, K.-E. Gottschalk, The influence of substrate stiffness on integrin mediated cell properties.
- Poster presentation at the spring meeting of the 'Deutsche Physikalische Gesellschaft' in Berlin, 2012. M. Gulic, R. Fässler, K.-E. Gottschalk, The influence of substrate stiffness on integrin mediated cell properties.

# Declaration of Authorship

I certify that the work presented here is, to the best of my knowledge and belief, original and the result of my own investigations, except as acknowledged, and has not been submitted, either in part or whole, for a degree at this or any other University.

Ulm, October 23, 2016

Maja Gulic

# Acknowledgements

Die Danksagung wurde aus Datenschutzgründen aus der elektronischen Version entfernt.

# Curriculum vitae

Der Lebenslauf wurde aus Datenschutzgründen aus der elektronischen Version entfernt.